



HAL
open science

GPS observation of geophysical deformations induced by non tidal loading

Marcell Ferenc

► To cite this version:

Marcell Ferenc. GPS observation of geophysical deformations induced by non tidal loading. Climatology. Conservatoire national des arts et metiers - CNAM, 2014. English. NNT : 2014CNAM0977 . tel-01644807

HAL Id: tel-01644807

<https://theses.hal.science/tel-01644807>

Submitted on 22 Nov 2017

HAL is a multi-disciplinary open access archive for the deposit and dissemination of scientific research documents, whether they are published or not. The documents may come from teaching and research institutions in France or abroad, or from public or private research centers.

L'archive ouverte pluridisciplinaire **HAL**, est destinée au dépôt et à la diffusion de documents scientifiques de niveau recherche, publiés ou non, émanant des établissements d'enseignement et de recherche français ou étrangers, des laboratoires publics ou privés.

ÉCOLE DOCTORALE SPIGA
LABORATOIRE GÉOMATIQUE & FONCIER

THÈSE présentée par :

Marcell FERENC

soutenue le : **9 Décembre 2014**

pour obtenir le grade de : **Docteur du Conservatoire National des Arts et Métiers**

Discipline / Spécialité : **GÉOMATIQUE**

**Observation par GPS
des déformations géophysiques
dues aux surcharges non maréales**

THÈSE dirigée par :

M. POLIDORI Laurent

Professeur, Cnam

Mme. NICOLAS-DUROY Joëlle

Maître de conférences, Cnam

RAPPORTEURS :

M. CALAIS Eric

Professeur, École Normale Supérieure (UMR 8538)

M. WÖPPELMANN Guy

Professeur, Université de La Rochelle (UMR LIENSs 7266)

JURY :

M. BOY Jean-Paul

Physicien, EOST - Université de Strasbourg (IPGS - UMR 751)

M. MOCQUET Antoine

Professeur, Université Nantes (LPG UMR CNRS 6112)

Mme. van DAM Tonie

Professeur, Université du Luxembourg

*"Don't cry because it's over, smile because it happened."
Dr. Seuss*

Acknowledgements

First of all I would like to express my special gratitude to my thesis director Laurent Polidori and co-advisor Joëlle Nicolas for their continuous scientific and personal support and guidance as well as their boundless patience. I sincerely thank them for the opportunity and their trust they have demonstrated after my short period visit at the ESGT/L2G laboratory in 2010 and which led us to this thesis. I gratefully acknowledge the other members of my thesis committee, Richard Biancale, Antoine Mocquet and Tonie van Dam for their feedback, constructive comments and co-operation during these three years.

I would like to thank Richard Biancale, and the GRGS for organizing the GRGS summer schools from which I have benefited a lot. Particular thanks goes to Tonie van Dam who played an important role in this thesis as she generously hosted me in her laboratory at the University of Luxembourg and took time explaining me about loading effects and shared her experiences together with Zhao Li. I am very grateful to the GINS-PC team in Toulouse, especially to Félix Perosanz for his time he gave me in Toulouse and his non-stop available technical support and of course to Jean-Charles Marty, Sylvain Loyer, Denis Laurichesse and Flavien Mercier for their continuous development and provision the GPS community with a powerful geodetic software that I have used for my research. I thank the GINS-PC team also for the organization of the GINS trainings and GINS days events which contributed significantly to my studies. I sincerely thank Xavier Collilieux to guide me into the world of CATREF and for sharing his knowledge and experiences with me on geodetic time serie analysis. I would like to thank Jean-Paul Boy for his comments and suggestions as well as his time for providing me his loading series. I also would like to acknowledge the supporting words and the help of Alexis Rigo and Philippe Vernant. We

are grateful to SONEL¹ and REFMAR² providing us tide gauge time series and also to Météo France for surface pressure data. However, these datasets finally are not presented here.

Of course, this thesis would not be able to begin without any funding, therefore, I seize the opportunity to thank the CNES and Région des Pays de la Loire for their financial support.

I thank István Zergi, Sándor Bíró and István Havasi for my initial steps in the field of geodesy. I also thank József Ádám and the team at the Hungarian Space Geodetic Observatory, especially Gyula Grenerczy and Ambrus Kenyeres for the opportunity to continue and to reach this point where I am now. I thank also Attila Komjáthy for his encouraging words concerning my thesis.

These three years were difficult far from my beloved ones, however thanks to the cheerful colleagues and friends at the ESGT and in Le Mans I didn't felt alone. I would like to thanks Monica, her husband and her daughter for their kindness and hospitality who were like my family in Le Mans. I will never forget the great times we passed together in and outside the ESGT with Mohamed, Paulo, André and Frédéric as well as my friends outside ESGT, who they call themselves group Le Mans.

Before my final words I can say about this three year long journey the famous quote "I think this is the beginning of a beautiful friendship" which is true both for my personal and professional life.

My special thanks go to my family and friends who always supporting and encouraging me to never give up.

Finally, I would like to express my endless love to my fiancée Éva "Vicus" for her patience and support during this long distance relationship period. These difficult moments will soon belong to the past and we continue our future together.

¹Système d'Observation du Niveau des Eaux Littorales

²Réseaux de référence des observations marégraphiques

Abstract

The temporal and spatial redistribution of the environmental masses deform the surface of the Earth. These deformations are observable by space geodetic techniques such as GPS. Since highly accurate IGS satellite and clock data are available and sophisticated algorithms have been developed, the integer fixed ambiguity Precise Point Positioning (iPPP) method opened a new era for the Global Positioning System (GPS) analysis and its application in geophysical studies. This work is among the first studies to investigate the different loading effects using iPPP time series, particularly using the GINS-PC software and the new, reprocessed REPRO2 orbit and clock products of GRGS (GR2). We aim to exploit the sub-daily iPPP time series to study various Earth deformation effects at different time scales, from sub-daily to seasonal and annual periods. Our goal is to contribute to the validation of geophysical models, to the observation of the various non-tidal phenomena, as well as the presentation of the performance of the iPPP mode and the GINS-PC package that is a powerful tool for geodynamical applications, and to investigate the influence of the loading effects on geodetic time series interpretation. After an overview of the main deformations of the Earth's surface induced by loading effects, we present the geodetic techniques that already demonstrated their potential in deformation analysis, in particular in loading deformation studies. We then review the GPS technique and the iPPP processing mode as it was our choice for the data analysis. We continue towards a global study which gives base for future research. After, we demonstrate two regional studies. The first one investigates the influence of the loading effects on GPS campaign to determine tectonic velocities in the Pyrenees mountain chain. The second case study attempts to track the spatial and temporal evolution of an extreme storm event, the Xynthia windstorm that occurred in France, in 2010. This study also tries to identify the ocean's response to the fast moving low pressure system using sub-daily iPPP time series.

Keywords :

GPS, GINS-PC, iPPP, deformation, non-tidal loading, Xynthia, Pyrenees

Résumé

La redistribution temporelle et spatiale des masses environnementales déforment la surface de la Terre. Ces déformations sont observables par des techniques de géodésie spatiale telles que le GPS (Global Positioning System). Depuis que les produits d'orbite et d'horloge très précis de l'IGS (International GNSS Service) sont disponibles, que des algorithmes sophistiqués ont été développés, l'iPPP (integer fixed ambiguity Precise Point Positioning) a ouvert une nouvelle ère pour l'analyse du GPS et pour son application dans les études géophysiques. Ce travail fait partie des premières études pour analyser les différents effets de surcharge, en utilisant des séries temporelles de positionnement, en particulier avec le logiciel GINS-PC et les nouveaux produits d'orbite et d'horloge REPRO2 du GRGS (Groupe de Recherche en Géodésie Spatiale) (GR2). Nous visons à exploiter les positions sub-diurnes d'iPPP pour étudier divers effets de déformation de la Terre à différentes échelles de temps : sub-diurne à saisonniers et annuels. Notre objectif est de contribuer à la validation des modèles géophysiques, à l'observation des différents phénomènes non-maréaux, mais aussi de présenter la performance du mode iPPP et du logiciel GINS-PC. Ce dernier est un outil puissant pour les applications géodynamiques, qui permet d'étudier l'influence des effets de surcharge sur l'interprétation géodésique des séries temporelles de positionnement. Après un aperçu des principales déformations de la surface de la Terre induites par les effets de surcharge, nous présentons les techniques de géodésie qui ont déjà démontré leur potentiel dans l'analyse de déformation, en particulier dans les études de déformation de surcharge. Nous présentons ensuite la technique GPS et le mode de traitement iPPP que nous utilisons pour l'analyse des données. Nous continuons vers une étude globale qui pose les bases pour de futures recherches. Nous montrons ensuite les résultats de deux études régionales. La première analyse étudie l'influence des effets de surcharge sur la détermination des vitesses tectoniques dans la chaîne des Pyrénées à partir de campagnes GPS espacées dans le temps. Le deuxième cas d'étude tente de suivre l'évolution spatiale et temporelle des déformations induites par un événement de tempête extrême, à savoir la tempête Xynthia qui a eu lieu en France en 2010. Cette étude tente également d'identifier la réponse dynamique de l'océan pour le système de basse pression atmosphérique se déplaçant rapidement en utilisant des séries temporelles sub-diurnes.

Mots clés :

GPS, GINS-PC, iPPP, déformation, surcharge non-maréale, Xynthia, Pyrenees

Contents

Abbreviations	xxvii
Résumé long	xxxii
Introduction	1
I Loading deformations and observation techniques	5
1 Deformation of the Earth's surface	7
1.1 Environmental loading effects	8
1.1.1 Tidal loading effects	9
1.1.2 Non-tidal loading effects	10
1.1.3 The origin of the different effects	10
1.2 Summary of the chapter	19
2 Space geodetic observations of loading deformations	23
2.1 Reference system	23
2.2 Space geodetic observations	25
2.2.1 Very Long Baseline Radio Interferometry (VLBI)	25
2.2.2 Satellite Laser Ranging (SLR)	26
2.2.3 Global Navigation Satellite System (GNSS)	26

2.2.4	Satellite Gravimetry with Gravity Recovery And Climate Experiment (GRACE)	27
2.2.5	Interferometric Synthetic Aperture Radar (InSAR)	29
2.3	Loading effects as errors in deformation measurements	29
2.3.1	Validity of loading corrections	30
2.3.2	Influence of loading on data interpretation	30
3	Global Positioning System (GPS)	33
3.1	General principle	33
3.2	Error sources in GPS positioning	34
3.2.1	Clock errors	35
3.2.2	Orbit error	35
3.2.3	Effect of propagation medium	36
3.2.4	Relativistic effects	39
3.2.5	Phase wind-up	40
3.2.6	Antenna phase center offset and variation	40
3.2.7	Multipath	41
3.2.8	Site displacement effects	42
3.3	GPS processing strategies	43
3.3.1	Double Differencing (DD)	43
3.3.2	Precise Point Positioning (PPP)	45
II	Towards a global study	51
4	Towards a global study	53
4.1	Introduction	53
4.2	The selected regions	54

4.3	The GPS data	57
4.4	Results	60
4.4.1	RMS analysis	61
4.4.2	Seasonal amplitudes	63
4.5	New tool for seasonal analysis	65
4.5.1	Method of the analysis	65
4.5.2	Two examples of the results	67
4.6	Conclusion	71
III	Regional studies	73
5	Loading artifact in tectonic deformation monitoring of the Pyrenees	77
5.1	Introduction	78
5.2	Loading effect models and displacement signals in the studied area	80
5.3	Velocity signal induced by loading effects	86
5.4	Comparison with preliminary GPS results	89
5.5	Dependence of loading effects on survey timing and frequency	92
5.6	Conclusions	97
6	Monitoring the impact of the Xynthia windstorm	101
6.1	Introduction	101
6.2	European windstorm Xynthia	103
6.3	The GPS data	107
6.4	The spatial window	111
6.5	Applied models of the non-tidal loading effects	113
6.5.1	Non-tidal atmospheric loading	114
6.5.2	Non-tidal ocean loading	116

CONTENTS

6.5.3	Hydrological loading	117
6.5.4	Summary	118
6.6	Small discussion on model space resolution	119
6.6.1	Few words on the S1 and S2 tidal atmospheric signal	123
6.6.2	Few words on the hydrological signal	125
6.7	Results	126
6.7.1	Comparison between GRG and GR2 GPS solutions	126
6.7.2	Comparison of the GR2 results and the models	133
6.8	Conclusion	162
7	Challenges	165
7.1	Discontinuities in the time series	166
7.2	Ocean tidal correction in GINS-PC	170
7.3	Processing time using the interface	179
	Conclusion and Perspectives	183
	Bibliography	185
	Appendix	
	A Global	
	B Xynthia	
	C Challenges	

List of Tables

2	Amplitudes horizontales et verticales de l'effet des déformations.	xxxiii
3	Les acronymes des modèles de surcharge appliquées.	xliv
1.1	Various online services which provide non-tidal atmospheric, hydrologic and oceaning loading models.	19
1.2	Horizontal and vertical magnitudes of the deformational effect.	20
4.1	Processing parameters that we applied to obtain our GPS time series.	59
4.2	RMS up in mm of the different time series.	62
4.3	RMS up in terms of percentage for the different time series.	62
4.4	The annual amplitudes determined from the 6 year long time series.	64
4.5	The semi-annual amplitudes determined from the 6 year long time series.	64
5.1	Statistical data for ATML, CWSL, NTOL models, and the corresponding accumulated effect.	83
5.2	Velocity effects for the original ResPyr campaigns on the North, East, and Up components in mm/yr.	87
5.3	GPS velocity estimates statistical results for the ResPyr stations in mm/yr.	90
5.4	Velocity effects for the virtual ResPyr campaigns on the North, East, and Up components in mm/yr.	93
5.5	Field measurement frequency and their resulting horizontal azimuth for a particular month (July).	95

LIST OF TABLES

6.1	GPS processing parameters.	109
6.2	The acronyms of the applied loading models.	118
6.3	The availability of the GPS and model datasets used in this study.	118
6.4	The median RMS of the differences between the point calculated and the grid version of the loading series.	122
6.5	Descriptive statistics of the GRG results.	129
6.6	Descriptive statistics of the GR2 results.	130
6.7	Descriptive statistics of the differences between GRG and GR2 results.	131
6.8	The occurrence of the values of the GRG and GR2 RMS ratios compared to 1.	132
6.9	Atmospheric model differences.	135
6.10	GPS a posteriori corrections applying different models.	136
7.1	RMS values of iPPP results estimated using the nominal_FES2004 OTL at 10 RGP stations.	173
7.2	RMS values of iPPP results estimated using the Scherneck_FES2004 OTL at 10 RGP stations.	173
7.3	RMS values of iPPP result differences.	174
7.4	Number of stations with M2 up tidal wave absolute differences above certain values between nominal_FES2004 and Scherneck_FES2004 OTL files.	176
A.1	Correlation table of GPS and CWSL model up component at BRAZ station.	
A.2	Correlation table of GPS and sum of models up component at BRAZ station.	
A.3	Correlation table of GPS and ATML model up component at BRAZ station.	
A.4	Correlation table of GPS and NTOL model up component at BRAZ station.	
A.5	Correlation table of GPS and ATML up component at ALIC station.	
A.6	Correlation table of GPS and the sum of models up component at ALIC station.	

LIST OF TABLES

C.1 Absolute differences between nominal_FES2004 and Scherneck_FES2004
OTL files in terms of M2 and S2 tidal waves.

List of Figures

1	Notre réseau contenant 10 stations GPS.	xxxv
2	Séries temporelles GPS GRG (rouge) et GR2 (bleu) dans les stations BRAZ. xxxvi	
3	Différences entre les modèles atmosphériques ATML et TOPO.	xxxix
4	Effet de surcharge cumulé et les vitesses GPS horizontales dans mm/an. . .	xli
5	Image satellite du Xynthia.	xliii
6	La trace de la tempête Xynthia et le réseau GPS étudié.	xliv
7	Séries temporelles GPS et modèles des surcharges.	xlvi
8	Réseaux partiels.	xlvii
9	Epoch 2: Les résultats des mesures GPS après application d'un filtrage spatial. xlix	
10	Epoch 2: Déplacements verticaux issus des différents modèles en fonction de la distance à la côte représentée en échelle logarithmique.	xlix
1.1	The IB ocean response and the non-IB assumption.	12
1.2	Coastal station with IB ocean response and non-IB assumption.	13
1.3	Surface deformation processes on the Earth.	21
3.1	Map of ionospheric scintillation frequency at solar maximum.	38
3.2	Illustration of ARP, PCO and PCV.	41
3.3	Principle idea of GPS-PPP configuration.	45
3.4	Phase range measurement and the corresponding ambiguity over the satellite pass.	46

LIST OF FIGURES

3.5	Integer ambiguity fixing that is applied at CNES-CLS IGS AC.	47
4.1	Our network containing 10 GPS stations.	56
4.2	GPS time series at BRAZ station.	57
4.3	The power spectra of GPS time series at BRAZ station.	59
4.4	The developed analysis tool.	66
4.5	GPS time series components and their spectrum at BRAZ station.	68
4.6	CWSL time series components and their spectrum at BRAZ station.	69
4.7	The correlation figures for BRAZ and ALIC stations for ATML, CWSL, NTOL and the sum of the models.	70
5.1	Differences between atmospheric ATML and TOPO predicted coordinate displacements.	83
5.2	Non-tidal ocean loading effects at TLSE station.	85
5.3	Horizontal and vertical velocities in mm/yr for different loading effects.	88
5.4	Accumulated loading effect and GPS horizontal velocities in mm/yr.	90
5.5	Virtual horizontal and vertical loading velocity results in mm/yr.	94
5.6	TRMO station simulation results in terms of velocity (mm/yr) for accumulated loading effects.	96
6.1	The ground track of the center of the storm Xynthia and the studied GPS network.	104
6.2	Atmospheric pressure variations at LROC station.	105
6.3	Satellite image of Xynthia.	105
6.4	Isobar maps of Xynthia.	106
6.5	GRG and GR2 iPPP time series at LROC (La Rochelle) station.	110
6.6	GRG and GR2 iPPP time series at STJ9 (Strasbourg) station.	110
6.7	Subnetworks.	112

LIST OF FIGURES

6.8	GPS and model time series during Xynthia for two stations.	119
6.9	RMS map of the differences between ATMIB and its grid interpolated version.	120
6.10	RMS map of the differences between ATMMO and its grid interpolated version.	121
6.11	RMS map of the differences between HYDRO and its grid interpolated version.	122
6.12	RMS map of the differences (after separately determined and removed offset, trend, S1 and S2 periods) between ATMIB and its grid interpolated version.	124
6.13	RMS map of the differences (after separately determined and removed offset, trend, S1 and S2 periods) between ATMMO and its grid interpolated version.	124
6.14	Soil moisture map of Europe at the end of February 2010.	125
6.15	RMS map of the differences (after separately determined and removed offset and trend) between HYDRO and its grid interpolated version.	126
6.16	RMS of GRG and GR2 results for a two month period centered on the storm.	127
6.17	RMS of GRG and GR2 results for a two month long calm period.	128
6.18	Ratio of the RMS of the GRG and the GR2 solutions during the storm and during the calm period.	128
6.19	The power spectral density of the stacked GRG and GR2 time series.	134
6.20	Expected horizontal displacements associated to uplift and subsidence.	137
6.21	Epoch 1: Horizontal and vertical GPS results (in mm) (without spatial filter).	138
6.22	Epoch 2: Horizontal and vertical GPS results (in mm) (without spatial filter).	138
6.23	Epoch 3: Horizontal and vertical GPS results (in mm) (without spatial filter).	139
6.24	Epoch 4: Horizontal and vertical GPS results (in mm) (without spatial filter).	139
6.25	Epoch 1: Horizontal and vertical GPS results (in mm) applying a spatial filter.	140
6.26	Epoch 2: Horizontal and vertical GPS results (in mm) applying a spatial filter.	140
6.27	Epoch 3: Horizontal and vertical GPS results (in mm) applying a spatial filter.	141

LIST OF FIGURES

6.28	Epoch 4: Horizontal and vertical GPS results (in mm) applying a spatial filter.	141
6.29	Epoch 1: Horizontal and vertical GPS results (in mm) after a posteriori correction with CWSL.	143
6.30	Epoch 2: Horizontal and vertical GPS results (in mm) after a posteriori correction with CWSL.	143
6.31	Epoch 3: Horizontal and vertical GPS results (in mm) after a posteriori correction with CWSL.	144
6.32	Epoch 4: Horizontal and vertical GPS results (in mm) after a posteriori correction with CWSL.	144
6.33	Epoch 1: Horizontal and vertical GPS results (in mm) after a posteriori correction with the sum of ATML and CWSL.	146
6.34	Epoch 2: Horizontal and vertical GPS results (in mm) after a posteriori correction with the sum of ATML and CWSL.	146
6.35	Epoch 3: Horizontal and vertical GPS results (in mm) after a posteriori correction with the sum of ATML and CWSL.	147
6.36	Epoch 4: Horizontal and vertical GPS results (in mm) after a posteriori correction with the sum of ATML and CWSL.	147
6.37	Epoch 1: Horizontal and vertical GPS results (in mm) after a posteriori correction with the sum of NTOL and CWSL.	148
6.38	Epoch 2: Horizontal and vertical GPS results (in mm) after a posteriori correction with the sum of NTOL and CWSL.	149
6.39	Epoch 3: Horizontal and vertical GPS results (in mm) after a posteriori correction with the sum of NTOL and CWSL.	149
6.40	Epoch 4: Horizontal and vertical GPS results (in mm) after a posteriori correction with the sum of NTOL and CWSL.	150
6.41	Epoch 1: Horizontal and vertical components of the sum of ATML, CWSL and NTOL models (in mm).	150

LIST OF FIGURES

6.42 Epoch 2: Horizontal and vertical components of the sum of ATML, CWSL and NTOL models (in mm).	151
6.43 Epoch 3: Horizontal and vertical components of the sum of ATML, CWSL and NTOL models (in mm).	151
6.44 Epoch 4: Horizontal and vertical components of the sum of ATML, CWSL and NTOL models (in mm).	152
6.45 Epoch 1: Horizontal and vertical GPS results (in mm) after a posteriori correction with the sum of ATML, CWSL and NTOL.	153
6.46 Epoch 2: Horizontal and vertical GPS results (in mm) after a posteriori correction with the sum of ATML, CWSL and NTOL.	153
6.47 Epoch 3: Horizontal and vertical GPS results (in mm) after a posteriori correction with the sum of ATML, CWSL and NTOL.	154
6.48 Epoch 4: Horizontal and vertical GPS results (in mm) after a posteriori correction with the sum of ATML, CWSL and NTOL.	154
6.49 The estimated location of the depression at four consecutive epochs.	156
6.50 Epoch 1: Instantaneous plot of up displacements as a function of coastal distance.	157
6.51 Epoch 2: Instantaneous plot of up displacements as a function of coastal distance.	157
6.52 Epoch 3: Instantaneous plot of up displacements as a function of coastal distance.	158
6.53 Epoch 4: Instantaneous plot of up displacements as a function of coastal distance.	158
6.54 Epoch 1: Instantaneous plot of up displacements as a function of coastal distance (logarithmic scale).	159
6.55 Epoch 2: Instantaneous plot of up displacements as a function of coastal distance (logarithmic scale).	159

LIST OF FIGURES

6.56	Epoch 3: Instantaneous plot of up displacements as a function of coastal distance (logarithmic scale).	160
6.57	Epoch 4: Instantaneous plot of up displacements as a function of coastal distance (logarithmic scale).	160
6.58	Correlation between the GR2 and the grd-ATMMO time series during two months.	161
7.1	Superposition of four month long iPPP time series, estimated with GRG products.	166
7.2	Superposition of four months long PPP time series, estimated with IGS products.	167
7.3	Two months long, 6-hourly sampled iPPP GRG time series before and after CATREF.	168
7.4	Translation parameters obtained with CATREF.	168
7.5	Scale parameters obtained with CATREF.	168
7.6	Two months long time series, estimated with GRG, GR2, and IGS products.	169
7.7	Absolute differences between nominal_FES2004 and Scherneck_FES2004 OTL files in terms of M2 and S2 tidal wave up amplitudes.	171
7.8	Nominal_FES2004 and Scherneck_FES2004 M2 tidal wave up amplitudes (in mm) in function of coastal distance.	171
7.9	Nominal_FES2004 and Scherneck_FES2004 M2 tidal wave up amplitude differences (in mm) in function of coastal distance.	171
7.10	Nominal_FES2004 and Scherneck_FES2004 M2 tidal wave east amplitudes (in mm) in function of coastal distance.	172
7.11	Nominal_FES2004 and Scherneck_FES2004 M2 tidal wave east amplitude differences (in mm) in function of coastal distance.	172
7.12	Nominal_FES2004 and Scherneck_FES2004 M2 tidal wave north amplitudes (in mm) in function of coastal distance.	172

LIST OF FIGURES

7.13	Nominal_FES2004 and Scherneck_FES2004 M2 tidal wave north amplitude differences (in mm) in function of coastal distance.	172
7.14	Comparison of 11 tidal waves from nominal_FES2004 and Scherneck_FES2004 files.	175
7.15	Power spectral density of GPS time serie estimated using two different OTL corrections at LROC station.	177
7.16	Power spectral density at LROC.	178
7.17	Two months long iPPP GRG time series of LROC station with two different OTL correction.	178
7.18	Processing scheme that we apply at the moment.	180
7.19	Processing scheme that we would like to achieve.	180
A.1	ATML time series components and their spectrum at BRAZ station.	
A.2	NTOL time series components and their spectrum at BRAZ station.	
A.3	Sum of loading time series components and their spectrum at BRAZ station.	
B.1	Correlation between GR2 and ATML for two months.	
B.2	Correlation between GR2 and MERRA atmospheric pressure for two months.	
B.3	Correlation between GR2 and ECMWF atmospheric pressure for two months.	
B.4	Correlation between GR2 and NOIB for two months.	

Abbreviations

AC	Analysis Center
ACN	total loading signal with ATML, CWSL and NTOL
ANTEX	antenna exchange format
ARP	antenna reference point
ATL	atmospheric pressure tidal loading
ATML	atmospheric pressure loading
ATMMO	atmospheric loading using a dynamic ocean response to pressure
CATREF	Combination and Analysis of Terrestrial Reference Frame
CESBIO	Centre d'Études Spatiales de la BIOSphère
CF	Center of Frame (solid Earth)
CLS	Collecte Localisation Satellites
CM	Center of Mass (solid Earth plus atmosphere and ocean)
CNAM	Conservatoire National des Arts et Métiers
CNES	Centre National d'Études Spatiales (French Space Agency)
CRF	Celestial Reference Frame
CWSL	continental water storage loading
DD	Double Differencing
DEM	Digital Elevation Model
DLR	Deutsches Zentrum für Luft- und Raumfahrt e.V., the German Aerospace Center
ECCO	Estimating the Circulation and Climate of the Ocean
ECMWF	European Centre for Medium-Range Weather Forecasts
EOP	Earth Orientation Parameters
EOST	École et Observatoire des Sciences de la Terre
EPN	European Permanent GNSS Network
ESGT	École Supérieure des Géomètres et Topographes
EU	European Union
FAMOUS	Famous Analysis Mapping On Unusual Sampling
GAMIT	GPS Analysis package at Massachusetts Institute of Technology
GGFC	Global Geophysical Fluids Center
GINs-PC	Géodésie par Intégrations Numériques Simultanées PC
GIPSY-OASIS	GNSS-Inferred Positioning System and Orbit Analysis Simulation Software
GLDAS	Global Land Data Assimilation System
GLOBK	Global Kalman filter VLBI and GPS analysis program
GLONASS	Globalnaya Navigatsionnaya Sputnikovaya Sistema (Russia)
GMF	Global Mapping Function

ABBREVIATIONS

GNSS	Global Navigation Satellite System
GPS	Global Positioning System
GPT	Global Pressure Temperature
GRACE	Gravity Recovery And Climate Experiment
GRGS	Groupe de Recherche en Géodésie Spatiale
IB	inverse barometer
IERS	International Earth Rotation and Reference Systems Service
IGS	International GNSS Service
IHM	Interface Homme Machine (Man Machine Interface)
InSAR	Interferometric Synthetic Aperture Radar
iPPP	integer fixed ambiguity Precise Point Positioning
ITRF	International Terrestrial Reference Frame
ITRS	International Terrestrial Reference System
JPL	Jet Propulsion Laboratory
L2G	Laboratoire de Géomatique et Géosciences
LLN	loading Love numbers
MERRA	Modern Era Retrospective analysis for Research and Applications
MOG2D	2 Dimensions Gravity Waves model
NAO	North Atlantic Ocean Circulation
NASA	National Aeronautics and Space Administration
NCAR	National Center for Atmospheric Research
NCEP	National Centers for Environmental Prediction
NL	narrow-lane
NTOL	non-tidal ocean loading
OBP	ocean bottom pressure
OTL	ocean tidal loading
PANDA	Position And Navigation Data Analyst
PCO	phase center offset
PCV	phase center variation
POLSSM	Proudman Oceanographic Laboratory Storm Surge Model
PPP	Precise Point Positioning
PSD	power spectral density
RADAR	Radio Detecting and Ranging
REFMAR	Réseaux de référence des observations marégraphiques
RGP	Réseau GPS Permanent (French Permanent GNSS Network)
RMS	root mean square
SAR	Synthetic Aperture Radar
SELFE	Semi-implicit Eulerian-Lagrangian finite-element
SI	Système International d'Unités (International System of Units)
SLR	Satellite Laser Ranging
SMOS	Soil Moisture and Ocean Salinity
SONEL	Système d'Observation du Niveau des Eaux Littorales
SSA	Singular Spectral Analysis
STD	Slant Tropospheric Delay
TCN	total loading signal with TOPO, CWSL and NTOL

ABBREVIATIONS

TEC	Total Electron Content
TECU	TEC units
TOPO	topography corrected ATML
TRF	Terrestrial Reference Frame
UNAVCO	University NAVSTAR Consortium
VLBI	Very Long Baseline Radio Interferometry
VMF1	Vienna Mapping Function
WL	wide-lane
WRB	wide-lane receiver bias
WRMS	weighted root mean square
WSB	wide-lane satellite bias
XBT	expendable bathythermograph
XWS	eXtreme Wind Storms
ZHD	Zenith Hydrostatic Delay
ZTD	Zenith Total Delay
ZWD	Zenith Wet Delay

Résumé long

L'observation des déformations de la surface terrestre est un sujet de grand intérêt scientifique. Tout au long de l'histoire de la géodésie, plusieurs phénomènes de déformation de la croûte terrestre ont montré l'intérêt de telles observations. Ainsi la technique GPS (Global Positioning System) a prouvé son rôle décisif dans les applications géodésiques en raison des nombreux instruments répartis sur toute la Terre et de l'amélioration continue de sa précision. Aujourd'hui les séries temporelles GPS contribuent à la réalisation de repères de référence terrestre, à la détermination du mouvement des plaques tectonique, à l'observation de l'ajustement isostatique glaciaire ou à l'étude de la variation du niveau de la mer. Toutes ces activités et domaines de recherche nécessitent un positionnement de haute précision qui exige la correction de toutes les sources d'erreur possibles et des déplacements à haute fréquence pendant l'analyse des données géodésiques afin d'obtenir une réduction du bruit. Avec la précision croissante des techniques de géodésie spatiale, des signaux qui étaient auparavant considérés comme du bruit sont devenus significatifs. Ils ne peuvent plus être négligés compte tenu de la précision disponible actuellement. Certains de ces effets sont bien connus et peuvent être modélisés avec précision en raison de la nature explicite et déterministe de leurs forces motrices. Ces effets sont par exemple la marée de la Terre solide ou la surcharge océanique maréale [Melachroinos et al. 2006; Vergnolle et al. 2008; Fu et al. 2012]. D'autres phénomènes sont également observés et compris mais ils ne sont pas de nature déterministe. Ainsi, ces signaux résiduels et leurs modèles doivent être étudiés de manière approfondie pour décider s'ils sont importants ou non en regard de la précision géodésique réelle. Ces effets sont principalement les déformations qui sont induites par les variations de masse non-maréales de l'atmosphère [van Dam et al. 1994; Petrov and Boy 2004; Tregoning and van Dam 2005; Boy 2007; Collilieux et al.

2010; Dach et al. 2011; Jiang et al. 2013], de l'océan [Zerbini et al. 2004; Fratepietro et al. 2006; Geng et al. 2012; Williams and Penna 2011; van Dam et al. 2012; Mémin et al. 2014] et de l'eau continentale [van Dam et al. 2001; Davis et al. 2004; Bevis et al. 2005; Nahmani 2012; Valtý 2013]. Les ordres de grandeur des amplitudes des déformations sont indiqués dans le tableau 2. A titre indicatif, l'erreur formelle de calcul de positionnement GPS par la méthode iPPP est également indiquée (Voir Table 2).

Depuis que des produits très précis sont disponibles pour les satellites et les horloges IGS (International GNSS Service) et que des algorithmes sophistiqués ont été développés, la méthode iPPP (integer fixed ambiguity Precise Point Positioning) a ouvert une nouvelle ère pour l'analyse des mesures GPS et son application dans les études géophysiques. Plusieurs logiciels existent pour estimer les positions en utilisant la méthode iPPP, par exemple GIPSY [Zumberge et al. 1997], BERNESE, PANDA ou GINS [Marty et al. 2012]. Le logiciel GINS-PC développé par le CNES (Centre National d'Etudes Spatiales) et le GRGS (Groupe de Recherche de Géodésie Spatiale) est de plus en plus utilisé par la communauté géodésique. En particulier, grâce à l'effort de développement de GINS, ce logiciel est doté des fonctionnalités les plus récentes pour le traitement des données GPS, notamment la méthode iPPP [Laurichesse et al. 2009; Loyer et al. 2012; Fund et al. 2013].

Ce travail constitue l'une des premières études des différents effets de surcharge avec les séries temporelles GPS en mode iPPP, en particulier en utilisant le logiciel GINS-PC. Nous visons à exploiter les séries temporelles iPPP pour étudier les différents effets de surcharge non-maréale à différentes échelles temporelles, depuis des périodes subdiurnes jusqu'à des périodes saisonnières et annuelles. Ici, nous abordons la question de savoir si elles ont des répercussions importantes sur notre interprétation lors de l'analyse des séries temporelles géodésiques; si nous sommes capables de détecter les variations journalières de position par l'utilisation du GPS; et si oui, quels modèles peuvent améliorer la répétitivité des positions à ces échelles de temps.

L'un des principaux domaines de recherche du laboratoire L2G (CNAM/ESGT/L2G), récemment renommé GeF (Géomatique et Foncier) est l'étude des processus de déformation et de positionnement en utilisant différentes techniques géodésiques. Plusieurs recherches effectuées dans le L2G ont fortement contribué aux applications du GPS [Melachroinos

et al. 2008; Vergnolle et al. 2008; Fund et al. 2011b,a]. Il y a aussi des recherches en cours sur la combinaison du GPS avec d'autres techniques, notamment la topométrie terrestre et l'interférométrie radar [Legru 2011; Polidori et al. 2013].

Cette thèse a été entreprise dans le cadre de la poursuite des études menées précédemment dans notre laboratoire sur les mesures de déformations. Dans ce contexte, notre objectif est de contribuer à la validation des modèles géophysiques, à l'observation des différents phénomènes non-maréaux, ainsi qu'à l'étude des performances du mode iPPP et à la validation du logiciel GINS-PC qui est un puissant outil pour les applications géodynamiques. Cette thèse a été financée par le CNES et la Région des Pays de la Loire et a été menée en collaboration avec Tonie van Dam (Université du Luxembourg).

Table 2 – Amplitudes horizontales et verticales de l'effet des déformations.

	Horizontal	Vertical	Unit
Déformation tectonique	100	10	mm/yr
Rebond post-glaciaire	2	10	mm/yr
Surcharge océanique maréale	20	100	mm
Surcharge atmosphérique maréale	0.5	2	mm
Surcharge hydrologique continentale	10	30	mm
Surcharge atmosphérique non maréale	3	20	mm
Surcharge océanique non maréale	2	10	mm
Erreur formelle GPS ³	~1	~5	mm

Etude globale

Nous avons déjà vu que les variations spatiales et temporelles non-maréales des masses atmosphériques, hydrologiques et océaniques peuvent avoir une influence importante sur la surface de la Terre [van Dam and Wahr 1998] (Voir Table 2). Il a également été démontré par plusieurs chercheurs que le GPS est capable de détecter ces variations de masse [Blewitt and Lavallée 2002; Tregoning et al. 2009; Williams and Penna 2011; van Dam et al.

³en utilisant le mode iPPP dans GINS-PC avec une période d'échantillonnage de 6 heures.

1994, 2001; Nahmani 2012; van Dam et al. 2012; Valty 2013]. Nous pouvons évaluer la performance de la série temporelle de déplacement prédit par les modèles de surcharge à des échelles régionales et mondiales avec notre série temporelle de positions GPS iPPP.

À l'heure actuelle, les effets de surcharge non-maréale ne sont pas encore pris en compte pour une correction a priori dans l'analyse mondiale des données GPS. En outre, les longues séries temporelles de position qui sont utilisées pour étudier les processus géodynamiques à long terme ne sont pas toujours corrigées a posteriori pour tenir compte de l'impact des phénomènes de surcharge. Ces phénomènes peuvent néanmoins avoir un effet important sur les séries temporelles géodésiques, en particulier si l'on examine les signaux qui sont de l'ordre du millimètre. Pour une correction a posteriori, il existe différents modèles disponibles gratuitement en ligne, mais aucune information n'est totalement adaptée aux besoins des utilisateurs. L'étude des effets saisonniers de surcharge est généralement effectuée en utilisant des séries temporelles GPS hebdomadaires ou diurnes. Nous cherchons ici à quantifier l'amélioration apportée par les séries temporelles iPPP subdiurnes par rapport aux études précédentes basées sur des séries journalières ou hebdomadaires. Par conséquent, nous étudions les séries temporelles de position avec une période de 6 heures pour une sous-sélection de stations dans différentes régions qui sont potentiellement exposées à divers effets de surcharge. Nous avons sélectionné ces régions sur la base des résultats des études mondiales antérieures et des cartes de susceptibilité pour la surcharge non-maréale atmosphérique et hydrologique et les effets océaniques. Les premiers tests ont été réalisés sur un réseau restreint (Voir Figure 1). Estimer les positions des sites éloignés de ceux qui sont influencés par la surcharge nous permet d'évaluer la performance des séries temporelles de déplacement à l'échelle mondiale et régionale.

Les calculs ont été réalisés avec deux types de produits d'horloge et d'orbite du centre d'analyse IGS du GRGS, notés GRG et GR2. Les produits GR2 correspondent à la solution REPRO2, à savoir un retraitement complet des données GPS depuis 1994 avec l'ensemble des modélisations et paramétrages les plus récents et précis disponibles au moment de la thèse.

Concernant les erreurs RMS des séries temporelles GPS, nous avons vu des

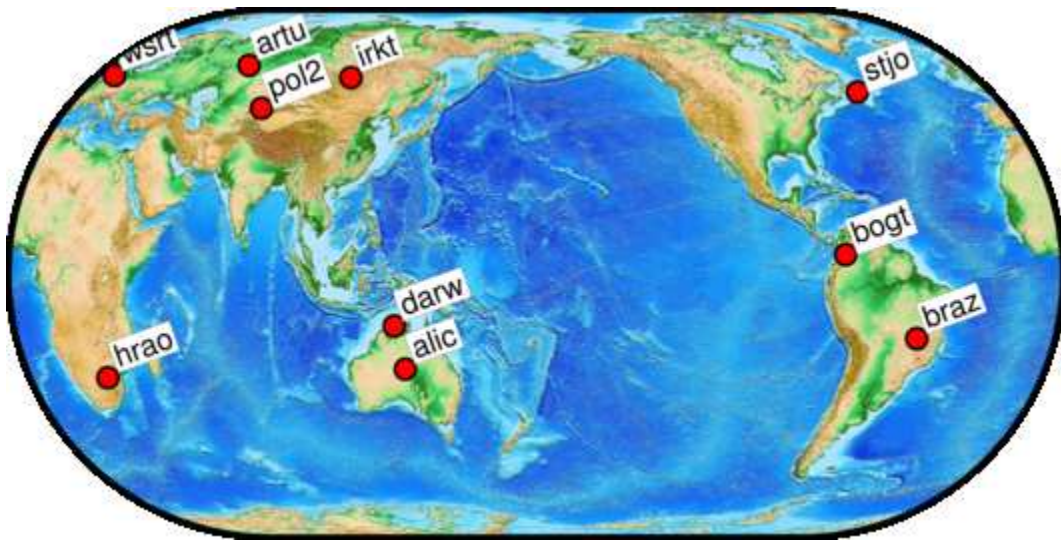


Figure 1 – Notre réseau contenant 10 stations GPS.

améliorations après corrections a posteriori. Ces améliorations sont rendues possibles par la prédiction du signal de surcharge, indiquant la pertinence de notre sélection. Nous avons démontré que la série temporelle GR2 améliorerait significativement nos résultats GPS en termes d'interprétation de surcharge (Voir Figure 2). En effet, ceux-ci ne présentent plus de sauts d'amplitude aléatoire avec une périodicité hebdomadaire, et leur niveau de bruit est nettement plus faible. Nous avons démontré que les solutions subdiurnes iPPP permettent de surveiller les effets de surcharge sur les séries temporelles à long terme. Nous avons examiné comment les valeurs statistiques et aussi les amplitudes annuelles et semi-annuelles sont changées avec la correction a posteriori. En outre, nous avons examiné comment les différentes composantes périodiques des différents modèles peuvent expliquer les séries temporelles des positions. L'outil développé par Asri [2014] et basé sur la SSA est prometteur pour l'interprétation et la validation du modèle ainsi que pour séparer les différentes contributions des signaux GPS. Ainsi il sera possible de contribuer à la validation du modèle additif et à la compréhension de l'interaction entre les différents effets de surcharge.

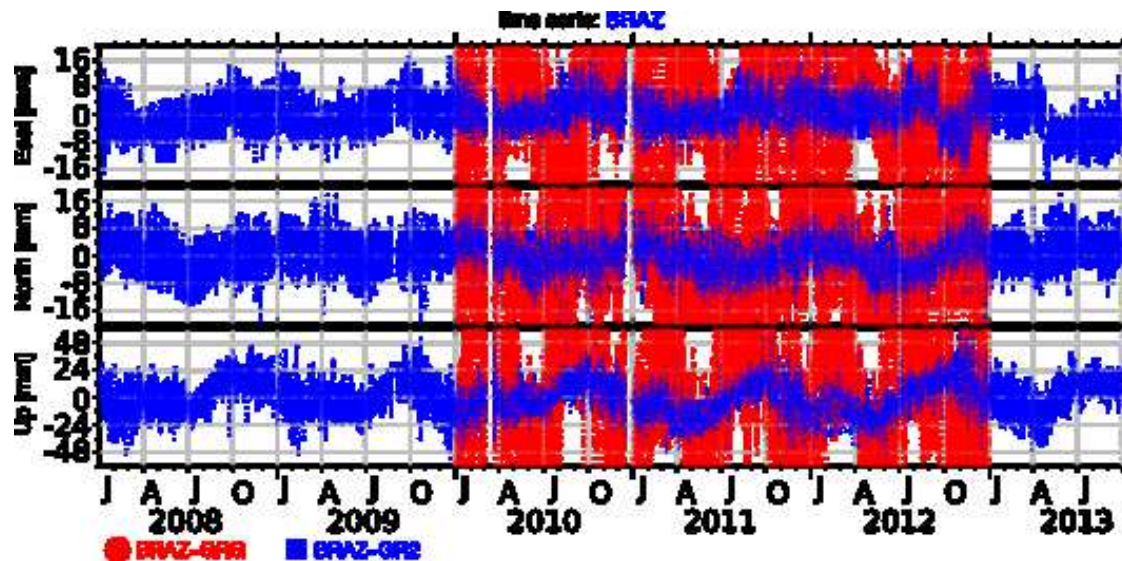


Figure 2 – Séries temporelles GPS GRG (rouge) et GR2 (bleu) dans les stations BRAZ.

Application à la surveillance de la déformation tectonique des Pyrénées

Dans cette étude, nous avons étudié l'effet de la surcharge sur des estimations de la vitesse tectonique calculée à partir d'observations GPS issues de campagnes espacées dans le temps. La région d'étude se situe dans la chaîne des Pyrénées entre la France et l'Espagne. ResPyr est le nom d'un réseau qui a été installé et mesuré dans les Pyrénées en 1995 et 1997. Dans cette zone, l'activité sismique est continue et modérée et l'amplitude de la vitesse tectonique horizontale attendue est inférieure à 0,5 mm/an. Afin de déterminer la vitesse, 4 campagnes GPS ont été réalisées de 1995 à 2010. Compte tenu du faible taux de déformation attendu, les phénomènes de surcharge peuvent engendrer un artefact non négligeable pour le calcul de la vitesse, ce qui pourrait affecter notre interprétation géodynamique. Dans cette étude, nous avons examiné spécifiquement les phénomènes de surcharge non-maréale atmosphériques, hydrologiques et océaniques. Enfin, nous avons effectué des simulations pour identifier le meilleur moment et la fréquence des futures campagnes GPS de manière à minimiser l'influence des effets de surcharge sur les estimations de vitesse tectonique.

Pour obtenir les tendances précises à partir de données continues, il faut des périodes

d'observation plus longues que 2,5 années [Blewitt and Lavallée 2002]. La précision de la tendance est proportionnelle au nombre d'observations et au laps de temps analysé [Zhang et al. 1997], de sorte que les tendances obtenues à partir des mesures de ces campagnes seront toujours moins précises que des observations continues sur la même période. Une façon de réduire l'incertitude est d'utiliser des observations longues. Une autre solution est de réduire ou d'éliminer le bruit et les signaux indésirables dans les données en modélisant les signaux environnementaux. On peut ainsi concevoir une situation dans laquelle un grand système de pression atmosphérique anormale traverse la région pendant une campagne GPS ou une campagne au cours de laquelle la pression moyenne est beaucoup plus faible que dans d'autres campagnes. Supprimer l'effet de surcharge atmosphérique devrait réduire la dispersion des observations individuelles au sein d'une campagne et le décalage des observations entre les campagnes.

Pour l'étude des vitesses tectoniques, nous sommes intéressés par l'évolution des coordonnées géodésiques du site à long terme. Si la vitesse tectonique d'une région est estimée en comparant les positions de chaque campagne, alors le traitement des données GPS doit être effectué avec précaution. En ce qui concerne la précision actuelle du positionnement GPS (autour de quelques millimètres pour la composante horizontale), tous les effets non tectoniques dans le signal doivent être considérés et retirés afin d'extraire une vitesse géodynamique plus précise. En conséquence, plusieurs sources d'erreur affectant le signal doivent être prises en compte, telles que l'erreur introduite par les retards ionosphériques et troposphériques et les effets de charge dus à des redistributions de masse. En effet, des redistributions de masse de l'environnement (atmosphère, eau continentale et océan) pourraient causer des déplacements significatifs de la surface de la Terre jusqu'à plusieurs millimètres (voir Table 2). Parmi ces effets, le signal de surcharge océanique maréale est bien documenté, modélisé et incorporé dans les différents logiciels de traitement GPS.

Dans cette étude, nous nous concentrons sur les effets de surcharge dus à la variation non-maréale de la masse de l'atmosphère, au stockage de l'eau continentale et à l'océan. Ces déplacements dus aux surcharges pourraient influencer les coordonnées GPS dans la chaîne des Pyrénées. Leur influence sur les observations géodésiques continues par VLBI

a été bien documentée dans la littérature géodésique [van Dam and Herring 1994; Petrov and Boy 2004; Tesmer et al. 2009]. Les signaux sont périodiques (annuel, semi-annuel, diurne) et peuvent atteindre des amplitudes importantes. Ces effets ne sont généralement pas pris en compte dans les logiciels GPS et lors de l'analyse de données pour les études géophysiques qui exigent pourtant une grande précision [Williams and Penna 2011].

Nous étudions l'impact des effets de surcharge sur les vitesses du site estimées lors de campagnes GPS espacées dans le temps. Les données GPS sont traitées en utilisant les standards d'IERS (International Earth Rotation Service and Reference System) Conventions 2010 [Petit and Luzum 2010]. Nous examinons les séries temporelles de surcharge calculées pour 40 stations de campagne GPS (ResPyr) dans les Pyrénées. Quatre campagnes GPS de courte durée (quelques jours pour chaque site) ont été menées depuis 1995 (1995, 1997, 2008 et 2010) pour déterminer la vitesse tectonique de la partie intérieure de la plaque eurasienne. En effet, cette région est la région la plus active sismiquement en France avec une activité sismique continue et modérée [Souriau and Pauchet 1998]. Des vitesses tectoniques sont déterminées à partir des différences de coordonnées de chaque résultat de mesure de la campagne depuis 1995. Une brève description des campagnes ResPyr et les résultats préliminaires obtenus avant les dernières mesures de la campagne de 2010 sont donnés dans Nicolas et al. [2012].

Pour obtenir des tendances tectoniques de l'ordre de 0,5 mm/an, soit le taux de déformation attendu dans cette région [Nocquet 2012], un positionnement de haute précision est nécessaire. Imaginons que le stockage de l'eau continentale ait été particulièrement élevé au cours d'une des campagnes par rapport aux autres. Si cet effet de surcharge n'a pas été pris en compte dans l'analyse, les vitesses tectoniques peuvent être erronées et les interprétations géodynamiques ultérieures pourraient contenir des erreurs. Ainsi, pour comprendre les tendances dérivées de nos observations des campagnes, l'impact des différents effets de charge à différentes époques doit être pris en compte. Nous estimons l'impact des effets potentiels de surcharge sur nos vitesses en analysant le modèle de séries temporelles en détail aux moments de nos campagnes GPS. Nous calculons ensuite la contribution de chaque effet de surcharge en termes de vitesse. En outre, comme l'étude est réalisée dans une région montagneuse, nous analysons aussi

la différence entre les modèles atmosphériques classiques [van Dam et al. 2010] et le modèle atmosphérique qui prend en compte la topographie locale (Voir Figure 3). Enfin, nous introduisons des campagnes virtuelles pour estimer la relation entre le nombre et le calendrier des observations de la campagne et les effets de vitesse.

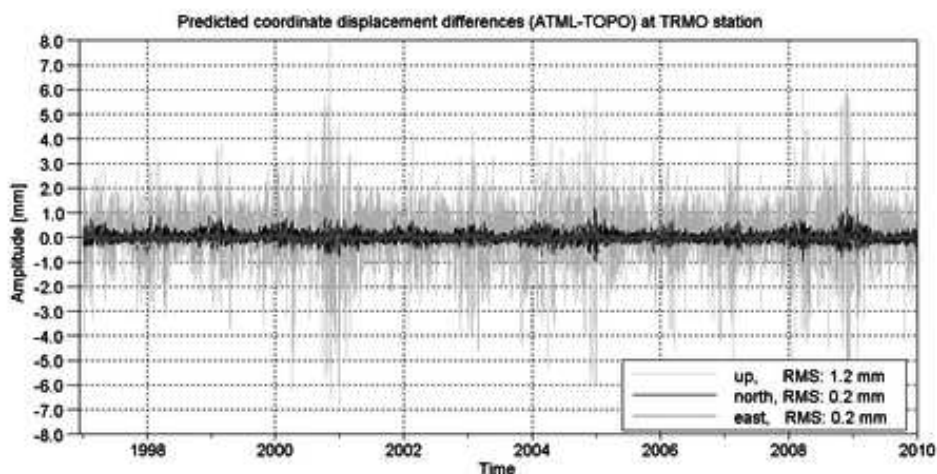


Figure 3 – Différences entre les déplacements ATML et TOPO à la station TRMO (site de la campagne, le Cirque de Troumo, France) de 1995 à 2010.

L'amplitude horizontale du signal de surcharge est dominée par la surcharge océanique non-maréale (moyenne de l'ordre de 8 mm au nord et 6 mm à l'est) et pour la composante verticale, par l'atmosphère et la surcharge hydrologique continentale (moyenne de l'ordre de 21 mm et 17 mm, respectivement). Le signal de surcharge cumulé peut atteindre une moyenne de 10 mm au nord, 8 mm à l'est, et 33 mm pour les déplacements verticaux, respectivement.

Nous savons que les effets de surcharge peuvent avoir des amplitudes importantes et peuvent varier sur des périodes courtes. Nous avons examiné ces signaux de surcharge par rapport à leur effet potentiel sur la mesure GPS de la vitesse. Nous avons constaté que pour le réseau ResPyr entre 1995 et 2010, l'effet de surcharge dominant sur la vitesse horizontale reste la surcharge océanique non-maréale (moyenne de 0,11 mm/an), tandis que l'hydrologie continentale est le principal contributeur à la composante verticale (moyenne de 0,21 mm/an). Dans une certaine mesure, même si les charges cumulées semblent faibles en termes absolus (maximum 0,24 mm/an et 0,65 mm/an,

respectivement dans les composantes horizontale et verticale), elles peuvent modifier l'orientation de la vitesse du site, et par conséquent influencer l'interprétation géodynamique. En outre, l'impact total de la surcharge sur la composante horizontale peut représenter une grande partie du signal tectonique prévu, et pourrait même être plus grand que le signal tectonique. L'effet de la charge sur les vitesses déterminées en utilisant les observations GPS de la campagne dans les régions tectoniques qui sont plus éloignées des côtes peut être plus grand. Dans tous les cas, nous recommandons de prêter une attention particulière à ces effets au niveau du traitement de données GPS (comme il est montré dans Tregoning and van Dam [2005] pour la surcharge atmosphérique).

Nous n'avons pas trouvé une différence significative entre ATML (surcharge atmosphérique) et TOPO (surcharge atmosphérique avec topographie raffinée) en termes de vitesse horizontale pour les effets de surcharge dans les Pyrénées : les effets de surcharge océanique non-maréale sont même plus grands que les différences entre les effets de surcharge atmosphérique estimés avec ou sans la topographie raffinée. Néanmoins, concernant la composante verticale, les différences entre ATML et TOPO sont plus fortes et peuvent modifier l'effet cumulé de 22%. Par conséquent, nous recommandons de prendre en compte la topographie locale dans le calcul de la surcharge atmosphérique. De plus, l'étude des vitesses verticales est de plus en plus considérée dans les études tectoniques afin de mieux comprendre les mécanismes mis en jeu.

Concernant l'estimation des vitesses horizontales par GPS (campagne), l'ordre de grandeur se situe entre 0,1 et 1,5 mm/an avec une valeur moyenne de 0,6 mm/an et une erreur d'environ 0,3 à 0,4 mm/an. En ce qui concerne la composante verticale, les valeurs absolues des estimations GPS varient entre 1 et 24 mm/an avec une erreur de 3 mm/an (Voir Figure 4). Sur la base de ces résultats, il est difficile de tirer des conclusions significatives concernant la tectonique générale de la zone. Ces vitesses pourraient être mieux déterminées si une nouvelle campagne devait être effectuée ou si un réseau permanent était mis en place.

Dans le cas des campagnes ResPyr, malgré les déplacements relativement importants donnés par les différents modèles, les effets de surcharge semblent négligeables en termes de vitesse, même dans le cas du signal de surcharge totale (noté ACN ou TCN selon que l'on

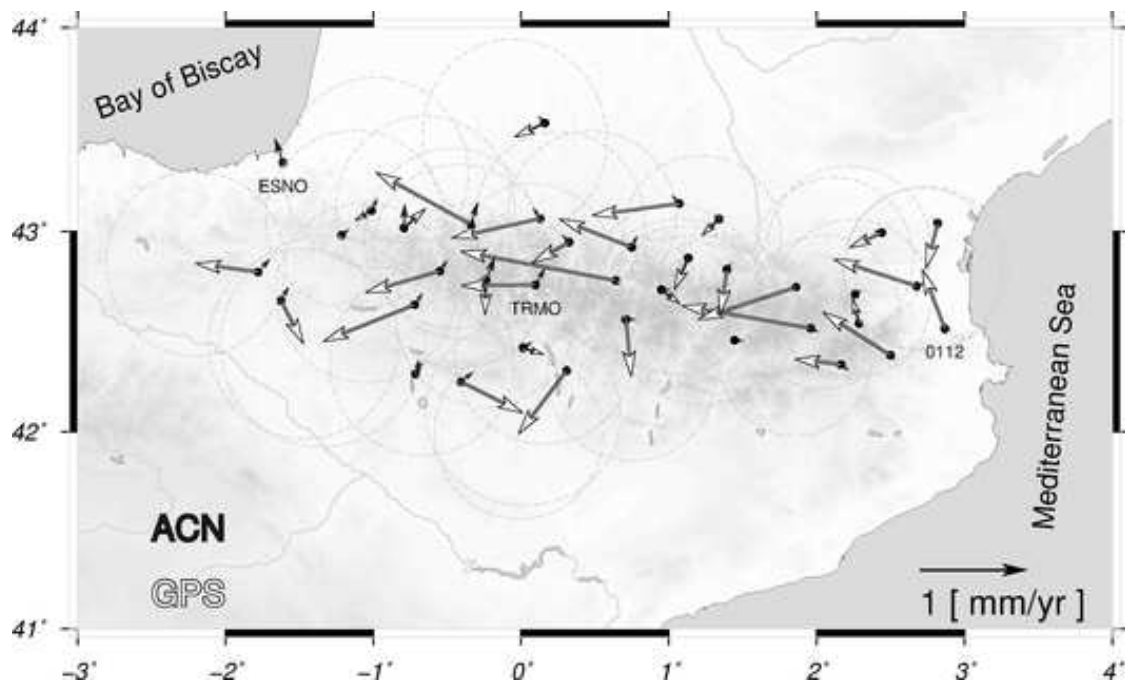


Figure 4 – Effet de surcharge cumulé (ACN) et vitesses GPS horizontales (en mm/an). TRMO (Cirque de Troumo, France), ESNO (Esnour Mont, France) et 0112 (Montesquieu, France) sont les stations de la campagne.

considère ATML ou TOPO). Néanmoins, il peut être loin d'être négligeable dans certains cas. Deux facteurs contrôlent le signal d'artefact de surcharge induit dans notre cas. Le premier est le fait que nous ayons une longue durée de temps (15 ans) entre la première campagne et la dernière. Dans ce cas, la variation annuelle est moyennée au cours de cette longue période de temps. Le second facteur est le fait que toutes les campagnes aient été effectuées à la même époque de l'année (en été).

Nous avons testé différentes méthodes pour estimer comment la surcharge ignorée pourrait affecter les résultats de vitesses tectoniques dans le cas des campagnes GPS. Une analyse virtuelle basée sur des simulations de campagnes montre que l'amplitude et l'orientation du signal de vitesse induit par les phénomènes de surcharge varient selon le mois où les données sont acquises (y compris avec de fortes différences entre deux mois consécutifs) et sur le laps de temps entre deux campagnes consécutives. Nous concluons que l'impact des différents effets de surcharge est le plus petit si les campagnes sont réalisées exactement à la même période de chaque année, par exemple, au milieu de l'été. Enfin, nous concluons que le meilleur scénario pour l'observation semble être d'effectuer

les campagnes GPS tous les 5 ans en août. Ce choix permet de trouver un compromis entre une amplitude de surcharge trop petite et une période trop longue pour la mesure sur le terrain. En effet, de nos jours il est essentiel de tenir compte non seulement des composantes horizontales mais aussi verticales afin d'être en mesure d'étudier la déformation 3D de la chaîne de montagne. Dans ce cas, les effets de surcharge peuvent être beaucoup plus grands par rapport au signal attendu. Ainsi, nos calculs montrent qu'une nouvelle campagne Respyr serait nécessaire en août 2013 ou 2014 afin d'être en mesure de fournir une estimation de la vitesse précise et de réduire au minimum les artefacts causés par les signaux de surcharge. Cela n'a pas pu être réalisé faute de financements.

Cette étude a été publiée en tant que [Ferenc et al. 2014].

Étude de l'impact de la tempête Xynthia

Les séries temporelles GPS intègrent des signaux différents liés à la géophysique, à la propagation dans l'environnement et aux effets instrumentaux. Nous supposons que les derniers effets sont bien atténués en utilisant des modèles standards d'IERS Convention 2010 [Petit and Luzum 2010] ou que leurs effets résiduels sont bien en dessous de l'amplitude attendue du signal de surcharge. Par conséquent, nous pouvons utiliser des séries temporelles GPS pour étudier les variations rapides de masse et déterminer la réponse associée de l'océan. A cet effet, nous avons calculé des séries temporelles iPPP avec le logiciel GINS-PC (CNES/GRGS) dans une étude régionale visant à analyser l'évolution spatiale et temporelle des différents phénomènes de surcharge induits par un événement météorologique extrême, la tempête Xynthia survenue dans la nuit du 27 au 28 février 2010 (Voire Figure 5).

Lors du calcul des effets de surcharge atmosphérique, hydrologique ou océanique non-maréale sur les coordonnées géodésiques, nous devons tenir compte de la variation de masse de surcharge sur la terre et sur l'océan. Il faut également déterminer la réponse de l'océan à la pression atmosphérique. Un baromètre inversé pur et une réponse de l'océan de type terre solide pour la surcharge de pression définissent les extrêmes de la réponse. Sur des périodes

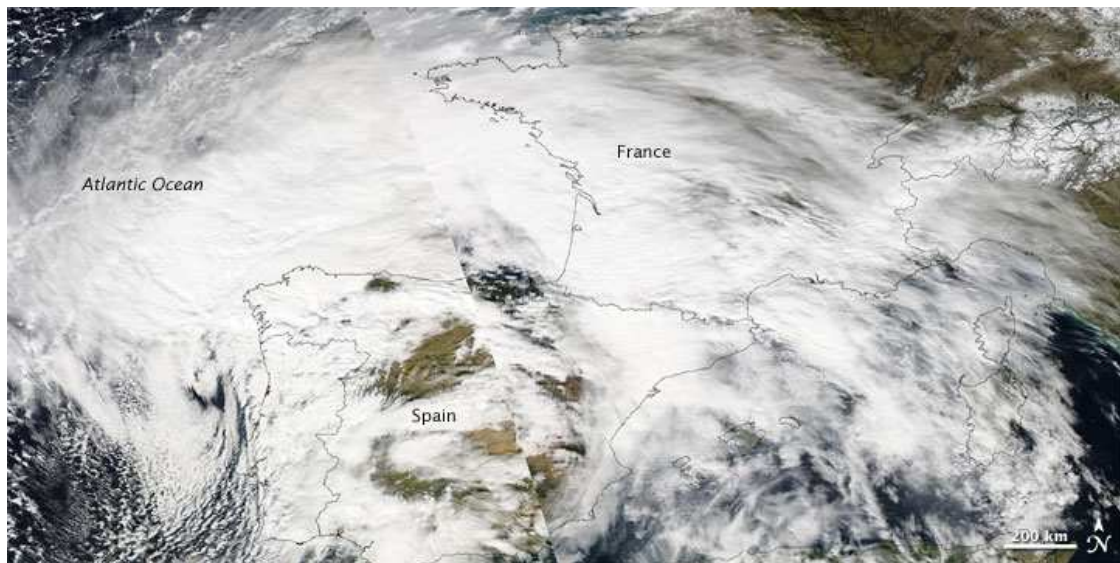


Figure 5 – Image satellite du Xynthia. Source: NASA.

supérieures à quelques jours, la réponse du baromètre inversé est suffisante [Wunsch and Stammer 1997]. Cependant, comment l’océan répond-il à des tempêtes rapides?

Dans cette étude, nous étudions l’effet d’une tempête violente qui a progressé sur l’Europe de l’ouest pendant l’hiver 2010 à partir d’une série temporelle GPS iPPP subdiurne calculée en utilisant le réseau RGP (Réseau GPS Permanent) et les produits GR2 (REPRO2) du GRGS (Voir Figure 6).

Xynthia est un cyclone extratropical qui a traversé la France du sud-ouest au nord-est pendant environ 12 heures. Une chute de pression d’environ 46 mbar a été observée dans le réseau et une onde de tempête d’environ 1,5 m a été mesurée sur le marégraphe de La Rochelle [Bertin et al. 2012]. Nous étudions le soulèvement des sites côtiers et intérieurs à partir de la comparaison des séries temporelles GPS iPPP ayant une période d’échantillonnage de 6 heures (GINS-PC), avec les séries de surcharge non-maréale. Nous utilisons les modèles des déplacements dus à la surcharge atmosphérique en supposant une réponse IB (baromètre inversé) et non-IB de l’océan comme paramètres. Nous analysons encore la réponse de l’océan à l’atmosphère dynamique comme un scénario réaliste. Nous comparons également nos résultats iPPP aux modèles de surcharge océanique non-maréale purs basés sur un modèle océanique dynamique régional et un modèle de circulation global. Ensuite, nous essayons d’utiliser les séries temporelles des

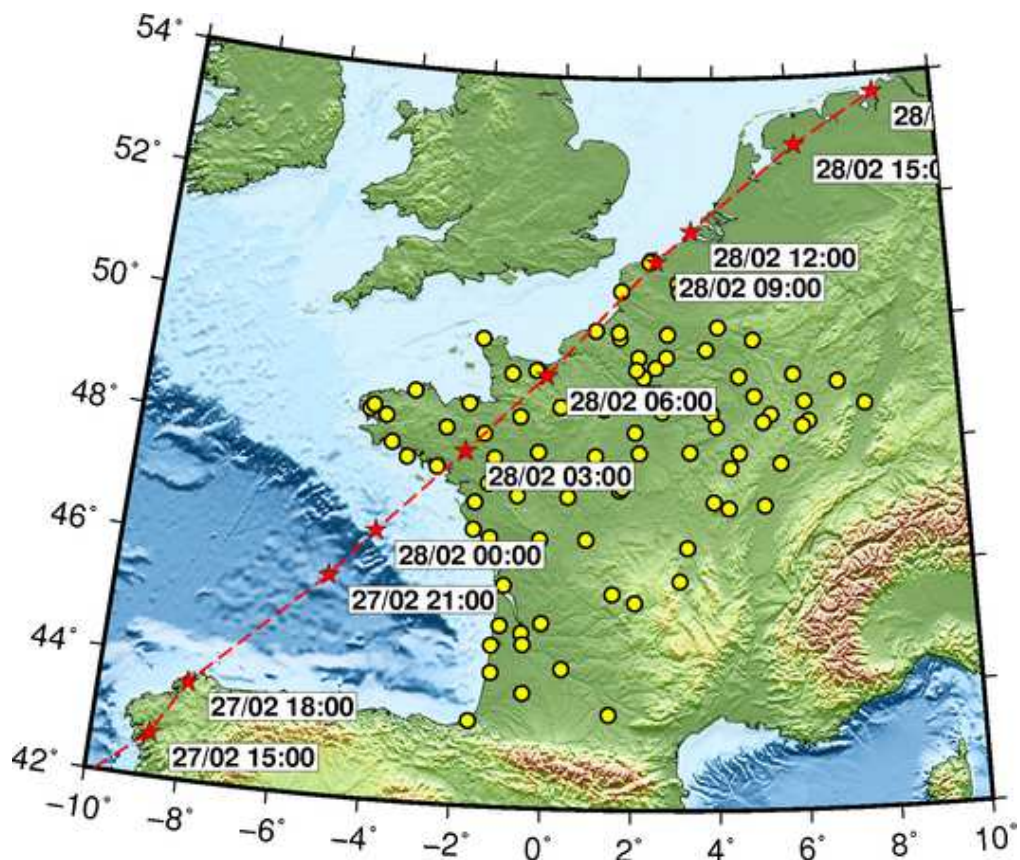


Figure 6 – La trace de la tempête Xynthia est représenté par la ligne pointillée rouge et les étoiles rouges indiquent les positions instantanées approximatives. Les cercles jaunes représentent l'ensemble de nos stations de réseau GPS de RGP étudié. Les données pour la trace Xynthia sont fourni par Xavier Bertin.

déplacements obtenus par GPS, la surcharge atmosphérique et océanique non-maréale basée sur un modèle océanique régional pour identifier les dynamiques véritables de l’océan sur le plateau continental lors du passage de cette tempête violente et rapide.

Puisque cet événement environnemental extrême s’est produit après une saison des pluies, nous examinons également les signatures hydrologiques au cours de la période étudiée. La migration du système de basse pression contraint la croûte terrestre de s’élever, tandis que la surcote s’oppose à cela, en particulier sur les sites côtiers. Ainsi, cela provoque l’affaissement de la région exposée.

En outre, la masse d’eau continentale a le même effet (subsidence) que l’océan.

Nous avons utilisé les modèles de surcharge cités dans le tableau 3 : modèles atmosphériques (ATML, ATMIB, ATMMO, NOIB), océaniques (NTOL, ECCO) et hydrologiques (CWSL, HYDRO). Lorsque, pour les séries temporelles de surcharge, nous avons examiné les différences entre les modèles de surcharge calculés au point considéré et ceux calculés à partir de l’interpolation d’une grille globale, nous avons vu des différences importantes qui peuvent apparaître sur de courtes périodes ou des événements environnementaux extrêmes. Nous suggérons aux utilisateurs GPS d’appliquer les séries temporelles de modèles de surcharge calculés au point considéré chaque fois que cela est possible pour une correction a posteriori dans les études sur des courtes périodes.

Table 3 – Les acronymes des modèles de surcharge appliquées.

Acronymes	Données d’entrée	Fourni par
ATML	MERRA	Zhao Li, Tonie van Dam
ATMIB*	ECMWF	Jean-Paul Boy
ATMMO*	ECMWF+MOG2D	Jean-Paul Boy
NOIB	MERRA	Zhao Li, Tonie van Dam
NTOL	water level model of Xavier Bertin	Zhao Li, Tonie van Dam
ECCO	ECCO	Zhao Li, Tonie van Dam
CWSL	MERRA	Zhao Li, Tonie van Dam
HYDRO*	GLDAS-Noah	Jean-Paul Boy

Pendant une période de deux jours, les effets de surcharge dans le sens de leur déplacement vertical ⁴ dû à la pression atmosphérique atteignent jusqu’à 11,4 ; 13,5 et 18,0 mm pour une réponse de l’océan dynamique, IB et non-IB, respectivement. En ce

⁴vers le haut ou vers le bas en fonction de l’effet.

qui concerne la surcharge océanique non-maréale et l'hydrologie, les modèles suggèrent un déplacement maximum de -9,1 et -4,4 mm. La Figure 7 illustre des séries temporelles sur deux stations, LROC (La Rochelle, où la plus grande surcote a été observée) et STJ9 (Strasbourg, la station la plus éloignée du centre de la tempête dans notre réseau).

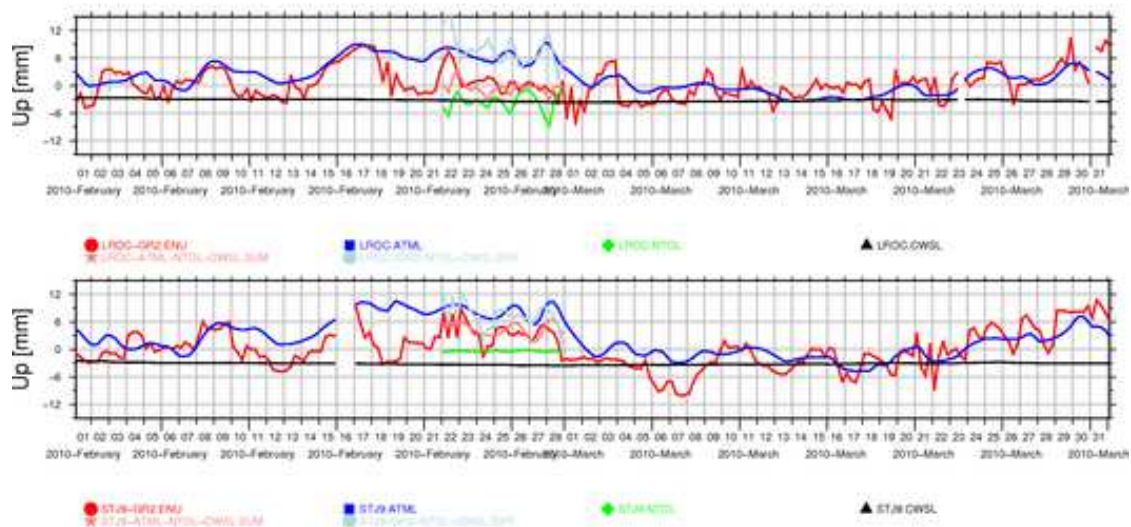


Figure 7 – Séries temporelles GPS et modèles des surcharges au stations LROC (haut) et STJ9 (bas) pendant deux mois centré sur la tempête Xynthia.

Les produits GR2 ayant été disponibles tardivement, nous avons dû réduire l'échantillonnage en exploitant des réseaux partiels. La figure 8 montre les 4 réseaux partiels ainsi définis : continental étendu (AI pour all inland), continental proche (NI pour nearby inland), côtier étendu (AC pour all coastal) et côtier proche (NC pour nearby coastal), les stations étant considérées proches lorsqu'elles sont situées à moins de 200 km de la trace de la tempête. Ainsi, nous avons analysé spatialement le signal de surcharge.

A chaque époque, nous avons tracé et analysé le signal GPS par rapport aux modèles afin de suivre l'évolution temporelle des effets de la tempête lors de son passage. La figure 9 illustre les résultats des mesures GPS après application d'un filtrage spatial passe-bas (moyenne sur des blocs de $2 \times 2^\circ$ pour la représentation graphique uniquement), en composante horizontale (à gauche) et verticale (à droite), le centre de la dépression étant représenté par l'étoile (époque 2).

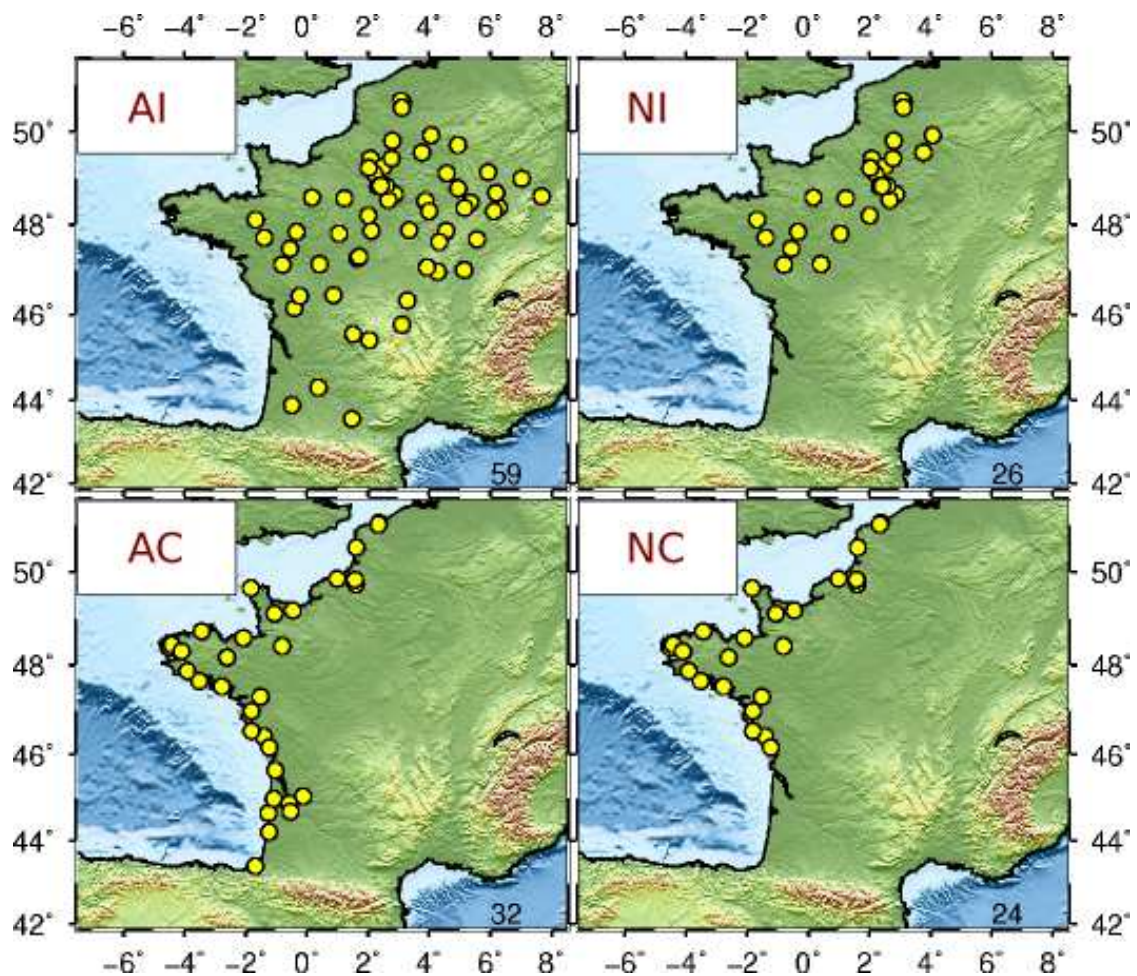


Figure 8 – Sélection des stations: Continental étendu (AI pour all inland), continental proche (NI pour nearby inland), côtier étendu (AC pour all coastal) et côtier proche (NC pour nearby coastal), les stations étant considérées proches lorsqu'elles sont situées à moins de 200 km de la trace de la tempête. Les nombres dans les coins gauche indiquent le nombre de stations.

Afin d'analyser spatialement les résultats et d'étudier l'impact de la distance à la côte sur les différents effets, nous avons également tracé les déplacements verticaux issus des différents modèles en fonction de la distance à la côte représentée en échelle logarithmique. Ces calculs sont effectués à différentes époques. La figure 10 illustre les résultats obtenus pour l'époque 2 (centre de la dépression au milieu de la Bretagne).

Nous ne sommes pas parvenus à améliorer la répétabilité de toutes nos séries temporelles pour leurs différentes sélections spatiales. Cependant, nous avons montré que les modèles ATMMO (modèle de surcharge atmosphérique prenant en compte une réponse océanique dynamique) et ATML + NTOL améliorent la répétabilité des positions GPS estimées ou du moins augmentent moins le bruit par rapport aux autres modèles atmosphériques (ATML, ATMIB, NOIB). Cette observation montre que nous devons prendre en compte NTOL, en particulier pour les sites côtiers.

Nous avons vu que les déplacements de surcharge subdiurnes sont significativement différents sur les sites côtiers et intérieurs. Tant les prédictions du modèle que les résultats GPS ont confirmé ce comportement. Nous voyons aussi ce modèle à partir des valeurs de corrélation entre les estimations de position et les différents modèles. Nous avons vu que la corrélation entre les séries temporelles GPS et les modèles atmosphériques est plus faible sur la côte que sur les sites intérieurs, mais cette relation a été plus prononcée pendant la période perturbée, indiquant un énorme impact de la tempête. En ce qui concerne ATMMO, la corrélation est même légèrement plus forte, ce qui peut refléter le fait que la réponse de l'océan était plus dynamique et que l'hypothèse IB appliquée dans ATML n'est pas la plus adéquate dans le cas de tempêtes se déplaçant rapidement, d'autant plus que cette région présente un large plateau continental peu profond.

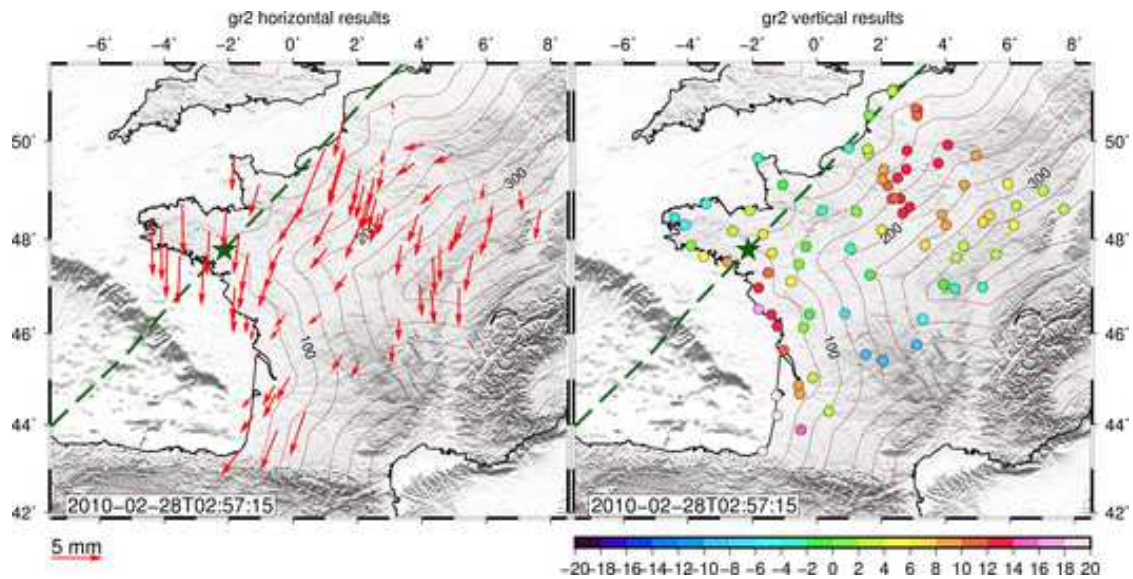


Figure 9 – Epoch 2: Les résultats des mesures GPS après application d’un filtrage spatial passe-bas (moyenne sur des blocs de $2 \times 2^\circ$ pour la représentation graphique uniquement), en composante horizontale (à gauche) et verticale (à droite), le centre de la dépression étant représenté par l’étoile. Les lignes de contour représentent la distance des côtes à tous les 50 km.

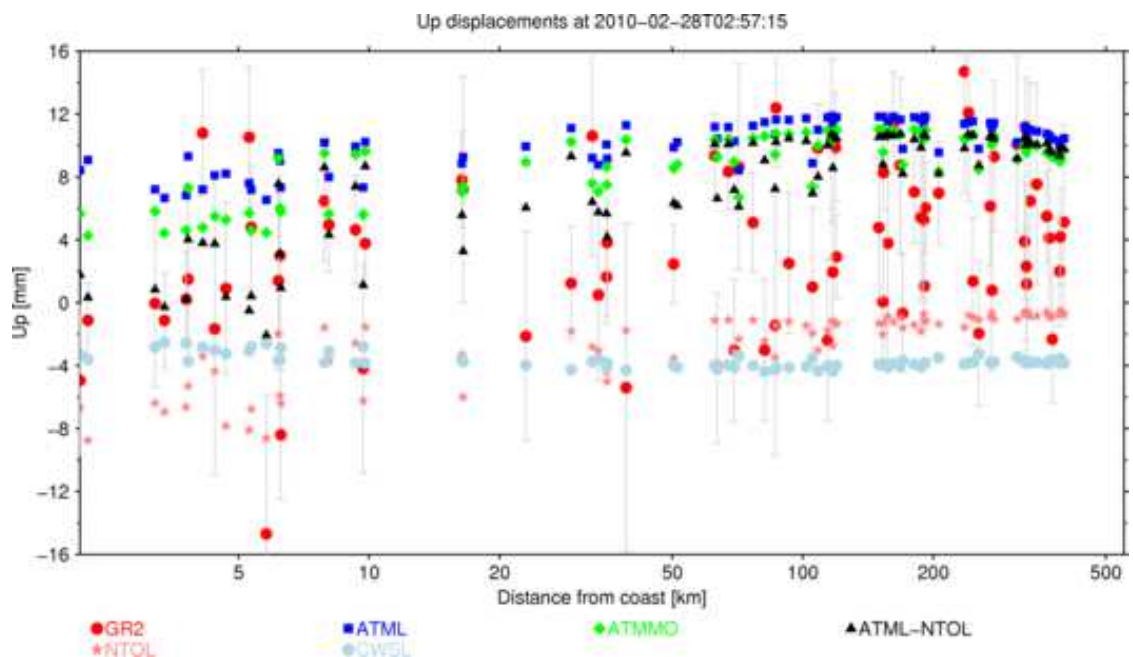


Figure 10 – Epoch 2: Déplacements verticaux issus des différents modèles en fonction de la distance à la côte représentée en échelle logarithmique.

Ainsi, nous avons démontré la capacité du GPS iPPP pour suivre l’évolution spatiale

et temporelle d'une tempête. Il ressort en particulier de cette étude que les effets de déplacement subdiurnes dépendent fortement de l'éloignement par rapport à la côte et que l'hypothèse IB semble réaliste avant et après la tempête. Une telle approche pourrait être étendue à la composante horizontale et déployée à l'échelle d'un réseau européen.

Conclusion

Nous avons décrit les techniques d'observation et détaillé la technique GPS que nous avons appliquées pour obtenir nos résultats. Enfin, nous avons présenté nos résultats concernant la faisabilité d'une étude globale et deux études régionales. Ce travail a apporté une contribution à la communauté géodésique en général et à la communauté des utilisateurs GINS-PC en particulier, validant les efforts de développement récents de la communauté GINS-PC et du centre d'analyse CNES-CLS. Plusieurs difficultés techniques ont été rencontrées pendant cette thèse. D'une part, des sauts hebdomadaires se produisent dans les séries temporelles calculées avec les produits GRG, pour toutes les stations mais avec des amplitudes variables. D'autre part, des composantes diurnes et semi-diurnes subsistent dans les spectres, et elles affectent principalement les mesures des stations situées à moins de 25 km du littoral, ce qui suggère une élimination incorrecte des effets liés aux marées océaniques. Ces artefacts ont pu être corrigés lorsque les produits GR2 (solution REPRO2 du GRGS) ont été disponibles, mais ils n'ont pu l'être que pendant la dernière année de la thèse ce qui a considérablement limité la possibilité d'obtenir de bons résultats sur de grandes quantités de points de mesure. En revanche, le constat et l'analyse de ces difficultés techniques a permis un retour d'expérience potentiellement très utile pour les utilisateurs et développeurs de l'outil GINS-PC.

Cette étude a été l'une des premières à utiliser des séries temporelles sub-diurnes iPPP estimées avec GINS-PC pour étudier les effets de surcharge ainsi que pour démontrer la performance des produits REPRO2 du GRGS (GR2). Nous avons démontré que les améliorations dans les modèles appliqués et la stratégie d'estimation pour les produits de GR2 ont grandement amélioré nos résultats. Une étude plus poussée des effets des surcharges, utilisant GINS-PC et bénéficiant de sa fonctionnalité iPPP ainsi que les nouveaux produits de GR2, est très prometteuse. Nous avons également montré

RÉSUMÉ LONG

que les effets de surcharge peuvent influencer notre interprétation géodynamique (chapitre sur les Pyrénées) et suggéré d'appliquer leur effet cumulé dans les études géodynamiques. Nous avons démontré que le choix des modèles géophysiques est très important lors de périodes courtes et pour les études locales.

Bibliographie

- Asri A. Développement d'un outils d'analyse des séries temporelles pour l'étude des effets saisonniers déterminés par GPS. Master's thesis, University of Rennes, September 2014.
- Bertin X., Bruneau N., Breilh J.-F., Fortunato A. B., and Karpytchev M. Importance of wave age and resonance in storm surges: The case Xynthia, Bay of Biscay. *Ocean Modelling*, 42(0):16 – 30, 2012. ISSN 1463-5003. doi: <http://dx.doi.org/10.1016/j.ocemod.2011.11.001>.
- Bevis M., Alsdorf D., Kendrick E., Fortes L. P., Forsberg B., Smalley R., and Becker J. Seasonal fluctuations in the mass of the Amazon River system and Earth's elastic response. *Geophysical Research Letters*, 32(16), 2005. ISSN 1944-8007. doi: 10.1029/2005GL023491.
- Blewitt G. and Lavallée D. A. Effect of annual signals on geodetic velocity. *Journal of Geophysical Research: Solid Earth*, 107(B7), 2002. ISSN 2156-2202. doi: 10.1029/2001JB000570.
- Boy J.-P. *Modélisation des surcharges induites par les fluides superficiels*. PhD thesis, l'Université Louis Pasteur, Strasbourg I, 2007.
- Collilieux X., Altamimi Z., Coulot D., van Dam T., and Ray J. Impact of loading effects on determination of the International Terrestrial Reference Frame. *Advances in Space Research*, 45(1):144 – 154, 2010. ISSN 0273-1177. doi: <http://dx.doi.org/10.1016/j.asr.2009.08.024>.
- Dach R., Böhm J., Lutz S., Steigenberger P., and Beutler G. Evaluation of the impact of atmospheric pressure loading modeling on GNSS data analysis. *Journal of Geodesy*, 85(2):75–91, 2011. ISSN 0949-7714. doi: 10.1007/s00190-010-0417-z.
- Davis J. L., Elósegui P., Mitrovica J. X., and Tamisiea M. E. Climate-driven deformation of the solid Earth from GRACE and GPS. *Geophysical Research Letters*, 31(24), 2004. ISSN 1944-8007. doi: 10.1029/2004GL021435.

BIBLIOGRAPHIE

- Ferenc M., Nicolas J., van Dam T., Polidori L., Rigo A., and Vernant P. An estimate of the influence of loading effects on tectonic velocities in the Pyrenees. *Studia Geophysica et Geodaetica*, 58(1):56–75, 2014. ISSN 0039-3169. doi: 10.1007/s11200-012-0458-2.
- Fratepietro F., Baker T. F., Williams S. D. P., and Camp M. V. Ocean loading deformations caused by storm surges on the northwest European shelf. *Geophysical Research Letters*, 33(6), March 2006. doi: 10.1029/2005GL025475.
- Fu Y., Freymueller J. T., and van Dam T. The effect of using inconsistent ocean tidal loading models on GPS coordinate solutions. *Journal of Geodesy*, 86(6):409–421, 2012. ISSN 0949-7714. doi: 10.1007/s00190-011-0528-1.
- Fund F., Morel L., and Mocquet A. A discussion of height reductions for Zenith Hydrostatic Delays derived from weather models. *Journal of Applied Geodesy*, 5(2):71–80, 2011a. doi: 10.1515/jag.2011.006.
- Fund F., Morel L., Mocquet A., and Boehm J. Assessment of ECMWF-derived tropospheric delay models within the EUREF Permanent Network. *GPS Solutions*, 15(1):39–48, 2011b. ISSN 1080-5370. doi: 10.1007/s10291-010-0166-8.
- Fund F., Perosanz F., Testut L., and Loyer S. An Integer Precise Point Positioning technique for sea surface observations using a GPS buoy. *Advances in Space Research*, 51(8):1311 – 1322, 2013. ISSN 0273-1177. doi: <http://dx.doi.org/10.1016/j.asr.2012.09.028>.
- Geng J., Williams S. D., Teferle F. N., and Dodson A. H. Detecting storm surge loading deformations around the southern North Sea using subdaily GPS. *Geophysical Journal International*, 191(2):569–578, 2012. ISSN 1365-246X. doi: 10.1111/j.1365-246X.2012.05656.x.
- Jiang W., Li Z., van Dam T., and Ding W. Comparative analysis of different environmental loading methods and their impacts on the GPS height time series. *Journal of Geodesy*, 87(7):687–703, 2013. ISSN 0949-7714. doi: 10.1007/s00190-013-0642-3.
- Laurichesse D., Mercier F., Berthias J.-P., Broca P., and Cerri L. Integer Ambiguity Resolution on Undifferenced GPS Phase Measurements and Its Application to PPP

BIBLIOGRAPHIE

- and Satellite Precise Orbit Determination. *NAVIGATION, Journal of the Institute of Navigation*, 56(2):135–149, 2009.
- Legru B. *Apport de la fusion de mesures GPS et Topométriques pour l'auscultation de précision*. PhD thesis, L'école doctorale du CNAM, 2011.
- Loyer S., Perosanz F., Mercier F., Capdeville H., and Marty J.-C. Zero-difference GPS ambiguity resolution at CNES-CLS IGS Analysis Center. *Journal of Geodesy*, 86(11): 991–1003, 2012. ISSN 0949-7714. doi: 10.1007/s00190-012-0559-2.
- Marty C. J., Loyer S., Perosanz F., Mercier F., Bracher G., Legresy B., Portier L., Capdeville H., Fund F., Lemoine M. J., and Biancale R. GINS: The CCNES/GRGS GNSS Scientific Software, 2012. URL http://hpiers.obspm.fr/combinaison/documentation/articles/GINS_Marty.pdf.
- Melachroinos A. S., Biancale R., Llubes M., Perosanz F., Lyard F., Vergnolle M., Bouin M.-N., Masson F., Nicolas J., Morel L., and Durand S. Ocean tide loading (OTL) displacements from global and local grids: comparisons to GPS estimates over the shelf of Brittany, France. *Journal of Geodesy*, 82(6):357–371, 2008. ISSN 0949-7714. doi: 10.1007/s00190-007-0185-6.
- Melachroinos S., Biancale R., and Perosanz F. Ocean loading effects in a high time resolution GPS analysis: Implications and artefacts with GINS software. In *International Global Navigation Satellite Service (IGS) Workshop proceedings*. ESA European operation space center, Darmstadt, Germany, 2006.
- Mémin A., Watson C., Haigh I. D., MacPherson L., and Tregoning P. Non-linear motions of Australian geodetic stations induced by non-tidal ocean loading and the passage of tropical cyclones. *Journal of Geodesy*, 88(10):927–940, 2014. ISSN 0949-7714. doi: 10.1007/s00190-014-0734-8.
- Nahmani S. *Méthodologies en traitement de données GPS pour les Sciences de l'Environnement: Contributions à l'étude de la Mousson en Afrique de l'Ouest*. PhD thesis, Université Pierre et Marie Curie, Paris, 2012.

BIBLIOGRAPHIE

- Nicolas J., Perosanz F., Rigo A., Le Bliguet G., Morel L., and Fund F. Impact of Loading Phenomena on Velocity Field Computation from GPS Campaigns: Application to RESPYR GPS Campaign in the Pyrenees. In Kenyon S., Pacino M. C., and Marti U., editors, *Geodesy for Planet Earth*, volume 136 of *International Association of Geodesy Symposia*, pages 643–649. Springer Berlin Heidelberg, 2012. ISBN 978-3-642-20337-4. doi: 10.1007/978-3-642-20338-1_79.
- Nocquet J.-M. Present-day kinematics of the Mediterranean: A comprehensive overview of GPS results. *Tectonophysics*, 579(0):220 – 242, 2012. ISSN 0040-1951. doi: <http://dx.doi.org/10.1016/j.tecto.2012.03.037>. Orogenic processes and structural heritage in Alpine-type mountain belts.
- Petit G. and Luzum B. IERS Conventions (2010). Technical report, Frankfurt am Main: Verlag des Bundesamts für Kartographie und Geodäsie, 2010. (IERS Technical Note ; 36), 2010. 179 pp., ISBN 3-89888-989-6.
- Petrov L. and Boy J.-P. Study of the atmospheric pressure loading signal in very long baseline interferometry observations. *Journal of Geophysical Research: Solid Earth*, 109 (B3), 2004. ISSN 2156-2202. doi: 10.1029/2003JB002500.
- Polidori L., Bacci P.-A., Simonetto E., Morel L., Durand F., Durand S., and Nicolas J. On the potential of GPS-InSAR combination to improve the accuracy of ground deformation monitoring: simulation-based validation. In *Anais XVI Simpósio Brasileiro de Sensoriamento Remoto - SBSR, Foz do Iguaçu, PR, Brasil, INPE*, volume 16, pages 8467–8474, April 2013.
- Souriau A. and Pauchet H. A new synthesis of Pyrenean seismicity and its tectonic implications. *Tectonophysics*, 290(3-4):221 – 244, 1998. ISSN 0040-1951. doi: [http://dx.doi.org/10.1016/S0040-1951\(98\)00017-1](http://dx.doi.org/10.1016/S0040-1951(98)00017-1).
- Tesmer V., Steigenberger P., Rothacher M., Boehm J., and Meisel B. Annual deformation signals from homogeneously reprocessed VLBI and GPS height time series. *Journal of Geodesy*, 83(10):973–988, 2009. ISSN 0949-7714. doi: 10.1007/s00190-009-0316-3.

BIBLIOGRAPHIE

- Tregoning P. and van Dam T. Atmospheric pressure loading corrections applied to GPS data at the observation level. *Geophysical Research Letters*, 32(22), 2005. ISSN 1944-8007. doi: 10.1029/2005GL024104.
- Tregoning P., Watson C., Ramillien G., McQueen H., and Zhang J. Detecting hydrologic deformation using GRACE and GPS. *Geophysical Research Letters*, 36(15), 2009. ISSN 1944-8007. doi: 10.1029/2009GL038718.
- Valty P. *Apport de la géodésie à l'étude des transferts de masse d'origine climatique*. PhD thesis, Institut de physique du globe de Paris Ecole doctorale des sciences de la terre, 2013.
- van Dam T., Wahr J., Milly P. C. D., Shmakin A. B., Blewitt G., Lavallée D. A., and Larson K. M. Crustal displacements due to continental water loading. *Geophysical Research Letters*, 28(4):651–654, 2001. ISSN 1944-8007. doi: 10.1029/2000GL012120.
- van Dam T., Altamimi Z., Collilieux X., and Ray J. Topographically induced height errors in predicted atmospheric loading effects. *Journal of Geophysical Research: Solid Earth*, 115(B7), 2010. ISSN 2156-2202. doi: 10.1029/2009JB006810.
- van Dam T., Collilieux X., Wuite J., Altamimi Z., and Ray J. Nontidal ocean loading: amplitudes and potential effects in GPS height time series. *Journal of Geodesy*, 86(11): 1043–1057, 2012. ISSN 0949-7714. doi: 10.1007/s00190-012-0564-5.
- van Dam T. M. and Herring T. A. Detection of atmospheric pressure loading using very long baseline interferometry measurements. *Journal of Geophysical Research: Solid Earth*, 99 (B3):4505–4517, 1994. ISSN 2156-2202. doi: 10.1029/93JB02758.
- van Dam T. M., Blewitt G., and Heflin M. B. Atmospheric pressure loading effects on Global Positioning System coordinate determinations. *Journal of Geophysical Research: Solid Earth*, 99(B12):23939–23950, 1994. ISSN 2156-2202. doi: 10.1029/94JB02122.
- van Dam T. and Wahr J. Modeling environment loading effects: a review. *Physics and Chemistry of the Earth*, 23(9-10):1077 – 1087, 1998. ISSN 0079-1946. doi: [http://dx.doi.org/10.1016/S0079-1946\(98\)00147-5](http://dx.doi.org/10.1016/S0079-1946(98)00147-5).

BIBLIOGRAPHIE

- Vergnolle M., Bouin M.-N., Morel L., Masson F., Durand S., Nicolas J., and Melachroinos S. A. GPS estimates of ocean tide loading in NW-France: Determination of ocean tide loading constituents and comparison with a recent ocean tide model. *Geophysical Journal International*, 173(2):444–458, 2008. doi: 10.1111/j.1365-246X.2008.03734.x.
- Williams S. D. P. and Penna N. T. Non-tidal ocean loading effects on geodetic GPS heights. *Geophysical Research Letters*, 38(9), 2011. ISSN 1944-8007. doi: 10.1029/2011GL046940.
- Wunsch C. and Stammer D. Atmospheric loading and the oceanic "inverted barometer" effect. *Reviews of Geophysics*, 35(1):79–107, 1997. ISSN 1944-9208. doi: 10.1029/96RG03037.
- Zerbini S., Matonti F., Raicich F., Richter B., and van Dam T. Observing and assessing nontidal ocean loading using ocean, continuous GPS and gravity data in the Adriatic area. *Geophysical Research Letters*, 31(23), 2004. ISSN 1944-8007. doi: 10.1029/2004GL021185.
- Zhang Y., Wallace J. M., and Battisti D. S. Enso-like interdecadal variability: 1900-93. *J. Climate*, 10:1004–1020, 1997. doi: [http://dx.doi.org/10.1175/1520-0442\(1997\)010<1004:ELIV>2.0.CO;2](http://dx.doi.org/10.1175/1520-0442(1997)010<1004:ELIV>2.0.CO;2).
- Zumberge J. F., Heflin M. B., Jefferson D. C., Watkins M. M., and Webb F. H. Precise point positioning for the efficient and robust analysis of GPS data from large networks. *Journal of Geophysical Research: Solid Earth*, 102(B3):5005–5017, 1997. ISSN 2156-2202. doi: 10.1029/96JB03860.

Introduction

The observation of the Earth's surface deformations is a subject of great scientific interest. Throughout the geodetic history several crustal deformation phenomena gave evidence of their existence. Also the Global Positioning System (GPS) technique soon proved its decisive role in the geodetic applications owing to the numerous instruments all over the Earth and its continuously improving precision. Nowadays GPS time series contribute to the terrestrial reference frame realisation, tectonic plate motion determination, constraining of the models and the observation of the glacial isostatic adjustment or to the study of sea-level variation. All these activities and research fields require high precision positioning which demands for the correction of all the possible error sources and the high frequency site displacement effects during geodetic data analysis which result in noise reduction. With the increasing precision of the space geodetic techniques new signals that were previously considered as noise are becoming meaningful. They cannot be neglected anymore considering the present day's best available accuracy. Some of these effects are well known and can be accurately modeled due to the explicit and deterministic nature of their driving forces. Such effects for example are the solid Earth tide or the tidal ocean loading [Melachroinos et al. 2006; Vergnolle et al. 2008; Fu et al. 2012b]. Other phenomena are also observed and understood but they are out of a deterministic scope. Thus these remaining signals and their models need to be further investigated to decide whether they are significant or not beside the actual geodetic precision. These effects are mainly those deformations that are induced by the non-tidal atmospheric [van Dam et al. 1994; Petrov and Boy 2004; Tregoning and van Dam 2005; Boy 2007; Collilieux et al. 2010; Dach et al. 2011; Jiang et al. 2013], oceanic [Zerbini et al. 2004; Fratepietro et al. 2006; Geng et al. 2012;

Williams and Penna 2011; van Dam et al. 2012; Mémin et al. 2014] and continental water storage loading [van Dam et al. 2001; Davis et al. 2004; Bevis et al. 2005] mass variations which are particularly our interest.

Since highly accurate IGS satellite orbit and clock data are available and sophisticated algorithms have been developed, the integer fixed ambiguity Precise Point Positioning (iPPP) method opened a new era for the GPS analysis and its application in geophysical studies. There are several software packages that can estimate positions using the iPPP method, such as GIPSY-OASIS⁵ [Zumberge et al. 1997], BERNese [Dach et al. 2007a], PANDA⁶ [Jing-nan and Mao-rong 2003] or GINS-PC⁷ [Marty et al. 2012]. The GINS-PC developed by CNES⁸/GRGS⁹ is gaining more and more popularity in the geodetic community.

Thanks to the endeavour of its background development it is armed with the state-of-the-art capabilities of GPS processing, in particular iPPP [Laurichesse et al. 2009; Loyer et al. 2012; Fund et al. 2013] therefore we have opted for the use of the GINS-PC software. Last but not least it is a multitechnique purpose software, although we did not use this advantage. The actual version of the software is a fruit of a 30 year aspiring research work.

This work is among the first studies to investigate the different loading effects using iPPP time series, particularly using the GINS-PC package. We aim to exploit sub-daily iPPP time series to study the various non-tidal loading effects at different time scales, from sub-daily to seasonal and annual periods. Here we are addressing the question whether they have important impact on our interpretation when analysing geodetic time series; whether we are capable to detect sub-daily position variations by the use of GPS; and if so, whether the models can improve the repeatability of the positions at these time scales.

One of the main research domains at the L2G laboratory (CNAM¹⁰/ESGT¹¹/L2G¹², recently renamed GeF) is the study of the deformation processes and positioning using

⁵GNSS-Inferred Positioning System and Orbit Analysis Simulation Software

⁶Position And Navigation Data Analyst

⁷Géodésie par Intégrations Numériques Simultanées PC

⁸Centre National d'Études Spatiales (French Space Agency)

⁹Groupe de Recherche en Géodésie Spatiale

¹⁰Conservatoire National des Arts et Métiers

¹¹École Supérieure des Géomètres et Topographes

¹²Laboratoire de Géomatique et Géosciences

different geodetic techniques. Several research conducted in the L2G firmly contributed to the GPS applications [Melachroinos et al. 2008; Vergnolle et al. 2008; Fund et al. 2011b,a]. There is also ongoing research on GPS and technique combination [Legru 2011; Polidori et al. 2013].

This thesis was undertaken in the context of continuation of the deformation studies that were conducted previously in our laboratory. In this aspect our goal is the observation of the various non-tidal phenomena, to contribute to the validation of geophysical models, as well as the presentation of the performance of the iPPP mode and the GINS-PC package that is a powerful tool for geodynamical applications.

This document is organised into 3 parts. In the first part we overview the main deformations of the Earth's surface induced by loading effects. Then, we present the geodetic techniques that already demonstrated their potential in deformation analysis, in particular in loading deformation studies. We then review the GPS technique and the iPPP processing mode as it was our choice for the data analysis. In the second part, we go towards a global study which gives base for future research. Then, in the third part, we demonstrate two regional studies. The first one investigates the influence of the loading effects on GPS campaign to determine tectonic velocities in the Pyrenees mountain chain. The second case study attempts to track the spatial and temporal evolution of an extreme storm event, the Xynthia windstorm that occurred in France, in 2010. This chapter also tries to identify the ocean's response to the fast moving low pressure system using sub-daily iPPP time series. After, we summarise our experiences which challenged us during the data processing and present our perspectives which would be useful for subsequent studies. Finally we give words for our conclusions.

Part I

Loading deformations and observation techniques

Chapter 1

Deformation of the Earth's surface

This chapter gives an overview about various surface deformation processes, which occur with different time (T) and wavelength (λ) signatures. In our constantly moving, living planet besides other phenomena and Earth components, the atmospheric, hydrologic and oceanic media are in continuous interaction and form a complex system which endlessly impacts our planet at diverse frequencies in space and time. Due to its complexity¹ the Earth is far from absolutely rigid, thus a realistic Earth model is somewhere between the two extremes, that is between being absolutely rigid and being absolutely liquid. The idea of the Earth's deformable body dating back to the 19th century, which says it is not adequate to assume the Earth as a completely rigid body [Darwin 1882; Witchayangkoon 2000]. The Earth's crust is exposed to gravitational forces, surface loads, movements of lithospheric plates, landslides, volcanos and so on and these forces deform or displace its surface. The displacement or deformation signifies the change in the shape of the Earth from its reference state in response to the exerting forces. The long term geophysical processes and their associated phenomena, e.g. tectonic deformation, global glacial isostatic adjustment or sea-level rise are of great interest in geosciences. To achieve the most accurate estimates of these longterm and steady phenomena using space geodetic observations, we have to take into account all the other possible site displacement mechanisms. Such effects are, for example, the non-tidal loading deformations whose investigation is the main goal of this work. These are not yet routinely corrected for during GPS data analysis. Nonetheless, they can have a significant

¹We mean its structure and the continuously interacting environmental masses on its surface.

impact on the resulting time series (See the following Section 1.1). So, the precise knowledge and testing of loading models can contribute to the longterm geodynamical studies. The improvements in the precision of the individual techniques (now we particularly speak about GPS) can change and improve our geodynamical interpretations.

1.1 Environmental loading effects

The main goal of this work is the investigation of the environmental loading effects and particularly the non-tidal phenomena. The variation of the environmental masses (atmospheric, continental water and oceanic mass) loads the Earth's surface and causes its displacement, which takes place over very broad spatial and temporal scales [van Dam and Wahr 1998]. According to their driving forces tidal and non-tidal loading effects can be distinguished. The state-of-the-art technical note on geodetic data processing is the IERS Conventions 2010 by Petit and Luzum [2010]. At present, only the tidal deformation effects are recommended for correction during the data analysis using displacement models². The non-tidal load effects are suggested not to be involved to derive conventional instantaneous positions owing to their model's lower precision and their smaller variability during the typical data integration spans used in the data analyses [Petit and Luzum 2010]. The models of the non-tidal loading effects are said to be less precise due to their not fully disclosed complexity, anisotropic effects in the Earth's response and the lack of globally suitable high resolution precise environmental dataset. However, load driven surface displacements can have remarkable amplitudes (see later sections). In addition, the unmodeled or mismodeled subdaily geophysical signals can alias into lower frequencies [King et al. 2003; Penna et al. 2007; King et al. 2008]. Collilieux et al. [2012] declared that further non-tidal model validations with space geodetic techniques are still needed. These statements arouse our interest and encourage us in this work to investigate different non-tidal geophysical loading models at regional and global scales. The comparisons of GPS and loading time series in the subsequent chapters may serve as useful information for the geophysical modellers as well as for GPS users and data processing software developers.

²Chapter 7.1 in Petit and Luzum [2010]

1.1.1 Tidal loading effects

Tidal deformation effects are attributed to the periodic variations of the solid Earth, the oceanic and the atmospheric masses induced by the gravitational pull of celestial bodies such as the Moon or the Sun. The tidal loading and other tidal³ deformations are considered well known because their driving forces can be derived using celestial mechanics from the knowledge of the Sun, Moon, Earth and other celestial bodies's orbit configuration. Therefore they are accurately modelled and can relate the regularized positions $X_R(t)$ of the reference points to their conventional instantaneous positions during the data analysis. For these phenomena, corrections are provided in Petit and Luzum [2010] and space geodetic users are encouraged to use those or something equivalent. The following two subsections only give some thoughts about those deformations which are properly tidal loading effects, namely the ocean tidal loading (OTL) and the atmospheric pressure tidal loading (ATL). We remark here that these effects will not be studied in this work since they are already routinely corrected for in GPS data analysis.

1.1.1.1 Ocean tidal loading

The periodic variation of the Earth's surface attributed to the tidal variations of the oceanic mass induced by the Moon or the Sun is called ocean tidal loading. It can be described as the total effect of a set of tidal constituents⁴. This deformation can reach more than 100 mm in the vertical component at coastal sites [Petit and Luzum 2010]. The horizontal displacements are about one third of the vertical, thus around 30 mm. The response of the ocean to the tidal forces is heavily influenced by the regional conditions, so the coastal geography and ocean topography [Witchayangkoon 2000]. Their effects are broadly studied in particular using GPS [e.g. Melachroinos et al. [2008]; Llubes et al. [2008]; Fu et al. [2012b]; Li et al. [2014]], thus they will not be investigated here.

³The solid earth tides and pole tides belong here

⁴The 11 largest main harmonics are: M_2 , S_2 , N_2 , K_2 , K_1 , O_1 , P_1 , Q_1 , M_f , M_m and S_{sa} . Their naming convention is as follows: the capital letters stands for the generating body, that is lunar, solar or lunisolar, e.g.: M signifies the Moon, S stands for the Sun. The subscripts denote the period e.g.: 1 is diurnal, 2 is semidiurnal.

1.1.1.2 Atmospheric tidal loading

The atmospheric tides, the diurnal S_1 and semidiurnal S_2 are the result of the daily changing solar radiation and the lunisolar tidal forces, however the latter has a smaller impact on it. These tides depend on the Earth's rotation and the geometry of the Earth-Sun system as they determine the insolation of the atmosphere. The estimated atmospheric tidal loading deformations are about 1-2 mm in the vertical and approximately one third of these values in the horizontal components [Böhm and Schuh 2013].

1.1.2 Non-tidal loading effects

As we already mentioned, the surface deformations owing to non-tidal loading perturbations are of our interest. We are not aware of any existing system model for the environment which accurately describes how these three systems interact with one another. That is, how water moves between the atmosphere, the ocean, and the continents (Personal communication: van Dam [2012]). Therefore studies which deal with different loading effects either investigate each particular phenomena separately or sum them up simply to obtain a total load model [Schuh et al. 2004; van Dam 2012; Collilieux et al. 2011, 2012]. Based on this we act likewise during our analysis to infer knowledge from loading models and GPS position time series comparisons, since GPS observes (or measures) the combination of all the effects.

1.1.3 The origin of the different effects

Depending on the forcing media which can be the continental water, the atmosphere and the ocean, three types of non-tidal deformations can be identified. They are namely the following: atmospheric pressure loading (ATML), continental water storage loading (CWSL) and non-tidal ocean loading (NTOL).

1.1.3.1 Atmospheric pressure loading (ATML)

The atmospheric pressure loading models describe displacements of the surface of the Earth induced by temporal and geographical variations of the atmospheric mass. The

1.1. ENVIRONMENTAL LOADING EFFECTS

loading mass needs to be geographically extensive (≈ 1000 km) to cause observable deformation [van Dam et al. 1994]. The horizontal displacement values are 3 to 10 times smaller than the vertical ones. Coastal stations of big continents show the largest horizontal deformations in general [Dach et al. 2011]. van Dam et al. [1994] found the largest vertical loading signal RMS to be 5 mm in Alaska. Petrov and Boy [2004] examined the atmospheric pressure loading effect using VLBI time series and found that the displacement can reach up to 20 mm amplitude in the vertical component and around 3 mm in the horizontal directions. From GPS, Tregoning and van Dam [2005] showed that maximum height variations during a day can be expected up to 18 mm at high latitudes where pressure variations are larger. This important loading variation in the course of a day was also mentioned by Boehm et al. [2009]. The largest atmospheric loading effect was found in Russia in the study of Dach et al. [2011]. They found that applying atmospheric loading correction during the data analysis improves the repeatability of weekly position estimates by 20 %. When they *a posteriori* corrected their GPS series they experienced 10 % of improvements compared to series that excluded the atmospheric loading effect.

Atmospheric data (surface pressure), which is necessary for these estimations can be found at various spatial and temporal resolutions provided by different research centers. They are, for example, National Centers for Environmental Prediction (NCEP) and National Center for Atmospheric Research (NCAR), European Centre for Medium-Range Weather Forecasts (ECMWF), and Modern Era Retrospective analysis for Research and Applications (MERRA). When we estimate the atmospheric pressure loading we have to deal with the atmosphere above the land and above the ocean. Therefore a hypothesis has to be applied to characterise the ocean response to atmospheric pressure variations. The adapted assumption impacts the output of coastal stations as the choice for the ocean response roughly means the considered mass load above the ocean basins. The two end bounds of the hypothetical deformations are defined by the inverse barometer (IB) assumption (as lower limit) and the non-IB assumption (as upper limit). Figure 1.1 shows the two scenarios.

The inverse barometer (IB) hypothesis implies that the ocean surface entirely adjusts

itself to the atmospheric pressure variations, that is 1 mbar change in the atmospheric pressure causes 1 cm change in the ocean surface [van Dam et al. 1994]. Simply stated the mass load above the ocean basin at a particular area remains constant. Therefore the ocean bottom does not experience any effect of the atmospheric fluctuations.

The non-IB hypothesis implies an oceanless environment⁵, only the solid Earth, thus there is no ocean response. Therefore the ocean bottom experience the effect of the atmospheric fluctuations.

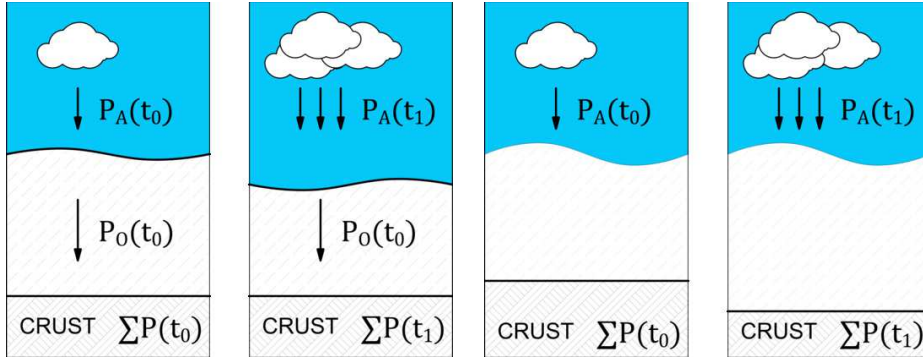


Figure 1.1 – This simple figure shows the ocean’s response to the atmospheric pressure change in the case of inverse barometer hypothesis (left) and in the case of an oceanless Earth model (right). At t_0 the pressure on the ocean basin is $\sum P(t_0) = P_A(t_0) + P_O(t_0)$ while at t_1 it is $\sum P(t_1) = P_A(t_1) + P_O(t_1)$. Due to the IB assumption $\sum P(t_0) = \sum P(t_1)$. $P_A(t_0) < P_A(t_1)$ but $P_O(t_0) > P_O(t_1)$. Meanwhile due to the oceanless assumption $\sum P(t_0) < \sum P(t_1)$. $P_A(t_0) < P_A(t_1)$ but there is no ocean, thus the P_O term.

In the case of a perfect inverted barometer response a coastal station would only be exposed to about 50 % of the total regional pressure field centered at the station (Figure 1.2).

Inland stations with ≥ 1000 km coastal distance are not sensitive to the ocean response [van Dam et al. 1994]. The IB assumption is slightly modified thus the oceanic mass is constrained to be conserved. The modified inverse barometer (IB) response to atmospheric pressure fluctuations is usually set in the Earth model that is used for the surface displacement calculations. As a result, the ocean basins experience an uniform pressure $\Delta \bar{P}_0$ whenever there is a net change in the mass of the air above the oceans [van Dam and Wahr 1987; van Dam et al. 1994]. This assumption is only suitable for periods

⁵Oceanless Earth model.

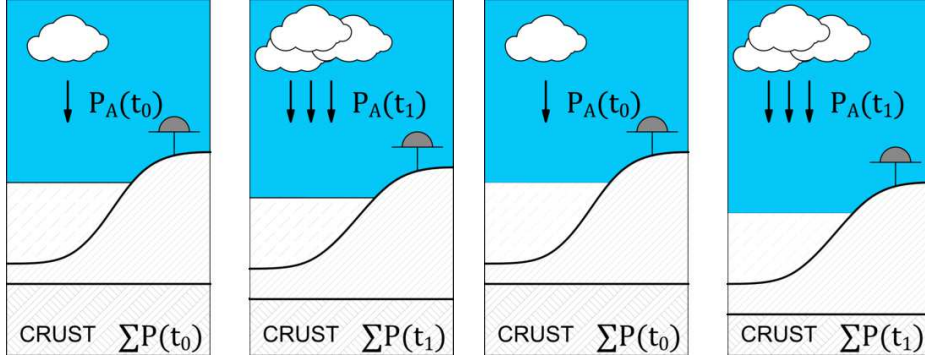


Figure 1.2 – Coastal station with IB ocean response (left) and coastal station with non-IB assumption (right).

longer than 5 to 20 days because the ocean needs time to adjust itself and to obtain equilibrium with the pressure system. Therefore for shorter periods a dynamic ocean response is more realistic [Petrov and Boy 2004]. The slightly modified IB hypothesis is written as follows:

$$\Delta \bar{P}_0 = \frac{\iint [P(r', t) - P_{ref}(r')] \cos \vartheta' d\vartheta' d\lambda'}{\iint_{ocean} \cos \vartheta' d\vartheta' d\lambda'} \quad (1.1)$$

Where $(P(r', t) - P_{ref}(r'))$ is the relative atmospheric pressure at epoch t , ϑ' and λ' are the geocentric latitude and longitude, respectively. The integrals are evaluated over the entire surface of the ocean.

Using equation (1.1) we can take into account the IB effect for loading deformation estimation by breaking down the formulas (1.2) to (1.4) into two parts, as a land and an ocean contributions (not shown here) presented by van Dam and Wahr [1987]; Böhm and Schuh [2013]; Petrov and Boy [2004].

1.1.3.2 Continental water storage loading (CWSL)

The 3-dimensional displacements provoked by the continental water storage loading (CWSL) are due to the relative water storage variations over a region. The sources are the snow mass, soil-water and surface water changes. These quantities are captured with various levels of details depending on the hydrological model. Vertical displacements of up to 30 mm were documented in a global scale research (over 147 globally distributed GPS stations) performed by van Dam et al. [2001]. They stated that this signal is mainly

annual. These biggest variations are in South America at the Amazon Basin and in South-East Asia. Other studies for example Bevis et al. [2005] reported a peak-to-peak amplitude of 50-75 mm in the seasonal cycle of hydrological loading at the Amazon Basin (over 15 GPS sites).

Global hydrological datasets exist e.g. Noah-Version 1 Global Land Data Assimilation System (GLDAS) [Rodell et al. 2004; Rui et al. 2011] model, NCEP/NCAR [Kalnay et al. 1996] or MERRA-Land [Reichle et al. 2011], ECMWF ERA-Interim/Land reanalysis data [Balsamo et al. 2013] that involve estimates of all kinds of water in the hydrosphere. For example, the GLDAS monthly grids (1.0° in longitude and latitude resolution) besides other variables provide estimates of snow water equivalent and until 3.5 m depth the soil moisture information, that our CWSL model applies. One can think that maybe this 3.5 m depth information is not sufficient for an appropriate estimation of the displacement driven by hydrological effect but several studies showed good agreement between GLDAS and GRACE estimates [Davis et al. 2004; Bevis et al. 2005; Fu et al. 2012a; van Dam et al. 2012; van Dam 2012].

1.1.3.3 Non-tidal ocean loading (NTOL)

The ocean bottom pressure (OBP) variations generate non-tidal ocean loading (NTOL) effects that cause surface displacements of coastal sites. The OBP is the combined effect of ocean and atmosphere masses above the seafloor. Inland stations far from the coast sites (more than few hundred km) are not subject to this phenomenon.

Storm surges can generate ≈ 20 -30 mm displacement around the North Sea at coastal geodetic sites [Fratepietro et al. 2006]. Nordman et al. [2009] have derived non-tidal Baltic Sea loading series from 22-26 tide gauge data to investigate the agreement between GPS at Fennoscandia. They succeeded to reduce the RMS by around 20 % for a 3 year long time series. Williams and Penna [2011] used a high resolution ocean model to estimate NTOL displacements. They have applied the NTOL model for 3-4 year long GPS time series around the North Sea. Their network included 17 coastal sites and they successfully reduced the RMS on all of their series by about 14 % on average. They have seen that the

1.1. ENVIRONMENTAL LOADING EFFECTS

high resolution model that they applied (POLSSM⁶) outperforms the global circulation ECCO model by 11 %. Therefore they recommended to use high resolution models when possible. After a global study using the ECCO OBP product over 344 GPS sites, van Dam et al. [2012] reported that the largest vertical displacements due to NTOL are expected at semi-enclosed basins and coastal sites around the coast of Asia, Australia, North and South America, North Sea, the British Isles and the Aleutians. They also showed that coastal sites experience 6-10 mm variations meanwhile the inland stations can be displaced by only about 1-3 mm in the vertical. They successfully reduced the RMS by up to 0.7 mm over 65 % of their studied stations. Moreover they have found that the annual signal is responsible for the 80 % of this RMS reduction.

One example of a global data source is the Estimating the Circulation and Climate of the Ocean (ECCO) OBP product, specifically, the Jet Propulsion Laboratory (JPL)'s Kalman Filter (kf080) series [Fukumori 2002]. The model assimilates altimetric sea surface heights, expendable bathythermograph (XBT) profiles and other ocean in situ data. The OBP is a by-product of the model for the primary product that is the general circulation of the ocean driven by winds.

1.1.3.4 Calculation of the non-tidal loading effects

There are three different methods to predict radial and horizontal displacements induced by different environmental loading effects which could be grouped in two main approaches: a) geophysical and b) empirical approach [van Dam and Wahr 1987; Schuh et al. 2004; Petit and Luzum 2010; Böhm and Schuh 2013]. The name *geophysical approach* signifies that the estimation is based on geophysical models while the *empirical approach* means an empirical, loading regression coefficient determination for a given site [Schuh et al. 2004; Böhm and Schuh 2013]. However, the empirical approach is only used in atmospheric pressure loading estimation, due to the relatively good availability of local pressure data. The subsequent descriptions and formulas of the two approaches mainly follow Böhm and Schuh [2013] who have provided an excellent summary of the atmospheric loading calculation in their work. Beside the previously cited work,

⁶Proudman Oceanographic Laboratory Storm Surge Model

numerous comprehensive, synthetic studies can be found, which give insight into loading estimation, without being exhaustive they are as follows: van Dam and Wahr [1987]; van Dam et al. [1997]; van Dam and Wahr [1998]; van Dam et al. [2010]; Schuh et al. [2004]; Petrov and Boy [2004]; Dach et al. [2011]; Jiang et al. [2013].

Geophysical approach

As we can infer from the word *geophysical*, this approach is based on our physical understanding of how our Earth behaves due to surface loads [Schuh et al. 2004]. We will see in details, that this approach has four essential pillars, namely: global pressure grid, reference pressure, Green's functions together with loading Love numbers (LLN) and land-sea mask [Böhm and Schuh 2013]. According to Schuh et al. [2004] two methods belong here. One is the Green's function point loading approach and the other is the spherical harmonics approach. Both of them require the knowledge of the loading Love numbers (which reflect the scale of a deformation due to an external influence), preferably up to very high degree $n=10000$ (this number was suggested by Farrell [1972]). In this thesis, we do not detail the spherical harmonic approach since all the displacement time series used in the different studies were derived applying the Green's function method. Also, Chen et al. [2013b] showed that the RMS of the differences between these two approaches over 914 GPS stations are less than 0.11 mm in the horizontal direction and 0.55 mm in the vertical direction. Thus, the two approaches are identical with respect to the GPS noise floor. The following equations (1.2)-(1.4) represent the point loading, Green's function formulation at a desired station location (r) and epoch (t) for vertical (*radial*) ($U_r(r, t)$), east ($U_e(r, t)$) and north ($U_n(r, t)$) displacements as a function of the relative pressure ($P(r', t) - P_{ref}(r')$) at epoch t over the whole surface of the Earth:

$$U_r(r, t) = \iint_S [P(r', t) - P_{ref}(r')] G_r(\psi) \cos\vartheta' d\vartheta' d\lambda' \quad (1.2)$$

$$U_e(r, t) = \iint_S [P(r', t) - P_{ref}(r')] G_h(\psi) \sin\alpha_{rr'} \cos\vartheta' d\vartheta' d\lambda' \quad (1.3)$$

$$U_n(r, t) = \iint_S [P(r', t) - P_{ref}(r')] G_h(\psi) \cos\alpha_{rr'} \cos\vartheta' d\vartheta' d\lambda' \quad (1.4)$$

The integrals in equations (1.2) to (1.4) are evaluated over S , the entire surface of the Earth. ϑ' and λ' are the geocentric latitude and longitude, respectively and $\alpha_{rr'}$ is the azimuth angle between our station and the pressure source. The terms $G_r(\psi)$ and $G_h(\psi)$ are the radial and horizontal Green's functions, which describe the response of an elastic Earth to a point load on its surface [van Dam and Wahr 1987]. They depend on the angular distance ψ between the location of the given station and the pressure data and they are used as the weighting functions of the relative pressure. The Green's functions are constructed as follows, using the h'_n and l'_n loading Love numbers:

$$G_r(\psi) = \frac{GR}{g^2} \sum_{n=0}^{\infty} h'_n P_n(\cos\psi) \quad (1.5)$$

$$G_h(\psi) = \frac{GR}{g^2} \sum_{n=0}^{\infty} l'_n \frac{\partial P_n(\cos\psi)}{\partial\psi} \quad (1.6)$$

In equations 1.5 and 1.6, G is the universal gravitational constant, g is the mean gravitational acceleration at 45° geodetic latitude at the surface of the Earth with a mean radius R , and P_n is the n^{th} degree Legendre polynomial.

The displacements are mainly vertical ([van Dam and Wahr 1987; Petrov and Boy 2004]. The horizontal component is only one-third to one-tenth of the vertical displacement [van Dam et al. 1994; Petrov and Boy 2004; Schuh et al. 2004; van Dam et al. 2012]. Böhm and Schuh [2013] after Hofmann-Wellenhof and Moritz [2005] used the formula for the cosine and the sine of the azimuth angle:

$$\cos\alpha_{rr'} = \frac{\cos\vartheta\sin\vartheta' - \sin\vartheta\cos\vartheta'\cos(\lambda' - \lambda)}{\sin\psi} \quad \sin\alpha_{rr'} = \frac{\cos\vartheta'\sin(\lambda' - \lambda)}{\sin\psi} \quad (1.7)$$

Since it takes into account the pressure variations all over the Earth considering a well developed, complex geophysical model, we can summarise that this method is preferable with respect to the empirical approach. However, it has some limitations such as the spatial and temporal resolution of the global pressure data, uncertainties in the Green's functions and uncertainties in the ocean response model [van Dam et al. 1994; Schuh et al. 2004].

Empirical approach

As the word *empirical* suggests, this estimation method considers geodetic measurements and observation of environmental parameters. Then it characterises the

phenomena finding a possible relationship between these data. We have to remark here that this method is only relevant for atmospheric pressure loading. The loading effect is empirically computed by determining a fit between the vertical residuals of the geodetic measurements and the local barometric pressure [van Dam and Wahr 1987; Schuh et al. 2004; Böhm and Schuh 2013]. Note this approach can only be used to estimate vertical crustal motion because we only take into account the local pressure variation and we consider it as a normal force. Schuh et al. [2004] presented two formulas for empirical atmospheric loading estimation, one of them is formulated by Rabbel and Zschau [1985] and is a two-coefficient estimation:

$$U_r(r, t) = \alpha \times (P(2000km, t) - p_{ref}) + \beta \times (P(r, t) - P_{ref}) \quad (1.8)$$

The above formula is based on regional relative average $(P(2000km, t) - P_{ref})$ and local $(P(r, t) - P_{ref})$ relative barometric pressure. α and β are the regression coefficients (please note that Schuh et al. [2004] published the value of the coefficients instead of the variables), which depend on the location of the station, epoch and the length of the used time series. The other equation is a simpler one, since it takes into account only the local relative pressure [Manabe et al. 1991]:

$$U_r(r, t) = \alpha \times (P(r, t) - P_{ref}) \quad (1.9)$$

It had been shown that this method is a reasonably good alternative to the geophysical approach in most regions of the Earth [Schuh et al. 2004; Böhm and Schuh 2013] if global grids of surface pressure are not available at the desired time or if we want to estimate quickly and easily the displacement evoked by the loading. However, we must be aware of the side-effects and limitations of this method, which were pointed out by Schuh et al. [2004]. For a reliable regression coefficient a large number of observations is required. It is ambiguous whether other pressure correlated geodetic signals are not being absorbed into the regression coefficient. The determined coefficients depend on the length of the dataset and change by observing technique. The site-dependent regression coefficients cannot be extrapolated to a new site.

Loading services

The Special Bureaus (SB) of the Global Geophysical Fluids Center (GGFC)⁷ are responsible for research and data service activities related to mass transports in the atmosphere, oceans, and hydrological systems. Under the coordination of the Special Bureaus of GGFC we can find different online services to obtain already computed loading displacement estimates. In the following Table 1.1, we present different datasets available for loading effect computation and the different online services. As it was mentioned in the previous sections, these data could be used to correct geodetic measurements to improve accuracy. However, the spatial and temporal resolutions vary dataset by dataset and services by services. Thus, the user needs to find the most adequate input source or loading service to the scientific objectives.

Table 1.1 – Various online services which provide non-tidal atmospheric, hydrologic and oceanic loading models.

SERVICE	LOADING EFFECTS		
	ATML	NTOL	CWSL
GSFC	NCEP ⁸	ECCO ⁹	GLDAS ¹⁰
TU-WIEN ¹¹	ECMWF	–	–
UNI-LU ¹²	NCEP	ECCO	GLDAS
UNI-ST ¹³	ECMWF+IB ECMWF+MOG2D	ECCO	GLDAS

1.2 Summary of the chapter

The previous sections provided a brief overview about the various deformations that can be observed by nowadays space geodetic techniques, the calculation and magnitudes of the different non-tidal environmental loading effects. The following table (Table 1.2)

⁷The GGFC is established in 1998 by International Earth Rotation and Reference Systems Service (IERS) and restructured in 2009.

⁸<http://gemini.gsfc.nasa.gov/results/aplo>

⁹<http://lacerta.gsfc.nasa.gov/oclo>

¹⁰<http://lacerta.gsfc.nasa.gov/hydlo>

¹¹<http://ggosatm.hg.tuwien.ac.at/loading.html>

¹²<http://geophy.uni.lu>

¹³<http://loading.u-strasbg.fr>

1.2. SUMMARY OF THE CHAPTER

summarises their expected horizontal and vertical effects on the local station coordinates. We can see that, these magnitudes are small, however they exceed the formal error of our GPS results, indicating that they are observable quantities.

Table 1.2 – Horizontal and vertical magnitudes of the deformational effect.

	Horizontal	Vertical	Unit
Tectonic deformation	100	10	mm/yr
Post-glacial rebound	2	10	mm/yr
Ocean tidal loading	20	100	mm
Atmospheric tidal loading	0.5	2	mm
Continental water storage loading	10	30	mm
Atmospheric pressure loading	3	20	mm
Non-tidal ocean loading	2	10	mm
GPS formal error ¹⁴	~1	~5	mm

The geodetic techniques observe the complex contributions of the various phenomena on the Earth. Therefore, the geodetic time series contain the combined effect of all the processes. Thus, the effect of the variation of the atmospheric, continental water or oceanic masses are also present in the position time series through unknown transfer functions. So the challenge is the separation of the mass transport related signals from phenomena with other origin and the noise of the measurement. Figure 1.3 summarises and represents this complex problem.

We have seen, so far, the non-tidal deformations and their amplitudes. We have also seen some examples of the kind of long-term deformations (Table 1.2) that are signals of great scientific interest too. After all we can conclude that the investigation and the validation of the non-tidal loading models possibly can contribute to geodynamical model development or data determination. Now we will overview the techniques that can be used to observe them, then our choice, the GPS system will be detailed. In Chapters 4 and 6 we use GPS iPPP time series to investigate these effects.

¹⁴using iPPP mode in GINS-PC, 6 hourly sampling.

1.2. SUMMARY OF THE CHAPTER

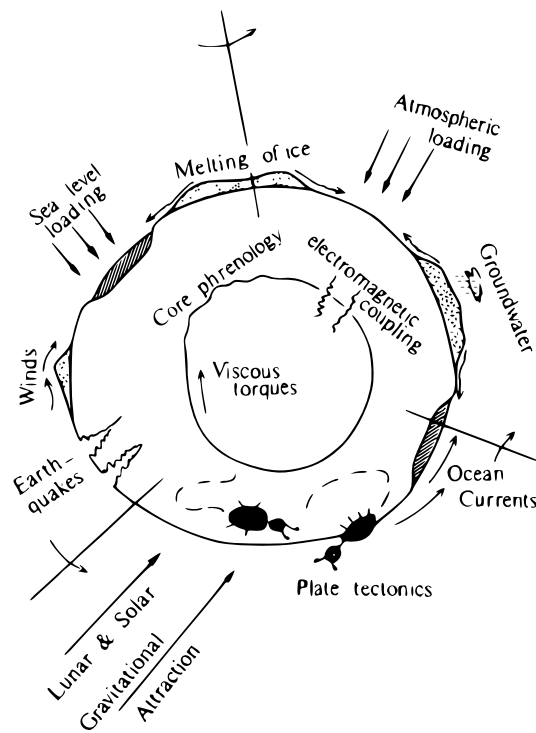


Figure 1.3 – Surface deformation processes on the Earth. Source: Lambeck [1980].

Chapter 2

Space geodetic observations of loading deformations

The time variation of the surface of the Earth due to surface mass redistributions¹ is precisely observable by space geodetic techniques with high spatial and temporal resolution. The observations are carried out particularly with Global Positioning System (GPS), Very Long Baseline Radio Interferometry (VLBI), Satellite Laser Ranging (SLR) and satellite gravimetry, such as Gravity Recovery And Climate Experiment (GRACE).

To give physical meaning to our observations, to interpret geodetic measurements and to study deformations we have to apply a proper, global reference system. This factor will be discussed in the following section.

2.1 Reference system

The thoughts of Kovalevsky et al. [1989] give an idea of the concept, which says the position and the motion are not absolute terms therefore we always describe any physical phenomena relative to a reference frame. We can always find a reference system where the description of the observed physical events are simplified. Therefore the chosen reference depends on the objectives of our study that is why we can meet with the word *conventional* reference frame in the scientific literature. For example, the study of the Earth's surface deformation requires a crust-fixed reference frame known as Terrestrial Reference Frame (TRF). The observation of the Earth's motion demands a frame referring to celestial bodies

¹atmospheric, oceanic and continental water masses (Section 1.1.2).

and called the Celestial Reference Frame (CRF) [Collilieux 2008]. Blewitt et al. [2010] highlighted the importance of the TRF and CRF as they described them as the building stones of the solid Earth sciences and as universal standards. The two terms, the reference system and the reference frame have to be properly distinguished. The former one means the description of the physical environment and its concept. The latter is the physical realisation of the system as written in Collilieux [2008] after Kovalevsky et al. [1989]. The notion of the International Terrestrial Reference System (ITRS) implies some important conditions such as: (1) its origin is geocentric in a way that it lies at the joint mass center of the solid Earth, oceans and atmosphere; (2) the system is co-rotating with the Earth in its diurnal motion in space; (3) its orientation is equatorial with the fact that the Z axis is the direction of the pole and its unit length is an SI meter [Collilieux 2008; Petit and Luzum 2010]. The ITRS is accessible for the geodetic users through its most accurate realisations as the International Terrestrial Reference Frame (ITRF) [Altamimi et al. 2002, 2007, 2011] thanks to the work of the International Earth Rotation and Reference Systems Service (IERS) ITRS Center by the means of a set of station coordinates and velocities [Petit and Luzum 2010]. These site coordinates are the vertices of a polyhedron which discretizes the Earth's surface [Collilieux 2008]. A TRF can be absolutely characterized at a given epoch by the knowledge of its origin, orientation and scale parameters. In such a frame the variation of the observed positions is minimal in terms of kinetic energy, they only experience small but eternal deformations over time. The year after the ITRF acronym indicates the latest data used for its realisation. At the year of this work², the latest official ITRF version is the ITRF2008, however there is already an ongoing effort on the new ITRF2013 release. The equation (2.1) is taken from Petit and Luzum [2010] and relates the instantaneous position $\vec{X}(t)$ of an Earth fixed station (e.g. GPS) at epoch t to its regularized position $\vec{X}_R(t)$ (ITRF). Applying this concept it is possible to remove high frequency or other geophysical effects using conventional corrections $\Delta\vec{X}_i(t)$ in order to obtain a position with more regular time variation [Petit and Luzum 2010].

$$\vec{X}(t) = \vec{X}_R(t) + \sum_i \Delta\vec{X}_i(t) \quad (2.1)$$

²2014

2.2 Space geodetic observations

This chapter briefly introduces the space geodetic techniques which are generally applied in loading research and already contributed to the scientific community in this field of study.

2.2.1 Very Long Baseline Radio Interferometry (VLBI)

VLBI was originally developed to take pictures of radio sources³ and to study their detailed structure at a high angular resolution that depends on the telescope size. A huge radio antenna can be emulated whose diameter corresponds to the largest separation distance between the individual telescopes (baseline), that is nearly the diameter of the Earth. Thus, the corresponding resolution to this synthetic antenna is better than 1 mas. The principle idea of VLBI bases on simultaneous observations of the same radio sources at two or more independently working radio telescopes that are located thousands of kilometers apart and interconnected via precise atomic clocks. The emitted radio waves are recorded at different antennas at different epochs. This time dependent signal delay is the most important observable for geodetic application. The geometrical relationship of the configuration and appropriate corrections are considered to form the observation equations and define a reference station. Site coordinates of the participating telescopes and other site dependent variables together with global parameters of the network such as Earth Orientation Parameters (EOP) and the position of the radio sources are very precisely estimated [Seeber 2003]. van Dam and Wahr [1987]; van Dam and Herring [1994]; Petrov and Boy [2004] used VLBI data to investigate atmospheric loading effects globally and for model validation.

Despite the fact that this technique provides very precise observations, it is not the best choice for regional and local loading studies due to its sparse network⁴. The number of stations is explained by the fact that it is expensive to extend and maintain the network. For example there are 48 fixed VLBI stations globally that are used for the ITRF realisation

³They are quasars, that are distant celestial bodies, which are well outside from our galaxy and show minimal proper motions

⁴133 fixed stations according to <ftp://cddis.gsfc.nasa.gov/vlbi/ivscontrol/ns-codes.txt>

[Altamimi et al. 2014] providing the information on the scale parameter [Altamimi et al. 2002, 2007, 2011].

2.2.2 Satellite Laser Ranging (SLR)

The SLR technique provides millimeter precision distance measurements between satellites and ground stations based on the two-way travel time measurement of a short laser pulse. The observation system includes a network of ground stations that generate and transmit the short laser pulse and the target satellites that are equipped with proper array of retro-reflectors to return the signal back to the stations. The propagation time of the signal is determined from the clock readings of emission and reception times and scaled up by the speed of the light to form the basic observation equation. Then appropriate parameters and corrections are adjusted to the instantaneous distance measurement between the satellite and the ground station to derive geocentric station coordinates or EOP among other quantities [Seeber 2003].

The effect of non-tidal loading can be significant for SLR solutions. The neglected atmospheric non-tidal loading corrections may contribute to inconsistencies between SLR and GNSS solutions that can reach 2.5 mm for inland stations, as it was demonstrated by Sośnica et al. [2013]. Collilieux et al. [2009] assessed the contribution of loading to SLR network effect using two distinct loading models. They estimated its magnitude to be at the level of 1.5 mm RMS. The SLR is an optical technique, therefore the observations are restricted to cloudless sky conditions. Thus, it can not guarantee continuous measurements which would be essential to high frequency loading variation observations. In spatial aspect, there are not enough fixed SLR stations⁵ for detailed regional or local studies. The strength of this technique is that it provides information for the origin of the ITRF realisations, that is the center of mass [Altamimi et al. 2002, 2007, 2011].

2.2.3 Global Navigation Satellite System (GNSS)

The GNSS is a general name of space based positioning systems such as GPS, Globalnaya Navigatsionnaya Sputnikovaya Sistema (Russia) (GLONASS), GALILEO

⁵For example 32 fixed global stations used for ITRF [Altamimi et al. 2014].

(European Union (EU)) and COMPASS/Beidou (China). Since we present only results based on GPS data in later chapters, we will use the term GPS instead of the more general one, GNSS. This positioning technique in principle is a distance measurement based on timing. In a geometrical sense it is a three dimensional trilateration. If all the applied clocks would be perfectly synchronized and set to the GPS system time then in our 3D space the geocentric position vector of a ground receiver could be explicitly determined from simultaneous range measurements to three satellites where these distances could be considered as the radius of three spheres whose intersection locate our position. However, GPS ground receivers use inexpensive crystal clocks⁶ that are offset compared to the system time. Therefore the ranges derived from time measurements are different from the true geometric distances. Accordingly, these distances are called pseudoranges. Thus, we have to consider a range correction term and we require measurements minimum to four satellites to determine the three components of position and the receiver clock bias [Hofmann-Wellenhof et al. 2007]. Due to the precision of GPS that could be achieved during post-processing mode it became a powerful tool in geoscientific applications. The technique will be overviewed in Chapter 3.

The potential of GPS in loading effect studies was demonstrated for example by van Dam et al. [1994], Collilieux et al. [2012], Nahmani et al. [2012], Jiang et al. [2013], Valtý [2013], van Dam et al. [2010], and van Dam et al. [2012] exploiting the GPS system's relatively dense spatial and temporal resolution. The available number of GPS receivers on the globe (global and regional networks) is suitable for each, local, regional and global scale loading effect researches. Since GPS is a microwave technique, it is weather-independent providing continuous observations that is essential for loading studies at different time scales⁷ with adequate accuracy.

2.2.4 Satellite Gravimetry with Gravity Recovery And Climate Experiment (GRACE)

The objective of the mission is to map the temporal gravitational field variations of the Earth from shorter to long wavelength spatial resolution (from 400 km to 40.000 km) every

⁶they only set approximately to system time

⁷From sub-daily over daily, seasonal to annual time scales.

2.2. SPACE GEODETIC OBSERVATIONS

thirty days. The idea of a low Earth orbiting satellite pair on the same orbit to accomplish this mission using high precision measurement of the relative motion of two satellites was already presented by [Wolff 1969; Ilk et al. 2005]. The GRACE is a twin satellite mission that evolved from this concept in a joint partnership between the National Aeronautics and Space Administration (NASA) and Deutsches Zentrum für Luft- und Raumfahrt e.V., the German Aerospace Center (DLR). The two identical satellites were launched on the 17th of March 2002 into an almost circular, near-polar orbit with an initial altitude of 500 km where they follow each other on the same orbital path by a nominal distance of 220 km. The exact separation distance and its rate of change are measured with an accuracy of better than 10 μm via a K-band microwave connection [Tapley et al. 2004]. The mission was designed for a nominal lifetime of five years to accomplish its objectives, however it is still operating after more than twelve years of service providing measurements for global gravity field mapping every thirty days [Ilk et al. 2005]. The temporal variation of the gravitational field relies on the redistribution of masses. They are assumed to be related to climate-driven surface water changes. Thus GRACE can be used to derive seasonal displacement maps based on the captured monthly global gravity fields.

Several studies found good level of agreement between GPS and GRACE [Davis et al. 2004; Bevis et al. 2005; Fu et al. 2012a]. For example Fu et al. [2012a] defined a measure called the weighted root mean square (WRMS) Reduction Ratio which reflects the agreement of the GPS and GRACE time series in both amplitude and phase. A value of 1.0 of this measure would indicate perfect agreement between GPS observed and GRACE modelled annual plus semi-annual seasonal displacement. They found a median WRMS Reduction Ratio of 0.82 over their study area, Southern Alaska. However, at short periods (less than one month) and smaller spatial scale (less than 400 km) they are not comparable. From this aspect we can see the strength of the GPS technique that can serve regional studies as well. It can provide useful information about the underlying geophysical phenomena from a regional network with higher frequency data sampling. We can remark that GRACE can help the analysis of seasonal signals at large scale whereas GPS completes for small scales and larger temporal resolution.

2.2.5 Interferometric Synthetic Aperture Radar (InSAR)

Traditionally satellite geodesy does not comprise satellite borne radar techniques, such as InSAR, although they are the subject of remote sensing. InSAR is particularly valuable to map topography and to generate Digital Elevation Model (DEM), however it has great potential in geodynamic deformation studies thus it can be regarded as auxiliary to GPS in this field of study [Seeber 2003]. The Radio Detecting and Ranging (RADAR) antenna transmits microwave signal that scatters back from ground objects and the travel-time and the strength of the returned signal (brightness of radar image pixels) are recorded. The along-track satellite RADAR observations are collected and combined simulating a huge antenna aperture that is why the Synthetic Aperture Radar (SAR) expression. The interferometric principle arises when more than one image of the same territory is recorded from a slightly different antenna position. This image can be seen also as *phase-image* where only the fractional part of the phase is recorded considering bright pixels as 2π and black ones as 0 phase. Using these quantities the geometric distance between the transmitting antenna and the ground objects can be determined [Seeber 2003].

The InSAR technique has been used in many applications to monitor surface deformations for example land slides, subsidence, earthquakes and more recently seasonal hydrological loading in Brazil as it was presented by Ramos et al. [2014]. Nowadays the best available temporal resolution for InSAR is provided by the Cosmo-SkyMed constellation, that consists of 4 satellites. The shortest interval is one day between two acquisitions. However, the images are acquired based on requests with different modes which are not mutually compatible for InSAR. Thus, it is not possible to use images acquired by different modes for InSAR [Simonetto 2014]. However in temporal aspect it can not compete with GPS to detect sub-daily deformations.

2.3 Loading effects as errors in deformation measurements

The accumulated effect of various phenomena are present in the resulting coordinate time series of the different space geodetic observations. Some part of the variations is recognised as signal of interests, while another part is considered to be noise. Depending

on the aim of the study (1) on the one hand the non-tidal loading effects are in our focus for investigation and validation of their models (Section 2.3.1, Chapters 4 and 6) and (2) on the other hand they are seen as perturbing factors during data interpretation (Section 2.3.2).

2.3.1 Validity of loading corrections

The most recent and ongoing investigations of the non-tidal loading effects ([Collilieux et al. 2011; Dach et al. 2011; Chen et al. 2013b; Jiang et al. 2013] and others, Chapters 4 and 6) analyse the quality of these models using position time series of space geodetic techniques, particularly GPS. The used residual time series in these studies are with weekly or daily sampling in general. Among the previous researches this work would contribute to our better understanding of the geophysical processes and would help to answer the question whether the models are adequate enough to be considered in GPS data processing or not using sub-daily position time series.

This question serves meaningful information for instance for the new realisation of the terrestrial reference frame (ITRF2013⁸) and for orbitography. Maybe it is possible to achieve even better accuracy by applying appropriate models. Therefore, the rigorous validation of the models and the better understanding of the coupling of the different effects are important scientific goals. Also, it is essential to find the best choice of the models to use for geodetic time series corrections.

2.3.2 Influence of loading on data interpretation

Monitoring the small deformation of the Earth's surface (e.g. tectonic deformation, post glacial rebound, observing sea-level rise) is a challenging task as well as drawing correct conclusions about the surface forming phenomena. In such research, making a judgement as to the proper deformation analysis using high precision measurement is essential. This goal implies that all the measurement errors and signals of other origins have to be accounted for. However, it requires the use of correct and pertinent models that fit to our particular need, thus we somehow refer back to the evaluation of the loading models.

For example a GPS campaign determined tectonic velocity is potentially the subject

⁸http://itrf.ensg.ign.fr/ITRF_solutions/2013/CFP-ITRF2013-27-03-2013.pdf

2.3. LOADING EFFECTS AS ERRORS IN DEFORMATION MEASUREMENTS

of the loading influence since it can have important seasonal peaks that can impact epoch campaign measurements. We have shown in a regional study that the tectonic velocity results can be interpreted differently if the importance of the different non-tidal loading effects are neglected (Section 5).

The influence of loading effects is maybe not relevant for the observation and interpretation of deformations which occur over relatively small regions⁹ with high amplitudes in the course of a short time. This is due to the fact that (1) the loading amplitudes are insignificant compared to the tremendous deformation magnitude caused by for example an earthquake or a huge landslide. Or, (2) the questioned small area (much more smaller than the area of the geographically extensive atmospheric pressure that causes observable crust deformation) moves together the loading exposed crust, thus the loading would not influence the relative motion regarding to reference points in the vicinity of the studied region.

However, in terms of absolute positions the influence of loading would be visible and perturbing as far as slow and small magnitude deformations are concerned. Imagine a loading affected field which also suffers slow subsidence due to the failure of working or closed underground mine, oil, gas mining or water pumping sites or heavy dewatering around open pit mines. In this condition we would observe their combined effect referred to previously measured datum coordinates, thus the loading would affect our analysis.

We have seen in this chapter the potential techniques to observe signals attributed to non-tidal loading effects. We have chosen the GPS technique what we detail in the following Chapter 3. In Chapters 4 and 6 we see GPS in practice, particularly the integer fixed ambiguity Precise Point Positioning (iPPP) method to study the non-tidal loading effects.

⁹compared for example to atmospheric loading affected regions

Chapter 3

Global Positioning System (GPS)

This chapter gives an overview about the GPS, especially the integer fixed ambiguity Precise Point Positioning (iPPP) technique that is applied in our data processing. We focus on GPS positioning because the most accurate contemporary processing strategies can provide us 3D positions at the sub-centimeter level following the recommendations of the IERS Conventions 2010 [Petit and Luzum 2010]. Furthermore a vast amount of GPS stations (including global and regional networks) covers the whole globe and provides statistically significant number of observations inter alia to study the deformation of the Earth's surface at different spatial and time scales. Several research concentrated also on GPS position time series to investigate loading effects, however only few of them assessed various methods and models of different geophysical phenomena in the same framework as for example it was performed in Collilieux et al. [2012], Jiang et al. [2013] or Chen et al. [2013b]. Moreover these studies compared loading estimates to GPS time series that were obtained with other software packages, processing strategies and used different sampling (mainly weekly or daily) than we intend to analyze (sub-daily, 6-hourly series).

3.1 General principle

In GPS positioning the observed pseudo distances are derived from measurements of one-way signal propagation time (code pseudoranges) or phase differences (phase pseudoranges) between received and receiver-generated signals. The latest satellites have three or more carrier waves which frequencies are different one system to another. For

3.2. ERROR SOURCES IN GPS POSITIONING

example in the GPS system there are three operating frequencies (not on all satellites) which are $f_1 = 154 * f_0 = 1575.42 \text{ MHz}$, $f_2 = 120 * f_0 = 1227.60 \text{ MHz}$ and $f_5 = 115 * f_0 = 1176.45 \text{ MHz}$ where $f_0 = 10.23 \text{ MHz}$ is the fundamental frequency.

The basic observation equations for code and phase measurements for one station and one satellite are as follows:

$$P_i = \rho_i - c\Delta t_{rec} + c\Delta t_{sat} + I_i + Tr + \delta_i^P + \epsilon_i^P \quad (3.1)$$

$$\lambda_i \Phi_i = \rho_i - c\Delta t_{rec} + c\Delta t_{sat} - I_i + Tr + \lambda_i N + \omega_i + \delta_i^\phi + \epsilon_i^\phi \quad (3.2)$$

Both observables on the left handside are in meters and equal to the geometric distance between the satellite at the emission time and the receiver at the reception time plus additional correction terms. P and Φ refer to the code and the phase measurements, respectively. The subscript i marks the carrier wave frequency and λ stands for the carrier wavelength. On the right hand side the first term (ρ_i) is the pure geometrical distance between the receiver and the satellite. The clock error correction terms (Δt_{rec} and Δt_{sat}) are scaled up by the speed of light c . Furthermore, I and Tr are the ionospheric and tropospheric effects. Note the different signs in the case of ionospheric effects which reflect the code measurement is delayed while the phase measurement is advanced relative to the real geometric distance. The letter N stands for the phase ambiguity. ω_i denotes the phase windup that is relevant only for the phase measurement. δ_i^P and δ_i^ϕ represent the code and the phase biases and ϵ represents the remaining errors. After we have seen the basic observation equations we can see each correction terms briefly.

3.2 Error sources in GPS positioning

In order to achieve the best available solutions all the phenomena that have influence on the GPS positioning [Collilieux et al. 2011] have to be concerned (parametrized or corrected by models). When analysing agreement with loading models and validating them by the means of GPS time series we have to be aware all the possible errors for proper interpretation. Thus in the next sections we go through these error sources which are essential for precise geodetic application. The non-tidal loading effects which were presented in the first chapter and include the effect of the atmosphere, ocean circulation,

3.2. ERROR SOURCES IN GPS POSITIONING

and continental water storage loading are not listed here. It is due to the fact that they are not yet recommended for correction in contemporary GPS processing and they are still under investigation [Ray et al. 2008; Petit and Luzum 2010; Collilieux et al. 2011] as this work also investigates these non-linear variations (see later chapters).

3.2.1 Clock errors

In precise GPS positioning the clocks on satellites and receivers have a key role [Xu 2007]. For example a 1 *ns* clock error causes an ≈ 30 *cm* error on the satellite-receiver distance ($c \cdot \delta t$) and an ≈ 1.228 phase error (in cycles) on L₂ GPS frequency ($c \cdot \delta t / \lambda$). Stable atomic clocks are used on the satellites and their clock errors actually can be considered known through satellite orbit determination where they are modelled with polynomials and transmitted to the users in the navigation message. However due to the effort of the various analysis centers the better quality final precise clock error estimates that are determined together with the precise orbits are available in two weeks¹ after the last observation [Xu 2007; Kouba 2009] with 75 ps RMS accuracy relative to the IGS timescale. These precise clock error estimates are essential for Precise Point Positioning (PPP), meanwhile they are ruled out in relative Double Differencing (DD) positioning (see later). The receiver clocks are estimated parameters during the GPS data analysis.

3.2.2 Orbit error

The International GNSS Service (IGS) analysis centers use the most developed methods to compute their precise final orbit and corresponding clock products. These parameters are available in two weeks after the last observation with 2.5 cm accuracy (1D mean RMS values over the three geocentric components). However their accuracy is influenced by the distribution of the used stations and the length of observation used for their determination [Xu 2007]. The quality of single point positioning results highly depends on the accuracy and precision of the satellite orbit and clock products [Hofmann-Wellenhof et al. 2007].

¹<https://igsceb.jpl.nasa.gov/components/prods.html>

3.2.3 Effect of propagation medium

The GPS signal experiences delays or advances during its propagation through the Earth's atmosphere. It can be divided into two characteristic layers, namely ionosphere and troposphere according to its effect on the signal propagation. The emitted GPS signal first travels through ionosphere, then the troposphere before it arrives to the receiver [Hofmann-Wellenhof et al. 2007].

3.2.3.1 Ionospheric refraction

The ionosphere is the electrically charged uppermost part of the atmosphere between 50 km and about 1000 km of altitude. The resulting effect on the electromagnetic wave crossing the ionosphere layer depends on the carrier wave frequency and it is also different for the code and the phase measurements. Such that, it causes the code range measurement to be longer (delayed) and the phase range measurement to be shorter (advanced) than the real geometric distance. Its influence is described by the Total Electron Content (TEC) number [Seeber 2003]. The relation between the TEC and the ionospheric effect for the pseudorange measurement is given by equation 3.3, for the phase observation the corresponding value will be exactly the same but with an opposite sign [Leick 2004].

$$I_r^s = \frac{40.3}{f_i^2} TEC \quad (3.3)$$

Where I_r^s is the ionospheric refraction in meters between the satellite s and the receiver r , the term f_i represents the frequency of the carrier i . The TEC is used in TEC units (TECU) and one TECU is equivalent to 10^{16} *electrons/m²*. It is an important effect since it can reach up to 30 *m* error in the range measurements. During GPS data processing it is possible to eliminate its first order effect using a proper linear combination of the code or phase observations, that is called *ionosphere-free* combination, while the higher order terms have to be modelled for precise geodetic applications. Since the IERS Conventions 2010 [Petit and Luzum 2010] there are recommended models to eliminate its higher order effects. Although, the effect of the second order ionosphere effect is usually less than 1 *mm* for station position [Subirana et al. 2013]. The influence of this medium depends on the spatial distribution of electrons and ions which extent depends on the solar radiation, the

3.2. ERROR SOURCES IN GPS POSITIONING

gas density and transportation processes. Due to the time variation of the solar radiation and the transportation processes there are different layers of ionized gas with time varying spatial extension. The main temporal variations of the ionospheric refraction are diurnal, seasonal and long period cycles. These variations occur mainly due to the solar radiation that influences directly the changes of electrons density in the ionosphere. The diurnal variations are caused by alterations that arise in some regions of the ionosphere during the daily sunlight and disappear at night, in reason of recombination of electrons and ions. Throughout the day, the density of electrons depends of the local time and the maximum values happen around 15:00 h [Webster 1993]. The seasons of the year also influence the variation of electrons density, in reason of changes of the sun's zenith angle and of the ionization flux intensity, characterizing the seasonal variations. Therefore, during the equinoxes the ionospheric effects are bigger, while during the solstices they are smaller. Long period variations (cycles of about 11 years) are associated with the occurrence of sunspots. When the number of sunspots increases, the ionosphere ionization becomes stronger.

The location on the Earth has strong influence on the variation of ionosphere's electrons density, due to the heterogeneity of its global structure. It varies with the latitude affected by the sun's zenith angle, which influences directly the radiation level and consequently the density of electrons in the ionosphere. The equatorial regions are characterized by a big level of electron density, and the mid latitudes are considered relatively free from ionospheric anomalies, while polar regions are not so predictable [Webster 1993]. In terms of longitude, due to the non-coincidence of the geographic and magnetic poles, it is sensible only in higher regions of the ionosphere. The Figure 3.1 presents the regions with high ionospheric activity (equatorial region and high latitudes), as well the mid latitude regions, where the ionospheric activity is less significant [Seeber 2003; Kintner et al. 2009].

3.2.3.2 Tropospheric refraction

The troposphere is the lowest part of the atmosphere. Around the equator it reaches its maximum altitude that is $\approx 16 - 18$ km, however its thickness varies with the latitude. Its first ≈ 16 km from the surface of the Earth contains the 90% of the atmospheric mass

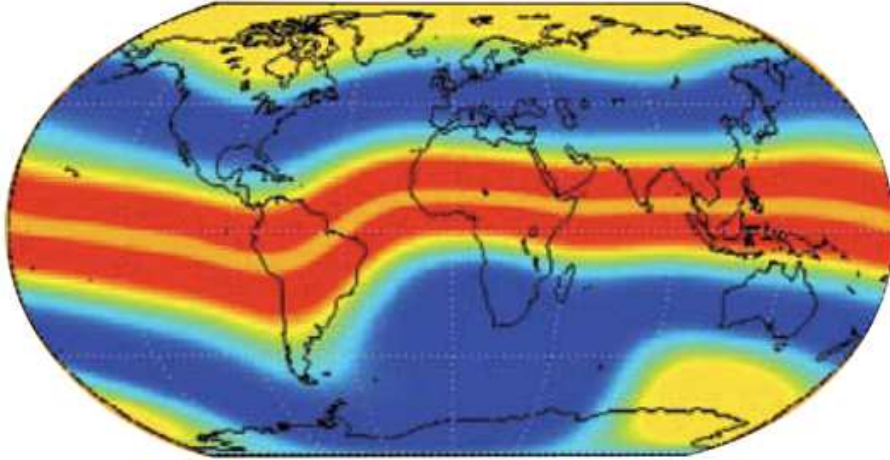


Figure 3.1 – Map of ionospheric scintillation frequency at solar maximum. Colors from blue to red show the ionospheric oscillation frequency from infrequent (blue) to frequent (red). Source: Kintner et al. [2009].

[Malardel 2009]. The tropospheric refraction causes a surplus propagation path length for the radiowave signal. This effect depends on the atmospheric parameters such as the pressure, temperature and humidity as well as on the satellite-receiver geometry, thus the elevation angle of the satellite and the site location. The tropospheric delay can be characterised by the refractivity index N that can be divided into two parts $N = N_{dry} + N_{wet}$, which are the *wet* and the *dry or hydrostatic* parts. The former one only includes the effect of the water vapour content and corresponds to about 10% of the total error. The latter one is responsible for the rest 90% of the entire propagation error. The hydrostatic delay is induced by the dry atmospheric gasses and fortunately predictable knowing the local atmospheric pressure and temperature. This effect cannot be mitigated using observation data combination, therefore adequate models have to be applied as *a priori* values and parameters have to be estimated during the GPS positioning as showed by the equation 3.4.

$$ZTD = ZHD + ZWD \quad (3.4)$$

Where the terms are Zenith Total Delay (ZTD), Zenith Hydrostatic Delay (ZHD) and Zenith Wet Delay (ZWD). The dry or hydrostatic part, that is the ZHD has slow time variation² and it is modelled and used as *a priori* value while the ZWD is estimated during

²according to Subirana et al. [2013] 1 % in the course of few hours.

the parameter estimation. The most commonly used models for the ZHD component are the ECMWF or the Global Pressure Temperature (GPT) estimates [Boehm et al. 2006]. The zenithal values are projected onto the line of sight to the satellite (equation 3.5), by a proper mapping function for example Global Mapping Function (GMF) or Vienna Mapping Function (VMF1) [Boehm et al. 2006].

$$STD(el) = ZHDmf_H(el) + ZWDMf_W(el) + (G_N \cos(az) + G_E \sin(az))mf_G(el) \quad (3.5)$$

Where the left hand side is the Slant Tropospheric Delay (STD) at a certain satellite elevation angle (el). mf_H , mf_W and mf_G are the appropriate mapping functions for the hydrostatic or dry part (ZHD), the wet part (ZWD) and the north and east tropospheric gradients (G_N , G_E), respectively.

The tropospheric hydrostatic delay typically causes ≈ 2.3 m while the wet delay is responsible for $\approx 10 - 150$ mm range measurement error in the zenith direction. For $\leq 10^\circ$ satellite elevations ≥ 10 m of propagation errors can easily occur [Seeber 2003; Subirana et al. 2013]. Moreover up to 50 m delays are possible at less than 3° elevation angles³.

3.2.4 Relativistic effects

Relativistic effects are present whenever different systems that are relatively moving to each other are concerned in a problem. It is the case for the GPS as the reference frame is located in the center of the Earth and used to observe the GPS satellites which are moving relative to the observers on the ground with a speed of ≈ 4 km/s [Hofmann-Wellenhof et al. 2007]. Because of their relative motion, the gravitational potential differences between the satellites and the ground observer and the rotation of the Earth must be taken into account. Thus the special and general relativity have to be applied [Xu 2007]. These affect satellite orbit, signal propagation and satellite and receiver clocks. For example a neglected relativistic correction on the receiver clock can introduce about 13 m range measurement error and about 20 m vertical positioning error [Subirana et al. 2013]. A relativistic effect on the signal propagation can reach up to 2 cm. The effects that are related to the Earth's rotation are called Sagnac effect [Hofmann-Wellenhof et al. 2007] and corrected with the IERS Conventions 2010 standards [Petit and Luzum 2010].

³http://gps.be/troposphere_tutorial.php

3.2.5 Phase wind-up

The phase wind-up effect depends on the satellite-receiver relative orientation and motion and affects only the phase measurements. The change in the relative orientation translates into measured phase variation that causes range error. At a fixed position, 360° rotation of a receiver antenna would induce one wavelength error in the satellite-receiver distance phase measurement [Subirana et al. 2013]. For positioning that demands high accuracy this frequency dependent effect has to be taken into account as it is relevant to the behaviour of the circularly polarised carrier waves.

3.2.6 Antenna phase center offset and variation

The antenna phase center offset and variation have to be taken into account in precise geodetic applications at both side of the GPS measurement. It is due to the fact that the observed satellite-receiver distance refers to the phase centers of the two participating antennas, meanwhile the precise orbit and clock products (e.g. IGS, GRG) refer to the center of mass of the satellite. Nevertheless the signal is emitted from its phase center what is offset from the satellite's center of mass. Similarly on the ground, the satellite emitted GPS signal arrives to the receiver antenna phase center, in turn it is offset from the antenna reference point (ARP)⁴. However the ARP does not necessarily indicate the geodetic marker which position is of our interest. The configuration is presented in Figure 3.2. This figure 3.2 shows the two important quantities that have to be corrected during GPS data processing, namely the phase center offset (PCO) and the phase center variation (PCV) and both quantities depend on the carrier frequency and the antenna type. The PCO is the offset of the mean phase center position from the ARP. The PCV is the real electrical phase center that differs from the mean phase center and it depends on the azimuth and the zenith angles of the satellite beside the carrier frequency [Hofmann-Wellenhof et al. 2007]. Their values are only a few millimeters in the horizontal direction while in the vertical they are different. In the vertical direction the PCO can reach up to 10 cm and the PCV shows maximum a few centimeters. The corresponding corrections

⁴The intersection of the vertical antenna axis and the bottom of the antenna [Hofmann-Wellenhof et al. 2007].

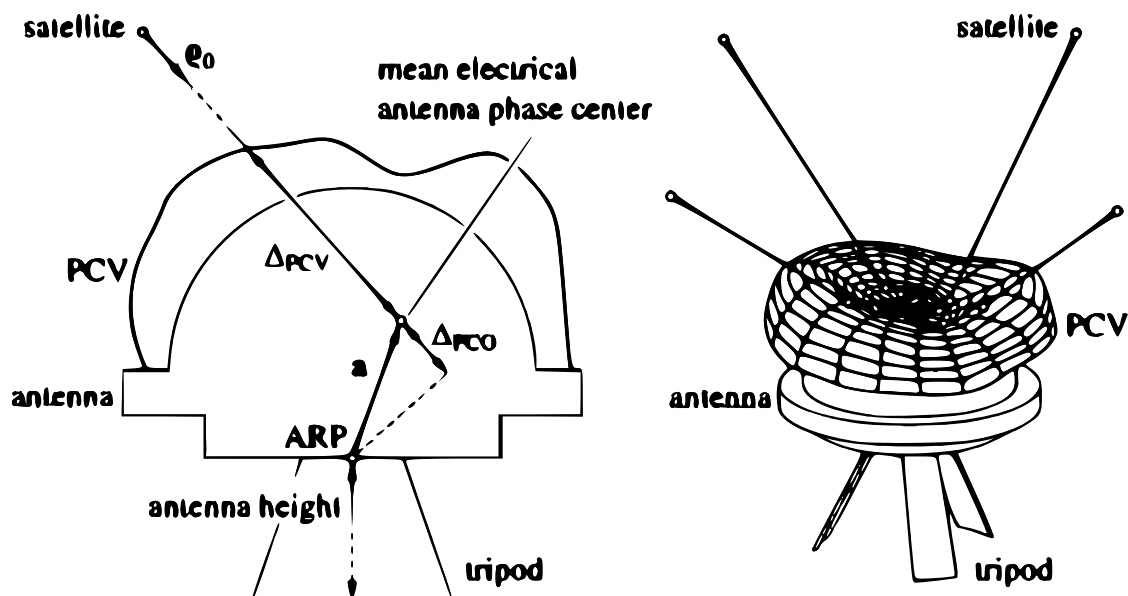


Figure 3.2 – Illustration of antenna reference point (ARP), phase center offset (PCO) and phase center variation (PCV) [Hofmann-Wellenhof et al. 2007].

are provided by the IGS for every satellites and geodetic antennas in the antenna exchange format (ANTEX) file⁵, the currently used version is the *igs08.atx*⁶.

3.2.7 Multipath

It is a carrier frequency dependent effect that is relevant for the code and the phase measurements. It is primarily caused by reflecting surfaces in the receiver's proximity. Its result is that the GPS signal reaches the antenna in more than one path. The transmitted signal also can experience reflections at the satellite level [Hofmann-Wellenhof et al. 2007]. This effect is particularly important when the signal is coming from a low elevation angle ($\leq 7^\circ$) [Subirana et al. 2013]. Due to the time and location dependent geometry and local conditions general model does not exist for this problem, however it can be estimated by applying linear combination of the code and phase observables [Hofmann-Wellenhof et al. 2007]. The location and the type of the applied antennas of the global IGS stations are carefully chosen to mitigate multipath effect, however a multipath-free configuration is rare.

⁵Description of the ANTEX file: <http://igs.cb.jpl.nasa.gov/igs/scb/station/general/antex14.txt>

⁶The current version: <http://igs.org/igs/scb/station/general/igs08.atx>

3.2.8 Site displacement effects

This subsection briefly overviews the site displacement effects which are necessary to be considered during GPS processing. They affect the geometric distance due to site displacements and do not have influence on the GPS signals [Subirana et al. 2013].

3.2.8.1 Solid Earth tide

The solid Earth tide deformation is the elastic response of the Earth body to the tide-generating potential of the Moon and the Sun [Petit and Luzum 2010]. This effect has the biggest contribution to the displacement within the tidal deformations in general and the variation in the vertical is more pronounced than in the horizontal direction. It can reach more than 30 cm vertical amplitude [Xu 2007]. It is corrected in our time series using the conventional model after [Mathews et al. 1997] recommended by IERS Conventions (2010) [Petit and Luzum 2010].

3.2.8.2 Ocean tidal loading

Similarly to the solid Earth tide it is induced by the tidal potential of external bodies, however the displacement is generated by the tidal redistribution of ocean mass that loads and deforms the Earth's crust. It can provoke up to 10 cm variation in the vertical component at coastal sites. According to the IERS Conventions 2010 [Petit and Luzum 2010] we applied ocean tidal loading corrections based on the *FES2004* [Lyard et al. 2006] and *FES2012* [Carrère et al. 2012] ocean models.

3.2.8.3 Pole tide

The pole tide arises because the Earth's rotation axis is not fixed relatively to the crust due to its elastic response for the time varying mass redistribution of the interior masses. This effect depending on the station position can be expected to cause less than 25 mm and 7 mm variations at Chandler wobble period (≈ 14 months) in the vertical and the horizontal direction, respectively. Therefore we need to correct it using the IERS Conventions 2010 standards [Petit and Luzum 2010; Subirana et al. 2013].

3.2.8.4 Atmospheric tidal loading

The thermally or gravitationally excited surface pressure oscillations at daily (S_1) and subdaily (S_2) frequencies can generate crust deformation that is called atmospheric tidal loading. As a remark, they can have 1-2 mm in the vertical component (horizontal components are 3-10 times smaller). They are listed as a recommendation for the station motion model in the IERS Conventions 2010 [Petrov and Boy 2004; Boy 2007; Petit and Luzum 2010]. To correct it in our analysis, we have applied the model of Ray and Ponte [2003] from the IERS Conventions 2010 standards.

3.3 GPS processing strategies

We show here two post-processing positioning methods which are commonly used for geophysical studies. These are the Double Differencing (DD) and the Precise Point Positioning (PPP) methods.

3.3.1 Double Differencing (DD)

The classical positioning method in GPS analysis is the DD approach. It is due to the fact that the spatially correlated errors are less crucial than in a single receiver point positioning case. The clock error terms are eliminated and the ionospheric and tropospheric effects are immensely reduced when forming double differences [Xu 2007]. Loading effect studies that use time series based on the DD approach, take advantage of this. Double differences are formed from two single differences, where a single difference implies the difference of the observation data of two stations that simultaneously measure the same satellite. So, the double difference process requires minimum two simultaneously observing stations measuring the same two satellites and the use of one of the stations as a reference which assumes that we adequately know its coordinates. Besides its mentioned benefits it has disadvantage for loading applications when forming short baselines (< 50 km). Indeed, the spatially coherent loading deformation signal is also mitigated with double differences. Thus the loading phenomena over small or regional networks can not be properly examined.

The DD method was widely used and successfully applied for atmospheric, continental

3.3. GPS PROCESSING STRATEGIES

water storage and hydrological loading deformation studies, for example by Tregoning and van Dam [2005], Tregoning et al. [2009], Nahmani et al. [2012], van Dam et al. [2012], Jiang et al. [2013], and Valty [2013]. Nahmani et al. [2012] studied the continental water loading in West Africa in the framework of AMMA (African Monsoon Multidisciplinary Analysis) and GHYRAF (Gravity and Hydrology in Africa) projects, using 12 year long time series at six stations. They showed that the monsoon system can produce a regional-scale loading effect between 10 and 15 mm, also their vertical GPS displacements showed a daily repeatability between 2 mm during the dry season and 5-6 mm during the wet season. Their most interesting result is that the semi-annual signal of the GPS deformation is 2-3 times larger than the corresponding GRACE and model estimates. Valty [2013] investigated South Europe over 36 stations using 7 year long time series and showed that the outputs of global circulation models and geodesy data agree on the main inter-annual load changes. Valty et al. [2013] assessed the precision of loading models using space geodetic techniques, involving GPS. They showed that the precision of the predicted vertical loading displacement based on global circulation models is around 1 mm. Both studies have applied the fourth solution of University of La Rochelle Analysis Center Consortium (ULR4⁷) solutions [Santamaría-Gómez et al. 2011], that is weekly station coordinates. These studies investigated the long wavelength signatures (time) of the hydrological loading. To obtain good results for double differenced sub-daily positioning⁸ the ambiguities should be fixed to integer values. Using GAMIT TRACK⁹ it can be achieved easily in case of small separation distances (< 10 km) and more challenging for greater distances ($10 < x < 100$ km). In case of this scenario (small separation distances) we are back to the point that maybe the spatially coherent loading deformation signal is mitigated with double differences. Moreover, to obtain double differenced time series several stations including reference sites¹⁰ need to be treated simultaneously, that would increase the computational time. Meanwhile, to achieve iPPP time series we can treat stand-alone sites, we can focus only on those that belong to our area of interest. To investigate short wavelength space

⁷<http://www.sonel.org/-GPS-Solutions-.html>

⁸To investigate short wavelength signatures (time)

⁹For details visit <http://chandler.mit.edu/~simon/gtgk/TRACK.ppt>, <http://geoweb.mit.edu/~simon/gtgk/help/track.hlp.htm> and http://geoweb.mit.edu/~tah/track_example/ websites.

¹⁰Carefully selected reference stations

and time signatures we decided on using the iPPP method.

3.3.2 Precise Point Positioning (PPP)

The Precise Point Positioning (PPP) method that first emerged in Zumberge et al. [1997] is an alternative way of positioning and increasingly considered in the geodetic community. Figure 3.3 shows the concept of PPP. We use phase and code measurements between our GPS receiver antenna and the GPS satellites to precisely determine our unknown position. The reference points are the GPS satellites that are considered well known by applying different orbit and clock products (e.g., IGS, JPL, MIT, ESA, GFZ, GRG, GR2). In other words, this technique allows the user to estimate stand-alone station coordinates using a set of fixed transmitter parameters (precise orbit and clock products) which determines the reference frame of the solutions [Zumberge et al. 1997]. Thus this solution indirectly depends on the network that was applied to estimate the orbit and clock products. During GPS phase measurements the unknown integer number of cycles (ambiguities) are limiting factors of the precision (See later). Due to the recent developments it is possible on the zero difference level [Laurichesse and Mercier 2007; Laurichesse et al. 2009; Loyer et al. 2012]. Once we fix the integer ambiguities we can speak about the integer ambiguity fixed PPP (iPPP).

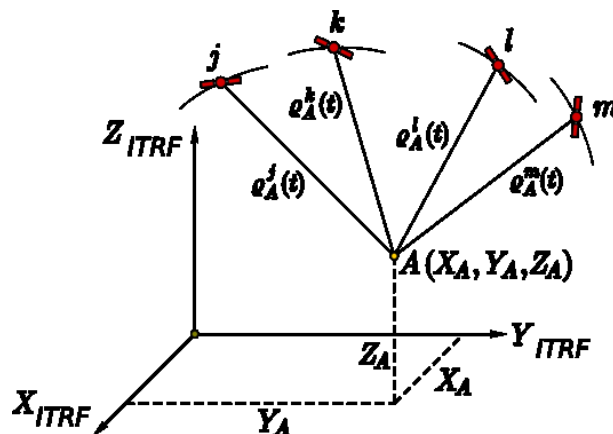


Figure 3.3 – Principle idea of GPS-PPP configuration. X_A , Y_A and Z_A are the cartesian coordinates of the GPS station. The small case latin letters j , k , l and m signify visible satellites at epoch. The greek letter ρ represents range measurements between the corresponding satellite and the geodetic site. The ITRF in the subscript shows the reference system. Source: Hofmann-Wellenhof and Moritz [2005].

3.3. GPS PROCESSING STRATEGIES

However to reach the highest accuracy during data processing the phase ambiguities have to be fixed to their integer value which was not conventionally done at the zero-difference (undifferenced) level until the last few years [Laurichesse et al. 2009; Geng et al. 2010; Loyer et al. 2012]. This solution is called integer fixed ambiguity Precise Point Positioning (iPPP) what is a key improvement in GPS and definitely contributes to the improvements of geophysical studies. Also all the corrections in the observation model that are listed on the previous sections have to be carefully applied. There are several softwares that can be used to estimate geodetic positions using ambiguity fixing PPP, such as: GINS-PC [Marty et al. 2012], GIPSY-OASIS [Zumberge et al. 1997], BERNESE [Dach et al. 2007b], RTKLIB [Takasu 2012].

The term ambiguity refers to the integer number of cycles between the signal emission and the signal reception time during the phase measurement. When a receiver is locked onto a satellite, the phase measurement is performed modulo 1 *cycle*, that means only the fractional part of the phase is measured. Then a cycle counter is initialized and keeps counting until the measurement is continuous, thus the integer number of cycles is unknown at the beginning of a measurement and it is constant along a pass [Hofmann-Wellenhof et al. 2007; Laurichesse et al. 2009; Loyer et al. 2012], see Figure 3.4. This ambiguity has to be properly determined for each satellite pass, since one cycle

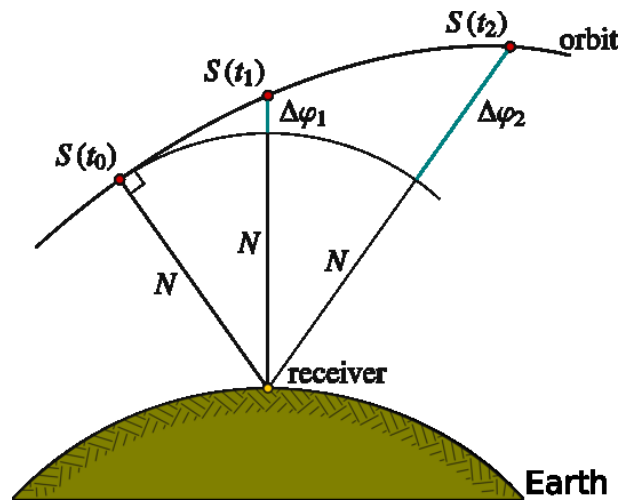


Figure 3.4 – Phase range measurement and the corresponding ambiguity (N) over the satellite pass [Hofmann-Wellenhof et al. 2007].

3.3. GPS PROCESSING STRATEGIES

count error introduces an error on the distance measurement that corresponds to one wavelength (λ) on the considered frequency, that is ≈ 19 cm on L_1 and ≈ 24 cm on L_2 . Different methods exist for ambiguity fixing at the undifferenced level [Bertiger et al. 2010; Geng et al. 2010]. Here we overview the innovative approach of Laurichesse and Mercier [2007]; Laurichesse et al. [2009]; Loyer et al. [2012] what is implemented in the Géodésie par Intégrations Numériques Simultanées PC (GINS-PC) software (Groupe de Recherche en Géodésie Spatiale (GRGS)/Centre National d'Études Spatiales (French Space Agency) (CNES)) and used for our data processing. Figure 3.5 shows the ambiguity fixing processing scheme after Fund et al. [2013] that is applied at CNES-Collecte Localisation Satellites (CLS) IGS Analysis Center (AC). Laurichesse

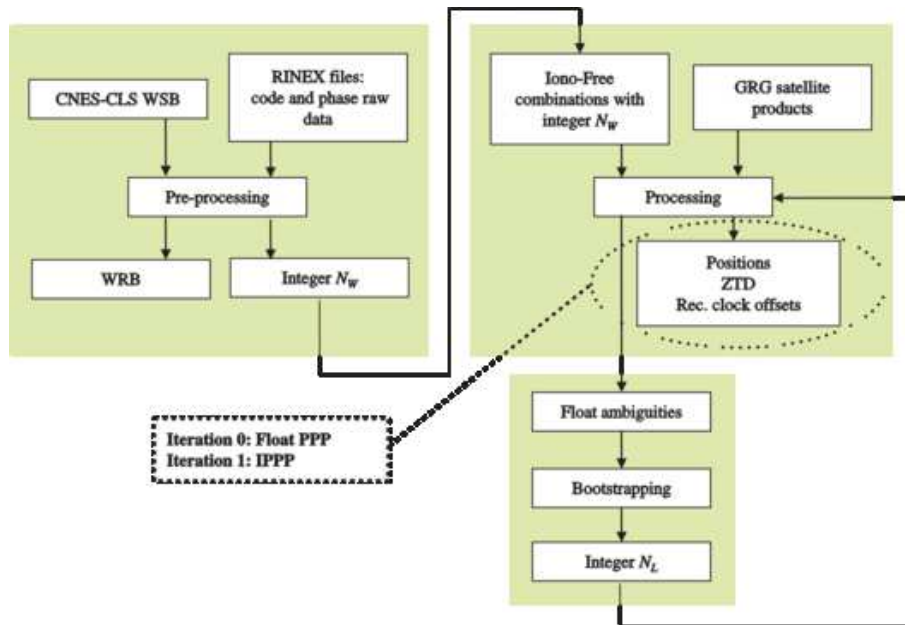


Figure 3.5 – Integer ambiguity fixing that is applied at CNES-CLS IGS AC and implemented in GINS-PC. The terms WSB and WRB are wide-lane satellite bias and wide-lane receiver bias, respectively. Source: [Fund et al. 2013].

et al. [2009] derived a two step method to solve the problem of undifferenced ambiguities using adequate linear combination of the four observables: 1) wide-lane (WL) (geometry and first order inosphere free, L_5) and 2) narrow-lane (NL) (ionosphere free, L_3) combinations. This section follows the notation of the work of Laurichesse et al. [2009], Loyer et al. [2012] and Fund et al. [2013] to present the ambiguity fixing from the aspects of an iPPP user. They worked out the idea starting from the pseudorange and phase

3.3. GPS PROCESSING STRATEGIES

model equations in the scenario of a dual-frequency receiver in order to observe directly the behaviour of the undifferenced phase ambiguities. For the sake of simplicity they have not shown explicitly all the measurement errors¹¹. They show only the most important ones together with all the system biases that are necessary for this derivation and presented by equations 3.6 to 3.9 for one receiver and one satellite. The numbers in the subscripts represent the two carrier frequencies f_1 and f_2 with wavelength λ_1 and λ_2 respectively:

$$P_1 = D_1 + e + \Delta h_P + \Delta \tau_P \quad (3.6)$$

$$P_2 = D_2 + \gamma e + \Delta h_P + \gamma \Delta \tau_P \quad (3.7)$$

$$\lambda_1 L_1 = D_{L_1} + \lambda_1 d_{p_wu} - e + \Delta h + \Delta \tau - \lambda_1 N_1 \quad (3.8)$$

$$\lambda_2 L_2 = D_{L_2} + \lambda_2 d_{p_wu} - \gamma e + \Delta h + \gamma \Delta \tau - \lambda_2 N_2 \quad (3.9)$$

where $\gamma = \lambda_2^2/\lambda_1^2$, P is the measured pseudorange in meters and L is the result of the phase measurement in cycles on the corresponding carrier frequencies. The model terms are the following quantities: D is the geometrical distance between the satellite and the receiver phase centers including troposphere delay, relativistic effects among other correction terms, d_{p_wu} is the effect of phase windup in cycles, e is the ionosphere delay in meters on f_1 and N are the carrier phase ambiguities on the corresponding frequencies. The rest unknowns are clock parameters. Δh_P and Δh are receiver and satellite clock offset differences¹², while $\Delta \tau_P$ and $\Delta \tau$ are receiver and satellite hardware bias differences¹³ expressed in meters for pseudorange and phase, respectively. They are expected to have slow variations with time.

Through the wide-lane combination¹⁴ of the code and phase observables during the preprocessing, the difference between the two elementary ambiguities (N_1 and N_2) can be observed. This difference is called wide-lane ambiguity. It can be fixed to integer value and estimated together with the wide-lane receiver bias (WRB) using wide-lane satellite bias (WSB) products¹⁵ provided by the CNES-CLS IGS Analysis Center [Loyer

¹¹that are presented in Section 3.2

¹² $\Delta h = h_i - h^j$ is the phase clock difference and Δh_P is the corresponding quantity for pseudorange for receiver i and satellite j .

¹³ $\Delta \tau = \tau_i - \tau^j$ is the phase clock bias difference and $\Delta \tau_P$ is the corresponding quantity for pseudorange for receiver i and satellite j .

¹⁴it is also called Melbourne Wübbena combination

¹⁵Available at: <ftp://ftpsedr.cls.fr/pub/igsac>

3.3. GPS PROCESSING STRATEGIES

et al. 2012; Fund et al. 2013]. The provided file is weekly updated and contains the list of all GPS satellites with their daily WSB values in units of *wide-lane cycles*. The wide-lane combination presented in Equation 3.10 is a unique tool in a sense that it is a geometry free combination that also eliminates the first-order ionospheric effects and has low measurement noise¹⁶.

$$L_5 = f_{wl}(L_2 - L_1, P_1, P_2)/\lambda_{wl} = N_{wl} + (\tau_{WRB} - \tau_{WSB}) \quad (3.10)$$

The WSB products are estimated over a network of around 140 global IGS stations according to the two step procedure that is detailed in Laurichesse et al. [2009] and Loyer et al. [2012].

After the integer wide-lane ambiguities (N_{wl}) are determined the remaining unknown ambiguity (N_1) can be estimated simultaneously with station positions, Zenith Total Delay (ZTD) and receiver clock offsets using the ionosphere free, narrow-lane equations meanwhile the ambiguity fixing is obtained in a bootstrap method [Fund et al. 2013]:

$$L_3 = \frac{\gamma\lambda L_1 - \lambda_2 L_2 - \lambda_2 N_{wl}}{\gamma - 1} = \frac{\gamma D_{L_1} - D_{L_2}}{\gamma - 1} + \lambda_{nl} d_{pww} + \Delta h_L - \lambda_{nl} N_1 \quad (3.11)$$

where the first term on the right hand side is the ionosphere free pseudorange equation that is related to the pseudorange clocks.

To obtain iPPP results using GINS-PC and the mentioned WSB products, consistent satellite orbits and clocks need to be applied that is also provided by the CNES CLS IGS analysis center under the name GRG products and more recently GR2. Using this processing scheme positioning results are improved excessively on the east, less spectacularly on the north and not significantly on the up components [Laurichesse et al. 2009; Fund et al. 2013]. This effect is associated to the observed satellite constellation. Thus at mid and low latitudes the east component is the most correlated to the ambiguity parameters due to the general south-north ground track of the GPS satellites at these latitudes [Melbourne 1985; Blewitt 1989; King et al. 2003; Melachroinos et al. 2006; King et al. 2010].

¹⁶The wide-lane wavelength (λ_{wl} or λ_5) is about 86 cm for GPS f_1 and f_2 frequencies.

The PPP technique already proved its potential in geoscientific applications, for example crustal deformation due to seismic waves [Grenerczy et al. 2011], tectonic velocity [Calais et al. 2006], glacial isostatic adjustment [King et al. 2010] and different loading effects [van Dam and Herring 1994; Petrov and Boy 2004; Tregoning and van Dam 2005; Fu et al. 2012b]. Besides these scientific successes we have decided to apply the iPPP method.

The following chapters are dedicated for a global and for two different regional studies. In Chapter 4 we investigate different loading effects in a global network. In Chapter 5 we examine the influence of different loading effects on the tectonic velocity, while in Chapter 6 our goal is to detect and investigate the various loading phenomena during an extreme climatic event. We note here the GPS results used in Chapter 5 are provided by Alexis Rigo and Philippe Vernant and calculated applying the DD method using the GAMIT software. There are no PPP time series in Chapter 5. In Chapter 4 and 6 we use our iPPP position time series that were estimated using the GINS-PC software package.

Part II

Towards a global study

Chapter 4

Towards a global study

We already saw in the previous chapters that the non-tidal spatial and temporal variations of atmospheric, continental water and oceanic masses can have important influence on the Earth's surface [van Dam and Wahr 1998]. Also it was demonstrated in the previous chapter and by several researchers that the GPS is capable to detect these mass variations [Blewitt and Lavallée 2002; Tregoning et al. 2009; Williams and Penna 2011; van Dam et al. 1994, 2001, 2012]. In this part, we use sub-daily, long time series estimated using the GINS-PC (CNES/GRGS) software [Marty et al. 2012; Fund et al. 2013] to demonstrate the sensitivity of the iPPP processing strategy. This work is among the first studies to investigate the different loading effects using sub-daily iPPP time series, particularly using the GINS-PC software. We aim to exploit the 6-hourly iPPP time series to study the various effects at different time scales, from sub-daily to seasonal and annual periods. In order to analyse annual signals long time series are required, thus we estimate 6 year long time series. We assume the remaining positioning signal is mainly dominated by the underlying non-tidal loading phenomena. Following this idea, we can assess the performance of the predicted displacement time series at global and regional scales on our iPPP time series.

4.1 Introduction

At present, the non-tidal loading effects are not yet recommended for *a priori* correction in the global GPS data analysis. Furthermore, the long position time series that are used

to study long-term geodynamical processes are not always corrected *a posteriori* to account for the impact of the loading phenomena. Nonetheless they can have important effect on geodetic time series, particularly if we examine signals that are on the millimeter level. For *a posteriori* correction there are different freely available models online, however there is no suggested ones that the users should apply during their time series analysis. The seasonal loading effects studies usually carried out using weekly or daily GPS time series. We would like to quantify the contribution of the sub-daily iPPP time series regarding to the previous studies that applied daily or weekly series.

For certain stations, we compared different sub-daily sampling interval in GINS-PC using those processing parameters that are coherent with the applied orbit and clock data (Section 4.3). Based on the obtained results, the noise level (higher at higher sampling rate) and the sampling rate of the models in general, we decided to use the 6 hour interval. The predicted loading displacements are significant compared to the achieved GPS time series and their formal errors. It is worth noting the data points of the GPS time series are independent of each other. Therefore, here we investigate 6-hourly, 6 year long position time series for a subset of stations in different regions that are potentially exposed to the various loading effects. We have selected these regions based on the results of previous global studies and suspectability maps of the atmospheric, continental water storage and oceanic loading effects. Estimating positions for sites distant from those influenced by the loading allows us to assess the performance of the predicted displacement time series at global and regional scales.

4.2 The selected regions

We have attempted to select stations based on observation quality and loading signal sensitivity criteria. Concerning the first parameter for our site selection it is based on the quality and the availability of observations for a subset of core IGS stations. We looked for stations where the number of available observations was at least 80 % of our desired study period¹. Also, we kept in mind a good global distribution. In parallel to the quality criteria

¹80 % of the 6 year long time series from 2008 to 2013, thus around 1750 available daily observation files.

4.2. THE SELECTED REGIONS

we looked for stations that satisfy our sensitivity parameters. Thus we looked for various regions that are potentially sensitive to the different environmental loading phenomena. We made this choice in order to group the stations and separate the various effects in order to contribute to the validation of the different models. Moreover, we are also interested how the combination of the different effects is driven by the nature, thus how far we are from the GPS observed signal when we simply sum up the models.

Thus, originally we have selected ≈ 150 global stations to serve this study. Unfortunately due to some difficulties² and limitations³ (See Chapter 7) when we applied the GRG products, we have reduced this selection and left it for a future investigation. We were inspired to derive the best achievable results in GINS-PC using the latest GRGS orbit and clock products⁴. Since we could access these new products REPRO2 of CNES-CLS AC (GR2) relatively late⁵ to the end of this thesis we made the compromise concerning the original selection and the necessary computational time, and privileged our test network. The REPRO2 is the reprocessing of the full GPS observation history since 1994 by each ACs using the latest models and methodology⁶. Due to this effort, the CNES-CLS AC has derived its own newly reprocessed orbit and clock products (GR2) using homogeneous processing strategy over the time of the reanalysis.

Thus, our test network is drastically reduced only to include 10 stations from the beginning of 2008 until the end of 2013 in order to have time to process data with the GR2 products. However, this test network compliance our criteria in the aspect of available observation, sensitivity to different effects and a good global distribution. Our test GPS network is represented in Figure 4.1.

As we mentioned in the first chapter the atmospheric loading phenomena is more pronounced at high latitudes due to the larger pressure variations present there [van Dam and Wahr 1998]. Inland sites on big continents with more than ≈ 1000 km coastal distance can also show deformation signatures induced by atmospheric mass load. In our

²Jumps in the time series using GRG products.

³GRG products can provide iPPP time series for GINS-PC IHM users since the beginning of 2010.

⁴See GR2 afterwards and in Chapter 7

⁵We had the opportunity to access the data only on the 19th of May 2014, which was before the official release.

⁶More information is available at <http://acc.igs.org/reprocess2.html>

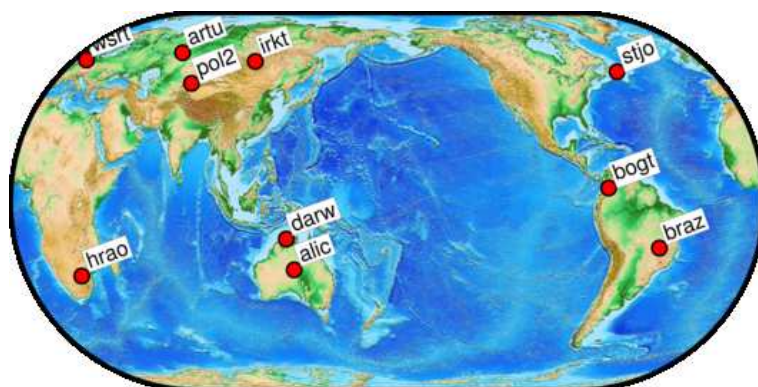


Figure 4.1 – Our network containing 10 GPS stations.

test network there are four stations that can presumably be effected by the atmospheric loading effect, namely *ARTU* (Arti, Russia), *IRKT* (Irkutsk, Russia), *POL2* (Bishkek, Kyrgyzstan) and *ALIC* (Alice Springs, Australia).

Considering the continental water storage loading effect, the Amazon Basin is considered to be the place with the greatest flux on the Earth. GRACE data suggest ≈ 13 mm vertical deformation at the center of this region [Davis et al. 2004]. Though the station *BRAZ* (Brasilia, Brazil) is not in the close proximity of this center, it still undergoes detectable deformations. Based on global hydrological displacement maps, *HRAO* (Krugersdorp, South Africa) is also a good candidate as a potentially affected station. *BOGT* (Bogota, Colombia) is a station that maybe shows some displacement signature due to continental water storage variations because of its relatively close situation to the Amazon Basin and the Northern Andes.

Finally, concerning the non-tidal oceanic loading effect, van Dam et al. [2012] found that semi-enclosed bays or seas are affected by OBP loading to a greater extent than other stations. Based on this aspect, we selected *WSRT* (Westerbork, The Netherlands), *STJO* (St. John's, Canada) and *DARW* (Darwin, Australia) which may represent stations sensitive to the NTOL effect.

4.3 The GPS data

We have estimated position time series using the GINS-PC (CNES/GRGS) software package with 6-hourly sampling from 1st of January 2008 until the end of 2013. For our initial series we have used the GRG orbit and clock products and the OTL correction with FES2004 that was provided together with the software. During our initial analysis we have seen these results showed unexpected results (See Chapter 7) thus we have changed to the use of the GR2 solution and FES2012 OTL correction. Figure 4.2 shows an example of the time series estimated using the GRG and GR2 products at BRAZ station. It shows clearly that the noise level is drastically reduced and that the signal amplitude seems to be reduced. We can see jumps in the East component of the GR2 time series at the end of 2012 and at the beginning of 2013 (See Figure 4.2) which are not related to the GRGS processing parameters since they are also present in the JPL solution⁷. Probably, these features are related to equipment changes.

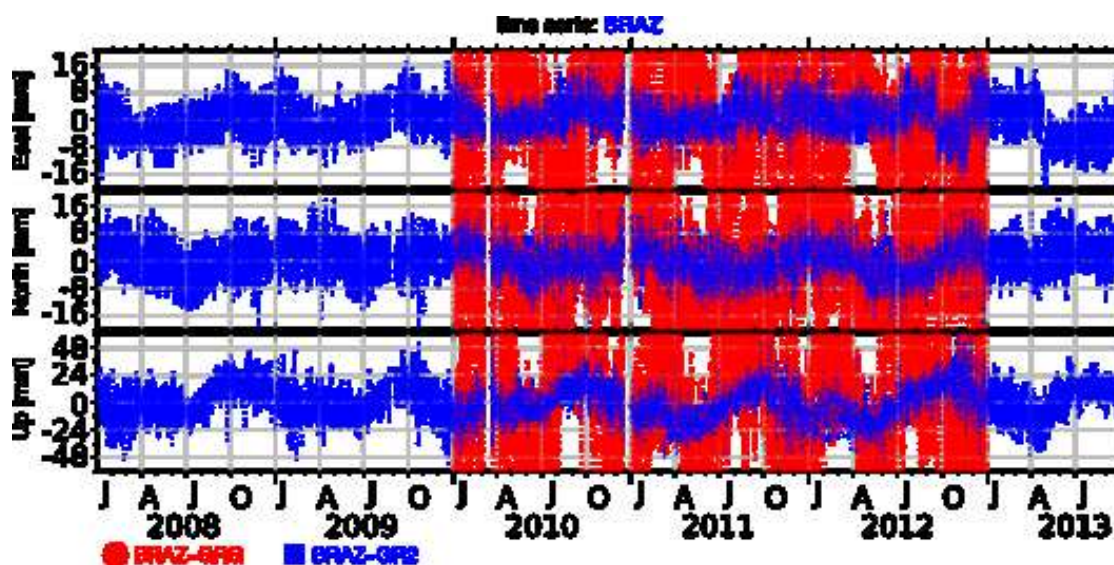


Figure 4.2 – GPS time series estimated using GRG (red) and GR2 (blue) products at *BRAZ* station.

Figure 4.3 shows the power spectral density (PSD) of the GRG and GR2 GPS time series at BRAZ station (Figure 4.2). We can remark that the spectra was improved in general (GRG vs. GR2). The vertical dashed lines denote different period. Namely, the half

⁷See the longitude component at <http://sideshow.jpl.nasa.gov/post/links/BRAZ.html>

4.3. THE GPS DATA

(3.625 days) [GRG_PWh (green)] and the full (7.25 days) [GRG_PWf (blue)] GRGS GPS processing week and a period that was found by Ray et al. [2013] (3.66 days) [GRG_1 (red)]. Ray et al. [2013] found a very pronounced peak at about 3.66 days in all three components of the GRG solution (over ≈ 1 year data span). They have stated this characteristic is not satellite linked since there is no matching feature in the GRG orbit results compared to the IGS combination, also a relation with tide model errors seems to be remote. They suspected that this observation might not be coincidental with the half of the GRG processing week (half of seven overlapping arcs of 30 h each (174 h), that is 3.625 days). They suggested that it could happen if GRG has a subtle station constraint or coding bug related to their weekly processing batches. They concluded this strong peak is unique to some aspect of the GRG data analysis and not a general GPS feature. We quantified the improvements in the spectrum derived from the overlapping GRG and GR2 time series at BRAZ station according to $((PSD_{GRG} - PSD_{GR2})/PSD_{GR2}) * 100$. This gives the relative change in percentage for each frequency that was found. Although, we didn't see any significant peak around the 3.66 day period in the spectrum (See Figure 4.3), but there was 1.4% improvement at the closest frequency when we used the GR2 data products. After we removed the outliers⁸ we observed an overall improvement in the spectrum of about 28.8%.

The processing parameters were according to the GRGS standards⁹ and they are summarised in Table 4.1.

Concerning the different loading models we have to deal with various data structures during our analysis. Therefore we have created some command-line tools to automatise the necessary conversions and to unify all the data for our needs. It involves the automatic recognition of the different input date formats and the necessary date and time conversions. Even though date conversion tools are provided with the GPS softwares but we made it in a way to be independent from them and directly applicable for any kind of time series. Then for model combination, *a posteriori* GPS correction or correlation studies we have to match the input time series. For this reason we have also wrote a script that automatically

⁸Where very high percentage values appeared.

⁹ftp://hpiers.obspm.fr/iers/eop/grgs/Models/models_ITRF2013.pdf

4.3. THE GPS DATA

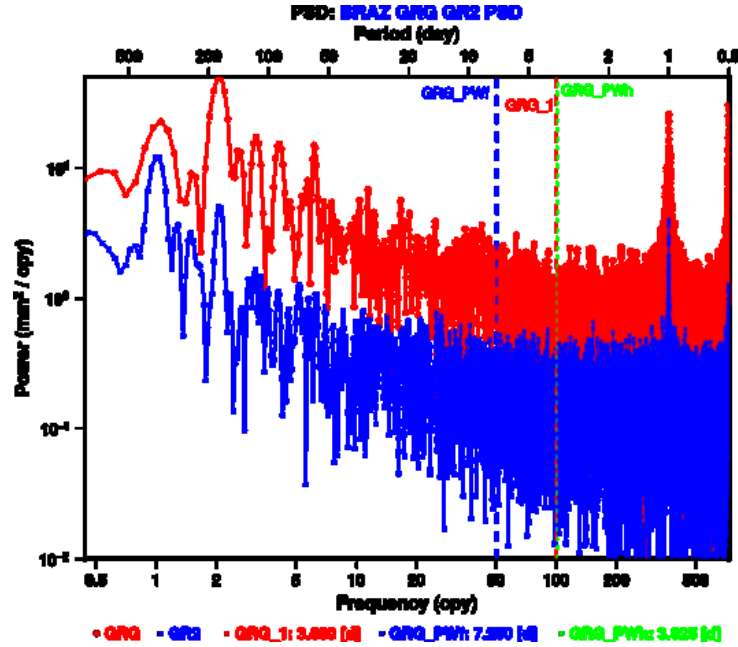


Figure 4.3 – The power spectra of GPS time series estimated using GRG and GR2 products at *BRAZ* station. The vertical dashed lines represent the period of the full GRGS GPS processing week [7.25 days] (blue), the half of this period [3.625 days] (green) and the signal that was observed by Ray et al. [2013] [3.66 days] (red).

Table 4.1 – Processing parameters that we applied to obtain our GPS time series.

PROCESSING PARAMETERS	GR2
Data	zero differenced L3 ionospheric free combination
Ambiguity fixing	Fixed in about more than 97 %
Position estimates	Every 6 hours
Orbit and clocks	GR2
Reference frame	ITRF2008 Altamimi et al. [2011]
Receiver and satellite antenna phase center correction	igs08.atx
Elevation cutoff	10°
Ionosphere refraction	2 nd order corrections using IGS TEC and igrf2011 magnetic field model
Troposphere refraction	GPT/GMF Boehm et al. [2006]
ZTD estimates together with positions	Every hour and gradients every 12 hours
Solid Earth tide	IERS Conventions 2010
Pole tide	IERS Conventions 2010
Ocean tidal loading	FES2012 (CM)
Atmospheric tidal loading	not applied
Non-tidal atmospheric loading	not applied
Non-tidal hydrology loading	not applied
Non-tidal ocean loading	not applied

identify the sampling rate of the given time series and depending on the sampling of the control time series (master file) the input time series (slave files) are resampled or averaged to match the same interval. Surprisingly, the mean horizontal and vertical formal errors over the 10 stations and the 6 year long, 6-hourly time series are very closed to each other, 2.4 mm for the horizontal and 2.0 mm for the vertical components. We remark, that these values derived only from 10 stations, and there were some sites with higher formal errors for the horizontal components.

4.4 Results

The following sections present our results that serve our objective, that is the analysis and comparison of loading models to the iPPP time series. Here, we study the models of the non-tidal atmospheric (ATML), continental water storage loading (CWSL), non-tidal oceanic loading (NTOL) and their accumulated effect (ACN).

The atmospheric pressure loading (ATML) estimated displacements are provided by Zhao Li and Tonie van Dam (University of Luxembourg). These series are determined using the 6-hourly $1/2^\circ$ in latitude and $2/3^\circ$ in longitude resolution grids of surface pressure from the Modern Era Retrospective analysis for Research and Applications (MERRA) dataset based on the inverse barometer (IB) hypothesis.

The 3-dimensional displacements caused by continental water storage loading (CWSL) are generated using soil moisture and snow from MERRA-Land model by Zhao Li and Tonie van Dam. The MERRA-Land data provides us the hydrologic mass variations in 12° in latitude and 23° in longitude resolution grid with hourly sampling.

The non-tidal ocean loading (NTOL) predicted surface displacements are also generated by Zhao Li and Tonie van Dam using the global Estimating the Circulation and Climate of the Ocean (ECCO) ocean bottom pressure (OBP) data. That is the byproduct of the baroclinic general ocean circulation model forced by winds, daily heat and air-sea fluxes. It has 12-hourly samples on its global grids. Its longitudinal spacing is 1° globally. In latitude, the spacing between the product's northern limit and 20° of the equator is 1° . The latitudinal spacing is gradually reduced to 0.3° within 10° of the equator.

4.4.1 RMS analysis

We present only the results for the vertical component which contains the largest signal. The GPS iPPP time series showed good agreement with the various models and their combinations. It is reflected by the RMS values of the up components before and after the *a posteriori* corrections. Our test network seems to be a good selection in terms of model sensitivity. Table 4.2 presents the RMS values for all the time series and Table 4.3 presents these values in terms of percentage for the up component. We labeled our stations depending of their presumed sensibility for the atmosphere (A), ocean (O) and hydrology (C). The columns contain the GPS, the loading (atmospheric pressure loading (ATML), continental water storage loading (CWSL) and non-tidal ocean loading (NTOL¹⁰), and the *a posteriori* corrected GPS time series. The first G letter and a following - sign indicate the corrected estimated time series with atmosphere (A), hydrology (C), ocean (N), the combination of atmosphere and the continental water (AC), atmosphere and ocean (AN), ocean and hydrology (NC) and their total effect (ACN).

In Table 4.3 the GR2 is the reference, thus it is 100.0 %. Then the following three columns, that are the pure models are expressed in terms of percentage compared to GPS. Meanwhile the following columns are representing the RMS difference. Where we see negative sign that means that the loading models degraded the repeatability of the position time series, while a positive value shows the improvements in percentage.

¹⁰We remark, it is different from the NTOL model used in Chapter 6. Here, it is based on the global ECCO model.

Table 4.2 – RMS up (in mm) of the different time series.

	Station	GR2	ATML	CWSL	NTOL	ACN	G-A	G-C	G-N	G-AC	G-AN	G-NC	G-ACN
A	ALIC	10.80	3.21	2.22	0.44	3.69	10.82	10.83	10.74	10.75	10.72	10.80	10.69
A	ARTU	12.22	5.90	3.98	0.30	7.75	9.46	11.25	12.16	8.69	9.39	11.21	8.65
A	IRKT	14.70	4.56	1.24	0.24	5.00	12.93	14.51	14.74	12.83	12.95	14.54	12.85
A	POL2	9.43	3.34	1.50	0.26	3.97	8.80	9.15	9.46	8.65	8.83	9.18	8.67
C	BOGT	13.51	0.82	2.12	0.41	2.61	13.34	13.04	13.42	12.89	13.25	12.97	12.83
C	BRAZ	14.98	1.51	4.66	0.35	4.60	14.99	12.79	14.94	12.67	14.95	12.75	12.63
C	HRAO	9.58	2.24	1.33	0.53	2.26	9.58	9.45	9.55	9.37	9.57	9.39	9.33
O	DARW	14.35	2.02	2.99	1.07	3.00	14.75	13.56	14.12	13.76	14.46	13.44	13.57
O	STJO	9.58	1.86	0.83	2.61	3.28	9.32	9.62	9.66	9.31	9.40	9.74	9.43
O	WSRT	6.56	3.52	3.17	3.38	5.80	6.00	6.17	6.72	5.51	6.20	6.36	5.75

62 **Table 4.3** – RMS up in terms of percentage for the different time series. The values from the 8th until the last column express the RMS change in percentage.

	Station	GR2	ATML	CWSL	NTOL	ACN	G-A	G-C	G-N	G-AC	G-AN	G-NC	G-ACN
A	ALIC	100.0	29.7	20.6	4.1	34.2	-0.2	-0.3	0.6	0.5	0.7	0.0	1.0
A	ARTU	100.0	48.3	32.6	2.5	63.4	22.6	7.9	0.5	28.9	23.2	8.3	29.2
A	IRKT	100.0	31.0	8.4	1.6	34.0	12.0	1.3	-0.3	12.7	11.9	1.1	12.6
A	POL2	100.0	35.4	15.9	2.8	42.1	6.7	3.0	-0.3	8.3	6.4	2.7	8.1
C	BOGT	100.0	6.1	15.7	3.0	19.3	1.3	3.5	0.7	4.6	1.9	4.0	5.0
C	BRAZ	100.0	10.1	31.1	2.3	30.7	-0.1	14.6	0.3	15.4	0.2	14.9	15.7
C	HRAO	100.0	23.4	13.9	5.5	23.6	0.0	1.4	0.3	2.2	0.1	2.0	2.6
O	DARW	100.0	14.1	20.8	7.5	20.9	-2.8	5.5	1.6	4.1	-0.8	6.3	5.4
O	STJO	100.0	19.4	8.7	27.2	34.2	2.7	-0.4	-0.8	2.8	1.9	-1.7	1.6
O	WSRT	100.0	53.7	48.3	51.5	88.4	8.5	5.9	-2.4	16.0	5.5	3.0	12.3

4.4. RESULTS

What comes first to our sight is that the combined effect that includes all the three models improved each GPS time series, since all the values are positive.

Where there are big values in the last column, those are mainly attributed to the expected dominant effect at that site. Whereas, the small numbers denote disagreement between the GPS and models.

For the 4 stations chosen for their atmospheric loading sensitivity we can see that after applying the *a posteriori* loading correction this effect was the most dominant in the signal. The maximum improvement was 22.6 % for *ARTU* station, meanwhile *ALIC* seems not to be sensitive to this specific loading effect. It can be explained with that the atmospheric loading is below the GPS noise level.

For *BRAZ* station the hydrological signal is obvious. Nevertheless even after *a posteriori* correction an important RMS signal still remains. For the two other stations we see moderate agreements between the GPS and the loading effects.

The non-tidal ocean loading displacements do not explain the signal of the GPS observations. It maybe explained by the phase shift between the estimated and predicted time series.

4.4.2 Seasonal amplitudes

We have analysed the seasonal signals of the different time series using Famous Analysis Mapping On Unusual Sampling (FAMOUS) software tools [Mignard 2005]. We have looked for the annual and semi-annual amplitudes of the GPS and model time series. The results are summarised in Tables 4.4 and 4.5. The annual signal was dominant in all cases. The dash (-) table entry denotes that there was no output of the estimation. In general, the GPS results show higher amplitudes for annual and semi-annual signals than the models. Thus the models only partly explain the annual and semi-annual amplitudes published previously (See Ray et al. [2012]). Interestingly for *POL2* station the ATML model and for *WSRT* station the CWSL models predict higher annual signals.

Table 4.4 – The annual amplitudes determined from the 6 year long time series.

	Station	GR2	ATML	CWSL	NTOL	ACN	G-A	G-C	G-N	G-AC	G-AN	G-NC	G-ACN
A	ALIC	2.3	3.7	1.8	0.2	3.7	3.5	1.9	2.2	2.5	3.3	2.0	2.3
A	ARTU	9.2	4.1	5.3	0.1	8.0	5.8	6.1	9.1	2.3	5.7	6.0	2.3
A	IRKT	9.7	4.1	1.5	–	5.2	5.7	9.0	9.8	5.0	5.8	9.0	5.1
A	POL2	3.1	3.5	1.9	–	4.4	2.8	1.6	3.1	2.3	2.8	1.7	2.3
C	BOGT	6.4	0.5	1.0	0.2	1.9	5.9	5.5	6.3	5.0	5.8	5.4	4.9
C	BRAZ	12.2	1.5	6.2	–	5.9	12.4	6.5	12.2	6.4	12.4	6.5	6.4
C	HRAO	1.6	2.4	1.6	0.3	2.2	2.7	1.0	1.8	1.6	3.0	–	1.7
O	DARW	6.8	2.5	3.8	0.8	3.3	8.2	3.5	6.3	4.5	7.5	3.3	3.9
O	STJO	3.4	1.4	1.0	1.2	1.1	2.5	3.7	4.4	2.4	3.3	4.8	3.5
O	WSRT	3.4	–	4.3	1.4	4.5	–	1.4	3.4	1.7	3.1	1.6	1.6

Table 4.5 – The semi-annual amplitudes determined from the 6 year long time series.

	Station	GR2	ATML	CWSL	NTOL	ACN	G-A	G-C	G-N	G-AC	G-AN	G-NC	G-ACN
A	ALIC	3.3	0.5	–	0.1	0.7	3.3	3.7	3.2	3.7	3.3	3.6	3.7
A	ARTU	3.6	–	0.8	0.1	–	2.9	4.0	3.6	3.3	2.9	4.0	3.2
A	IRKT	2.4	1.1	–	0.1	–	2.8	2.4	2.5	2.9	2.8	2.4	2.9
A	POL2	3.4	0.9	0.3	–	1.1	2.4	3.3	3.4	2.5	2.4	3.3	2.6
C	BOGT	–	0.2	1.4	–	1.1	–	–	–	–	–	–	–
C	BRAZ	4.8	0.4	–	0.1	0.5	4.8	5.0	4.8	5.1	4.8	5.0	5.1
C	HRAO	3.1	0.3	0.3	–	0.5	3.0	2.9	3.2	2.6	3.0	3.0	2.7
O	DARW	2.4	–	1.1	–	0.9	2.3	2.3	2.3	2.4	2.4	2.3	2.3
O	STJO	1.4	0.4	0.2	–	0.4	–	1.4	1.4	1.5	1.5	1.5	1.5
O	WSRT	0.9	0.7	–	0.4	1.1	1.0	0.8	1.1	0.9	1.2	1.1	1.2

4.5 New tool for seasonal analysis

4.5.1 Method of the analysis

In order to go further in the seasonal signal analysis, we wonder about another kind of method. Indeed, there are various methods to determine the seasonal characteristic of any geodetic time series, for example Singular Spectral Analysis (SSA), Kalman filter or least-squares fit [Vautard et al. 1992; Schoellhamer 2001; Blewitt and Lavallée 2002; Chen et al. 2012; Davis et al. 2012; Chen et al. 2013a]. Different methods were examined during the Science Master internship period of Ayoub Asri (University of Rennes) and finally the SSA was selected [Asri 2014]. We have adopted the SSA in our analysis because of its non-parametric characteristics. Thus, it can extract information from short and noisy time series without prior knowledge of the dynamics affecting the time series. Geodetic time series often contain missing data, however SSA requires continuous time series. Although, Schoellhamer [2001] presented a method using SSA with missing data, the tool that was developed by Asri [2014] overcomes the problem in a different way. It will be a valuable tool for future analysis concerning for example our original network, where it would be applied for globally well distributed stations (≈ 150). The time series analysis tool developed on MATLAB by Asri [2014] can be mapped out as shown on Figure 4.4. This tool makes the comparison between one GPS and one model time series at a time. This means the different effects and their sum are analysed separately in order to be able to separate each effect's contribution to the GPS signal. Concerning the input, we need previously to perform some pre-processing steps. Indeed we first need to match the time index of the GPS and the loading model time series that means we interpolate, average and truncate the loading time series to the GPS sampling. We apply interpolation when the sampling rate of the given model is greater than of the GPS, and moving average is used when its sampling rate is lower. We do not apply extrapolation, therefore we truncate the time series to match each other if necessary. Once the pre-processing of input data performed, we can tune the different parameters which are: (1) the covariance-lag M values for both GPS and model time series, (2) the filter order, and (3) the signal reconstruction percentages for both GPS and model time series.

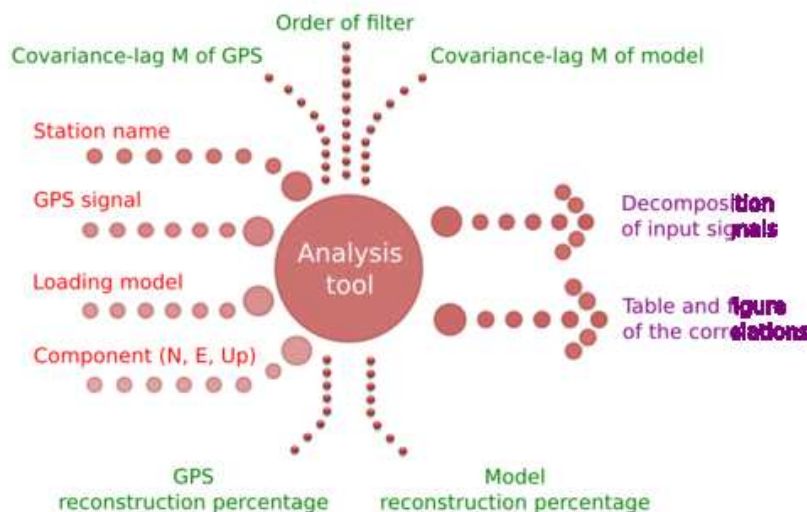


Figure 4.4 – The developed analysis tool.

The main outputs are as follows: (1) Temporal and spectral analysis of the different signal components and the reconstruction percentage (Figures 4.5 to 4.6 and Figures A.1 to A.3 in Appendix A), (2) correlation tables (Tables A.1 and A.4 in Appendix A) and figures that indicate the strongest correlations between the GPS and the model, such as the periodic signals, the ratio and order of correlation for each component of the SSA decomposition (Figure 4.7 top and bottom). The figures of correlation with color scale are very useful for quick interpretation and the tables allow us to quantify the correlations between the different components of the SSA decomposition.

The first types of output of the analyses are simple. The plot of the considered station time series and then the decomposed signals that corresponds to a narrow frequency band. It is followed by the spectral density figures for each of the previous signals, that is for the raw time series and its decomposed elements. As an example, this block of output is shown in Figure 4.5 top and bottom.

The second types of output also takes the advantage of the SSA algorithm. Here, each decomposed GPS signals are compared to the decomposed model signals then the highest correlation pairs are registered. However, it means, it is also possible that there is a correlation found, but the corresponding amplitude is very tiny and insignificant compared

to the GPS formal error. Based on these correlation pairs, we can construct the correlation figures, for which the top left subplot of Figure 4.7 serves an example. There the colors represent the value of the correlation coefficients between the GPS and the considered model, component by component of the SSA decomposition.

For example in Figure 4.5 the first component corresponds to an annual, the second to a daily and the fifth to a ≈ 12 day period. Also, in Figure 4.6 the first component corresponds to an annual period but the other components have different period that it was for the GPS.

This tool was validated with simulated signals. We have then applied this tool for some stations for GRG and GR2 solutions. GR2 time series provide better results in terms of loading signal interpretation than the GRG solution. The comparison confirms that it is essential to use the most recent GPS products to perform loading signal interpretation. This tool allows a good understanding of the different component of the annual and seasonal signals present in the GPS time series. It shows also how the different sources affect the signal and are combined one to each other.

4.5.2 Two examples of the results

Here we show only the example of results for *BRAZ* and *ALIC* stations (Figure 4.7 top and bottom) compared to the different loading models.

For instance for *BRAZ* station this tool indicates that the main component corresponds to the annual signal of the combination of the different loads (See Figure 4.7 top). Looking in detail at each effect this tool reveals that the main part of the annual signal is due to the hydrological effect whereas the non-tidal ocean loading has a moderate impact and atmospheric loading seems to not contribute to the observed signal. In Figures 4.6 top and bottom and 4.7 top we can see that for the CWSL model there is only one significant component (annual period) that contribute to the total loading amplitude. For ATML and for NTOL models there are other components which appear in the total contribution, however, they have very small amplitudes. For example the 4th component of the ATML model is a one day period signal that has 0.3 correlation coefficient with the 2nd component of the GPS that has the same period. However, the corresponding amplitudes are 0.1 and

4.5. NEW TOOL FOR SEASONAL ANALYSIS

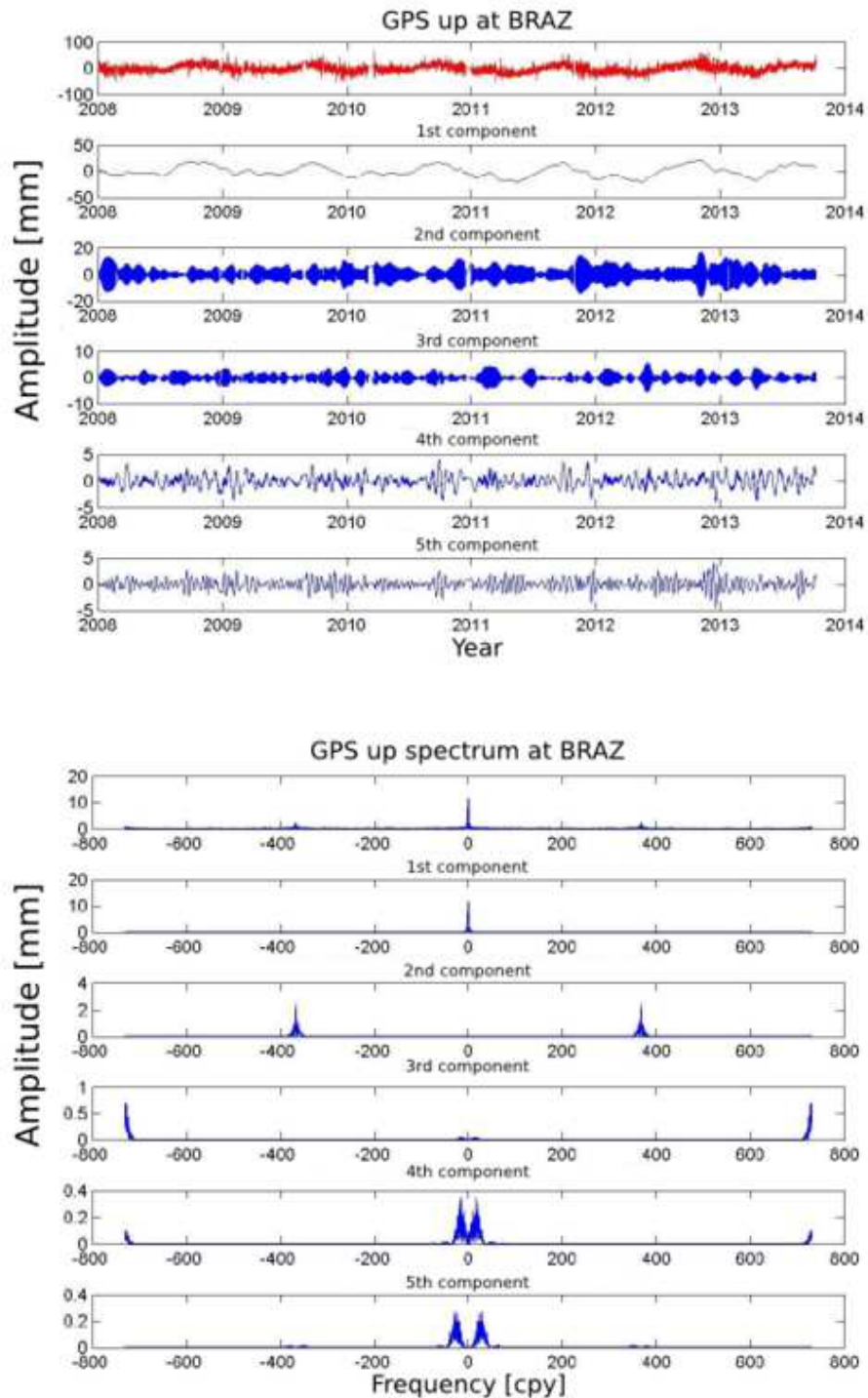


Figure 4.5 – GPS time series components (top) and their spectrum (bottom) at BRAZ station up component in decreasing order of amplitude (in mm).

4.5. NEW TOOL FOR SEASONAL ANALYSIS

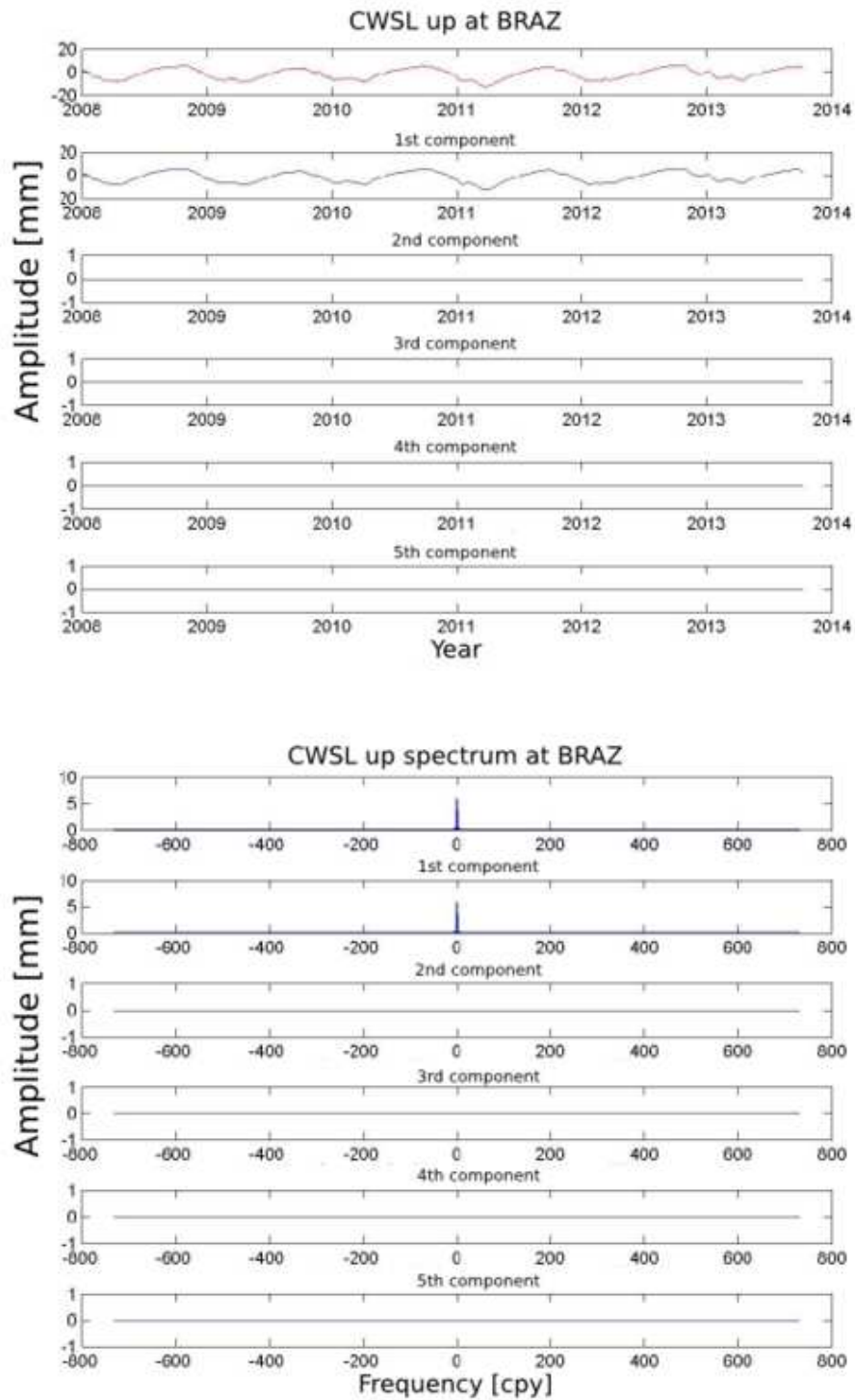


Figure 4.6 – CWSL time series components (top) and their spectrum (bottom) at BRAZ station up component in decreasing order of amplitude (in mm).

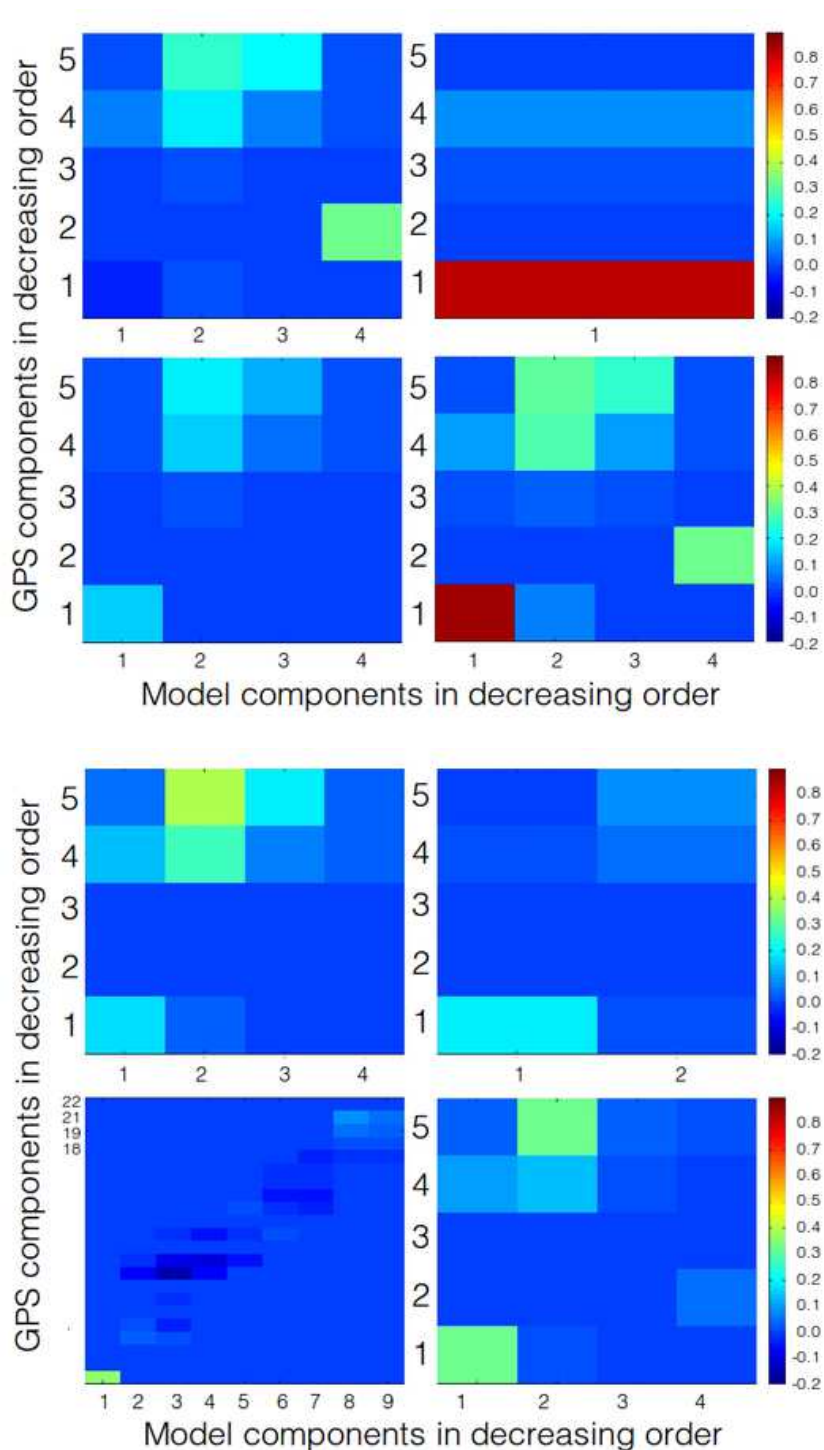


Figure 4.7 – The correlation figures for *BRAZ* (top) and *ALIC* (bottom) stations up component for *ATML* (top left), *CWSL* (top right), *NTOL* (bottom left) and the sum of the models (bottom right). The decreasing order means decreasing amplitude of the signal that corresponds to different periods. The colors represent the correlation coefficients between the GPS and the considered model, component by component of the SSA decomposition.

4.6. CONCLUSION

2.4 mm for the ATML and the GPS, respectively (See Table A.3). Similarly for NTOL, the 3rd model component is an 8 day period signal that shows 0.2 correlation coefficient with the 8th GPS component, that has 9.24 day period. Nevertheless, the corresponding amplitude of the NTOL is negligible and for the GPS it is 0.3 mm.

The presented signal analysis tool ([Asri 2014]) finds an annual amplitude for *BRAZ* station of 11.4 and 5.8 mm (See Table A.1), for GPS and for the CWSL model, respectively (Compare these values with those presented in Table 4.4, line *BRAZ*, 12.2 and 6.2 mm). These results are consistent with our knowledge of the environmental conditions of the station.

Concerning *ALIC* station, this tool confirms that there is no strong correlation between the GPS signal and any of the loading model as we saw in the bottom of Figure 4.7. However, there are also some relationship, for example the 1st component of the sum of models has 0.3 correlation coefficients with the 1st component of GPS. In turn the corresponding periods are 305.62 and 794.6 days, and the related amplitudes are 3.1 and 4 mm for the sum of models and the GPS, respectively (See A.6). The other component pairs are negligible at *ALIC* station. Even they show similar or a little bit stronger correlation, their corresponding amplitudes are irrelevant¹¹ compared to the GPS formal error. According to the geographic location of the station, for *ALIC* we expected the sum of model is dominated by an annual atmospheric loading signal. The decomposition shows that the 1st component of ATML has a 331.07 day period with an amplitude of 3.4 mm. However, this feature has only a 0.17 correlation coefficient with the 1st component of the GPS that has a period of 794.6 days with 4 mm amplitude.

4.6 Conclusion

Concerning the RMS of the GPS time series we saw improvements after *a posteriori* model corrections. Especially these improvements are related to the expected origin of the loading signal, indicating the relevance of our selection. However, to draw a general conclusion about the models, this question need to be further investigated with different

¹¹Less than 0.2 and 0.3 mm for the model and GPS, respectively.

type of datasets for each effects. Also, the network should be largely extended. We have demonstrated that the GR2 time series significantly improves our results in terms of loading interpretations. We demonstrated also that the sub-daily iPPP solutions are able to monitor the loading effects on long-term time series. The developed SSA tool is promising for signal interpretation and the model validation to separate the different contributions of the GPS signals. This tool needs to be automatised to be adapted for a large number of stations. We have seen that there are several correlated components between the GPS and the different loading models, which has different periods. Maybe the decomposition tool did not output any sub-daily signal that is correlated with the GPS, we have the impression that sub-daily GPS solutions should be used for such studies to reveal appearing short period signals that may alias into lower frequencies. In many cases some of the decomposed signals had insignificant amplitude compared to the GPS formal error. This aspect also need to be more investigated in the future. Also other GPS solutions estimated using different processing softwares and strategies, both DD and iPPP could be investigated to filter out common errors and features of the time series. An inter-comparison of the GINS-PC iPPP time series with the output of other iPPP softwares, for example with GIPSY would merit a future research, to validate the products that are used for loading model investigations.

Part III

Regional studies

We are interested in the non-tidal variations of GPS station positions and also how they impact our interpretation of the displacement time series. This intended to present two interesting scenarios concerning loading deformation analysis in France. The first one investigate the topic of how the different non-tidal loading effects would impact our tectonic velocity interpretation (Chapter 5). Meanwhile the second investigates the non-tidal atmospheric, continental water storage and ocean loading effects on GPS iPPP time series to study the different behaviour of coastal and inland sites and validate loading models during a huge storm (Chapter 6).

Chapter 5

Loading artifact in tectonic deformation monitoring of the Pyrenees

Surface displacements due to temporal changes in environmental mass redistributions are observable in the coordinate time series of many GPS sites. In this study, we investigated the effect of loading on estimates of tectonic velocity computed from campaign-style GPS observations. The study region is in the Pyrenees mountain range between France and Spain. *ResPyr* is the name of a network that was installed and measured in the Pyrenees in 1995 and 1997. In this area, seismic activity is continuous and moderate and the expected amplitude of the horizontal tectonic velocity is less than 0.5 mm/yr [Nocquet 2012]. This value corresponds to a maximum residual motion with respect to the stable Europe. Nocquet [2012] rigorously combined recent GPS results (that are based on different processing strategies and cover different areas) to derive geodetic horizontal velocity field in order to describe deformations and to review the kinematic boundary conditions of the Mediterranean¹.

In order to determine the velocity, 4 sparse GPS campaigns were carried out from 1995 to 2010 (*ResPyr* campaigns). Considering this small rate of deformation, loading phenomena can induce a non-negligible artifact to the velocity computation that could affect our geodynamical interpretation. In this investigation, we specifically considered the

¹The relative motion between the three major tectonic plates, Nubia, Eurasia and Arabia accommodated within the Mediterranean [Nocquet 2012].

atmospheric, hydrological, and non-tidal ocean loading phenomena. Finally, we performed simulations to identify the optimum timing and frequency of future GPS campaigns in this area that would minimize the loading effects on tectonic velocity estimates.

This study was published as *An estimate of the influence of loading effects on tectonic velocities in the Pyrenees* [Ferenc et al. 2014] in *Studia Geophysica et Geodaetica*.

5.1 Introduction

There are many geodynamic processes that are observable by GPS and other space geodetic techniques. Such geophysical phenomena include tectonic deformations, post-glacial rebound (for a comprehensive review on this topic see King et al. [2010]), sea-level rise (for a comprehensive review see Blewitt et al. [2010]), variations in water storage [van Dam et al. 2001; Tregoning et al. 2009], atmospheric pressure [van Dam et al. 1994; Petrov and Boy 2004], ocean mass redistribution [Williams and Penna 2011; van Dam et al. 2012] and a combination of these models [van Dam et al. 1997; Zerbini et al. 2001; Scherneck et al. 2003; Schuh et al. 2004; Nordman et al. 2009; Lavallée et al. 2010; Tesmer et al. 2011]. To obtain precise trends from continuous data, requires observation periods longer than 2.5 years [Blewitt and Lavallée 2002]. The precision of the trend is proportional to the number of observations and the time span analyzed [Zhang et al. 1997] so that, trends obtained from campaign measurements will always be less precise than continuous observations over the same period. One way of reducing the uncertainty is by using long observation times. Another solution is to reduce or eliminate noise and unwanted signals in the data by modeling the environmental signals. Imagine a situation in which a large atmospheric pressure system comes through during a GPS campaign or a campaign during which the average pressure is much lower than in other campaigns. Removing the atmospheric loading effect should reduce the scatter of the individual observations within a campaign and the offset of the observations between campaigns.

For tectonic velocity investigations, we are interested in the long-term changes of the geodetic site coordinates. If the tectonic velocity of a region is estimated by comparing positions from each campaign, then careful GPS data processing should be carried out.

Concerning the precision of contemporary GPS positioning (around a few millimeters in the horizontal component), all the non-tectonic effects in the signal have to be considered and removed so as to extract the most precise geodynamic velocity. As a consequence, several sources of errors and signals must be considered, such as the error introduced by ionospheric and tropospheric delays and the loading effects due to mass redistributions. Indeed, environmental mass redistributions (ocean, continental water, and atmosphere) could cause significant 3D displacements of the surface of the Earth of up to several millimeters (see the references in the paragraph above). Among these effects, the signal due to ocean-tidal loading is well documented, modeled and incorporated into the various GPS processing software.

In this study, we focus on loading effects that include surface displacements driven by atmospheric, continental water storage and non-tidal ocean mass variation. These load driven surface-displacements could influence the GPS position coordinates in the Pyrenees mountain range. Their influence on episodic VLBI and continuous geodetic observations has been well documented in geodetic literature [van Dam and Herring 1994; Petrov and Boy 2004; Tesmer et al. 2009]. The signals are periodic (annual, semiannual, diurnal) and can reach significant amplitudes. These effects are generally not implemented into the GPS processing softwares and are generally not taken into account during GPS data analysis for geophysical studies that demand high precision [Williams and Penna 2011].

We investigate the impact of these loading effects on site velocities derived from temporally sparse GPS field campaigns. The GPS data are processed using standards in International Earth Rotation and Reference Systems Service (IERS) Conventions 2010 [Petit and Luzum 2010]. We examine loading time series calculated for 40 GPS campaign stations (*ResPyr* campaign) in the Pyrenees. Four short GPS measurement campaigns (each lasting a few days for every site) have been carried out since 1995 (1995, 1997, 2008, and 2010) to determine the tectonic velocity of the inner part of the Eurasian plate. Indeed, this area is the most seismically active region in France with a continuous and moderate seismic activity [Souriau and Pauchet 1998]. Tectonic velocities are determined from the coordinate differences of each campaign measurement result taken since 1995. A short description of these ResPyr campaigns and preliminary results

5.2. LOADING EFFECT MODELS AND DISPLACEMENT SIGNALS IN THE STUDIED AREA

obtained before the last 2010 campaign measurements are given in Nicolas et al. [2012].

To obtain precise tectonic trends on a level of < 0.5 mm/yr, i.e. the expected rate of deformation in this region [Nocquet 2012], high-precision positioning is required. Let us imagine that the continental water-storage was particularly high during one of the field campaigns with respect to the others. If this loading effect were not accounted for in the analysis, erroneous tectonic velocities and subsequent geodynamic interpretations could contain errors. Thus, to understand the trends derived from our campaign observations, the impact of the different loading effects at the different epochs must be accounted for. We estimate the potential impact of the predicted loading effects on our velocities by analyzing in detail the model time series at the epochs of our GPS campaigns. We then calculate the contribution of each loading effect in terms of velocity. Further, as the study is carried out in a mountainous region, we also analyze the difference between atmospheric and topography dependent atmospheric loading models [van Dam et al. 2010]. Finally, we introduce virtual campaigns to estimate the relationship between the number and timing of campaign observations and velocity effects.

5.2 Loading effect models and displacement signals in the studied area

We considered the surface displacement induced by variations in atmosphere surface pressure, continental water and non-tidal ocean mass changes. In 2009 the IERS restructured the Global Geophysical Fluids Center (GGFC) to include loading models generated by various groups. Various models for the atmospheric pressure, continental water storage, ocean bottom pressure and combinations can be found here. To compute the different displacement time series, we convolve global grids of the surface mass variability (atmosphere, continental water and non-tidal ocean mass) with Farrell's Green's functions [Farrell 1972]. The method is identical to that described in van Dam et al. [2012].

The non-tidal ocean loading (NTOL) predicted surface displacements are generated using the Estimating the Circulation and Climate of the Ocean (ECCO) ocean bottom pressure (OBP) (which is the combined effect of ocean and atmosphere masses above the

5.2. LOADING EFFECT MODELS AND DISPLACEMENT SIGNALS IN THE STUDIED AREA

seafloor) product ². Specifically, we use the Jet Propulsion Laboratory’s Kalman Filter (*kf080*) series [Fukumori 2002]. The model assimilates altimetric sea surface heights, expendable bathythermograph (XBT) profiles and other ocean in situ data. The OBP is a byproduct of the model for the primary product, that is the general circulation of the ocean driven by winds. The OBP is produced daily for the epochs of 06 : 00 and 18 : 00 h between 78.5°N latitude to 79.5°S latitude over the global oceans. Longitudinal spacing is 1° globally. In latitude, the spacing between the product’s northern limit and 20° of the equator is 1°. The latitudinal spacing is gradually reduced to 0.3° within 10° of the equator (for a more indepth discussion of ECCO products, we refer the reader to Kim et al. [2007]). The input data for the NTOL computations have trends as reported in van Dam et al. [2012] respectively. The trend in the NTOL comes from the fact that water volume, and not water mass, is conserved in the general circulation model. The reader should be aware that real long-term variations in observed OBP are expected due to (1) trends in freshwater fluxes; (2) trends in the atmospheric forcing and (3) real long-term variations in the large-scale circulation, i.e. long-term climate variability [Chambers et al. 2007]. There is currently no possibility for determining what fractions of the ECCO OBP trends are realistic or not (M. Thomas, personal communication 12/2011). Thus, the long-term trends have been removed from these time series.

3-dimensional displacements caused by continental water storage loading (CWSL) are generated using Noah-Version 1 Global Land Data Assimilation System (GLDAS) model [Rodell et al. 2004; Rui et al. 2011]. These monthly grids (1° in longitude and latitude) provide estimates of snow water equivalent and soil moisture.

Atmospheric loading (ATML) effects are determined using the 6-hourly 2.5° latitude × 2.5° longitude global grids of surface pressure from the National Centers for Environmental Prediction (NCEP) Reanalysis dataset. Different studies [van Dam et al. 2010; Trenberth and Smith 2005] have emphasized the imprecision of the atmospheric surface pressure data sets at the 2.5° × 2.5° resolution in regions of highly variable surface topography. Therefore, improvements have been made to the conventional surface pressure models that more adequately describe the change in pressure with local topography. The impact

²http://ecco.jpl.nasa.gov:8080/lasFDS/LAS/Assimilation_kf_RADS/OBP.info

5.2. LOADING EFFECT MODELS AND DISPLACEMENT SIGNALS IN THE STUDIED AREA

of the local topography can be of importance in our study area since elevations of the campaign stations vary from 62 m to 2190 m above sea level. In addition to the coarse NCEP reanalysis surface pressure, we generate a finer resolution surface pressure ($0.125^\circ \times 0.125^\circ$) using the original $2.5^\circ \times 2.5^\circ$ resolution data and high resolution topography data (*ETOPO5*, [NOAA 1988]) to represent the change in pressure with local topography more precisely [van Dam et al. 2010]. We will refer to this data set as TOPO.

Differences between ATML and TOPO are usually less than 1.5 mm root mean square (RMS) in height on average for stations distributed over the globe. However, at some locations van Dam et al. [2010] find height differences of up to 3 mm on any particular day. They analyzed the difference between the ATML and TOPO model for one station close to this region, *TLSE*, Toulouse France. They found that removing both the ATML and TOPO model from the GPS height coordinate time series increased the RMS of the observations. However, TOPO increased the RMS to a lesser extent than ATML. For *ResPyr* network, for the TOPO model, the values are very similar to those for ATML. The mean of the differences between ATML and TOPO models are 0 and 0.1 mm for the horizontal and vertical components, respectively. The mean of the RMS of these differences is 0.2 mm for the horizontal components and 1.2 mm for the vertical component over the *ResPyr* stations. Figure 5.1 shows an example of the difference between ATML and TOPO predicted coordinate displacements at *TRMO* station (campaign station at the Cirque de Troumo site, France). Here we can observe a very small day-to-day variation in horizontal components but the vertical component displays larger variations, there are even periods (winters) with extremely high differences.

5.2. LOADING EFFECT MODELS AND DISPLACEMENT SIGNALS IN THE STUDIED AREA

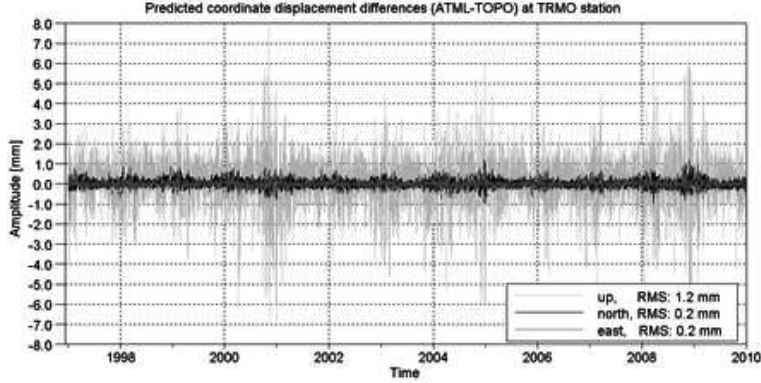


Figure 5.1 – Differences between atmospheric ATML and TOPO predicted coordinate displacements at *TRMO* station (campaign site, Cirque de Troumo, France) from 1995 to 2010.

Table 5.1 shows the minimum, maximum, mean and RMS values of the amplitude of the loading effects calculated over all the *ResPyr* sites between 1995 and 2010. In the Pyrenees, the peak-to-peak amplitudes of the ATML model vary between 3 – 4 mm and 18 – 23 mm for the horizontal and vertical coordinates, respectively. The mean value is around zero since this signal is mainly annual, despite the fact it shows large variations at higher frequencies (about 10 days). The RMS of ATML series throughout the *ResPyr* sites during the considered years is 0.5 mm, 0.4 mm for the horizontal components and 2.6 mm for the vertical component. The CWSL North, East, and Up amplitude ranges are 5 mm,

Table 5.1 – Amplitude statistical data (in mm) over the 40 *ResPyr* stations for atmospheric (ATML), continental water storage (CWSL), non-tidal ocean loading (NTOL) models, and the corresponding accumulated effect (ACN). N - North, E - East, U - Up.

	ATML			CWSL			NTOL			ACN		
	N	E	U	N	E	U	N	E	U	N	E	U
Min	-2.4	-1.8	-8.5	-2.0	-2.0	-10.4	-4.4	-2.9	-5.6	-5.2	-4.2	-19.2
Max	1.7	1.7	14.3	2.6	1.8	8.1	4.0	3.1	4.8	5.1	4.8	15.9
Mean	0.0	0.0	0.1	-0.1	0.0	-0.5	0.0	0.0	0.0	0.0	0.0	-0.3
RMS	0.5	0.4	2.6	0.9	0.8	4.2	1.0	0.8	1.3	1.3	1.2	5.5

3 – 4 mm and 14 – 19 mm for all *ResPyr* sites over the entire time interval (Table 5.1). The mean value is -0.1 mm for North component, 0 mm for the East and -0.5 mm for the vertical component. The mean of the RMS over all the stations is 0.9 mm, 0.8 mm and 4.2 mm for the North, East and Up components, respectively.

5.2. LOADING EFFECT MODELS AND DISPLACEMENT SIGNALS IN THE STUDIED AREA

The NTOL signal statistics for the *ResPyr* stations for the period 1995 to 2010 are also provided in Table 5.1. In North, East and Up components the peak-to-peak amplitudes are approximately 8 mm, 6 mm and 10 mm, respectively, averaged over all sites. The mean values are zero for the three components. These sites are affected by the NTOL signal in the Celtic Sea/Atlantic Ocean/Bay of Biscay and the Mediterranean Sea. The mean of the RMS over all of the *ResPyr* stations is 1 mm and 0.8 mm for the horizontal and 1.3 mm for the vertical components.

In most comparisons of loading with a geodetic height time series, the effect of continental water storage is normally the largest signal [van Dam et al. 2001]. In our study area, we find that the largest horizontal displacement amplitudes are driven by the NTOL (compare signals in Table 5.1). This is due to the location of the study area between the Atlantic Ocean and the Mediterranean Sea. Also, this great western influence of the NTOL is probably due to general oceanic circulation, the North Atlantic Ocean Circulation (NAO), that is partially driven by the thermohaline³ circulation. We compare the NTOL loading effects at *TLSE*, (Toulouse, France, a continuously operating site in our study region) using the global data set versus using only the OBP data from the Mediterranean Sea. We determine what fraction of the total scatter on the coordinate time series is driven by OBP changes in the Mediterranean Sea alone. Contributions from NTOL variations in the Mediterranean Sea represent 10 %, 26 % and 15 % of the North, East and Up coordinate scatter driven by the global NTOL effects. In Figure 5.2, the contribution of the Mediterranean Sea is shown. The largest vertical amplitudes are introduced by the continental water storage and the atmospheric loads. This may be mainly due to the snow cover in winter and to the local topography of the area.

³Deep-ocean currents that are driven by water density differences.

5.2. LOADING EFFECT MODELS AND DISPLACEMENT SIGNALS IN THE STUDIED AREA

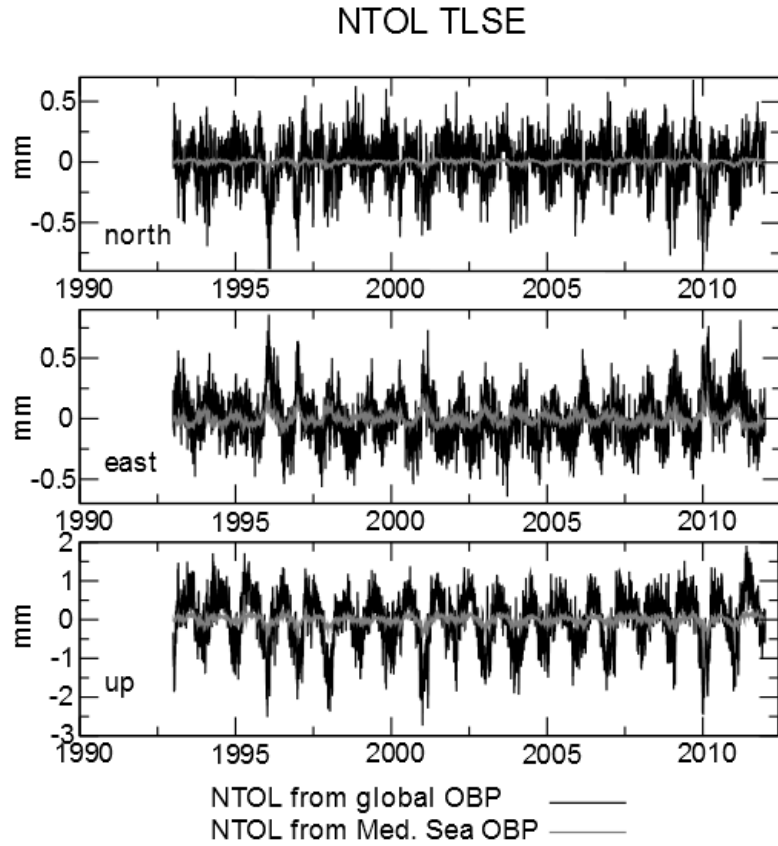


Figure 5.2 – Non-tidal loading effects NTOL at *TLSE* (Toulouse, France) station. Comparison of global data set versus the ocean bottom pressure (OBP) data from the Mediterranean Sea.

The amplitudes of these loading signals are non-negligible with respect to the high level of precision that we require to observe the < 0.5 mm/yr expected horizontal tectonic signal. To estimate the accumulated effect of the different loading phenomena, we interpolated in time all the loading model time series to the same temporal sampling. We chose a sampling of 6 hours. For this interpolation, we used a cubic spline process and verified that this interpolation had no effect on the trend and on the minimum and maximum values obtained before interpolating. The 6-hour time series from ATML, NTOL and CWSL were summed up. In the remainder of this document, the total signal computed with ATML is labeled ACN and that with TOPO is labeled TCN. For illustration, the ACN statistical results are provided in Table 5.1. The total loads induce peak-to-peak amplitudes, which can reach 9 – 10 mm, 8 – 9 mm and 30 – 35 mm for North, East, and Up components,

respectively. The corresponding mean values are 0 mm in the horizontal and -0.3 mm in the vertical. The mean of the RMS over all the *ResPyr* sites are 1.3 mm, 1.2 mm and 5.5 mm, for the North, East, and vertical directions, respectively.

5.3 Velocity signal induced by loading effects

As mentioned previously, the ResPyr campaigns last only a few days and have been very sparse over time. Given that the expected deformation is in the order of < 0.5 mm/yr, it is essential to reduce or eliminate noise and unwanted signal in our data. The loading effects show extreme variability in space and time and strongly depend on the environmental mass load that is acting during any field campaign. Some of the surface loading effects show high variability even over the course of a week. In this section, we use the loading data predicted for the *ResPyr* campaign epoch and stations to determine how the loading effects could influence the precision of the GPS velocity estimates. The epochs of the real GPS observations include: middle of summer of 1995, 1997, 2008 and 2010. Note that the starting epoch and the lengths of the observations were not exactly the same for the 40 stations in each campaign. In short, these observations were rather inhomogeneous in time.

The modeled load-induced horizontal surface displacements are 4 to 6 times smaller than those in the vertical. Thus, we expect the loading effects in the vertical trend to be much more significant than those in the horizontal. As this study is focused on determining the effect of loading on campaign measurements used to determine long-term trends, we will investigate the effect of loading on all three coordinate time series. In mountainous regions in particular, understanding the effects in all three components is useful for interpreting the geodynamic process acting at regional scales. We also investigate the velocity error due to accumulated effects (ACN and TCN). We derive loading induced velocity estimates by determining trends over the campaigns.

Table 5.2 shows the extreme cases and statistical values related to the loading models in terms of velocity estimated for the original *ResPyr* campaigns. The dominant loading effect in the horizontal velocity is still the non-tidal ocean loading with a mean effect of

5.3. VELOCITY SIGNAL INDUCED BY LOADING EFFECTS

0.11 mm/yr over all the sites, with a maximum of 0.22 mm/yr. The effects of continental water storage loading have the largest impact on the estimate of vertical velocity with a mean of about 0.21 mm/yr over all the sites and can reach 0.47 mm/yr. Atmospheric effects are much smaller than NTOL or CWSL but can reach 0.21 mm/yr for the vertical component. Figs 5.3a and 5.3b represent the estimates of the different velocity signals induced by the different loads for the original *ResPyr* campaigns.

The horizontal loading velocity signals (Figure 5.3a) are quite inhomogeneous on the *ResPyr* network, mainly because of the observation epoch inhomogeneity. It reflects the short term loading variations on the scale of the whole *ResPyr* campaign duration of one given year (a few weeks). For the vertical component (Figure 5.3b), the loading effects seem to affect more significantly the western part of the network which is more influenced by the Atlantic Ocean and by the air masses which mostly come from the West in this part of Europe. Despite the relatively large displacement amplitudes of the different loading

Table 5.2 – Velocity effects for the original *ResPyr* campaigns on the North, East, and Up components (in mm/yr). The North and East minima, maxima, mean and RMS are not necessarily for the same stations, whereas the 2D minima, maxima, mean and RMS involve both North and East components for the same station.

	ATML				CWSL			
	N	E	2D	U	N	E	2D	U
Min	-0.05	-0.04	0.00	-0.09	0.05	0.00	0.06	-0.03
Max	0.03	0.02	0.06	0.21	0.12	0.04	0.12	0.47
Mean	0.00	-0.01	0.02	0.04	0.09	0.02	0.09	0.21
RMS	0.02	0.02	0.03	0.09	0.09	0.02	0.09	0.28
	NTOL				ACN			
	N	E	2D	U	N	E	2D	U
Min.	-0.21	-0.08	0.01	-0.18	-0.06	-0.08	0.03	-0.14
Max.	0.21	0.11	0.22	0.12	0.23	0.12	0.24	0.65
Mean	-0.02	0.02	0.11	-0.03	0.07	0.04	0.11	0.22
RMS	0.11	0.05	0.13	0.06	0.10	0.07	0.12	0.30

effects, in terms of a velocity over a large time span (15 years) the amplitudes are small. This is mainly due, in our case, to the fact that all the measurements were carried out at the same season of the year (summer). Our results show that, in the *ResPyr* case where there are several years of observations and the observations are not entirely homogeneous in time, the velocity effect of the loading introduces only a moderate error. The total

5.3. VELOCITY SIGNAL INDUCED BY LOADING EFFECTS

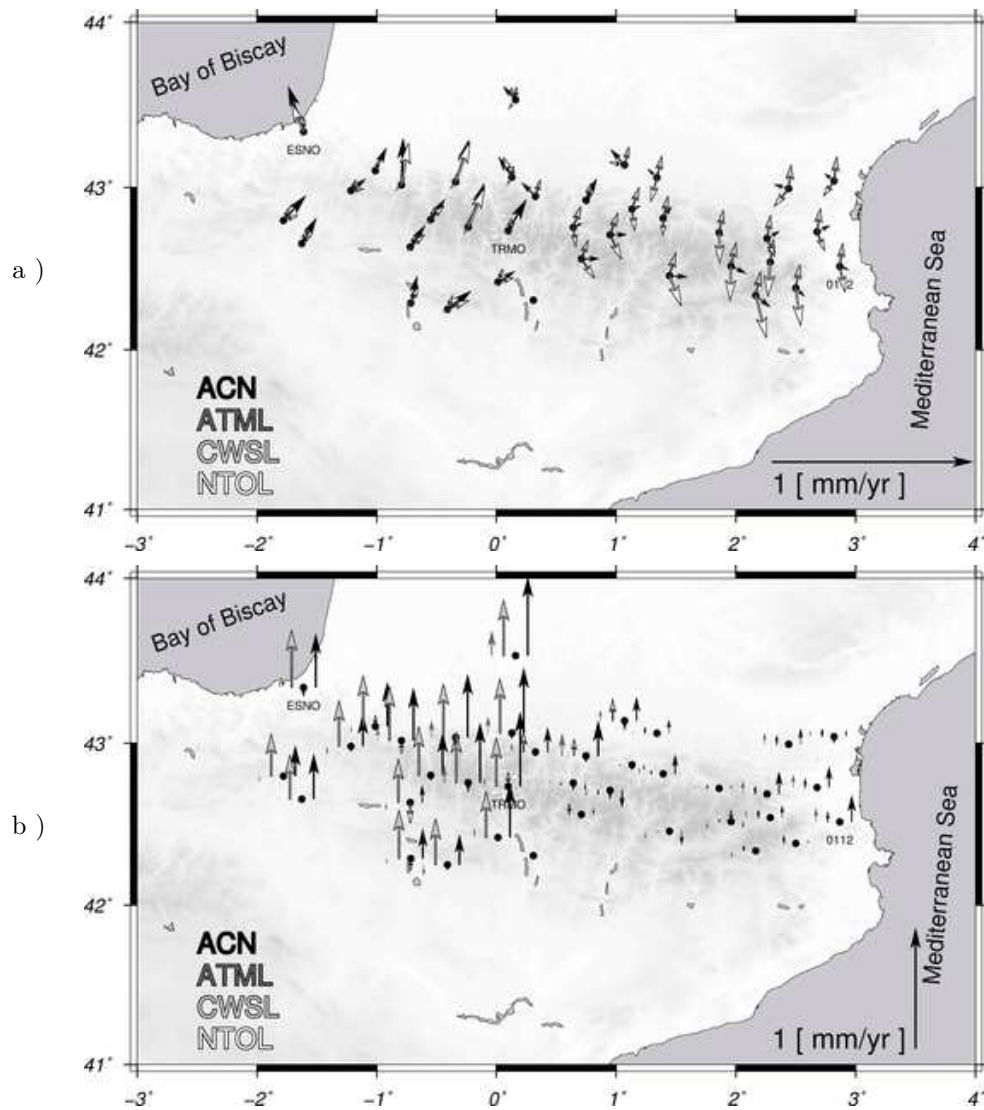


Figure 5.3 – (a) Horizontal and (b) vertical velocities (in mm/yr) for different loading effects. Accumulated (ACN, in *black*), atmospheric pressure (ATML, in *dark grey*), non-tidal ocean loading (NTOL, in *white*), and continental hydrology (CWSL, in *light grey*). *TRMO* (Cirque de Troumo, France), *ESNO* (Mont Esnour, France) and *0112* (Montesquieu, France) are campaign station names.

loading effects can reach 0.65 mm/yr in the vertical component. This result is mainly due to the fact that the loading effects are primarily annual in character. Measuring at the same time of the year will minimize the effect.

By contrast, the horizontal total load effects can represent up to 0.24 mm/yr which represents a large part of the expected tectonic signal in a specific azimuth that is probably different from that of the tectonic velocity itself. The difference between ATML and TOPO horizontal velocities are always lower than 0.1 mm/yr, but TOPO effect is systematically larger in amplitude. We conclude that the difference between the ATML and TOPO models is negligible in terms of the horizontal velocities and will not contribute to errors in the final horizontal velocity estimation. In the vertical, the ATML and TOPO differences are larger, the ACN and TCN can differ by 22 % in terms of velocity.

5.4 Comparison with preliminary GPS results

On the basis of these results, we are able to make a comparison with the GPS tectonic velocity estimates calculated using the GAMIT/GLOBK software [Herring et al. 2010]. For this computation, final IGS orbits (reprocess 1 orbits and clocks), absolute IGS [Dow et al. 2009] atx file, and Global Mapping Function (GMF) [Boehm et al. 2006] were used⁴. 21 permanent stations, when available, were included in the processing and no atmospheric loading correction was applied. Table 5.3 gives the statistical values of GPS estimates for each component over all the *ResPyr* sites. The norm of horizontal velocity vector is between 0.1 and 1.5 mm/yr with a mean value of 0.6 mm/yr and a RMS of 0.6 mm/yr. For the vertical velocities, the absolute values range between 1 and 24 mm/yr with a mean value of -0.9 mm/yr. The GAMIT formal errors are approximately 0.3 – 0.4 mm/yr and 3 mm/yr for the horizontal and vertical velocities, respectively. These formal errors are probably realistic for the *ResPyr* campaigns given that they show no significant motion to 95 % confidence interval for most of the horizontal velocities. The vertical velocities cannot be used since the velocities are based on measurements done on tripods and the antenna and receivers were not the same for the first survey (either 1995 or 1997) and the second survey (2008 or 2010) of each site. In Figure 5.4 the horizontal GPS velocities are compared to

⁴We remark here that the GPS results are estimated by Philippe Vernant (University of Montpellier).

5.4. COMPARISON WITH PRELIMINARY GPS RESULTS

the accumulated load ACN results. The vertical velocities are not shown since they are not realistic.

Table 5.3 – GPS velocity estimates statistical results for the *ResPyr* stations (in mm/yr). The North and East minima, maxima, mean and RMS are not necessarily for the same stations, whereas the 2D minima, maxima, mean and RMS involve both North and East components for the same station.

	GPS (mm/yr)			
	N	E	2D	U
Min	-0.6	-1.4	0.1	-24.3
Max	0.6	0.6	1.5	6.6
Mean	-0.1	-0.4	0.6	-0.9
RMS	0.3	0.6	0.6	6.1

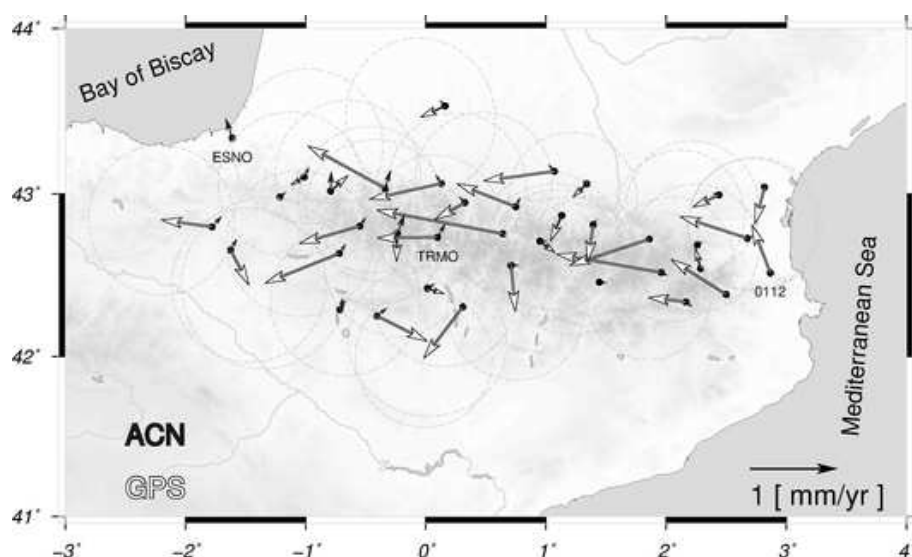


Figure 5.4 – Accumulated loading effect (ACN) and GPS horizontal velocities (in mm/yr). *TRMO* (Cirque de Troumo, France), *ESNO* (Mont Esnour, France) and *0112* (Montesquieu, France) are campaign station names.

Concerning the comparison between GPS and load phenomena velocities, we can make the following comments. Although the effect in terms of velocity is still small compared to the results of GPS processing and its uncertainties, in some cases the loading effects are comparable with the velocities resulting from the GPS processing. In a higher proportion of the stations they seem to add noise, rather than a useful signal for a correction. We have shown (Table 5.2) that the total impact of loading on the estimated velocity can reach 0.23 mm/yr in the North component, 0.12 mm/yr in the East component and 0.65 mm/yr

in the vertical component in absolute value. For the horizontal deformation it is far from negligible in the sense that it may represent up to 28% of the calculated GPS velocity signal. Moreover, it can modify the direction of the final site motion that consequently may affect the geodynamical interpretation of the results. On further examination, the modified azimuth induced by loading effects varies with the period of the observation and the delay between two campaigns, as we demonstrate with simulations which are set out in the next section. In this sense, load phenomena can really induce artifact in GPS tectonic velocity estimates. For the purpose of the Pyrenean tectonic study, we would like to perform a new campaign in the coming years. This new data would probably be sufficient when combined with the existing data set to compute a precise velocity estimate. Hence, on the basis of this new data, better GPS velocity estimates with higher precision would be obtained and would make the drawing of some conclusions about the geodynamical deformation of the area much easier. However this signal would be still affected by the loads. If our GPS campaigns were performed annually and the tectonic velocity calculated regardless of the loading effects, (i.e. just comparing the current and the previous observations) we could potentially obtain significant and surprising velocity estimates that are loading and not tectonically driven.

However, a comparison of a few years of data is not satisfactory for tectonic velocity determination. In practice, processing of a time span of several years is required for deriving tectonic velocities. For instance, Blewitt and Lavallée [2002] recommend a minimum 2.5 year data span of continuous data for velocity solutions used for geophysical studies. Insofar as we seek to observe some of the smallest amplitude tectonic deformation signals, the best way would be to have permanent stations. Nevertheless the signal would always be affected by the load phenomena. Thus, as Tregoning and van Dam [2005] did for atmospheric loading, we recommend that, as far as possible, total loading should be considered in GPS data processing.

5.5 Dependence of loading effects on survey timing and frequency

To additionally estimate the artifact induced by loading effects in the case of sparse GPS campaigns, we also simulated some hypothetical campaigns. Indeed, for observations lasting only a few days, the modeled displacements show variations sometimes larger than 2 mm in absolute value. Although, the loading amplitude, and therefore its velocity effect, depend on the season when GPS data has been acquired.

For these simulations, as a first step, we considered virtual campaigns lasting 3 days for each station at the beginning of each month in 1995, 1997, 2008 and 2010 (years of *ResPyr* campaigns). These 3 day windows ensure homogeneous observations in time. In a second step, we carried out virtual experiments with the same 3 day observing window at the beginning of each month, but taking into account all the years from 1995 until 2010 so as to have an idea of the amplitude of the effect for the different seasons and field survey repeat rates. We then derived velocity results where all the observations had been carried out during the same month over the years and we varied the number of observations, regularly taking into account all of the years, then every second, followed by every third and finally every fifth year at each site. In this way we analyzed the impact of the choice of the campaign observation epoch and rate of survey repetition in order to be able to optimize the planning of future campaigns. As for the real observation periods, we computed the velocity error induced by each loading effect as well as for the accumulated effects (ACN and TCN).

On the basis of these simulations, we are able to determine the best month and repetition rate for this kind of campaign trading off the smallest load impact with practical considerations such as the potential comfort of performing field work at a particular time.

Table 5.4 represents the statistical values for the virtual observations of the *ResPyr* years. These estimates are from temporally homogeneous observations due to their 3 day sampling at the beginning of each month of July. Figures 5.5a and 5.5b show the virtual results which correspond to the months and the years of the original *ResPyr* campaigns

5.5. DEPENDENCE OF LOADING EFFECTS ON SURVEY TIMING AND FREQUENCY

(3 days at the beginning of July). Figure 5.5a, which corresponds to Table 5.4, in analogy of Figure 5.3a represents the map of the different loading effects in terms of horizontal velocity. It shows that effects are fairly consistent in amplitude and azimuth due to the fact that the mass must be geographically extensive to produce an observable load. The NTOL effect is mainly in the North-West direction in line with an azimuth drawn between the Bay of Biscay, the stations and the Mediterranean sea. The horizontal effects of the CWSL are mainly in the North-Northwest direction. ATML and TOPO are too small in amplitude to be visible on the scale of this map. Thus, the total horizontal effect has a Northwest direction for all the stations, without any significant differences between the different geographic parts of the network. In Figure 5.5b (which corresponds to Table 5.4)

Table 5.4 – Velocity effects for the virtual *ResPyr* campaigns on the North, East, and Up components (in mm/yr), where 3-day observations are simultaneous at all stations at the beginning of July, in the year of the *ResPyr* campaigns. The North and East minima, maxima, mean and RMS are not necessarily for the same stations, whereas the 2D minima, maxima, mean and RMS involve both North and East components for the same station.

	ATML				CWSL			
	N	E	2D	U	N	E	2D	U
Min.	0.02	0.00	0.02	-0.04	0.07	-0.04	0.08	0.26
Max.	0.03	0.01	0.03	-0.03	0.09	-0.02	0.10	0.34
Mean	0.02	0.00	0.02	-0.03	0.08	-0.03	0.09	0.29
RMS	0.02	0.00	0.02	0.03	0.08	0.03	0.09	0.29
	NTOL				ACN			
	N	E	2D	U	N	E	2D	U
Min.	0.05	-0.10	0.08	-0.09	0.15	-0.12	0.17	0.14
Max.	0.07	-0.07	0.12	-0.05	0.18	-0.08	0.22	0.24
Mean	0.06	-0.08	0.10	-0.06	0.16	-0.10	0.19	0.19
RMS	0.06	0.08	0.10	0.06	0.16	0.10	0.19	0.19

we can see that all the CWSL and the ACN total (vertical) load signals are positive. The sites with the slightly larger vertical velocity are located in the central and western parts of the study region. The CWSL effect has the highest vertical velocity effect over all the *ResPyr* stations, the NTOL and ATML or TOPO effects are almost negligible. Concerning the simulations of the virtual campaigns, we are left with some interesting conclusions. First, the orientation and the size of the velocity vector change when the frequency of field measurements changes. Field measurement frequency and the resulting

5.5. DEPENDENCE OF LOADING EFFECTS ON SURVEY TIMING AND FREQUENCY

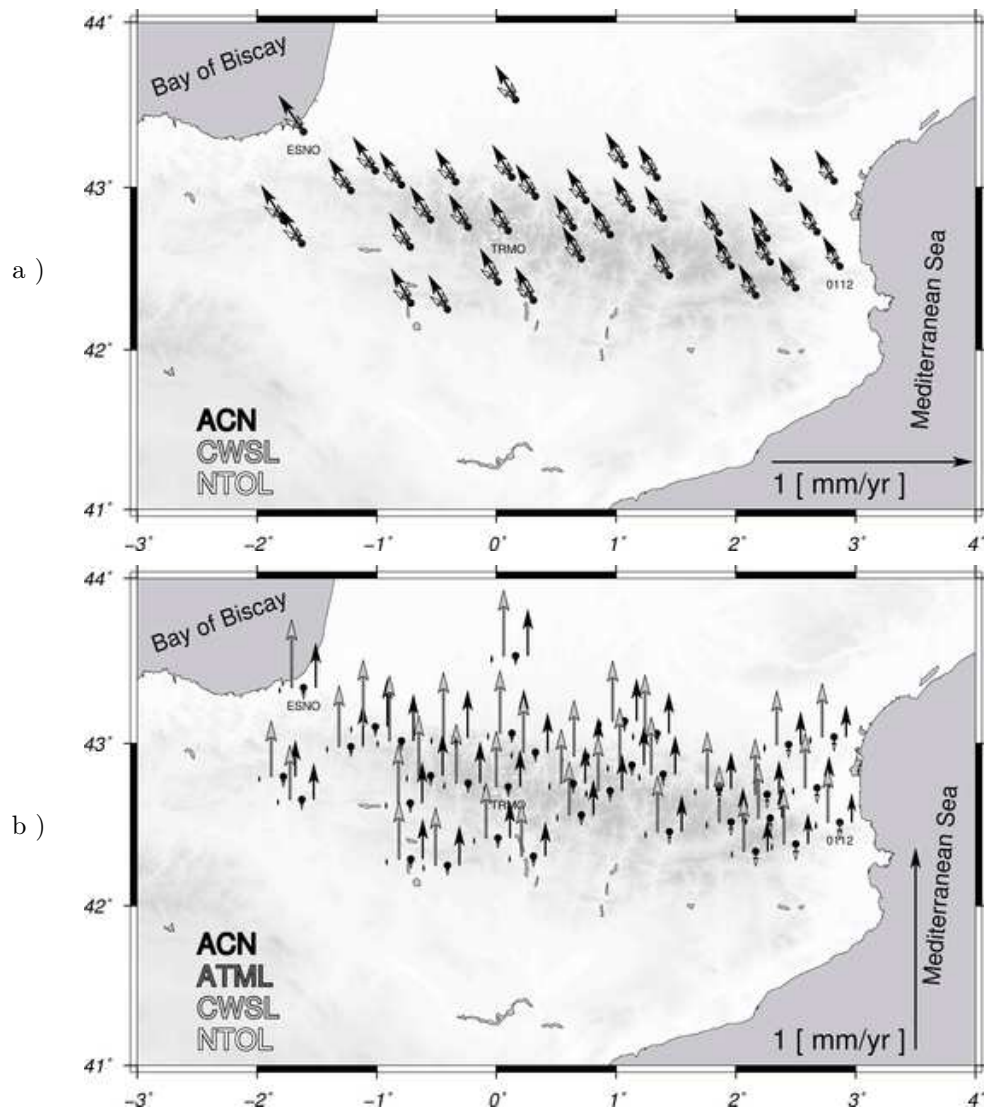


Figure 5.5 – (a) Virtual horizontal and (b) vertical loading velocity results (in mm/yr), corresponding to Table 5.4 (horizontal components), where 3-day observations are simultaneous at all stations at the beginning of July, in the year of the *ResPyr* campaigns, for the different effects. Accumulated (ACN in *black*), atmospheric pressure (ATML, *dark grey*), continental hydrology (CWSL, in *grey*) and non-tidal ocean loading (NTOL, in *white*). *TRMO* (Cirque de Troumo, France), *ESNO* (Mont Esnour, France) and *0112* (Montesquieu, France) are campaign station names.

5.5. DEPENDENCE OF LOADING EFFECTS ON SURVEY TIMING AND FREQUENCY

horizontal directions for a particular month (July) are shown in Table 5.5.

Table 5.5 – Field measurement frequency and their resulting horizontal azimuth for a particular month (July).

Field measurement frequency	Horizontal direction
original <i>ResPyr</i> campaigns (1995,1997,2008,2010)	north-west
each year (1995-2010)	north
every 2 years (1995-2010)	north-east, nearly zero
every 3 years (1995-2010)	north, north-east
every 5 years (1995-2010)	north-east

Thus, the interpretation of the final tectonic velocities may depend on the time span between the different observation campaigns used to determine it. Secondly, the amplitude of the velocity induced by the load phenomena depends upon which month the data is acquired. Even strong differences exist between two successive months. Examples of these velocity variations are given by Figure 5.6. These virtual, 3-day long observations are performed for the *ResPyr* observation years, every 3 and 5 years for *TRMO* station located in the central part of the Pyrenees. We observed nearly the same pattern for all the stations but with slightly smaller amplitudes in the eastern part of the network in the case of *ResPyr* campaign years.

We conclude that this kind of analysis can help to choose the best period to reoccupy the GPS benchmarks. Indeed, if the delay in the number of years changes between two successive campaigns we demonstrate that the general pattern changes for all the stations, nearly in the same way for the entire network but still with a lesser impact for the eastern stations. We can also see strong differences according to the month of observation for a given repetition rate. For instance, the North component changes signs between August and September for the original *ResPyr* campaign years and between May and June for virtual campaigns performed every 3 years. Figure 5.6 also demonstrates that if the campaign style GPS measurements are carried out in summer (as it was actually performed), then we have the smallest velocity effect due to loading phenomena.

From our computations, we find that the load effect can reach 0.3 mm/yr in horizontal velocity and 1 mm/yr for the vertical component. Considering only the epochs without snow in the Pyrenees, the worst months seem to be June for the horizontal components

5.5. DEPENDENCE OF LOADING EFFECTS ON SURVEY TIMING AND FREQUENCY

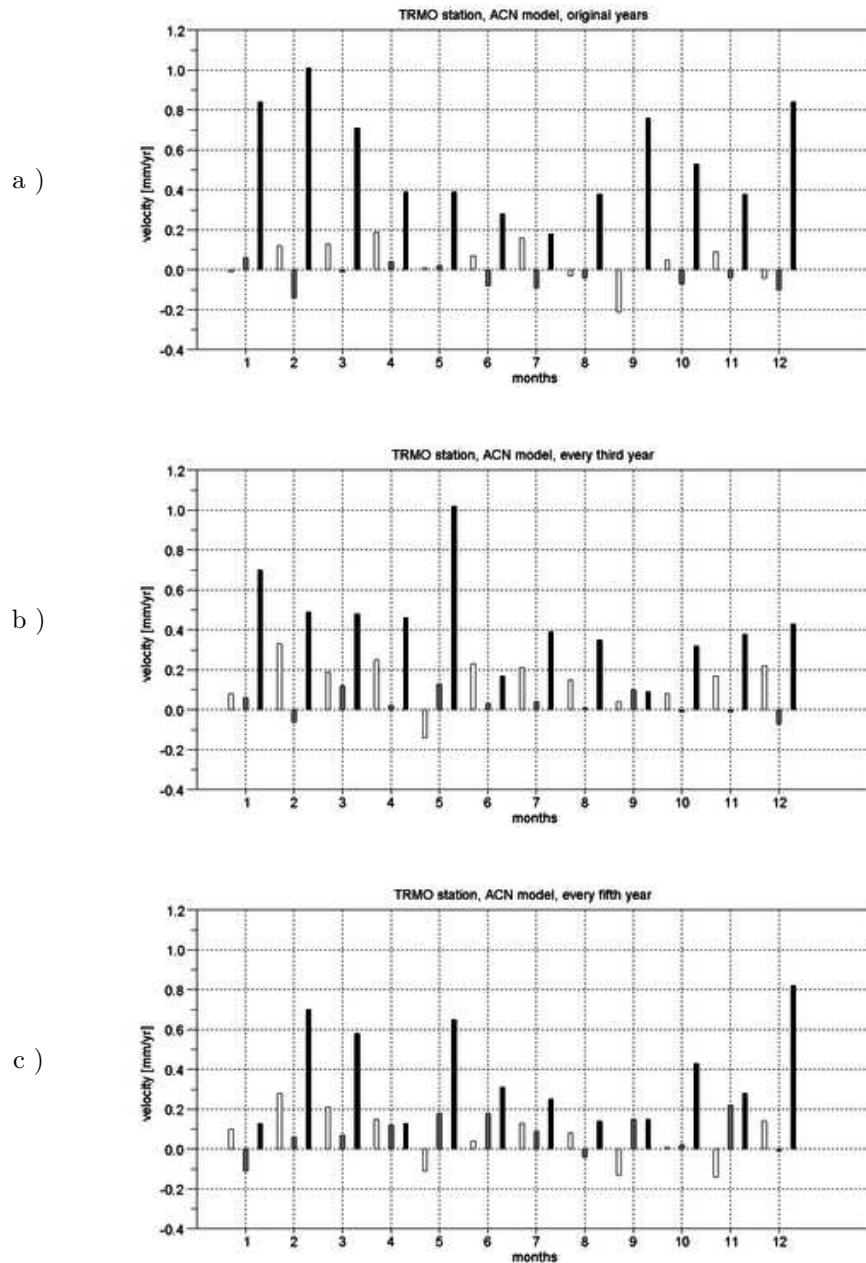


Figure 5.6 – *TRMO* station (campaign site Cirque de Troumo, France) simulation results in terms of velocity (mm/yr) for accumulated (ACN) loading effects. (a) For virtual campaigns at the same years than *ResPyr* campaigns, (b) for campaigns performed every 3 years, and (c) every 5 years. The columns correspond to the directions: North (*white*), East (*grey*) and Up (*black*) velocities. The horizontal axis numbers from 1 to 12 represent the months, January to December respectively.

and May for the vertical component independent of the number of years between the two campaigns. The best month to carry out GPS campaigns seems to be August, independent of the number of years between two successive campaigns. This result holds for both horizontal and vertical components. The load effects seem to be the smallest for campaigns performed every 2 years for horizontal components and every 5 years for the vertical. The worse field measurement repeat time seems to be every 3 years for the horizontal components and every 1 or 2 years for the vertical velocity. Finally, we conclude that the optimum result is to perform GPS field campaigns every 5 years in August.

5.6 Conclusions

We have analyzed the effects of surface mass loading in the Pyrenees mountain region for epochs corresponding to sparse GPS campaigns. The load signal amplitude is dominated by the non-tidal ocean loading for horizontal components (mean range of 8 mm in the North and 6 mm in the East) and by atmosphere and continental hydrological loadings for the vertical component (mean range of 21 mm and 17 mm, respectively). The accumulated load signal can reach a mean range of 10 mm for North, 8 mm for East, and 33 mm for vertical displacements, respectively. We know that the loading effects can have significant amplitudes and can vary over short periods of time. In the estimates of the station positions from campaign to campaign the loading effects can be significant. We examined these loading signals with respect to their potential effect on the measured GPS velocity. We have found that for the *ResPyr* network between 1995 and 2010, the dominant loading effect on the horizontal velocity remains the non-tidal ocean loading (mean of 0.11 mm/yr), whereas the continental hydrology is the main contributor to the vertical component (mean of 0.21 mm/yr). To a certain extent, even if the accumulated loads seem small in absolute terms (maximum 0.24 mm/yr and 0.65 mm/yr in horizontal and vertical components, respectively), they can modify the orientation of the final site velocity that will consequently affect the geodynamical interpretation. Moreover, the total load impact on the horizontal can represent a large part of the expected tectonic signal, and could even be larger than the tectonic signal. The effect of loading on velocities determined using campaign style GPS observations in tectonic regions that are more distant from coasts may be larger. In

5.6. CONCLUSIONS

any case, we recommend paying particular attention to these effects at the level of the GPS data processing (as it is shown in Tregoning and van Dam [2005] for the atmospheric loading).

We did not find any significant difference between ATML and TOPO loading effects in terms of horizontal velocity in the Pyrenees since the non-tidal ocean loading effects are larger than the differences between atmospheric loading with or without refined topography consideration. Nevertheless, concerning the vertical component, the ATML and TOPO differences are stronger and can change the accumulated effect by 22%. Therefore, we recommend taking into account the local topography in atmospheric loading computation.

Concerning the horizontal (campaign) GPS velocity estimates, the range is between 0.1 and 1.5 mm/yr with a mean value of 0.6 mm/yr and a formal error of about 0.3–0.4 mm/yr. As regards to the vertical component, the absolute values of GPS estimates range between 1 and 24 mm/yr with a formal error of 3 mm/yr. On the basis of these results, it is difficult to draw significant conclusions regarding the general tectonics of the area. That is, the residual tectonic velocity which is less than 0.5 mm/yr and the loading induced velocity effect are infinitesimal if we strictly consider the GPS formal errors obtained from campaign measurements. These velocities could be better determined if a new campaign were to be performed or if a permanent network were established.

In the case of *ResPyr* campaigns, despite the relatively large displacements of the different loading models the effects seem negligible in terms of velocity, even in the case of the total load signal (ACN or TCN). Nevertheless, it can be far from negligible in certain cases. Two factors control the loading artifact signal induced in our case. The first one is the fact that we have a long time span (15 years) between the first and the last campaigns. In this case, the annual frequency of the loads is averaged out during this long time span. The second factor is the fact that all the campaigns were performed at the same epoch in the year (summer).

We tested different methods to estimate how ignoring loading could affect the tectonic velocity results in the case of campaign style GPS measurements for velocity determination. From our virtual campaign simulation analysis, we show that the amplitude and orientation of velocity signal induced by the loading phenomena change depending on which month the

5.6. CONCLUSIONS

data is acquired (even strong differences between two successive months) and on the time span between two consecutive campaigns. We conclude that the impact of the different loading effects is the smallest if the campaigns are carried out exactly at the same period of each year, e.g. in the middle of the summer. Finally, we conclude that the best scenario for observation seems to perform the GPS field campaign every 5 years in August. This choice balances finding a small amplitude loading effect with finding a reasonable period for field measurement. Indeed, nowadays it is essential to consider not only horizontal components but also the vertical ones in order to be able to study the 3D deformation of the mountain range. In this case, loading effects can be far larger compared to the expected signal. Thus, on the basis of our computations, we suggest that a new *ResPyr* campaign in August 2013 or 2014 is needed in order to be able to provide a precise velocity estimate and to minimize the loading artifact signals.

Concerning the *ResPyr* campaigns the last one was performed in 2010. Before the next remeasurement the sites will be modified to be adapted for the UNAVCO's equipments. These modifications would provide a more precise site re-occupation and will avoid antenna height errors. Strictly speaking there is no campaign site that was transformed to be a permanent station. However, within 5 – 8 m of the FAJP (Fanjaux) site a permanent station is installed [Rigo and Vernant 2014].

Jiang et al. [2013] assessed different environmental loading methods and their impacts on the GPS height time series and showed that the most important difference between models are 1) the different input environmental datasets; 2) the effect of interpolating global grids contrary to performing the global convolution at the site of interest; and 3) whether the atmosphere is corrected for topography or not. This reminds us that further conclusions require different datasets for each loading effects for our investigation. It is necessary in order to quantify the contribution of the various models and examine whether the differences between them are significant compared to the expected tectonic velocity rate or not. This question merits further investigation.

Chapter 6

Monitoring the impact of the Xynthia windstorm

The processed GPS coordinate time series represent the integrated observation of the signals from the different geophysical, environmental propagation, and instrumental effects. We assume that the latter effects are properly mitigated using standard models from the IERS Convention 2010 [Petit and Luzum 2010] or their remaining effects are well below the expected amplitude of the loading signal. Consequently, we can use GPS time series to investigate quick mass load variations and determine the associated ocean response. For this purpose we computed iPPP time series with the Géodésie par Intégrations Numériques Simultanées PC (GINS-PC) (CNES/GRGS) software. In a regional study we analysed the spatial and temporal evolution of various loading phenomena induced by an extreme weather event, the violent windstorm Xynthia.

6.1 Introduction

When computing the effect of non-tidal atmospheric, hydrologic or oceanic loading on geodetic coordinates, we have to take into account the mass load variation over the land and over the ocean. Also determine the response of the ocean to atmospheric pressure loading. A pure inverted barometer and a solid Earth ocean response to pressure loading define the extremes of the response. At periods longer than a few days, the inverted barometer response is sufficient [Wunsch and Stammer 1997]. However, how does the ocean respond to fast moving storms? See Section 1.1.2 in Chapter 1 for the different

effects and hypotheses. In this study we investigate the effect of a violent windstorm that progressed over Western Europe in the winter of 2010 on sub-daily GPS iPPP time series computed using the Réseau GPS Permanent (French Permanent GNSS Network) (RGP).

Xynthia was an extratropical cyclone that crossed France from the southwest to the northeast over the course of about 12 hours. A maximum pressure drop of ≈ 46 mbar was observed in the network and a storm surge of ≈ 1.5 m was measured at La Rochelle tide gauge [Bertin et al. 2012]. We study the uplift of the coastal and inland sites based on the comparison of the estimated 6-hourly stand-alone GPS iPPP time series (GINS-PC) with the predicted non-tidal loading time series. We use the models of the predicted displacements due to atmospheric loading assuming the inverse barometer (IB) and the no ocean cases as endpoints. We further analyze the dynamic ocean response to the atmosphere as a presumably realistic scenario. We also compare our iPPP results to pure non-tidal ocean loading models based on a regional dynamic ocean model and a general circulation ocean model. Then we attempt to use the GPS surface displacements, the atmospheric, and non-tidal ocean loading based on regional ocean model to identify the true ocean dynamics on the continental shelf during the passage of this fast moving system.

Since this extreme environmental event occurred after a wet season, we also examine the hydrological signatures during the studied period. The migrating low pressure system forces the Earth's crust to uplift, while the associated storm surge counters this motion, especially at coastal sites. Thus, it causes subsidence of the exposed region. Moreover, the continental water mass has the same effect (subsidence) as the ocean. For a period of two days the predicted loading effects in the direction of their expected vertical displacement¹ due to the atmospheric pressure reach up to 11.4, 13.5 and 18.0 mm for dynamic ocean, IB response and oceanless environment, respectively. Concerning the non-tidal ocean loading and the hydrology the models suggest a maximum displacement of -9.1 and -4.4 mm.

First, we present Xynthia to have an idea how huge was this storm event. We continue with the presentation of the GPS data and the processing parameters. Then, we show our subnetworks, the different spatial selections that we used in order to help the

¹Upward or downward motion depending on the effect.

data interpretation, and characterise the behaviour of coastal and inland sites. After, the different loading models are presented that we used for this analysis. We then review some loading model related issues, that are their space resolution, and the handling of $S1/S2$ atmospheric tides when we compare them to different GPS results. We review the differences between two GPS solutions, although we only present the loading model comparison with the one that has higher quality. After the RMS analysis of different time series, we show our experiment to track the spatial and temporal evolution of Xynthia using pure and *a posteriori* corrected GPS time series. Finally we close this chapter with our conclusions.

6.2 European windstorm Xynthia

European windstorms or extra-tropical cyclones are synoptic-scale (≈ 1000 km) low pressure systems, which grow in the presence of strong north-south temperature gradient and a strongly baroclinic atmosphere. From October to March, the North Atlantic Ocean satisfies the conditions required to form extra-tropical cyclones, which, in general, travel eastwards towards Europe. The eXtreme Wind Storms (XWS) catalogue contains information of the 50 most violent and extreme windstorms², which hit Europe in recent history, between October 1979 and March 2013 [Roberts et al. 2014; XWS-Datasets 2014]. We investigate the European windstorm Xynthia (listed in the XWS database) that progressed over Western Europe between the 27th of February and the 1st of March 2010. Figure 6.1 shows the spatial evolution of Xynthia over our studied network based on the approximated ground track data provided by Xavier Bertin (University of La Rochelle). The lowest surface pressures were ≈ 950 mbar at *SEES* GPS station which is ≈ 82 km far from the coast and was close to the storm's ground track. This absolute surface pressure corresponds to ≈ -44 mbar pressure change relative to the 10 year mean (2000-2009) of the MERRA dataset in the course of a few days. However all stations in the considered network³ had at least 20 mbar pressure drop. Both, the average and the RMS of the two day's minimum and maximum pressure differences were

²Fifty are selected out of 5730 identified storms [Roberts et al. 2014].

³It does not mean the whole RGP network, see later.

6.2. EUROPEAN WINDSTORM XYNTHIA

≈ 32 mbar at locations within 200 km range of the storm track and maximum 50 km far from the ocean. The same values over the network were ≈ 29 mbar. These waves clearly show that this low pressure system was quite extensive, and the entire network was exposed to rapid pressure changes. A two day long window five months after the storm (from a selected calm period) over the network shows only an average range in surface pressure that is less than 4 mbar⁴. Figure 6.2 shows an example of the atmospheric pressure variations at *LROC* station (La Rochelle) during two months that includes the storm and the calm period. We can see the spatial extension of Xynthia on a satellite image (Figure 6.3) and its temporal evolution on Figure 6.4 that shows four consecutive epoch of the storm.

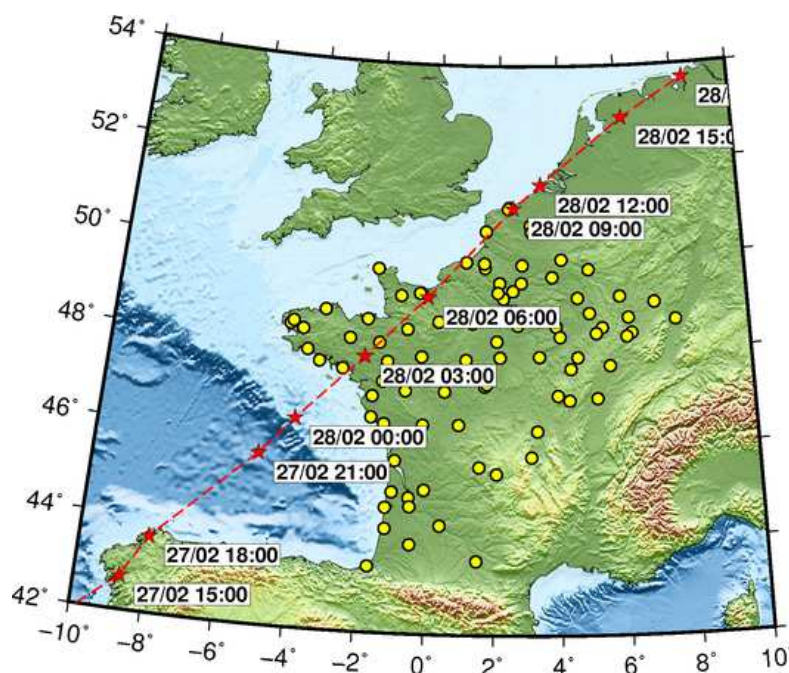


Figure 6.1 – The ground track of the center of the storm Xynthia is represented by the red dashed line and the red stars show its approximated instantaneous positions (estimated location of depression). The yellow circles represent all of our studied GPS stations from the RGP network. The ground track data of Xynthia is provided by Xavier Bertin.

⁴Although, surface pressure variations are always bigger in the winter.

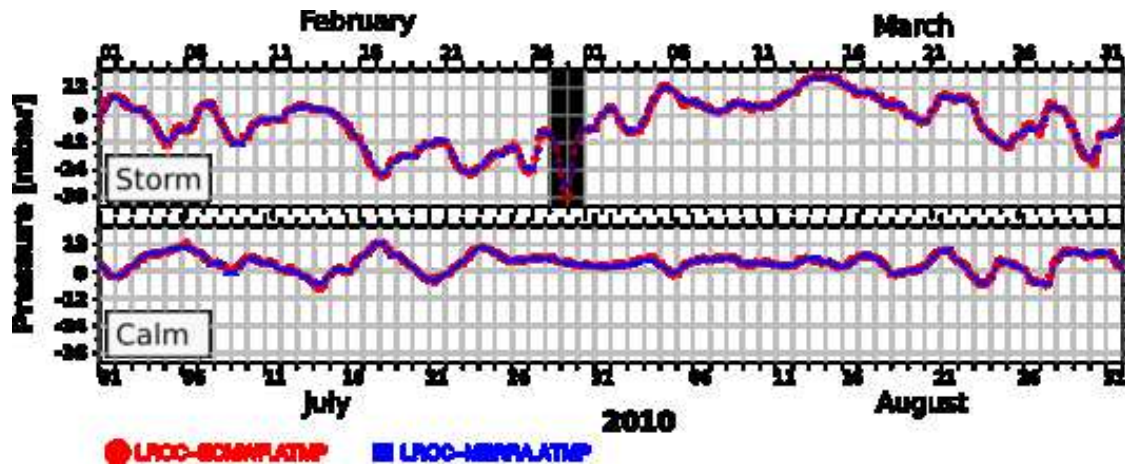


Figure 6.2 – Atmospheric pressure variations at *LROC* station from the ECMWF (red) and the MERRA (blue) datasets. The time series show the period during the storm in February and March 2010 (top) and during a calm period in July and August 2010 (bottom). The storm Xynthia is indicated with the gray rectangle.

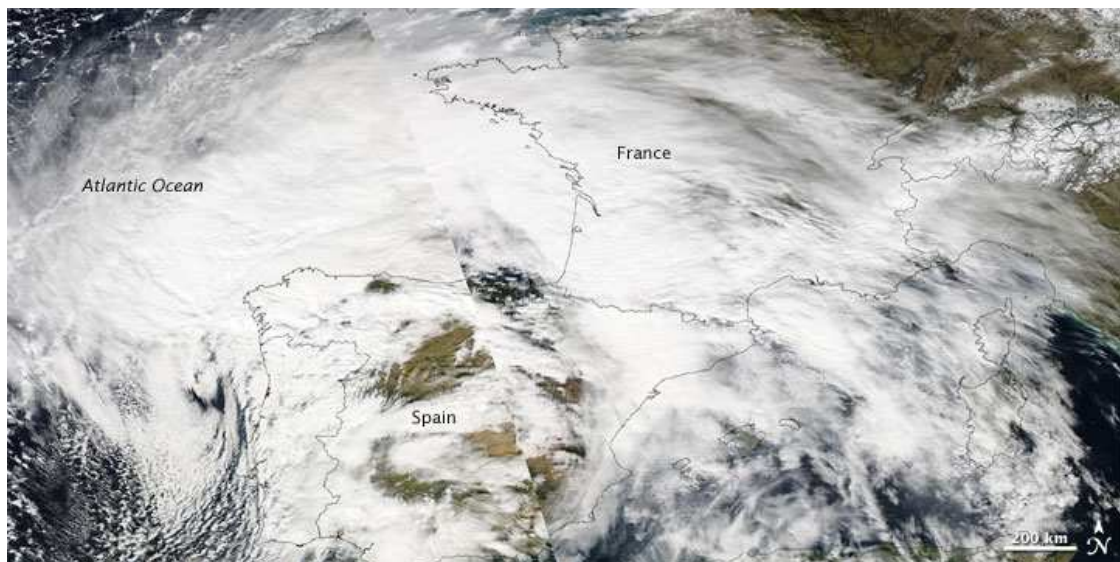


Figure 6.3 – Satellite image of Xynthia. Source: NASA.

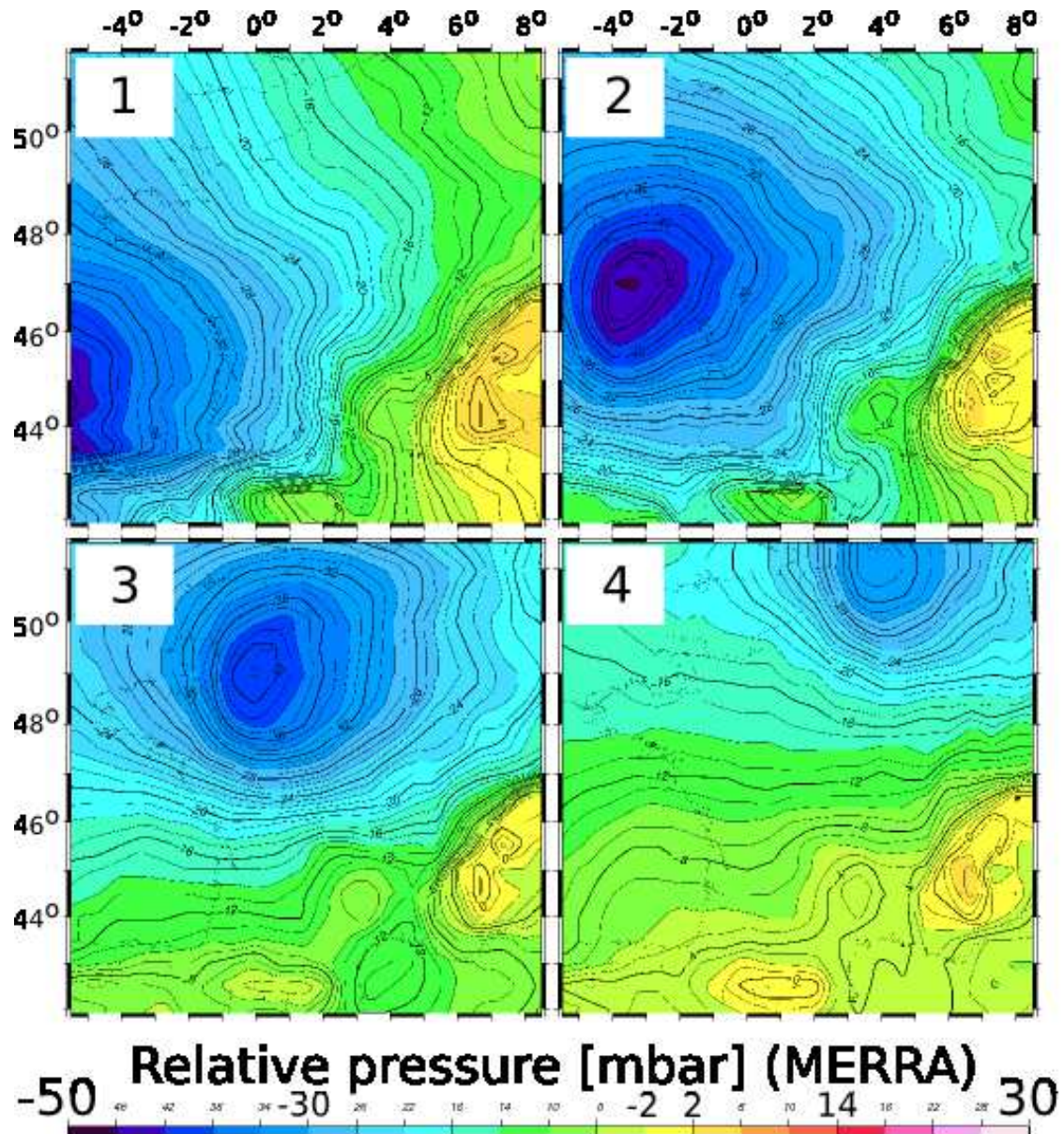


Figure 6.4 – Isobar maps of Xynthia based on the MERRA dataset. Four consecutive epochs at 1) 2010-02-27T18:00:00 (top left); 2) 2010-02-28T00:00:00 (top right); 3) 2010-02-28T06:00:00 (bottom left) and 4) 2010-02-28T12:00:00 (bottom right).

6.3 The GPS data

To estimate GPS positioning time series we used the GINS-PC⁵ software [Marty et al. 2012]. In particular, we took advantage of the software's integer ambiguity fixing capability at zero difference level [Laurichesse and Mercier 2007; Laurichesse et al. 2009; Fund et al. 2013], and thus its integer fixed ambiguity Precise Point Positioning (iPPP) mode. Observational data were collected from 94 stations of the RGP network from a two month period centered on the storm Xynthia (February and March 2010) and from a calm period including July and August 2010. Those stations were selected from the RGP network, which were within 400 km of the storm ground track. This reduced RGP network⁶ selection is due to a practical reason. That is, we were motivated to estimate the best achievable results using the latest GRGS orbit and clock products (See GR2 afterwards and in Chapter 7). However, these data products were lately available⁷ and we had to find a compromise between the desired data quantity and the necessary computational time (See Chapter 7). We removed observational files that covered less than 80 % of the observation periods. We applied and kept fixed the GRG (CNES-CLS AC legacy products) and the GR2 (CNES-CLS AC latest REPRO2 reprocessing products) final satellite orbit and clock products that serve as our reference frame. In particular, this means that the GRG⁸ results refer to the GRGS realisation of the ITRF2005 [Altamimi et al. 2007], meanwhile the GR2 estimates are related to the GRGS realisation of the ITRF2008 [Altamimi et al. 2011].

REPRO2 represents the second reanalysis endeavour of the IGS analysis centers. It is the reprocessing of the full GPS observation history since 1994 by each ACs using the latest models and methodology⁹. Due to this effort, the CNES-CLS AC has derived its own newly reprocessed orbit and clock products (GR2)¹⁰ using consistent background models over the time of the reanalysis.

⁵http://hpiers.obspm.fr/combinaison/documentation/articles/GINS_Marty.pdf

⁶Instead of nearly 200 operating stations at Xynthia's time.

⁷Available for GINS-PC IHM users from 19th of May 2014.

⁸For the GRG products the igs05.atx and ITRF2005 were used until GPS week 1632, 17th April 2011.

⁹More information is available at <http://acc.igs.org/reprocess2.html>

¹⁰Provided by CNES-CLS AC on the 19th of May 2014.

During the parameter estimation, we used the GRGS standards, thus their implementations of the IERS Conventions 2010 were applied. This means that we have accounted for the solid Earth tide, pole tide and ocean tidal loading (FES2012) [Carrère et al. 2012] displacement effects as well as for phase windup and absolute antenna phase center corrections.

IPPP users have to consistently use with the parameters that were used to generate the orbit and clock products [Kouba 2009; Petit and Luzum 2010; Fu et al. 2012b; Perosanz 2013]. Therefore, we have applied the ocean tidal loading corrections in the corresponding reference frames, that is in the CF frame for the GRG and in the CM frame for the GR2 orbit and clock products. Likewise, we did not apply atmospheric tidal loading corrections together with the GRG products and we accounted for the $S1/S2$ atmospheric tides based on Ray and Ponte [2003] when we used the GR2 data.

We note here that for the GRG products the FES2004 [Lyard et al. 2006] model based ocean tidal loading corrections were used. However, Fu et al. [2012b] showed that the choice of frame for ocean tidal loading computations is more significant than the choice of the ocean tide model. Therefore we used the latest model based on FES2012 for position determination together with the GRG products to minimise the differences between the processing parameters for our two scenarios.

Positions were estimated every 6 hours using the Global Mapping Function (GMF) together with the Global Pressure Temperature (GPT) for tropospheric delay parameters and a 10° elevation cutoff angle. Since the Xynthia event was a dynamic atmospheric perturbation, we chose a higher sampling rate for the tropospheric delay estimations than for the positions. Therefore the zenithal total delays (ZTD) were estimated hourly while horizontal tropospheric gradients were estimated every 12 hours. We compared different sub-daily sampling interval using the mentioned processing parameters in GINS-PC for certain stations and for the same period. Based on the obtained results and the noise level (higher at higher sampling rate) we decided to use the 6 hour interval. The median of the overall ambiguity fixing rate was greater than 97 %. A linear trend in the positions was determined over the two months data and was removed from the time series. Values were considered as outliers when they were outside five times the standard deviation [Geng et al.

6.3. THE GPS DATA

2012] and were removed from the resulting coordinate residuals. Table 6.1 summarises the processing parameters applied to obtain our GPS position time series. Figures 6.5 and 6.6 show the estimated residual time series for LROC (La Rochelle) and STJ9 (Strasbourg) stations using GRG and GR2 products. There is no significant differences between the formal errors of the GRG and GR2 based time series. The mean RMS of the formal error in our network is 1 mm for the horizontal and 5.1 mm for the vertical components when we used the GR2 products. The jumps in the east and north components of GRG time series are probably attributed to the GRG orbit and clock products. The jumps can reach ≈ 10 mm. See Chapter 7 and its Section 7.1 for the differences between the GRG and GR2 based time series.

Table 6.1 – Processing parameters applied during our GPS position time series estimation.

PROCESSING PARAMETERS	GRG	GR2
Data	zero differenced L3 ionospheric free combination	
Ambiguity fixing	Fixed in about more than 97 %	
Position estimates	Every 6 hours	
Orbit and clocks	GRG	GR2
Reference frame	ITRF2005 Altamimi et al. [2007]	ITRF2008 Altamimi et al. [2011]
Receiver and satellite antenna phase center correction	igs05.atx	igs08.atx
Elevation cutoff	10°	
Ionosphere refraction	2 nd order corrections using IGS TEC and igrf2011 magnetic field model	
Troposphere refraction	GPT/GMF Boehm et al. [2006]	
ZTD estimates together with positions	Every hour and gradients every 12 hours	
Solid Earth tide	IERS Conventions 2010	
Pole tide	IERS Conventions 2010	
Ocean tidal loading	FES2012 (CE)	FES2012 (CM)
Atmospheric tidal loading	not applied	S1/S2 Ray and Ponte [2003]
Non-tidal atmospheric loading	not applied	
Non-tidal hydrology loading	not applied	
Non-tidal ocean loading	not applied	

6.3. THE GPS DATA

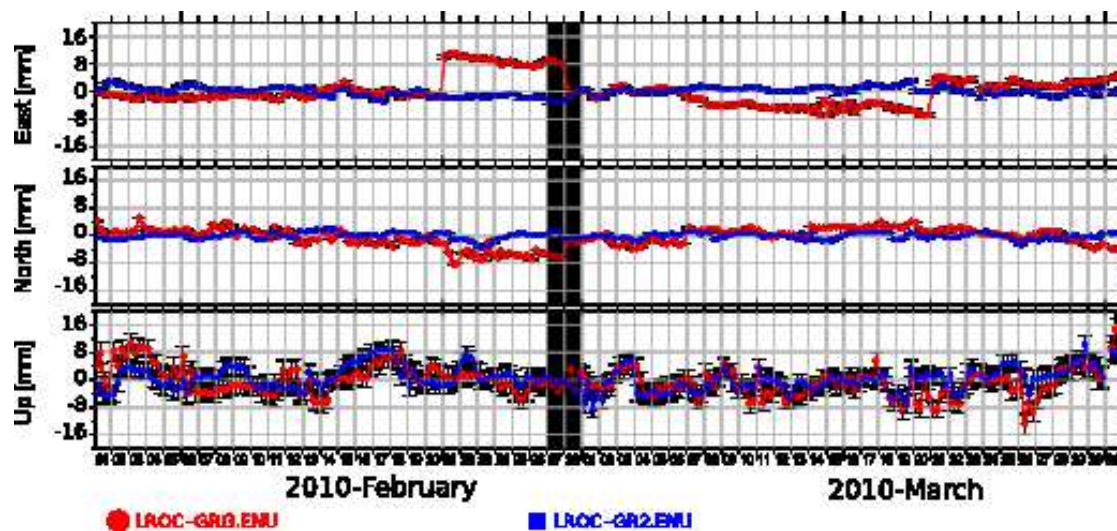


Figure 6.5 – GRG and GR2 iPPP time series at *LROC* (La Rochelle) station for two months centered on Xynthia storm. The storm Xynthia is indicated with the grey rectangle. LROC is the closest station to the storm ground track.

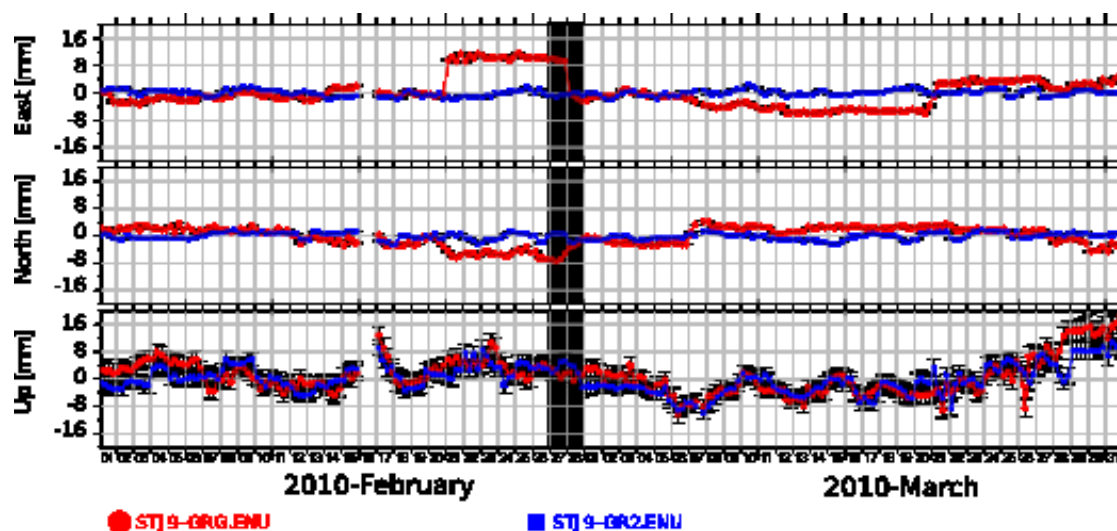


Figure 6.6 – GRG and GR2 iPPP time series at *STJ9* (Strasbourg) station for two months centered on Xynthia storm. The storm Xynthia is indicated with the grey rectangle. STJ9 is the farthest station from the storm ground track.

6.4 The spatial window

Due to the relatively late disponibility of the GR2 products we had to find an accord between the desired data quantity and the necessary computational time. Therefore, we compare the loading models and GPS over a restrained network. We remark here, that we only present the analysis using REPRO2 products of CNES-CLS AC, that is GR2. In order to better interpret the behaviour of coastal and inland sites we performed a spatial analysis. For this, we defined different sets of stations. Figure 6.7 shows the different subnetworks used for our analysis. The different labels used refer to our selections are: all, all coastal, all inland, nearby, nearby coastal and nearby inland. These are as follows: all the processes stations (all), stations with < 50 km coastal distance (all coastal, AC), stations with more than 50 km coastal distance (all inland, AI), stations within 200 km from the storm ground track (nearby), nearby stations maximum 50 km far from the coast (nearby coastal, NC) and nearby stations with more than 50 km coastal range (nearby inland, NI).

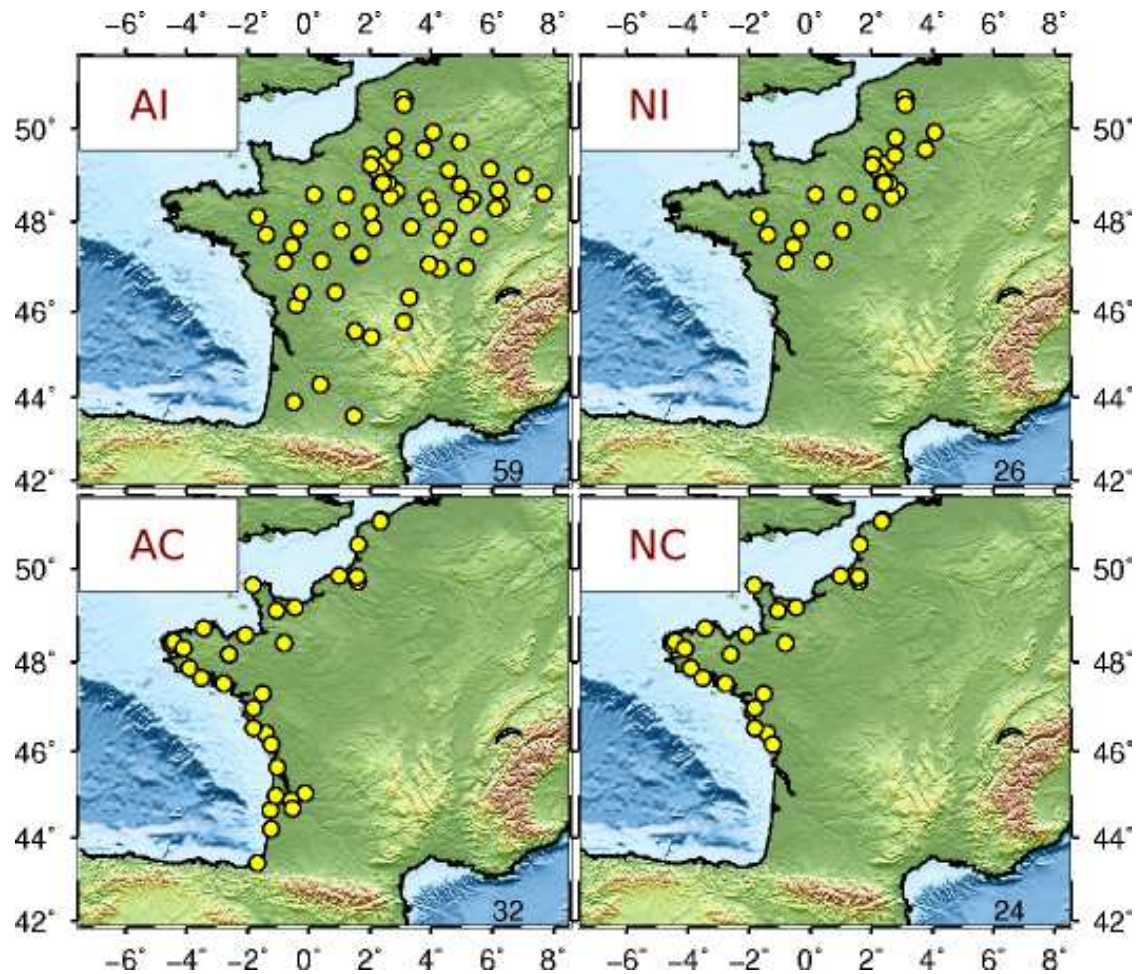


Figure 6.7 – Selection of the stations: all inland [AI] (top left), nearby inland [NI] (top right), all coastal [AC] (bottom left) and nearby coastal [NC] sites (bottom right). The "all" and the "nearby" labels signify whether our whole selection within 400 km was considered or only stations within 200 km range of the storm ground track. The numbers in the bottom left corners indicate the number of stations.

6.5 Applied models of the non-tidal loading effects

To estimate the site displacements induced by non-tidal loading effects we have to deal with the pressure changes occurring in the atmospheric or oceanic systems. The 3-dimensional surface displacement time series are estimated by convolving one of the global surface mass load grids with Farrel's Green functions. The method is detailed in [van Dam and Wahr 1998; Petrov and Boy 2004; Schuh et al. 2004; van Dam et al. 2012]. As our GINS-PC iPPP estimated time series are in the ITRF2005 or ITRF2008¹¹ and at seasonal and short time scales its origin is the centre of the Earth's figure (CF) [Dong et al. 2003; Blewitt 2003] we requested the loading induced displacement time series in the CF frame.

The station displacements due to the atmosphere are calculated based on global atmospheric pressure grids applying or not the inverse barometer hypothesis or taking into account a dynamic ocean or a general ocean circulation model. The pure non-tidal ocean loading models can be estimated using various ocean models. Several studies demonstrated that modelling the loading successfully improved the repeatability of daily or weekly GPS series to various extents [Zerbini et al. 2004; Williams and Penna 2011; van Dam et al. 2012]. These results suggest that the two loading models should be handled together to improve the GPS time series at coastal stations. Moreover Geng et al. [2012] highlighted that the sud-daily loading effects due to storm surges should be considered in GPS positioning.

Valty et al. [2013] assessed the precision of loading model estimates using geodetic techniques. They found that the precision of predicted vertical displacements based on global circulation models can reach up to 1 mm over Europe. Geng et al. [2012] investigated storm surge loading deformations around the southern North Sea. They propagated 10 cm sea level error into the predicted non-tidal loading displacement and found that the mean RMS was 0.5 mm for the vertical and 0.1 mm for the horizontal components what they recognised as the error of the predicted NTOL displacements. Since these studies were carried out at European locations we take their findings and consider that the error of our applied loading models are 1 mm for the vertical and around 0.1 mm for the horizontal

¹¹Depending on the used orbit and clock products GRG or GR2

components.

The following sections detail the models that were provided to us by other researchers. To be able to better understand the ocean response, for a specific loading effect, we have to deal with various models using different hypotheses. The labels used in the text are indicated in the corresponding paragraph titles.

6.5.1 Non-tidal atmospheric loading

ATML

The atmospheric pressure loading (ATML) estimated displacements are provided by Zhao Li and Tonie van Dam (University of Luxembourg). These series are determined using the 6-hourly $1/2^\circ$ in latitude and $2/3^\circ$ in longitude resolution grids of surface pressure from the Modern Era Retrospective analysis for Research and Applications (MERRA)¹² dataset. The inverse barometer (IB) hypothesis that is applied for the calculation of this effect considers that the ocean surface entirely adjusts itself to the atmospheric pressure variations¹³. In order to conserve oceanic mass, the hypothesis is slightly modified resulting in a uniform pressure acting over the ocean basins that is induced by a net change in the mass of air above the oceans [van Dam and Wahr 1987]. This assumption is valid for periods longer than 5-20 days. However, during fast moving storms when a rapid ocean response is expected, this assumption is may not be appropriate [van Dam and Wahr 1987; van Dam and Herring 1994; van Dam et al. 1994, 1997; van Dam and Wahr 1998; Wunsch and Stammer 1997; Petrov and Boy 2004; Mémin et al. 2014].

NOIB

We call the atmospheric loading effect estimated without any ocean response assumption¹⁴ to NOIB. These time series are also provided by Zhao Li and Tonie van Dam and they only differ from ATML in the applied ocean response hypothesis.

¹²MERRA DAS 3d analyzed state. Code name: `inst6_3d_ana_Nv`, MAI6NVANA

¹³1 mbar change in the atmospheric pressure causes 1 cm change in the ocean surface

¹⁴using an oceanless Earth model

ATMIB

The atmospheric pressure loading estimates named as ATMIB are provided by Jean-Paul Boy (École et Observatoire des Sciences de la Terre (EOST)). These time series also imply the inverse barometer hypothesis but these are generated applying the 3-hourly European Centre for Medium-Range Weather Forecasts (ECMWF) operational surface pressure dataset whose resolution has evolved through time so that now it is about 12.5 km [Boy 2014]. The ECMWF operational model has finer temporal and spatial resolution than the MERRA dataset, thus it maybe more suitable for a sub-daily atmospheric loading deformation study.

grd-ATMIB

Besides the provided point calculated ATMIB time series we have downloaded the global grids of the given model¹⁵ that we term grd-ATMIB. These global maps are estimated in similar way as their point calculated version, however we had to apply grid interpolation on the 0.5 resolution grids to extract the desired station time series.

ATMMO

The atmospheric loading using a dynamic ocean response to pressure (ATMMO) displacement time series are also provided by Jean-Paul Boy using the ECMWF surface pressure fields. Presumably this model is the most suitable to our study since the atmospheric loading displacements are estimated assuming a dynamic ocean response to winds and pressure forcing applying a 2 Dimensions Gravity Waves model (MOG2D) [Carrère and Lyard 2003]. For short periods, such as our study the MOG2D should significantly improve the atmospheric loading estimates compared to the widely applied IB hypothesis [Boy 2014].

¹⁵<http://loading.u-strasbg.fr/displa>, maintained by Jean-Paul Boy.

grd-ATMMO

Furthermore we also extracted the displacement time series for the desired GPS stations from their online available global grids¹⁵ that we call grd-ATMMO. However the time series obtained from the grid version are probably not optimal for this regional study because they can not reflect some of the short wavelength features of the loading field during the storm [Boy 2014].

Note that we also used the global displacement maps because the point calculated time series were not in our possession for the calm period.

6.5.2 Non-tidal ocean loading

NTOL

We call NTOL the non-tidal ocean loading deformation estimates that are based on the very high resolution regional barotropic, hydrodynamic ocean model of Xavier Bertin (See Bertin et al. [2012]). The model developed by Xavier Bertin (University of La Rochelle) is able to reproduce water levels during Xynthia (i.e. tide and storm surge) with a resolution of 25 m along the coast. However, due to time and computational limitations we have only requested water level data at a 0.3° (≈ 30 km) resolution. Zhao Li and Tonie van Dam provided us the displacement time series based on these water level estimates.

Bertin et al. [2012] developed a new storm surge modeling system based on the state-of-the-art circulation model SELFE¹⁶ [Zhang and Baptista 2008] and the spectral wave model WaveWatchIII [Tolman H. 2009]. Their modeling system is realised over the North-East Atlantic Ocean and provides tidal and wave predictions with only 3% and 15% errors. Their model well predicts the storm surge associated with Xynthia in the Bay of Biscay. They have observed only a slight underestimation of the surge peak by 3-8%. They used SELFE in a 2-dimensional horizontal barotropic mode. For a detailed description see Bertin et al. [2012].

¹⁶Semi-implicit Eulerian-Lagrangian finite-element model.

ECCO

We label our other non-tidal ocean loading model estimates after their input global dataset, thus Estimating the Circulation and Climate of the Ocean (ECCO). These predicted surface displacements are generated by Zhao Li and Tonie van Dam using the ECCO ocean bottom pressure (OBP) data. That is the byproduct of the baroclinic general ocean circulation model forced by winds, daily heat and air-sea fluxes. It has 12-hourly samples on a $1^\circ \times 1^\circ$ resolution grids above 10° of latitude, thus in our region.

6.5.3 Hydrological loading

The Xynthia storm caused flooding which might also induce loading. However, the flooding is caused by the storm surge and not precipitation, thus it is not captured by any hydrological model [Boy 2014; Breilh et al. 2013]. Moreover, if it would have any significant effect it would be detectable only in the close vicinity of the flooded area.

CWSL

The 3-dimensional displacements caused by continental water storage loading (CWSL) are generated using soil moisture and snow from MERRA-Land¹⁷ model by Zhao Li and Tonie van Dam. The MERRA-Land data provides us the hydrologic mass variations in 12° in latitude and 23° in longitude resolution grid with hourly sampling.

HYDRO

The other group of hydrological loading estimates that are calculated to our GPS stations are provided by Jean-Paul Boy using the Global Land Data Assimilation System GLDAS/Noah dataset. These 3-hourly grids (0.25° in longitude and latitude) provide estimates of snow water equivalent and soil moisture. We call these series HYDRO. We note that we also obtained the hydrological loading series from the 3-hourly, 0.5° resolution grids provided at the freely available loading service.

¹⁷MERRA-Land 2d land surface diagnostics. Code name: `tavg1_2d_mld_Nx`, `MST1NXMLD`.

6.5. APPLIED MODELS OF THE NON-TIDAL LOADING EFFECTS

6.5.4 Summary

Tables 6.2 and 6.3 list the models that are used in this study. The acronyms in Table 6.2 with an asterisk (*) superscript have also grid interpolated version.

Table 6.2 – The acronyms of the applied loading models.

Acronyms	Input dataset	Provided by
ATML	MERRA	Zhao Li, Tonie van Dam
ATMIB*	ECMWF	Jean-Paul Boy
ATMMO*	ECMWF+MOG2D	Jean-Paul Boy
NOIB	MERRA	Zhao Li, Tonie van Dam
NTOL	water level model of Xavier Bertin	Zhao Li, Tonie van Dam
ECCO	ECCO	Zhao Li, Tonie van Dam
CWSL	MERRA	Zhao Li, Tonie van Dam
HYDRO*	GLDAS-Noah	Jean-Paul Boy

Table 6.3 – The availability of the GPS and model datasets used in this study.

RAW DATA	TEMPORAL WINDOW			
	Storm		Calm	
	2 days	2 months	2 days	2 months
OBSERVATION				
GRG	x	x	x	x
GR2	x	x	x	x
ATMOSPHERE				
ATML	x	x	x	x
ATMIB	x	x		
grd-ATMIB	x	x	x	x
ATMMO	x	x		
grd-ATMMO	x	x	x	x
NOIB	x	x	x	x
OCEAN				
NTOL	x			
ECCO	x	x	x	x
HYDROLOGY				
CWSL	x	x	x	x
HYDRO	x	x		
grd-HYDRO	x	x	x	x

The atmospheric loading effect is suspected to be the dominant contributor to the loading displacement during this fast moving low pressure system. The atmospheric depression causes an uplift of the Earth's surface and expectedly the coastal stations have

individual behaviour due to the ocean's response to the atmospheric pressure changes. Namely the ocean responds differently than the solid Earth. The Xynthia induced storm surge is expected to generate a non-tidal ocean loading signal, which causes the subsidence of the effected region. Thus, these two effects compensate each other to some extent. Figure 6.8 gives an example of time series at two stations, at the site where the highest storm surge was measured (1.5 m) LROC (La Rochelle) and at the farthest station from the storm STJ9 (Strasbourg). On this figure we superimposed the GPS observations (GR2 IPPP result) and the predicted displacements for the different contributions of the vertical component. We also indicated the cumulated effect by adding the 3 models (ATML, NTOL, and CWSL) since GPS is sensitive to the total effect.

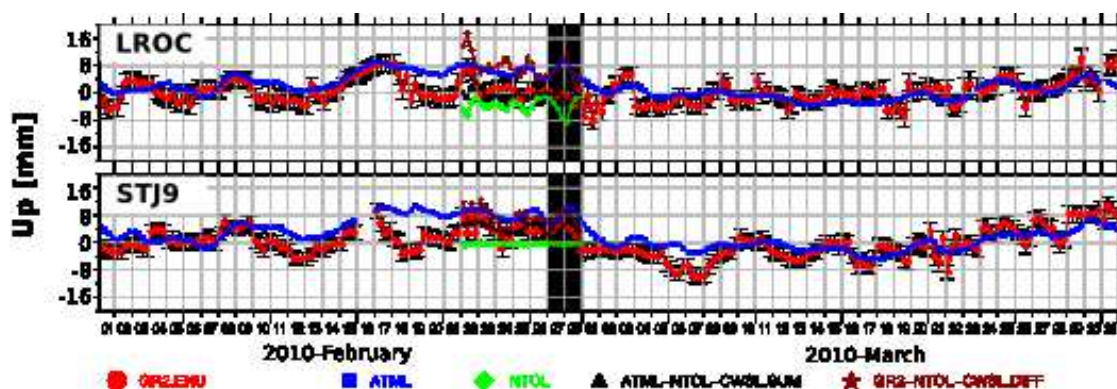


Figure 6.8 – GPS and model time series for two stations: LROC (top) and STJ9 (bottom), during two months centered on Xynthia. The storm Xynthia is indicated with the grey rectangle. The different colors are: GPS (red), ATML (blue), NTOL (green), sum of the models (black) and GPS *a posteriori* corrected with the sum of NTOL and CWSL (claret).

6.6 Small discussion on model space resolution

We would like to compare our GPS results to various models during two periods in 2010. However, we do not have all the point calculated loading models for our desired periods, that are two months centered on the storm Xynthia and two calm summer months. Thus, this section is dedicated to the comparison of the ATMIB, ATMMO, HYDRO and their corresponding grid derived displacement time series. We would like to see if the point calculated and the grid interpolated loading series are identical over a longer period or not.

6.6. SMALL DISCUSSION ON MODEL SPACE RESOLUTION

Thus, if we can use the grid versions in the place of the point calculated displacements for the summer months. Also we would like to know what can be the effect of the different resolution during a strongly perturbed period. Therefore we are interested in the differences between the point calculated and the grid interpolated loading time series.

Concerning the ATMIB point calculated and grid interpolated series the median RMS values for 2 days around the storm for the up component were 0.1, 0.7 and 0.1 mm for stations at least 50 km far from the coast, for stations with less than 50 km coastal range, and for all the stations, respectively. The same values during a two month period centered on the storm were 0.1, 0.5 and 0.1 mm for stations at least 50 km far from the coast, for stations with less than 50 km coastal range, and for all the stations, respectively. Table 6.4 and Figure 6.9 show the overall picture for the differences between the two versions of the ATMIB model during the 2 days and the 2 months period.

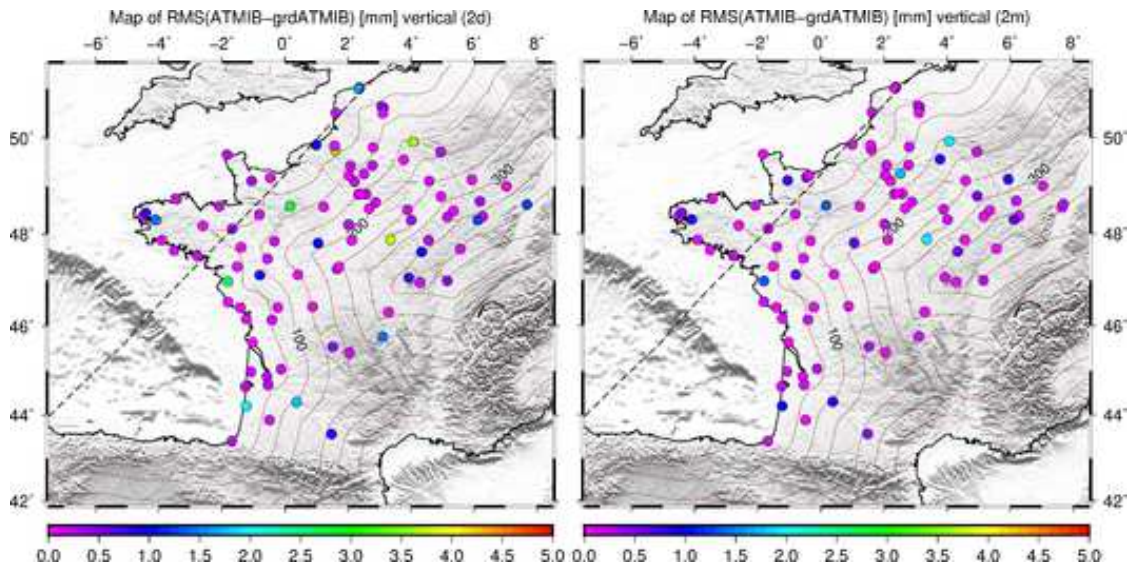


Figure 6.9 – RMS map of the differences between ATMIB and its grid interpolated version (grdATMIB) for two days (left) and for two months (right) around the storm event. The colored circles indicate the RMS values in [mm]. The brown contour lines represent the coastal distance at every 50 km. The black dashed line shows the approximated storm ground track (the trajectory of the estimated centers of the depression). Source of the ground track data: Bertin [2014].

Observing the differences between the two ATMMO time series we see slightly stronger differences. The median RMS values of the differences for the 2 days are as follows: 0.5, 1.2 and 0.6 mm for inland sites (≥ 50 km), for coastal stations (< 50 km) and for all the network correspondingly. The 2 months values are more moderate, they are 0.3, 0.7

6.6. SMALL DISCUSSION ON MODEL SPACE RESOLUTION

and 0.3 mm for inland, for coastal, and for the whole network. Table 6.4 and Figure 6.10 show the differences for the two ATMMO versions during two days and two months. The differences between the point calculated and the grid interpolated atmospheric loading mainly occur at coastal stations or sites near the storm track. They mainly reflect the short wavelength features of the storm that the grid versions are not able to properly capture during its passage.

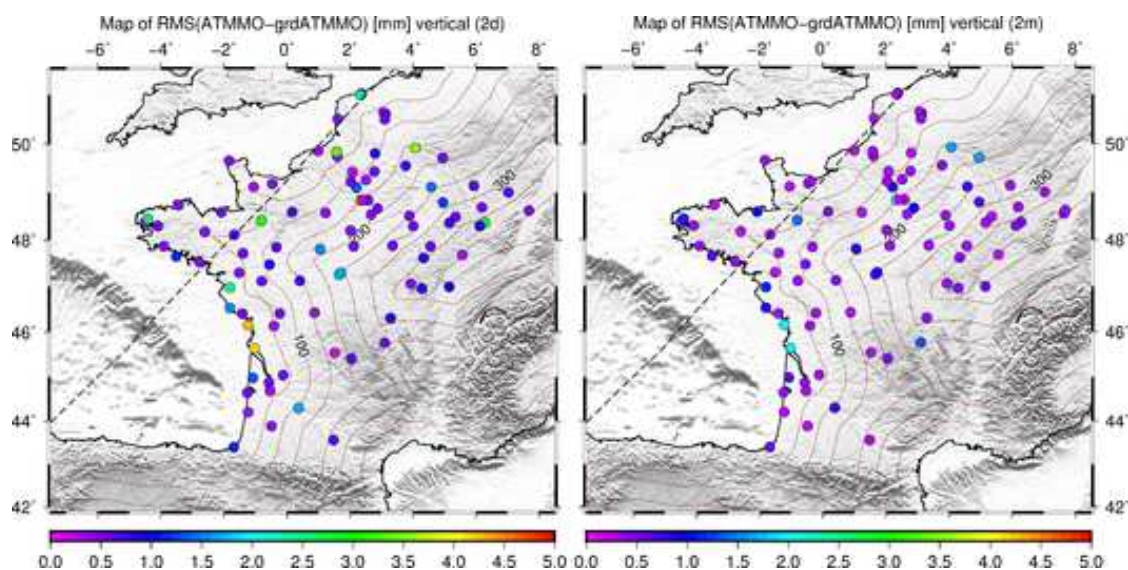


Figure 6.10 – RMS map of the differences between ATMMO and its grid interpolated version (grd-ATMMO) for two days (left) and for two months (right) around the storm event. The colored circles indicate the RMS values in [mm]. The brown contour lines represent the coastal distance at every 50 km. The black dashed line shows the approximated storm ground track (the trajectory of the estimated centers of the depression). Source of the ground track data: Bertin [2014].

The median RMS of the differences in the case of the HYDRO model and its grid interpolated series are under 0.4 mm in every case. Also, this value appears only at coastal sites. Table 6.4 and Figure 6.11 show the differences between the two HYDRO model versions.

We remark that we compared two datasets of the same loading phenomena during a fairly perturbed season. Nonetheless we have seen only small differences between the different resolution solutions that are mainly due to the storm event. During calm period differences would be negligible or identical. Consequently, we are able to use the grid derived series identical to the point calculated ones in comparison with our GPS results during calm environmental conditions.

6.6. SMALL DISCUSSION ON MODEL SPACE RESOLUTION

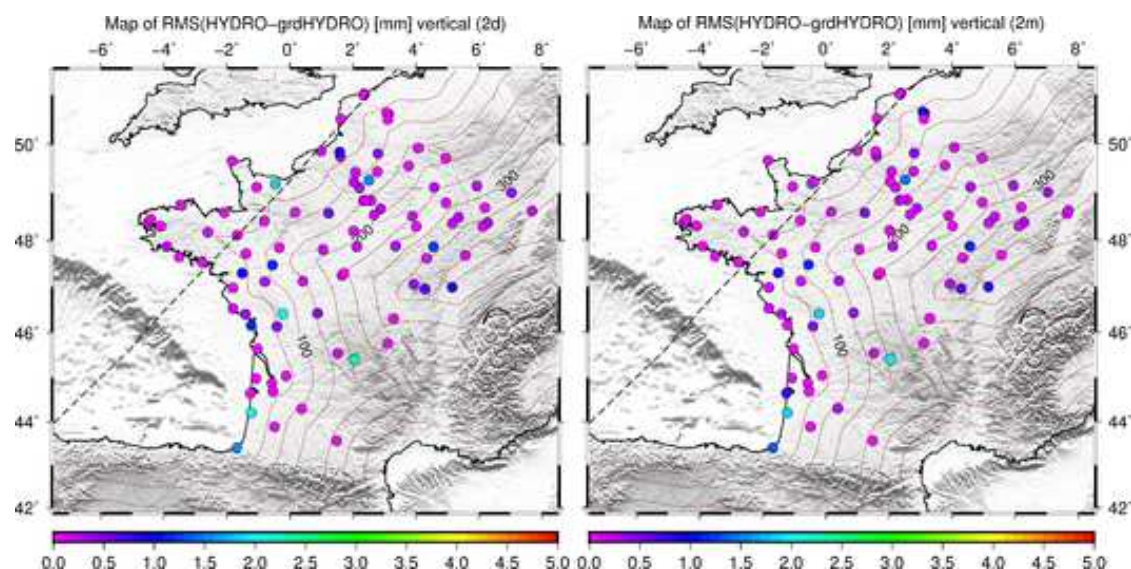


Figure 6.11 – RMS map of the differences between HYDRO and its grid interpolated version (grd-HYDRO) for two days (left) and for two months (right) around the storm event. The colored circles indicate the RMS values in [mm]. The brown contour lines represent the coastal distance at every 50 km. The black dashed line shows the approximated storm ground track (the trajectory of the estimated centers of the depression). Source of the ground track data: Bertin [2014].

Table 6.4 – The median RMS [mm] of the differences between the point calculated loading series and their appropriate grid version during their overlap period. That is two months centered on the Xynthia storm event. We remark that these values are before $S1$, $S2$ signal or trend removal. The "all" and the "nearby" descriptors signify whether the whole network was considered or only stations within 200 km range of the storm ground track. The *inland* and *coastal* keywords denote the coastal distances of the stations: ≥ 50 km, < 50 km, respectively.

		TEMPORAL WINDOW	
		2 days	2 months
ATMIB	all	0.1	0.1
	all-coastal	0.7	0.5
	all-inland	0.1	0.1
	nearby	0.2	0.1
	nearby-coastal	0.9	0.5
	nearby-inland	0.1	0.1
ATMMO	all	0.6	0.3
	all-coastal	1.2	0.7
	all-inland	0.5	0.3
	nearby	0.6	0.4
	nearby-coastal	1.5	0.8
	nearby-inland	0.5	0.3
HYDRO	all	0.1	0.1
	all-coastal	0.4	0.4
	all-inland	0.1	0.1
	nearby	0.2	0.2
	nearby-coastal	0.5	0.4
	nearby-inland	0.1	0.1

6.6.1 Few words on the S1 and S2 tidal atmospheric signal

The atmospheric loading models (ATML, (grd-)ATMIB, (grd-)ATMMO, NOIB) contain the diurnal ($S1$) and the semidiurnal ($S2$) tidal signals. Therefore they cannot be compared to the GR2 results directly, since these GPS solutions are already corrected for atmospheric tidal loading signals ($S1$ and $S2$). An error can arise if we have the same model for short and for long periods with an overlap and we attempt to remove the mentioned signals by a model fit (See equation 6.1).

Namely, the quality of the fit depends on the length of the input time series. It is our case, since we have the finer resolution, point calculated corrections only for two months period centered on Xynthia (February and March of 2010), while the grid version of the concerned models are available for all the year in 2010.

$$X(t) = a + b \times t + c \times \sin(\omega_{S1} \times t) + d \times \cos(\omega_{S1} \times t) + e \times \sin(\omega_{S2} \times t) + f \times \cos(\omega_{S2} \times t) \quad (6.1)$$

where $X(t)$ is our observation, a , b , c , d , e and f are coefficients of the model and ω_{S1} and ω_{S2} are the angular frequency of the $S1$ and $S2$ signals, respectively.

Thus, to avoid the aliasing of the short time series derived signals we have applied the coefficients determined from the long series to correct even the point calculated versions for trend, offset, $S1$ and $S2$ terms.

Figures 6.12 and 6.13 show the effect of the differences between ATMIB and grd-ATMIB after $S1$ and $S2$ correction, if the model (equation 6.1) is fitted separately to the almost identical, overlapping short and long time series. This result suggests to users who investigate atmospheric loading effects over short periods that they should pay attention to the applied coefficients when they aim to remove the intrinsic $S1$ $S2$ tidal signals from the predicted displacement time series.

We have looked at the differences between the two point calculated atmospheric loading series that apply the inverse barometer assumption (ATMIB and ATML). The differences between the series reflect their distinct grid resolution that is maybe important during the perturbed environmental conditions. The differences range from -0.3 mm to 3.5 mm. The median RMS of the differences is 1.2 mm for nearby coastal stations during two days of

6.6. SMALL DISCUSSION ON MODEL SPACE RESOLUTION

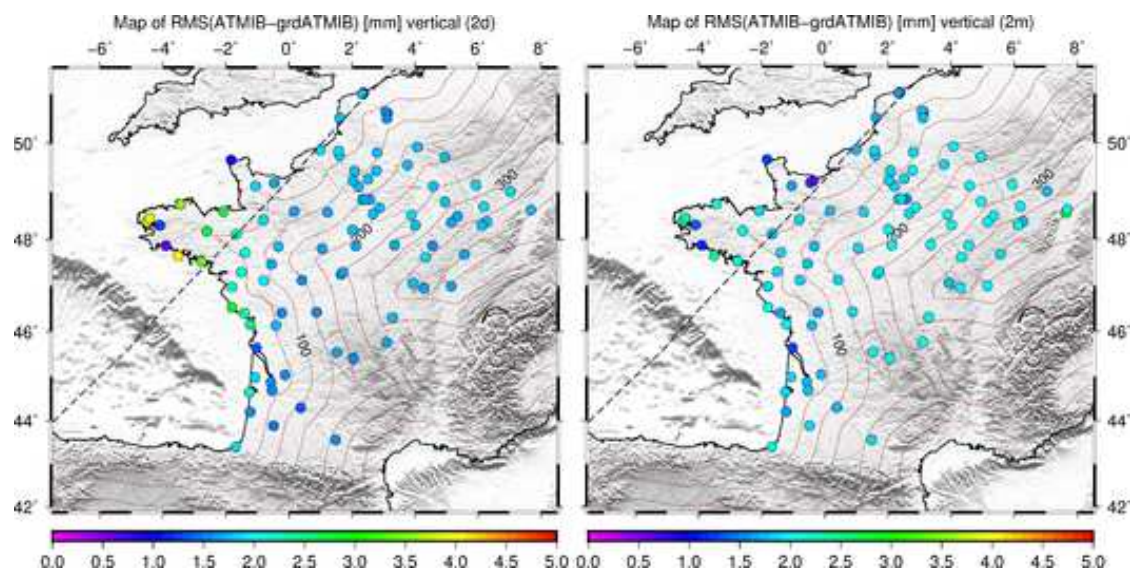


Figure 6.12 – RMS map of the differences (after separately determined and removed offset, trend, S1 and S2 periods) between ATMIB and its grid interpolated version (grd-ATMIB) for two days (left) and for two months (right) around the storm event. The colored circles indicate the RMS value in [mm]. The brown contour lines represent the coastal distance at every 50 km. The black dashed line shows the approximated storm ground track (the trajectory of the estimated centers of the depression).

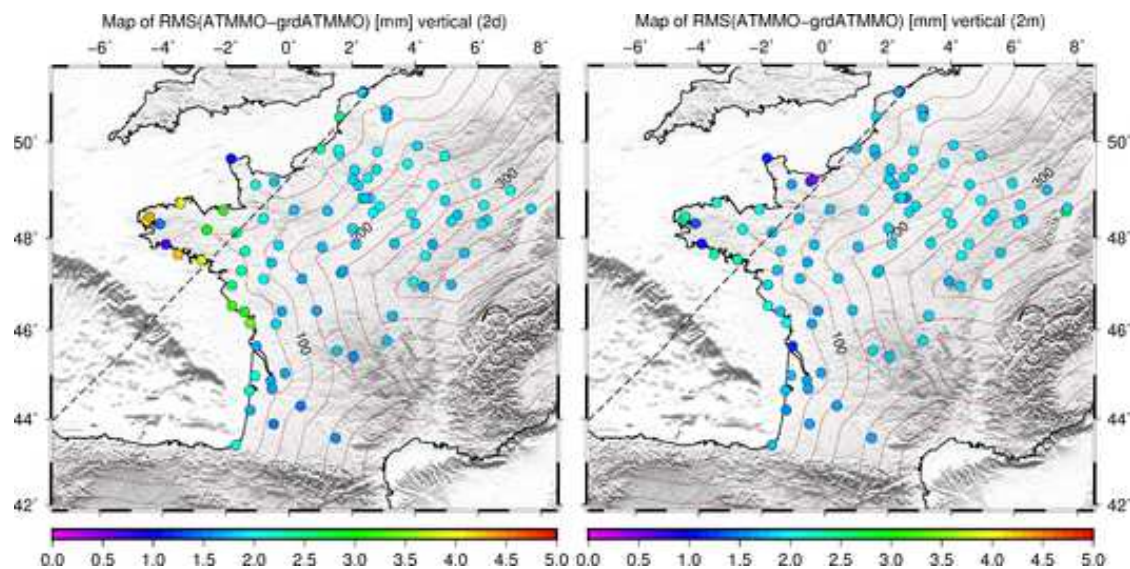


Figure 6.13 – RMS map of the differences (after separately determined and removed offset, trend, S1 and S2 periods) between ATMMO and its grid interpolated version (grd-ATMMO) for two days (left) and for two months (right) around the storm event. The colored circles indicate the RMS value in [mm]. The brown contour lines represent the coastal distance at every 50 km. The black dashed line shows the approximated storm ground track (the trajectory of the estimated centers of the depression).

the storm. Looking at the differences over a wider window (2 months), the median RMS is 0.8 mm for the same set of stations.

6.6.2 Few words on the hydrological signal

We investigate the hydrological effect also because our studied period was over a wet season. Figure 6.14 represents a humidity map over Europe (Soil Moisture and Ocean Salinity space mission/Centre d'Études Spatiales de la BIOSphère), when Xynthia was still over the continent, at the end of February 2010. We can also see on this figure how big volume of water was stored at the coastal and western part of France at the top level of soil. The slowly varying hydrological models suggest a maximum subsidence of -4.5 mm and -3 mm over the region for the two months by the CWSL and the HYDRO model correspondingly. The global median value is -3.4 mm for the CWSL and -1.8 mm for the HYDRO model. Concerning these values we think hydrological loading can add important signatures to the overall loading effects since they are $\approx 20\text{-}25\%$ of the atmospheric loading signal.

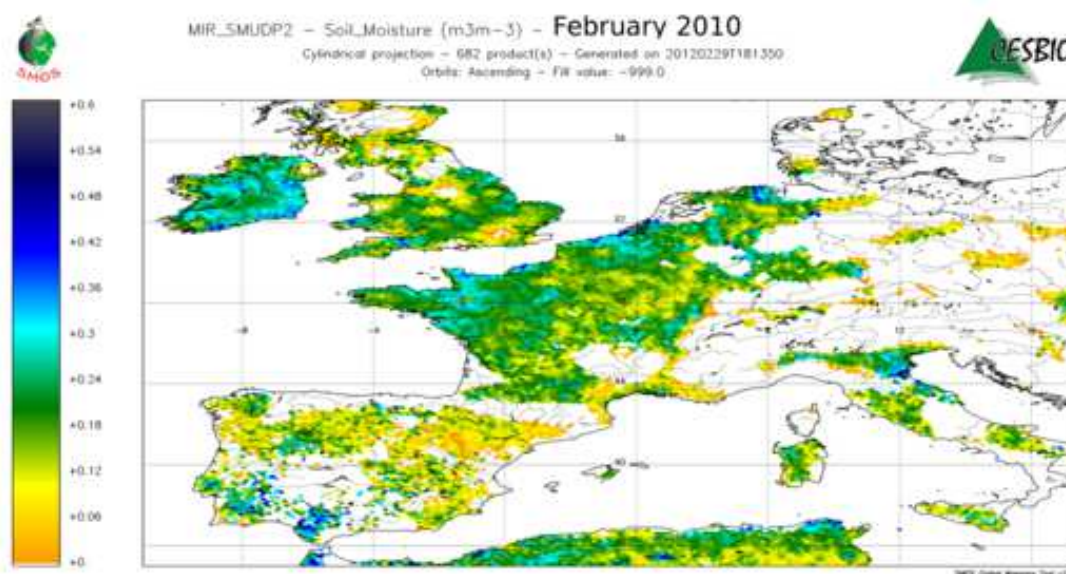


Figure 6.14 – Soil moisture map of Europe at the end of February 2010. Source: Soil Moisture and Ocean Salinity space mission/Centre d'Études Spatiales de la BIOSphère¹⁸.

We remark here that this aliasing is true for the determined trend and offset in the HYDRO series, thus we applied coefficients that were derived from the grd-HYDRO to

6.7. RESULTS

remove trend in the point calculated version. Figure 6.15 shows what is the effect on the differences between HYDRO and grd-HYDRO after removing a trend and an offset in the model (first two terms in equation 6.1) determined separately in the almost identical, overlapping short and long time series.

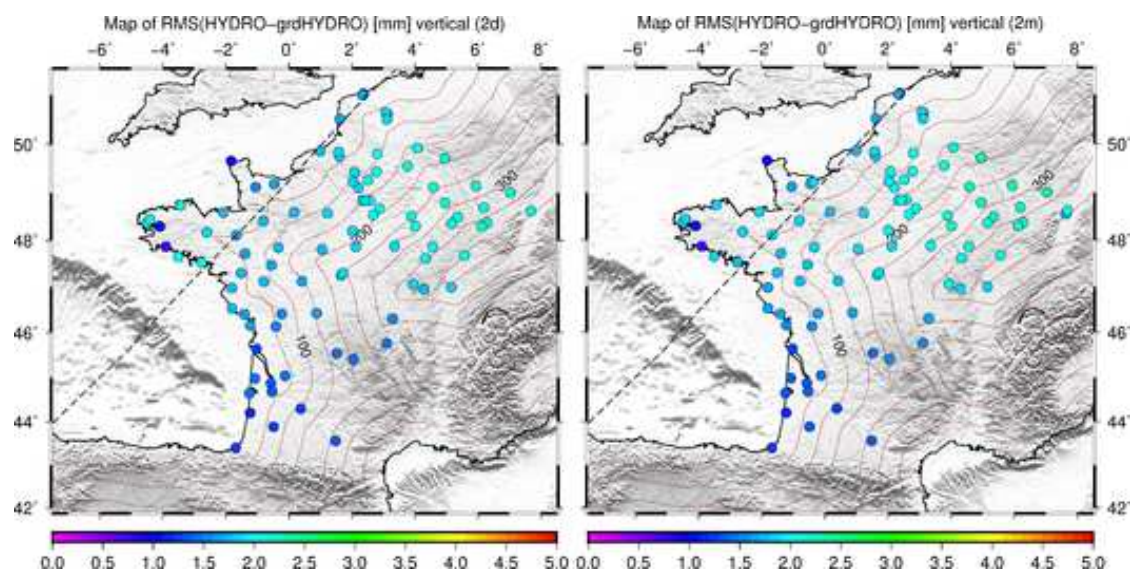


Figure 6.15 – RMS map of the differences (after separately determined and removed offset and trend) between HYDRO and its grid interpolated version (grd-HYDRO) for two days (left) and for two months (right) around the storm event. The colored circles indicate the RMS value in [mm]. The brown contour lines represent the coastal distance at every 50 km. The black dashed line shows the approximated storm ground track (the trajectory of the estimated centers of the depression).

6.7 Results

6.7.1 Comparison between GRG and GR2 GPS solutions

Before we go forward with the study we have to decide, which of our GPS solutions will we use. We have compared the two GPS solutions that are based on the *GRG* and the *GR2* products. The two months centered on the storm event for the *GRG* solutions show 5.2, 4.8 and 11.1 mm RMS over the network for the east, north and up components, respectively. Looking at the same period, the *GR2* solutions show marginal improvements of the positions that are represented by their RMS 2.5, 3.4 and 9.8 mm accordingly to the east, north and up components. We expected to see pronounced differences in the RMS

6.7. RESULTS

between the storm and a period without strong environmental perturbations. Nevertheless the values manifest only moderate changes, that are 3.5, 5.1 and 10.5 mm for the horizontal and vertical components based on the *GRG* series meanwhile 2.9, 3.4 and 9.1 mm based on the *GR2* series. The slightly smaller RMS of the horizontal components during the calm period can indicate the different environmental conditions, however it is not true for the vertical component since they are almost at the same level during the two periods.

We note that the statistical values presented in Tables 6.5 to 6.8 are derived from the raw GPS results, thus we did not apply any temporal or spatial filter over the time series.

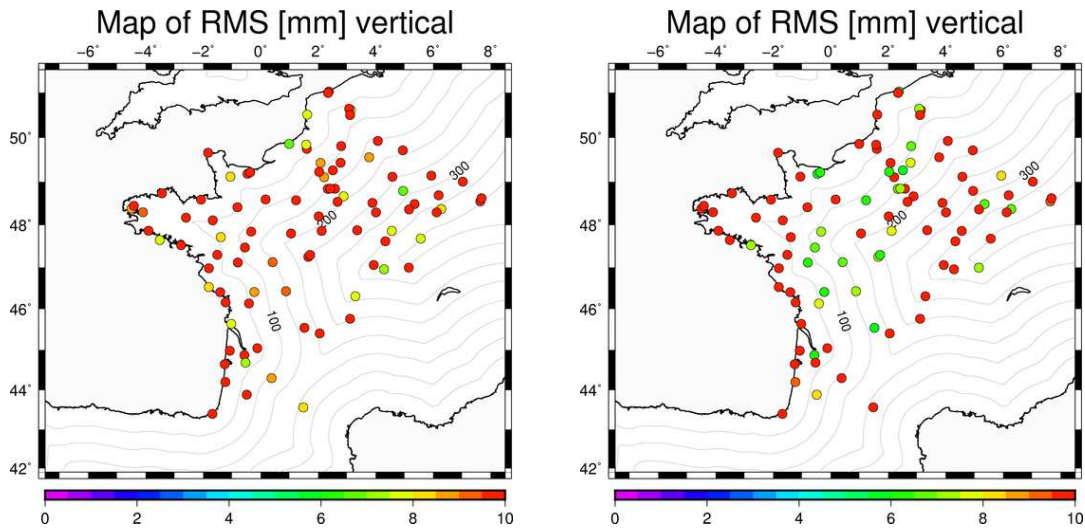


Figure 6.16 – RMS (in mm) of GRG (left) and GR2 (right) results for a two months period centered on the storm. The contour lines indicate the coastal distance in km.

Further, we have looked at the ratio of the RMS of the two GPS sub-daily solutions to study their stability, and we have seen that the *GR2* products improve the GPS time series to a slightly greater extent. However, these improvements are present without any specific geographic pattern. A ratio greater than 1 indicates that the *GRG* solutions have greater variations, thus the *GR2* results have smaller RMS in general. A value close to 1 shows that the two solutions are identical. A ratio less than 1 suggests that the results based on the *GR2* products are more scattered. These values are shown in Figure 6.18. In the case of the storm 65 stations had greater than 1 ratio while during the calm period 63 ratio were above 1. These values can be found in Table 6.8 (Storm, 2 months and Calm, 2 months columns for the up component). The average ratio over all the stations for the

6.7. RESULTS

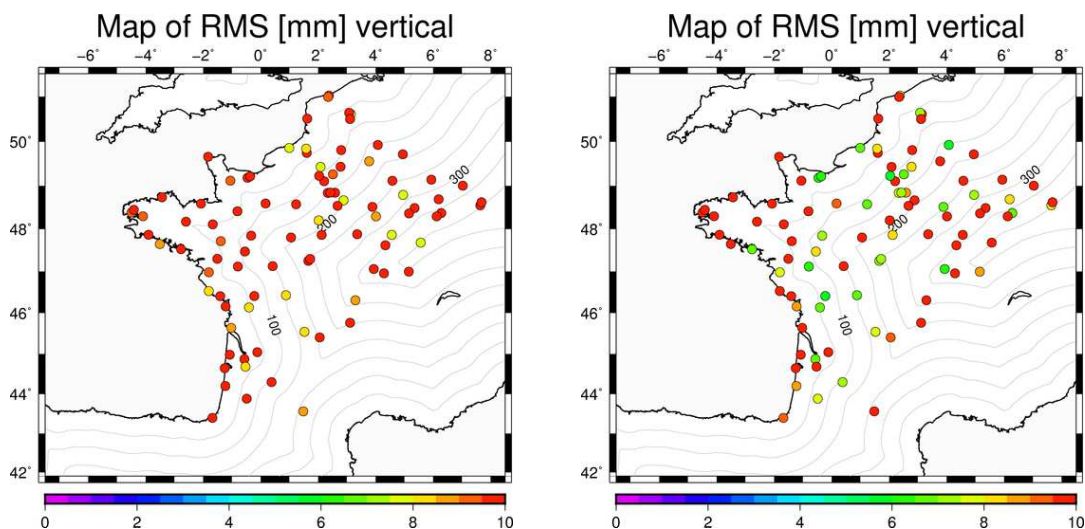


Figure 6.17 – RMS (in mm) of GRG (left) and GR2 (right) results for a two month long calm period. The contour lines indicate the coastal distance in km.

storm Xynthia is 1.3 while 1.5 for the calm period. Looking at these values and Figures 6.16 and 6.18 we can declare that the *GR2* products represent a general improvement in our GPS time series and they should be used in the following since they are based on the most recent conventions. The following tables (6.5 to 6.8) represent the statistical values for the

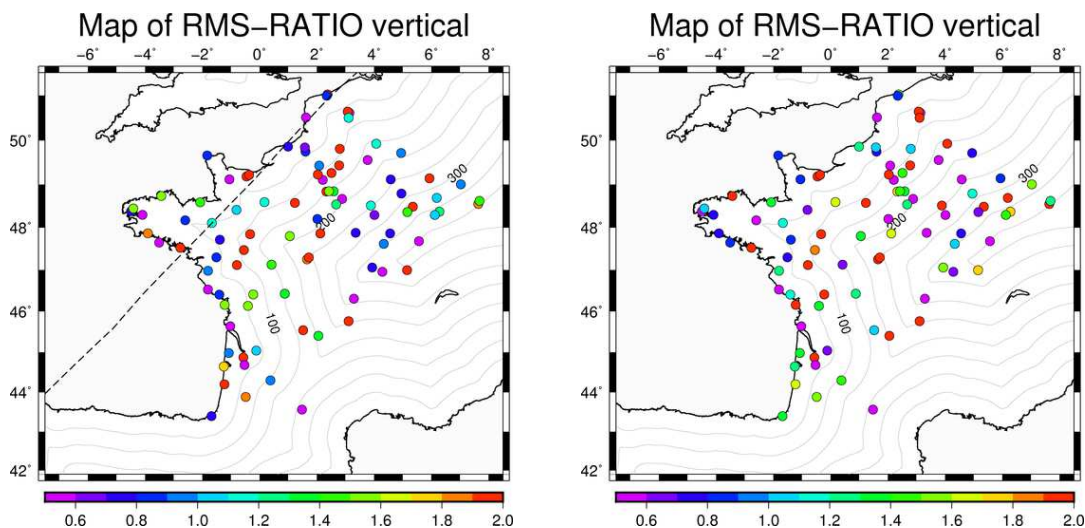


Figure 6.18 – Ratio of the RMS of the GRG and the GR2 solutions during the storm (left) and during the calm period (right). The dashed line indicates the storm ground track (the trajectory of the estimated centers of the depression). The contour lines indicate the coastal distance in km.

different spatial and temporal windows.

Table 6.5 – Descriptive statistics of the GRG results. The median values of the MIN, MAX, MED and RMS (in mm) are represented here for various spatial and temporal windows. The number indicated in square brackets indicates the number of GPS sites.

GRG		TEMPORAL WINDOW												
		Storm						Calm						
		2 days			2 months			2 days			2 months			
		e	n	u	e	n	u	e	n	u	e	n	u	
SPATIAL WINDOW	all [87]	MIN	-2.4	-9.7	-13.7	-11.3	-14.2	-32.1	-3.5	-0.3	-14.1	-10.9	-14.3	-29.8
		MAX	11.6	1.9	16.0	15.2	10.9	35.5	4.6	8.6	9.1	9.8	12.5	32.7
		MED	2.1	-3.9	2.1	-0.5	0.3	-0.5	-0.3	4.3	-4.0	0.0	0.1	-0.5
		RMS	6.9	5.5	10.5	5.2	4.8	11.1	2.8	5.0	9.0	3.5	5.1	10.5
	all coastal [30]	MIN	-2.4	-10.5	-15.3	-12.8	-14.8	-38.5	-4.0	-1.4	-15.4	-12.2	-14.8	-33.6
		MAX	12.6	3.0	16.3	17.3	13.0	37.8	5.6	8.8	11.2	10.3	14.0	37.0
		MED	3.0	-3.7	-0.2	-0.5	0.3	-0.3	-0.3	4.5	-3.7	0.1	0.0	-0.4
		RMS	6.9	5.7	10.8	5.3	5.3	12.0	3.3	5.0	9.9	3.8	5.6	11.4
	all inland [57]	MIN	-2.4	-9.4	-12.2	-10.4	-14.2	-30.4	-3.1	0.4	-13.6	-10.7	-14.3	-26.5
		MAX	11.4	1.5	15.9	14.8	10.6	32.7	4.5	8.2	8.8	9.7	12.0	30.9
		MED	2.1	-4.1	2.7	-0.5	0.3	-0.6	-0.3	4.3	-4.8	0.0	0.1	-0.5
		RMS	7.0	5.5	9.7	5.1	4.6	10.8	2.6	5.0	8.5	3.4	5.0	9.8
nearby [48]	MIN	-2.8	-9.2	-15.4	-11.0	-14.1	-31.4	-3.7	-0.3	-14.8	-11.0	-13.6	-27.4	
	MAX	11.5	2.3	16.5	15.2	10.7	34.9	4.6	8.8	9.1	9.6	12.7	32.8	
	MED	1.9	-3.5	0.1	-0.5	0.3	-0.3	-0.1	4.5	-3.7	0.0	0.1	-0.5	
	RMS	6.8	5.0	10.5	5.2	4.6	11.0	2.8	5.2	8.9	3.6	5.1	10.3	
nearby coastal [23]	MIN	-2.9	-10.6	-16.9	-13.0	-15.2	-38.8	-4.1	-1.7	-15.3	-12.1	-13.9	-33.1	
	MAX	11.6	3.1	15.1	16.6	13.3	37.2	5.5	9.6	11.2	10.7	14.0	34.1	
	MED	2.8	-3.7	-1.1	-0.5	0.3	-0.3	-0.4	4.6	-3.6	0.1	-0.1	-0.4	
	RMS	6.8	6.0	10.8	5.3	5.2	11.8	3.2	5.3	9.6	3.7	5.5	11.4	
nearby inland [25]	MIN	-2.7	-7.8	-10.3	-10.1	-13.2	-28.6	-3.3	0.9	-14.2	-10.5	-11.6	-25.2	
	MAX	11.3	1.5	19.4	14.5	9.8	31.9	4.2	8.6	8.7	9.1	12.3	30.9	
	MED	1.4	-3.0	2.1	-0.6	0.2	-0.6	0.0	4.3	-4.8	0.0	0.1	-0.5	
	RMS	6.6	4.3	9.8	4.9	3.8	10.8	2.6	5.2	8.3	3.3	4.6	9.1	

Table 6.6 – Descriptive statistics of the GR2 results. The median values of the MIN, MAX, MED and RMS (in mm) are represented here for various spatial and temporal windows.

GR2		TEMPORAL WINDOW											
		Storm						Calm					
		2 days			2 months			2 days			2 months		
		e	n	u	e	n	u	e	n	u	e	n	u
all [87]	MIN	-3.5	-5.0	-8.9	-7.5	-10.2	-29.7	-3.9	-3.5	-12.1	-8.2	-9.7	-27.9
	MAX	3.9	2.6	13.0	7.9	9.2	32.2	5.5	4.9	10.0	8.6	10.9	31.4
	MED	-0.6	-0.5	2.2	-0.1	-0.1	-0.4	0.5	0.3	-1.2	-0.1	-0.1	-0.0
	RMS	2.3	3.0	8.3	2.5	3.4	9.8	3.1	2.9	7.6	2.9	3.4	9.1
all coastal [30]	MIN	-4.3	-5.1	-11.2	-8.2	-11.7	-32.5	-4.4	-4.8	-12.8	-8.8	-12.6	-30.8
	MAX	4.2	3.5	14.1	9.4	10.9	33.7	6.6	6.3	11.5	9.5	12.7	34.8
	MED	-0.6	-0.6	0.9	0.0	-0.1	-0.3	0.4	0.3	-1.1	-0.2	-0.1	-0.1
	RMS	2.7	3.4	10.2	2.9	3.7	10.2	3.8	3.4	9.1	3.2	3.9	10.4
all inland [57]	MIN	-3.3	-4.9	-7.2	-7.1	-9.7	-28.4	-3.5	-3.2	-11.3	-8.2	-9.3	-26.3
	MAX	3.1	2.4	12.0	7.6	8.8	31.6	5.3	4.4	9.6	8.0	9.6	30.5
	MED	-0.6	-0.5	3.3	-0.1	-0.1	-0.5	0.5	0.3	-1.2	-0.1	-0.1	0.0
	RMS	2.2	2.9	7.7	2.4	3.1	9.5	3.0	2.8	7.2	2.8	2.9	8.9
nearby [48]	MIN	-3.6	-4.7	-9.9	-7.4	-9.5	-28.3	-3.7	-4.1	-11.7	-8.3	-9.6	-26.6
	MAX	3.1	3.3	12.2	7.8	9.1	30.5	5.8	5.6	9.6	8.7	11.3	31.5
	MED	-0.7	-0.4	1.1	-0.0	-0.0	-0.2	0.7	0.3	-1.0	-0.1	-0.1	-0.0
	RMS	2.3	3.0	8.0	2.5	3.3	9.7	3.2	3.3	7.5	3.0	3.6	9.1
nearby coastal [23]	MIN	-4.2	-5.2	-11.4	-8.2	-11.5	-32.0	-4.5	-5.0	-12.1	-9.7	-12.8	-29.4
	MAX	4.1	3.8	13.0	9.4	11.6	32.8	6.7	6.7	11.4	10.3	12.6	34.3
	MED	-0.7	-0.8	-0.2	0.0	-0.1	-0.2	0.4	0.4	-0.6	-0.2	-0.1	-0.1
	RMS	2.6	3.6	10.1	2.8	3.6	10.2	3.7	3.6	8.9	3.2	3.9	10.0
nearby inland [25]	MIN	-3.1	-3.7	-7.7	-6.2	-7.5	-25.2	-3.0	-3.2	-11.4	-8.2	-7.9	-25.0
	MAX	2.3	2.6	11.6	7.5	7.8	26.1	5.4	4.4	7.2	7.9	8.1	30.5
	MED	-0.6	-0.1	3.7	-0.1	-0.0	-0.2	0.7	-0.1	-1.2	-0.1	-0.1	0.0
	RMS	2.1	2.3	7.5	2.2	2.4	8.6	2.9	3.0	6.8	2.8	2.7	8.3

Table 6.7 – Descriptive statistics of the differences between *GRG* and *GR2* results. The median values of the MIN, MAX, MED and RMS (in mm) are represented here for various spatial and temporal windows.

GRG-GR2		TEMPORAL WINDOW											
		Storm						Calm					
		2 days			2 months			2 days			2 months		
		e	n	u	e	n	u	e	n	u	e	n	u
all [87]	MIN	-3.5	-8.7	-10.4	-8.8	-12.3	-19.8	-2.2	1.2	-7.0	-8.6	-10.0	-18.6
	MAX	12.5	2.7	10.4	14.2	7.8	17.1	1.4	6.3	2.8	6.1	9.4	25.9
	MED	1.8	-2.5	-1.3	-0.8	0.2	0.0	-0.8	3.5	-2.4	0.2	0.1	-0.6
	RMS	7.7	4.9	7.3	5.1	3.4	5.6	1.4	4.0	4.0	2.5	3.9	7.0
all coastal [30]	MIN	-3.5	-8.6	-9.1	-9.2	-12.2	-26.8	-2.5	0.9	-7.2	-9.2	-10.0	-23.0
	MAX	12.6	3.1	10.1	14.5	8.3	18.9	1.2	6.1	3.9	6.8	9.8	29.3
	MED	1.9	-2.6	-1.5	-0.9	0.1	0.1	-0.9	3.5	-2.3	0.2	0.1	-0.6
	RMS	7.9	4.7	6.7	5.2	3.4	6.2	1.5	3.9	3.9	2.6	4.0	7.4
all inland [57]	MIN	-3.5	-8.8	-10.6	-8.5	-12.4	-17.4	-2.1	1.6	-6.9	-8.6	-10.0	-18.1
	MAX	12.5	2.5	10.4	14.0	7.5	17.1	1.5	6.3	2.4	5.8	9.2	25.1
	MED	1.8	-2.5	-1.2	-0.8	0.2	-0.0	-0.7	3.5	-2.5	0.2	0.1	-0.6
	RMS	7.7	4.9	7.4	5.1	3.4	5.5	1.4	4.0	4.0	2.5	3.9	6.5
nearby [48]	MIN	-3.5	-8.5	-10.2	-8.8	-12.1	-19.6	-2.3	1.1	-6.8	-8.5	-9.6	-17.5
	MAX	12.5	2.8	10.5	14.1	7.5	16.6	1.3	6.4	2.9	6.1	9.5	26.6
	MED	1.8	-2.5	-1.8	-0.9	0.2	-0.0	-0.9	3.5	-2.4	0.2	0.1	-0.6
	RMS	7.7	4.7	7.2	5.1	3.3	5.6	1.4	4.0	4.0	2.5	3.9	6.9
nearby coastal [23]	MIN	-3.5	-8.5	-9.7	-9.1	-12.1	-31.5	-2.6	0.9	-6.8	-8.5	-10.0	-22.6
	MAX	12.6	3.0	9.6	14.5	8.1	17.5	1.3	6.5	3.9	6.8	10.0	28.4
	MED	1.8	-2.5	-1.6	-0.9	0.1	-0.1	-0.9	3.4	-2.4	0.2	0.1	-0.6
	RMS	7.8	4.6	6.6	5.2	3.4	6.3	1.5	3.9	3.9	2.6	4.0	7.2
nearby inland [25]	MIN	-3.5	-8.5	-10.3	-8.4	-12.0	-15.8	-2.2	1.6	-6.9	-8.5	-8.8	-16.7
	MAX	12.5	2.7	11.6	14.0	7.3	16.1	1.4	6.4	2.7	5.7	8.4	25.4
	MED	1.8	-2.4	-1.8	-0.8	0.2	-0.0	-0.8	3.5	-2.5	0.2	0.1	-0.6
	RMS	7.7	4.8	7.5	5.0	3.2	5.3	1.4	4.2	4.3	2.4	3.8	6.0

Table 6.8 – The occurrence of the values of the *GRG* and *GR2* RMS ratios compared to 1. The three values in each cells separated by a slash represent the occurrence of the ratio when greater than 1, equal to 1 and less than 1. The ratio 1 means that the GR2 results have better repeatability.

RMS(GRG)/RMS(GR2)		TEMPORAL WINDOW											
		Storm						Calm					
		2 days			2 months			2 days			2 months		
		e	n	u	e	n	u	e	n	u	e	n	u
SPATIAL WINDOW	all [87]	87/00/00	84/01/02	65/10/12	87/00/00	86/01/00	76/11/00	01/17/69	82/05/00	63/14/10	82/04/01	85/02/00	65/17/05
	all coastal [30]	30/00/00	29/01/00	21/05/04	30/00/00	29/01/00	26/04/00	01/05/24	28/02/00	17/09/04	27/02/01	28/02/00	22/05/03
	all inland [57]	57/00/00	55/00/02	44/05/08	57/00/00	57/00/00	50/07/00	00/12/45	54/03/00	46/05/06	55/02/00	57/00/00	43/12/02
	nearby [48]	48/00/00	45/01/02	38/04/06	48/00/00	47/01/00	43/05/00	00/10/38	44/04/00	36/07/05	46/01/01	46/02/00	37/09/02
	nearby coastal [23]	23/00/00	22/01/00	17/04/02	23/00/00	22/01/00	20/03/00	00/03/20	21/02/00	13/06/04	21/01/01	21/02/00	16/05/02
	nearby inland [25]	25/00/00	23/00/02	21/00/04	25/00/00	25/00/00	23/02/00	00/07/18	23/02/00	23/01/01	25/00/00	25/00/00	21/04/00

6.7.1.1 Issue when investigating periodic signals

Figure 6.19 shows the power spectral density plot of the stacked GRG and GR2 time series which also confirms the quality improvements in the GR2 series and our choice to apply them during our analysis. We remark here that the GRG orbit and clock products do not represent a homogeneous processing strategy, they developed continuously as newer models and standards were available. Meanwhile, the GR2 data are the latest reprocessing products of the CNES-CLS AC, which involves a homogeneous processing strategy with the best available models and standards. We note here that there were no epoch or station specific weights applied during the stacking, we simply took the median value of a particular epoch. The vertical dashed lines denote different period. Namely, the half (3.625 days) [GRG_PWh (blue)] and the full (7.25 days) [GRG_PWf (green)] GRGS GPS processing week and a period that was found by Ray et al. [2013] (3.66 days) [GRG_1 (red)]. We can remark that the spectra was improved in general (GRG vs. GR2), moreover the peaks around the period of the half GRGS processing weeks spectacularly reduced. Therefore we suspect about the jumps, maybe they are in relation with the peaks that were found by Ray et al. [2013] (See Chapter 4 and Figure 4.3 too). This will be discussed in Chapter 7.

6.7.2 Comparison of the GR2 results and the models

Although, we reviewed the differences between the GRG and GR2 time series, we only present the analysis with the most pertinent ones, the GR2 results, that implies homogeneous and stable processing strategy. Here, we show various outcomes that help to better understand the surface deformation processes generated by Xynthia. We start with the RMS analysis of the GPS, the different loading models and their combination. We also investigate the *a posteriori* corrected GPS time series with the different loading models. After we show the outcome of our spatial and temporal tracking experiment, which goal is to detect the horizontal and the vertical displacements generated by the violent windstorm. We show different maps of displacements at four epochs to study the influence of the various effects. Then we present figures which show the displacements at consecutive epochs for all the stations in the function of coastal distance to guide us in the spatial analysis.

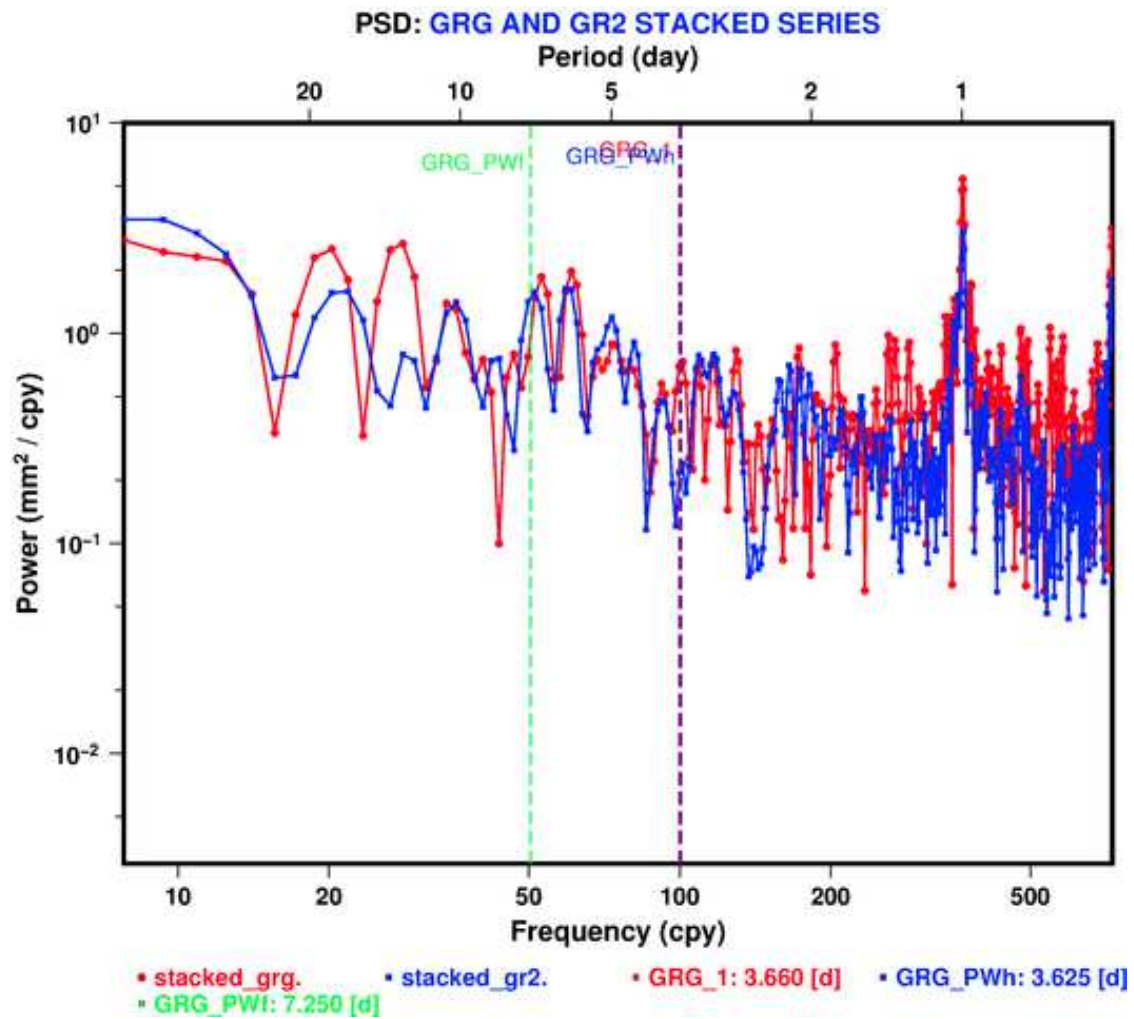


Figure 6.19 – The power spectral density of the stacked GRG (red) and GR2 (blue) time series. The vertical dashed lines represent the period of the full GRGS GPS processing week [7.25 days] (green), the half of this period [3.625 days] (blue) and the signal that was observed by Ray et al. [2013] [3.66 days] (red).

6.7.2.1 RMS analysis of the time series

The noise on the GPS time is too big to see the benefit of the point calculated displacement time series with respect to the grid interpolated values when we look at the correlations between the GR2 and the models. However, with respect to the GPS RMS improvement these differences are obvious (Table 6.10). The best RMS reduction (or the smallest degradation) corresponds to cases where we have applied atmospheric and dynamic ocean response corrections over the two days of the storm (8 records for each site). This indicates dynamic ocean response during the storm and IB hypothesis before and after the storm (RMS values over 2 months of time series). If we look the pure difference between two atmospheric models, one that took into account the IB hypothesis and an other with a dynamic ocean response, we see that this difference is insignificant compared to the GPS formal error (Table 6.9). However, this difference can be greatly pronounced and in the RMS analysis, we can see the advantage of using that atmospheric model which implies a dynamic ocean response. Therefore, based on the RMS analysis we suggest to use a dynamic ocean model together with the atmospheric loading to *a posteriori* correct GPS time series of short period. Table 6.9 also shows the difference between two atmospheric loading model that account for dynamic ocean, the main difference is their underlying atmospheric and oceanic models.

Table 6.9 – Atmospheric model differences compared to GPS formal error. The values corresponds to the median RMS (in mm) over the time series for different geographical selections: (ALL) all, (AI) all inland, (AC) all coastal, (NI) nearby inland, and (NC) nearby coastal sites. The numbers right to the labels represent the number of stations for a given spatial selection.

MED(RMS(x))	ALL [90]	AI [58]	AC [32]	NI [26]	NC [24]
ATML-ATMMO	2.0	1.8	2.3	1.8	2.2
(ATML+NTOL)-ATMMO	1.0	1.0	1.3	0.7	1.4
GPS formal error	4.7	4.5	5.2	3.8	5.1

6.7.2.2 The spatial and temporal tracking of Xynthia by GPS

Now we want to see if GPS allows to track spatially and temporally the crustal deformation induced by the storm pass. For this, we mapped our results at different epochs. Before we start looking at the different maps of the four epoch of the storm

6.7. RESULTS

Table 6.10 – Two days long GPS time series (8 records per site) a posteriori corrections using different models. The values correspond to the median RMS over the time series for different geographical selections: (ALL) all, (AI) all inland, (AC) all coastal, (NI) nearby inland, and (NC) nearby coastal sites. The numbers right to the labels represent the number of stations for a given spatial selection.

MED(RMS(x))	ALL [90]	AI [58]	AC [32]	NI [26]	NC [24]
GPS-ATML	9.5	9.0	10.5	9.0	11.3
GPS-ATMIB	9.1	8.3	10.1	8.2	10.7
GPS-ATMMO	8.8	8.0	9.9	7.5	10.5
GPS-NOIB	11.3	9.9	13.8	10.5	14.4
GPS-NTOL	9.0	8.6	9.7	8.6	9.3
GPS-ECCO	8.7	10.5	8.0	7.9	9.9
GPS-CWSL	10.2	10.0	10.4	10.0	9.6
GPS-HYDRO	9.1	9.0	10.1	9.0	8.8
GPS-(ATML+NTOL)	8.6	8.1	9.7	7.7	9.4
GPS	7.9	7.6	9.8	7.4	9.2
GPS formal error	4.7	4.5	5.2	3.8	5.1

Xynthia we show an example of what we expect to see for the horizontal maps. Figure 6.20 shows the expected horizontal displacements that inhered with the vertical movements (uplift or subsidence) associated to loading effect, e.g., over land or an oceanless environment. In the case of an uplift all the horizontal components go outside the center of the load source whereas in the case of subsidence all the horizontal components go towards the center of the load source. In the case of a storm like Xynthia which is a big depression we should be in the case where there is uplift at the center of the lower pressure system and thus we should expect horizontal movement towards the external part of the storm center.

6.7.2.2.1 Detection of the horizontal and vertical displacements

We have attempted to track the storm and the associated storm surge both horizontally and vertically. For this we created Figures 6.29 to 6.40. First, we applied a Gaussian filter to each time series¹⁹ (temporal filter) only for the graphical representation and not for

¹⁹5 Gaussian weights 0.0545, 0.2442, 0.4026, 0.2442, 0.0545 after Geng et al. [2012]. The features of the applied filter and weights (`filter1d`) approximate the behavior of a 24 hour wide moving average filter.

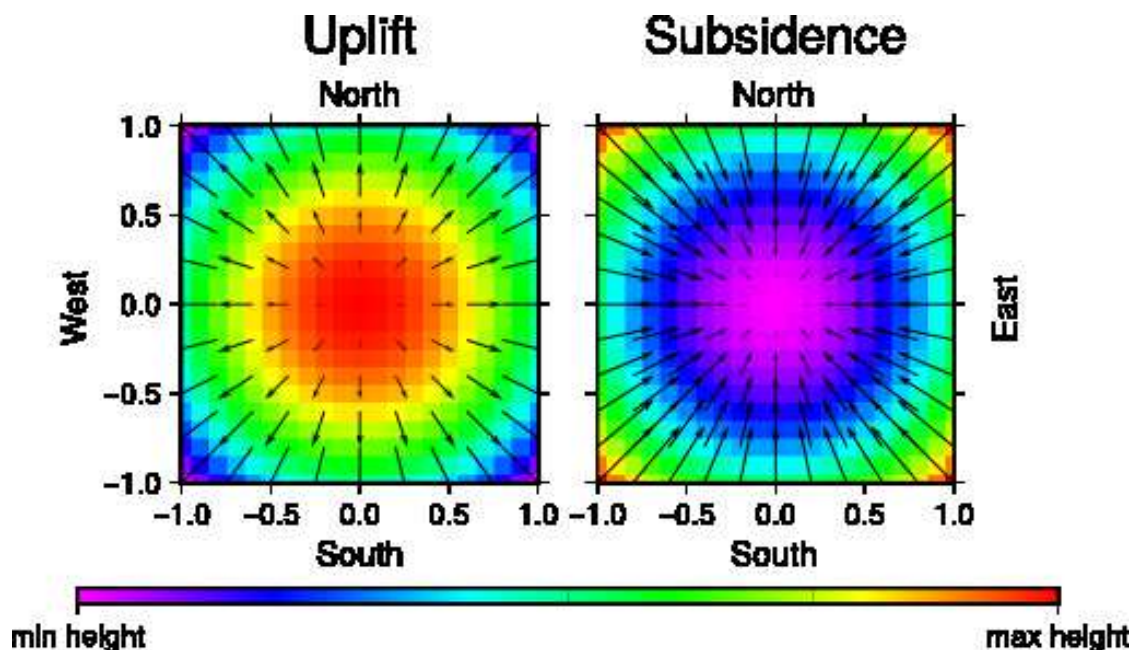


Figure 6.20 – Expected horizontal displacements associated to uplift (left) and subsidence (right). There is no unit, it is a relative scale. The length of the arrows represents the amplitude of the horizontal deformation and the orientation of the displacement. The color scale stands for the vertical amplitude.

the computation of the analysis parameters. Before we start looking at the different maps derived from *a posteriori* corrected GPS time series we show the maps of the temporal filtered GPS time series in Figures 6.21 to 6.24.

We can see on the previous maps (Figures 6.21 to 6.24), that it would be a challenging task to interpret the results in this way, where we only applied temporal filter. Therefore, we applied a spatial filter²⁰ over the available stations at the desired epoch to help our interpretation. We applied these steps to achieve better visibility on the maps and to rule out outliers that may appear at a certain epoch. Figures 6.25 to 6.28 show the maps of the spatially filtered GPS time series. However we still find ourself in front of a complex exercise.

²⁰We took the average value of the stations at a given epoch over a $2 \times 2^\circ$ sized block (`blockmean`) then we interpolated the grid of the averaged values onto station locations.

6.7. RESULTS

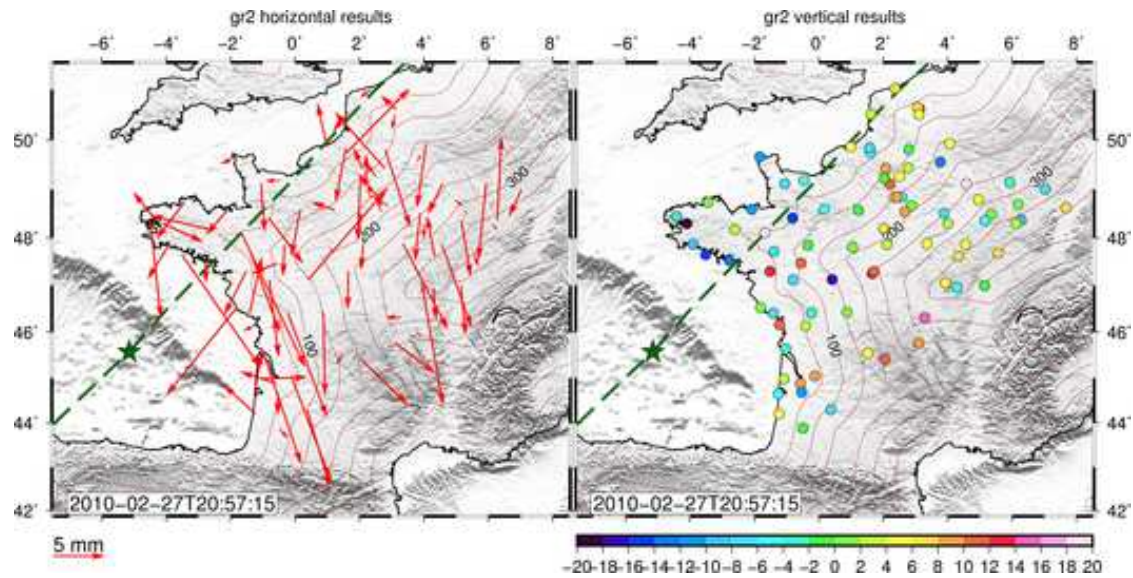


Figure 6.21 – Epoch 1: Horizontal and vertical GPS results (in mm) (without spatial filter). The green stars indicate the center of Xynthia (estimated location of depression) and the dashed line indicates the storm ground track. The contour lines represent the coastal distance at every 50 km.

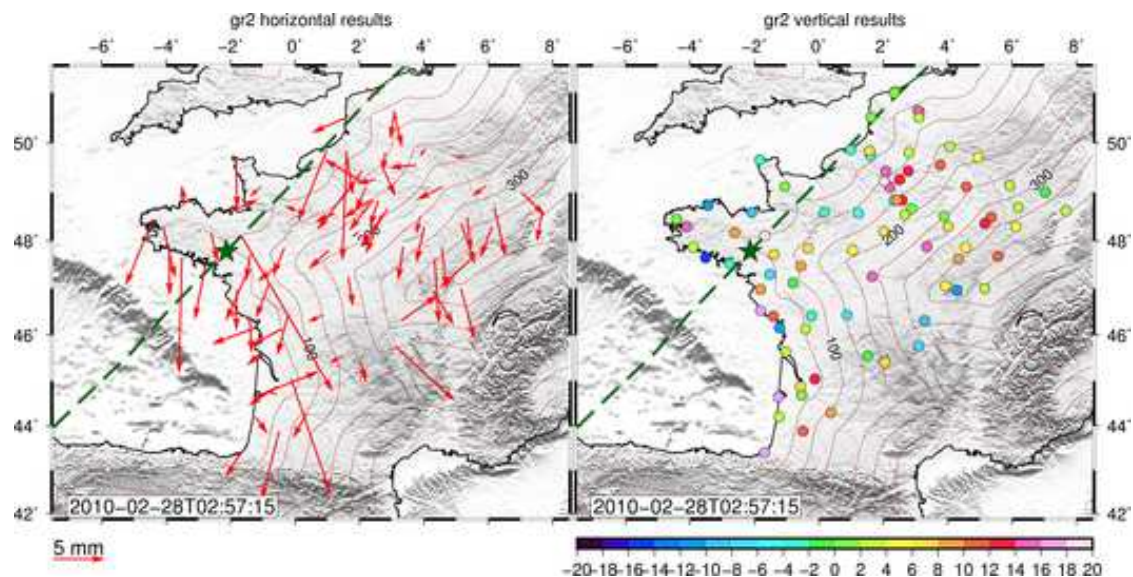


Figure 6.22 – Epoch 2: Horizontal and vertical GPS results (in mm) (without spatial filter). The green stars indicate the center of Xynthia (estimated location of depression) and the dashed line indicates the storm ground track. The contour lines represent the coastal distance at every 50 km.

6.7. RESULTS

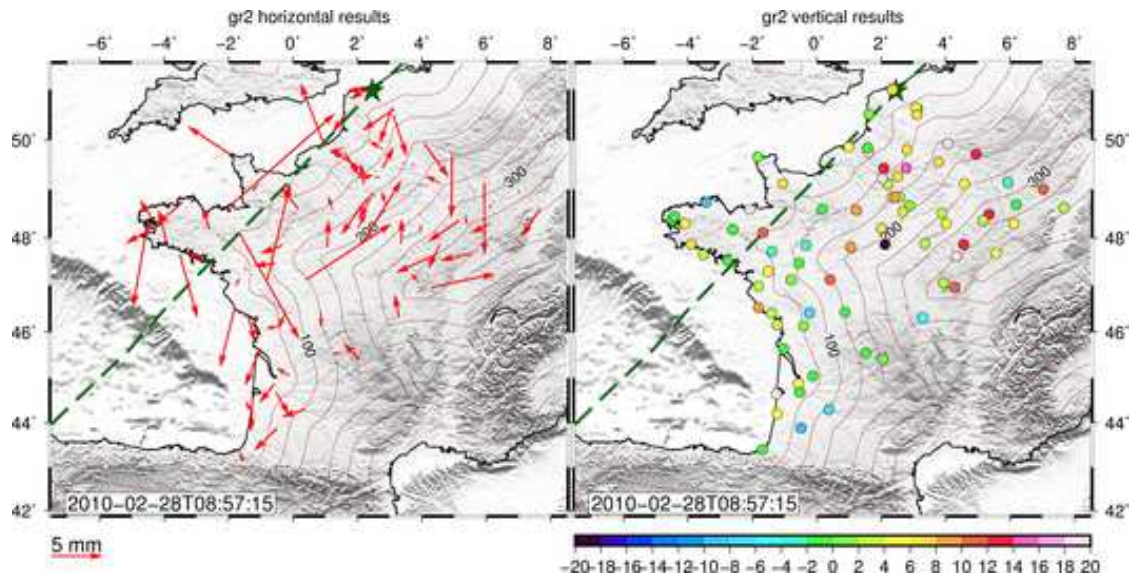


Figure 6.23 – Epoch 3: Horizontal and vertical GPS results (in mm) (without spatial filter). The green stars indicate the center of Xynthia (estimated location of depression) and the dashed line indicates the storm ground track. The contour lines represent the coastal distance at every 50 km.

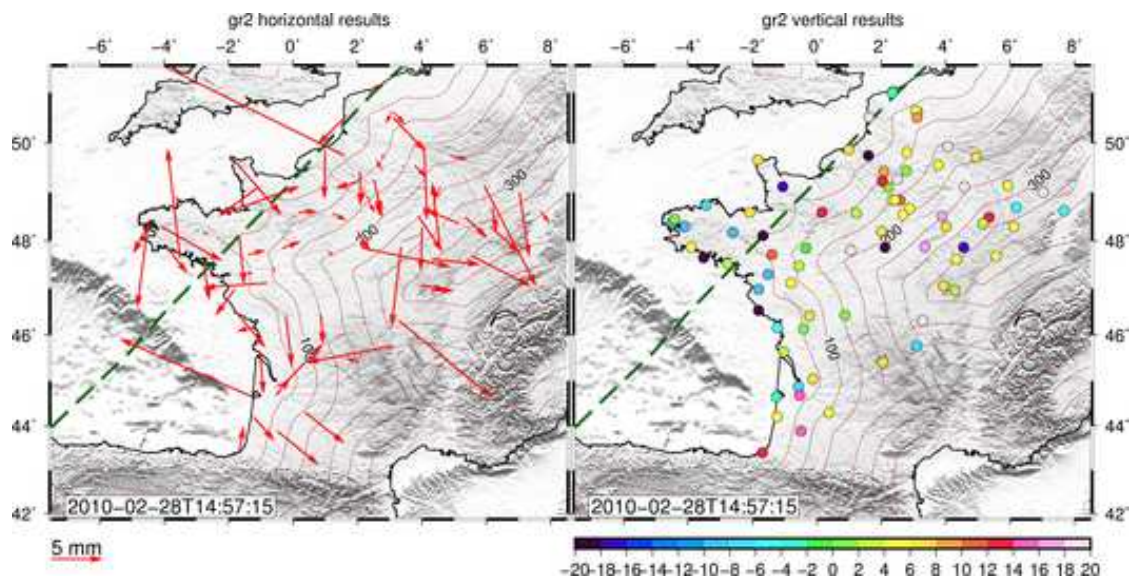


Figure 6.24 – Epoch 4: Horizontal and vertical GPS results (in mm) (without spatial filter). The green stars indicate the center of Xynthia (estimated location of depression) and the dashed line indicates the storm ground track. The contour lines represent the coastal distance at every 50 km.

6.7. RESULTS

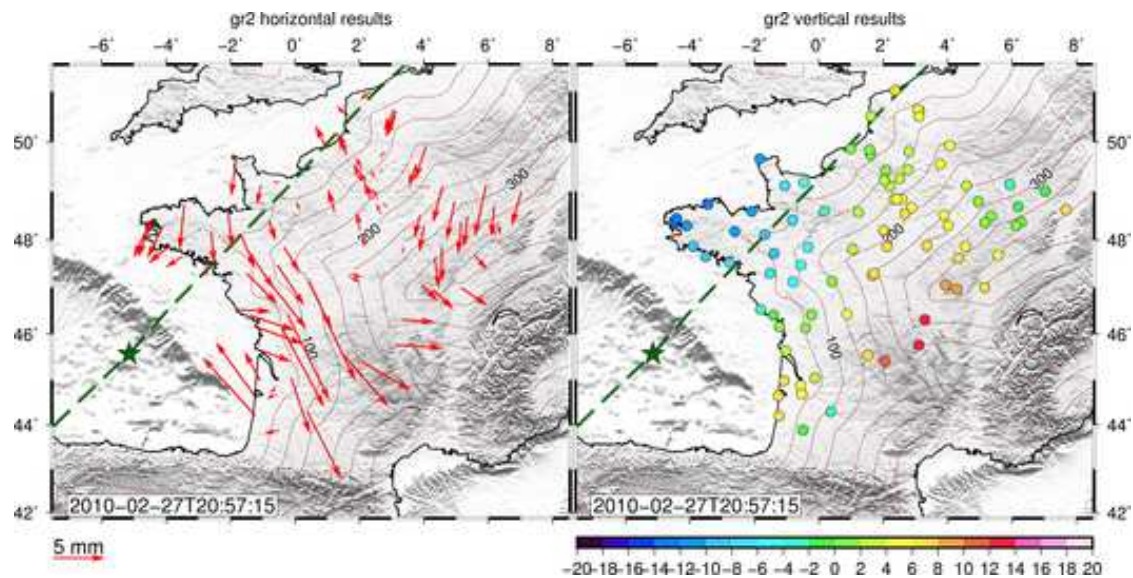


Figure 6.25 – Epoch 1: Horizontal and vertical GPS results (in mm) applying a spatial filter. The green stars indicate the center of Xynthia (estimated location of depression) and the dashed line indicates the storm ground track. The contour lines represent the coastal distance at every 50 km.

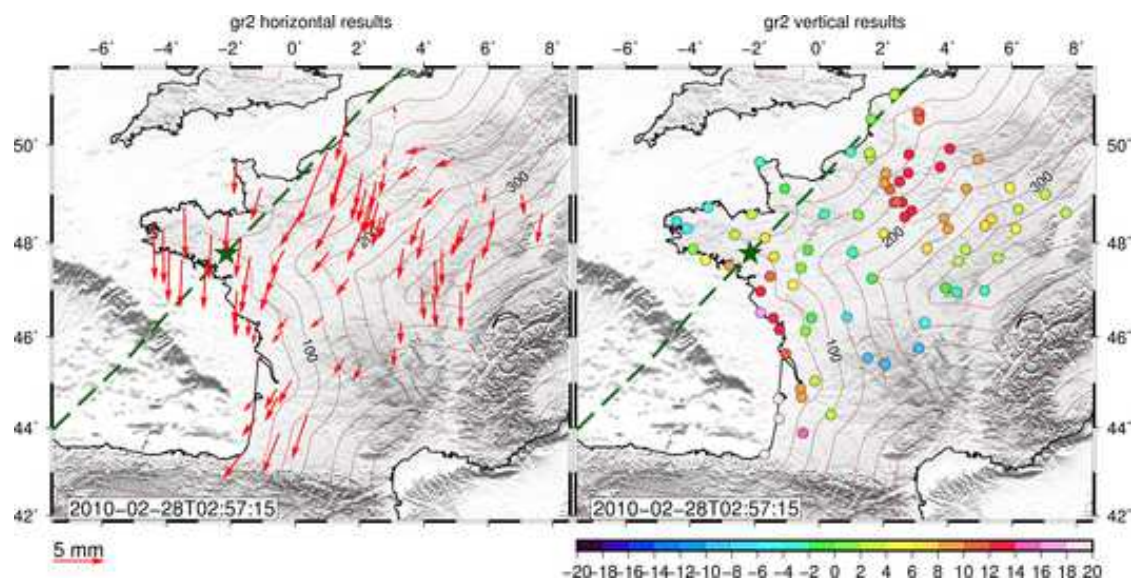


Figure 6.26 – Epoch 2: Horizontal and vertical GPS results (in mm) applying a spatial filter. The green stars indicate the center of Xynthia (estimated location of depression) and the dashed line indicates the storm ground track. The contour lines represent the coastal distance at every 50 km.

6.7. RESULTS

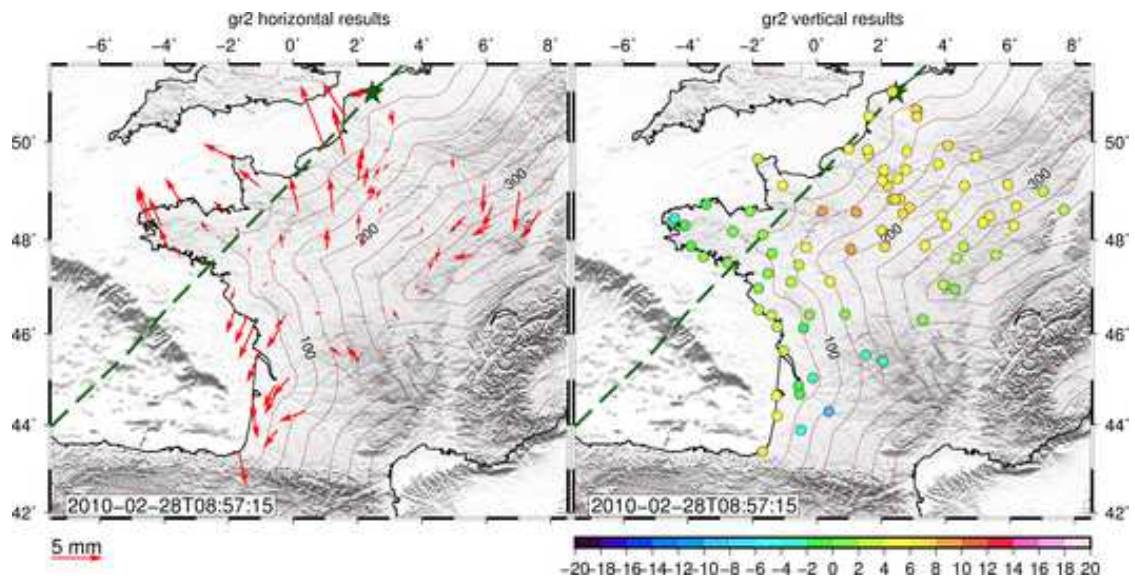


Figure 6.27 – Epoch 3: Horizontal and vertical GPS results (in mm) applying a spatial filter. The green stars indicate the center of Xynthia (estimated location of depression) and the dashed line indicates the storm ground track. The contour lines represent the coastal distance at every 50 km.

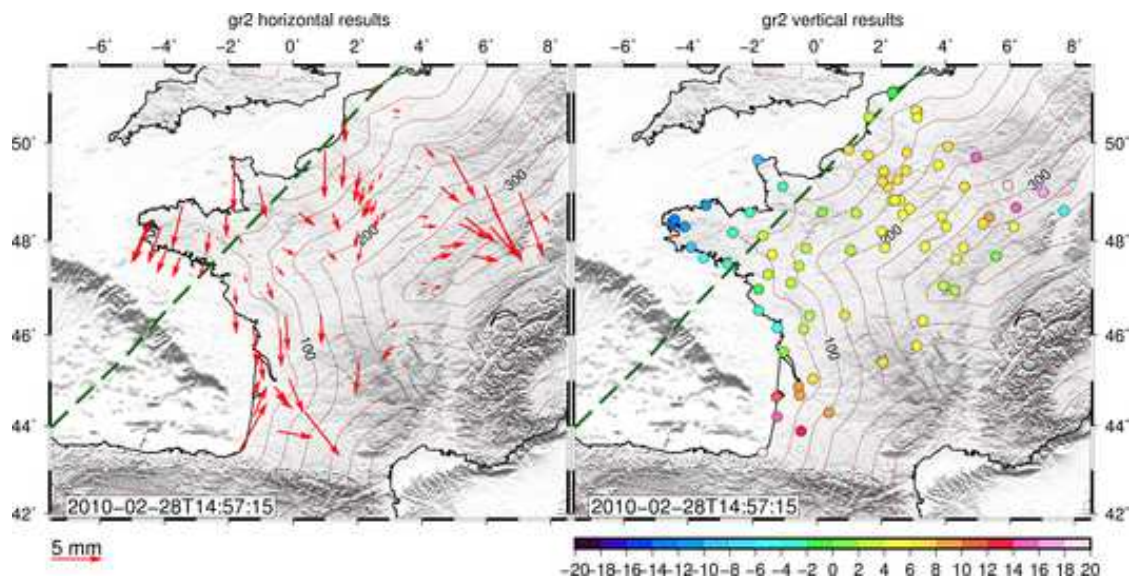


Figure 6.28 – Epoch 4: Horizontal and vertical GPS results (in mm) applying a spatial filter. The green stars indicate the center of Xynthia (estimated location of depression) and the dashed line indicates the storm ground track. The contour lines represent the coastal distance at every 50 km.

6.7.2.2.1.1 A posteriori corrected GPS time series by CWSL

We are interested in whether we can track the temporal and spatial signatures of the storm. Before this we have applied *a posteriori* continental water storage correction because (1) the hydrological loading can have important influence over all the stations during this period²¹ and (2) we want to only focus on the atmospheric and the non-tidal ocean loading generated by the quick pressure variations and the associated storm surge. Figures 6.29 to 6.32 show the space and time evolution of the storm event sensed by GPS after *a posteriori* hydrological loading correction. We mainly focus on the vertical variations because the horizontal displacements are small compared to their uncertainty. We can see that there is a strong uplift of inland sites over the four epochs. This may indicate that the influence of the non-tidal oceanic loading counteracts the atmospheric loading induced uplift.

The continental water storage loading has 0.4 and 3.3 mm mean RMS subsidence over the our network for the horizontal and the vertical components, respectively. In a distance, less than 25 km from the coast the mean RMS subsidence is 0.6 mm for the horizontal and 2.9 mm for the vertical components and the same values for stations with more than 25 km coastal distance are 0.4 and 3.4 mm.

²¹The effect of the hydrological loading is almost constant during this period and maybe including it makes our task to be complex, however it has important magnitude over the stations.

6.7. RESULTS

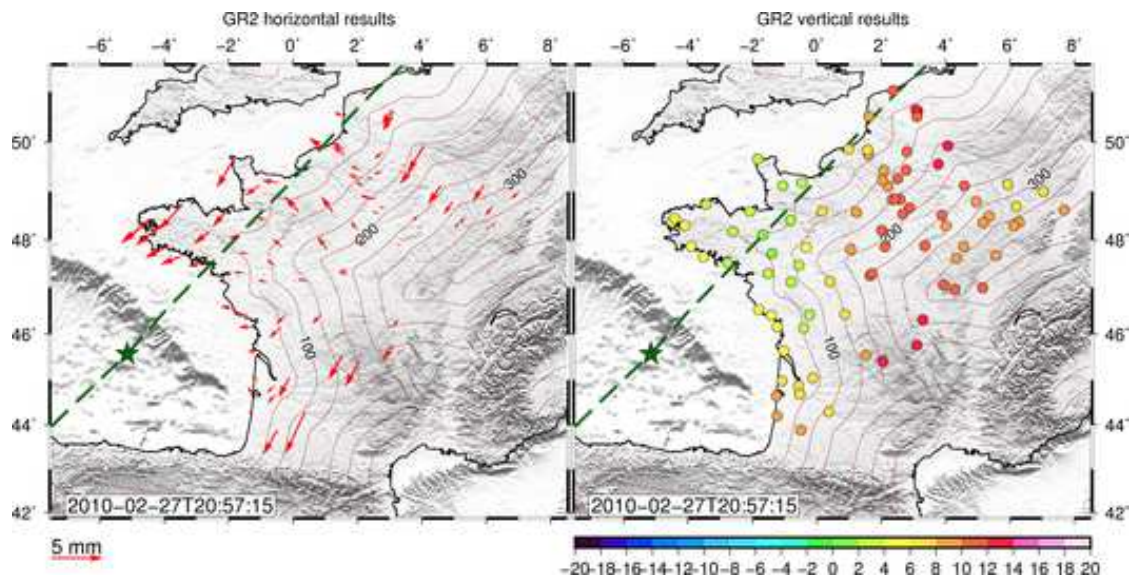


Figure 6.29 – Epoch 1: Horizontal (left) and vertical (right) GPS results (in mm) after *a posteriori* correction only with CWSL. The green stars indicate the center of Xynthia (estimated location of depression) and the dashed line indicates the storm ground track. The contour lines represent the coastal distance at every 50 km.

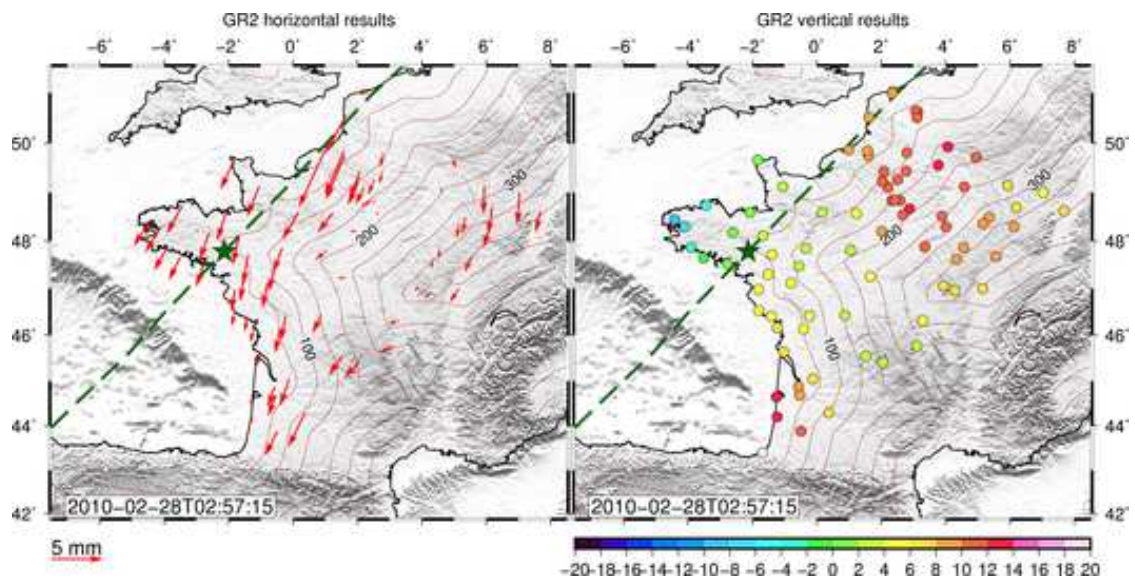


Figure 6.30 – Epoch 2: Horizontal (left) and vertical (right) GPS results (in mm) after *a posteriori* correction only with CWSL. The green stars indicate the center of Xynthia (estimated location of depression) and the dashed line indicates the storm ground track. The contour lines represent the coastal distance at every 50 km.

6.7. RESULTS

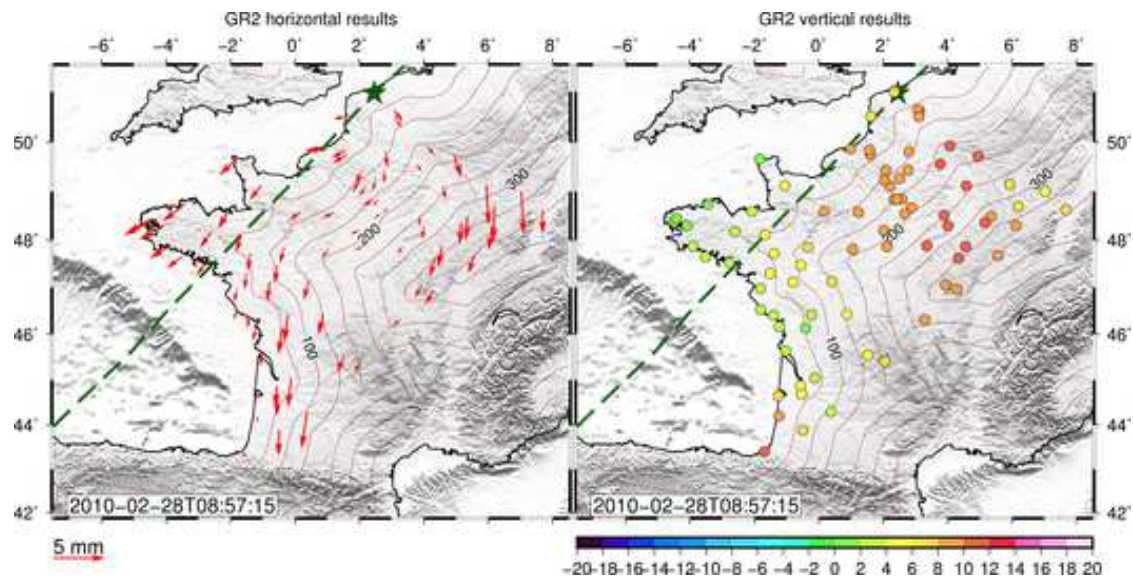


Figure 6.31 – Epoch 3: Horizontal (left) and vertical (right) GPS results (in mm) after *a posteriori* correction only with CWSL. The green stars indicate the center of Xynthia (estimated location of depression) and the dashed line indicates the storm ground track. The contour lines represent the coastal distance at every 50 km.

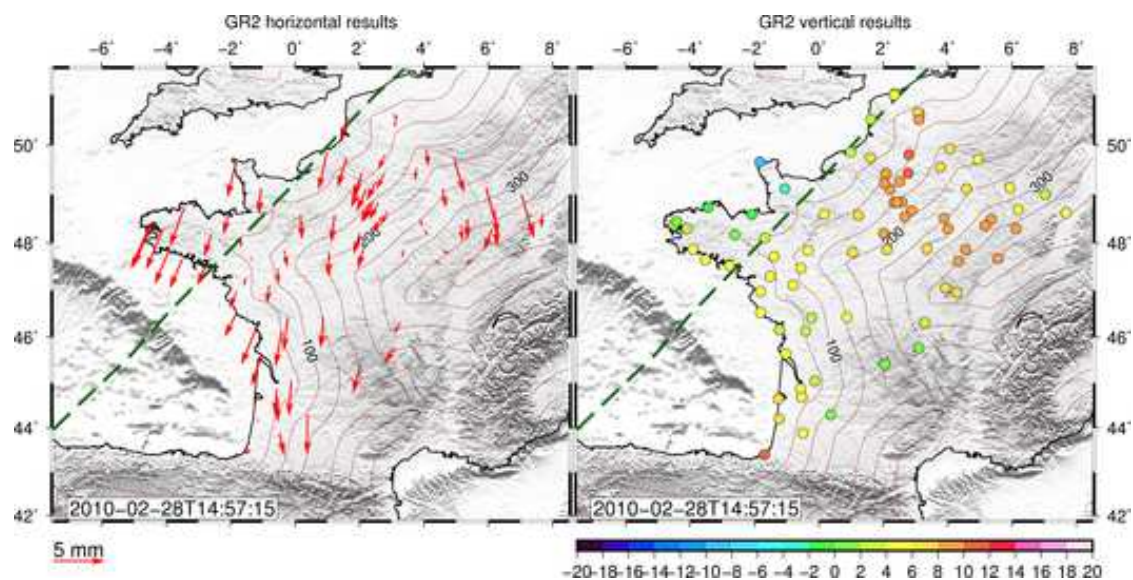


Figure 6.32 – Epoch 4: Horizontal (left) and vertical (right) GPS results (in mm) after *a posteriori* correction only with CWSL. The green stars indicate the center of Xynthia (estimated location of depression) and the dashed line indicates the storm ground track. The contour lines represent the coastal distance at every 50 km.

6.7.2.2.1.2 A posteriori corrected GPS time series by ATML and CWSL

After the RMS analysis we saw that those atmospheric loading models are more adequate which take into account a dynamic ocean response. In this work we experimented with a local non-tidal ocean model (NTOL) which should be combined with IB based atmospheric loading models. The difference, thus the choice between ATML and ATMIB, the two loading models that implies IB is irrelevant compared to the GPS formal error. Therefore, here we chose the ATML model from the list of the presented atmospheric loading models. In this scenario, we focused on the Xynthia generated storm surge and the associated non-tidal ocean loading. Therefore, we have applied atmospheric pressure and continental water storage loading corrections. Thus Figures 6.33 to 6.36 represent the GPS sensitivity regarding to the NTOL effect. Over the four epochs here we cannot see that strong uplift that we have seen previously for the only hydrology corrected GPS series. This is reasonable and it can indicate that our atmospheric and hydrological loading corrections were correct. We can observe a strong subsidence at coastal sites, which is mitigated after the storm passage. These figures may suggest that we are capable of detecting the loading deformation induced by the huge cyclone generated storm surge.

6.7.2.2.1.3 A posteriori corrected GPS time series by NTOL and CWSL

We apply here the NTOL model because it seems to be more relevant for the Xynthia event compared to the general ECCO model. It is due to its higher spatial and temporal resolution that probably more precisely reflects the ocean's response over this short period. According to our last scheme we were focusing only on the displacements induced by atmospheric pressure variations. Therefore, we applied *a posteriori* NTOL and CWSL correction to be as close to the atmospheric loading signatures as possible. Figures 6.37 to 6.40 shows this scenario. According to these figures, we can see the pure effect of the atmospheric loading. When the storm approaches the continent the network (also coastal stations) shows an important upward motion. After the landfall of the storm, as it is already over inland we can see that this uplift at some western coastal sites is mitigated.

6.7. RESULTS

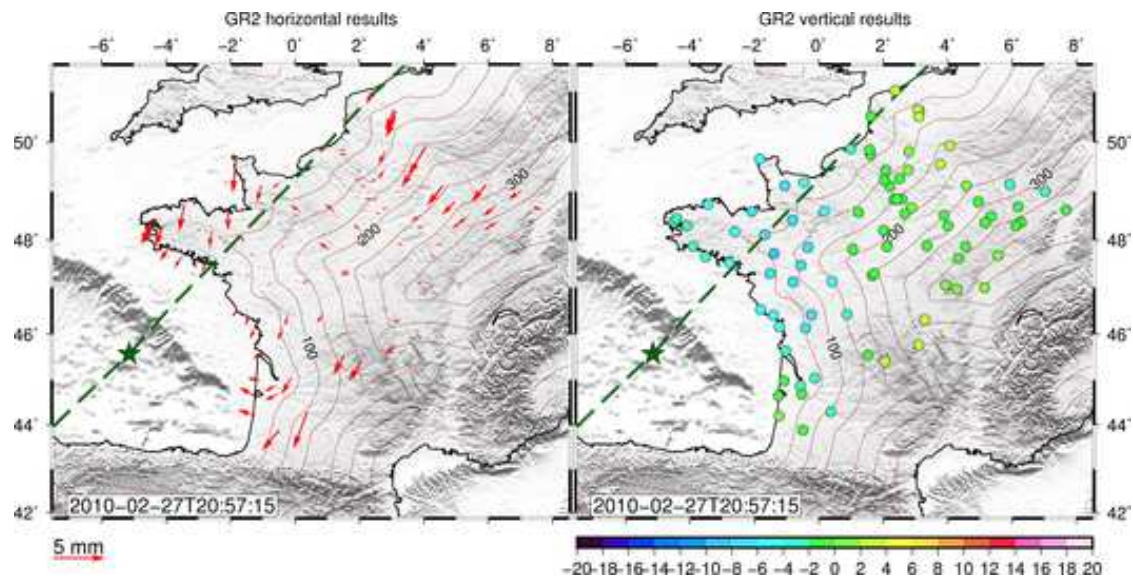


Figure 6.33 – Epoch 1: Horizontal (left) and vertical (right) GPS results (in mm) after *a posteriori* correction with the sum of ATML and CWSL. The green stars indicate the center of Xynthia (estimated location of depression) and the dashed line indicates the storm ground track. The contour lines represent the coastal distance at every 50 km.

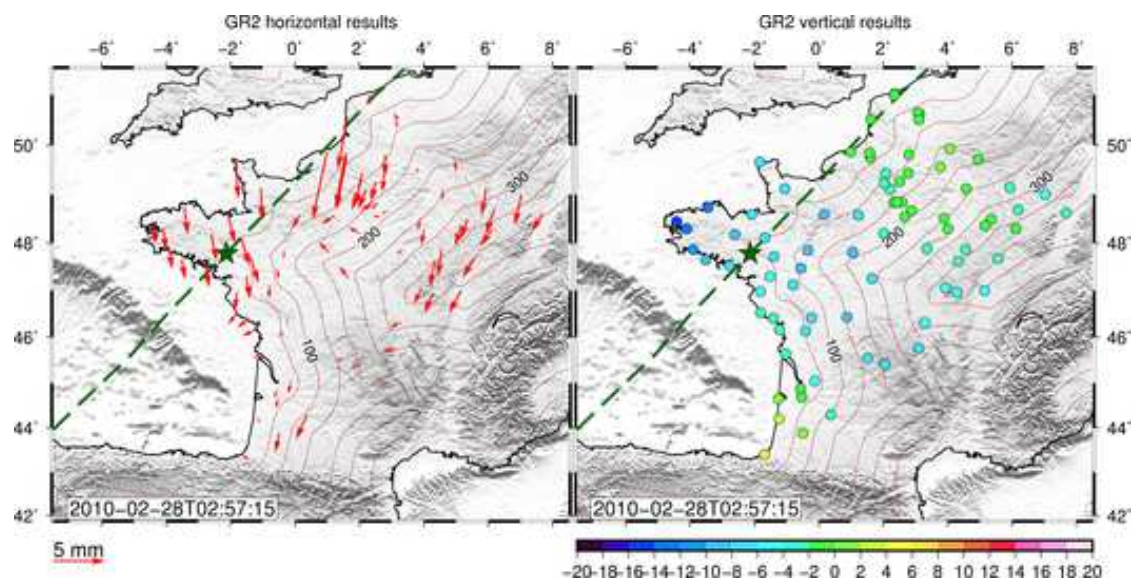


Figure 6.34 – Epoch 2: Horizontal (left) and vertical (right) GPS results (in mm) after *a posteriori* correction with the sum of ATML and CWSL. The green stars indicate the center of Xynthia (estimated location of depression) and the dashed line indicates the storm ground track. The contour lines represent the coastal distance at every 50 km.

6.7. RESULTS

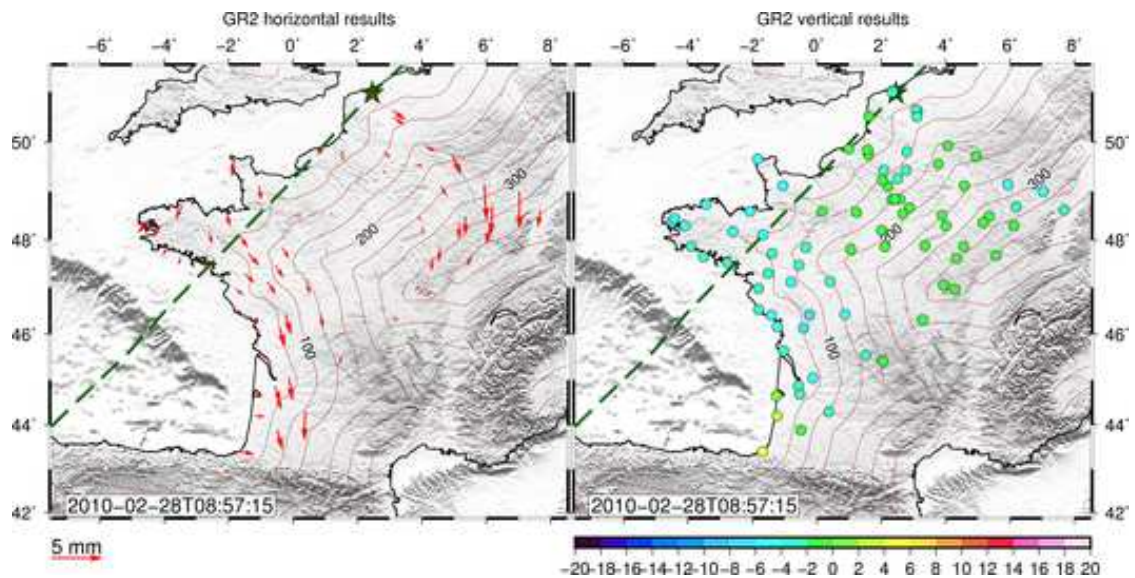


Figure 6.35 – Epoch 3: Horizontal (left) and vertical (right) GPS results (in mm) after *a posteriori* correction with the sum of ATML and CWSL. The green stars indicate the center of Xynthia (estimated location of depression) and the dashed line indicates the storm ground track. The contour lines represent the coastal distance at every 50 km.

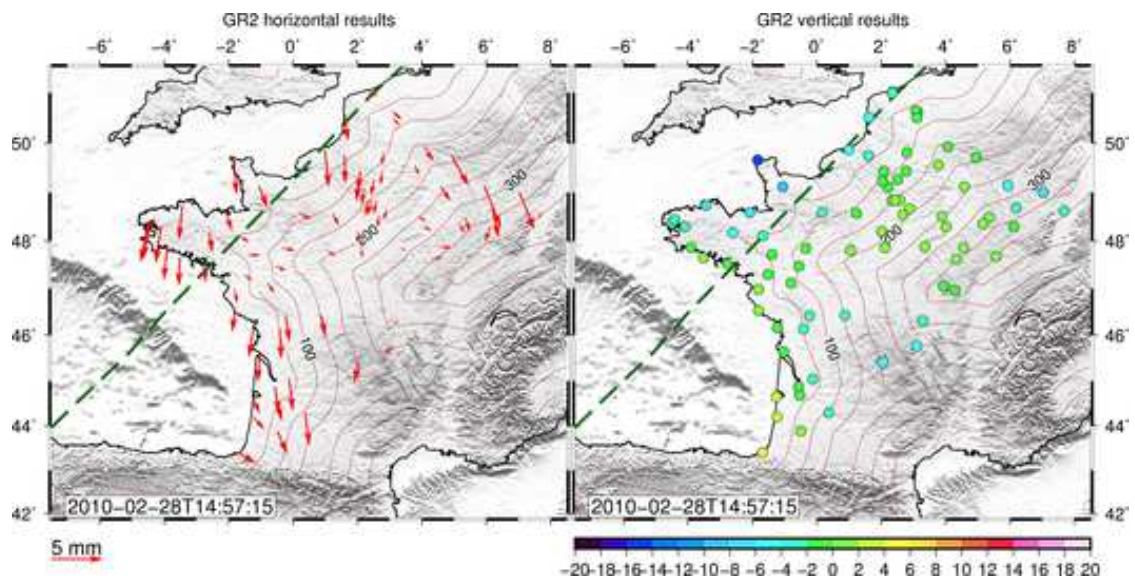


Figure 6.36 – Epoch 4: Horizontal (left) and vertical (right) GPS results (in mm) after *a posteriori* correction with the sum of ATML and CWSL. The green stars indicate the center of Xynthia (estimated location of depression) and the dashed line indicates the storm ground track. The contour lines represent the coastal distance at every 50 km.

6.7. RESULTS

When the storm evolves farther we can observe the subsidence of the coastal and near coastal stations in the Bay of Biscay. As the storm leaves our region we can see its effect on the north part of our network, while the coastal sites are not affected.

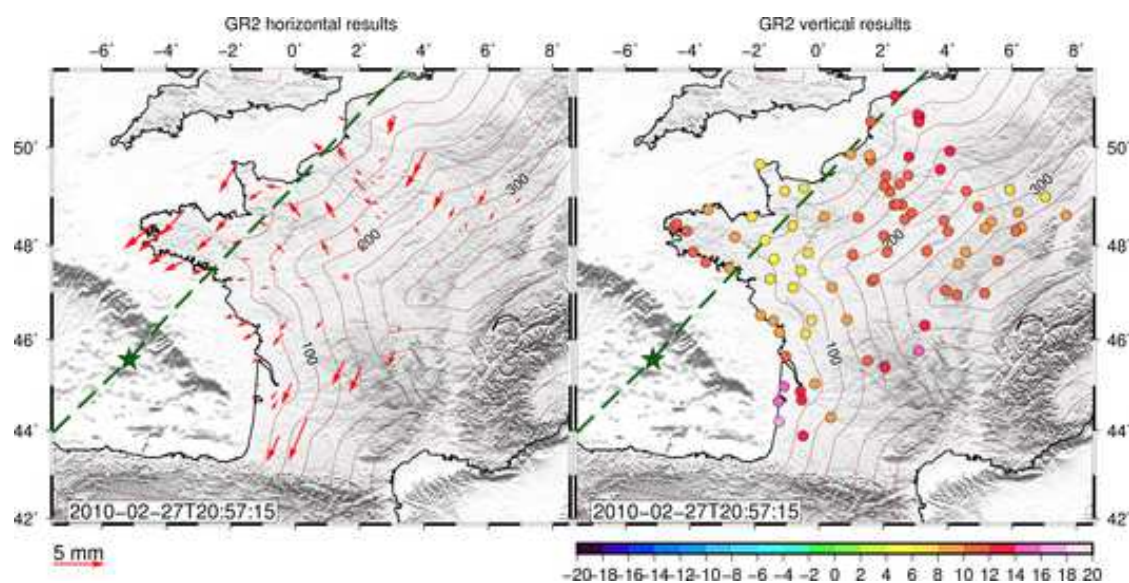


Figure 6.37 – Epoch 1: Horizontal (left) and vertical (right) GPS results (in mm) after *a posteriori* correction with the sum of NTOL and CWSL. The green stars indicate the center of Xynthia (estimated location of depression) and the dashed line indicates the storm ground track. The contour lines represent the coastal distance at every 50 km.

6.7.2.2.1.4 Sum of the models

Before we look at the *a posteriori* correction of the GPS with the total effect, we present the sum of the ATML, CWSL and NTOL models to see their accumulated impact during the passage of the storm. Figures 6.41 to 6.44 show how the surface deformed at four consecutive epochs. We note that the atmospheric loading has a contrary effect to the non-tidal oceanic and the hydrological loading, although they not extinguish each other completely. Considering the horizontal deformation, when the storm over land, it seems that the sum of the models suggest very small, but oriented displacements similarly to Figure 6.20. At coastal stations, it seems the three loading effects compensate each other generating no or very tiny vertical deformations. The Figures 6.41 to 6.44 suggest that the atmospheric effect is dominating in the total effect, as the ocean has weaker influence far from the coast.

6.7. RESULTS

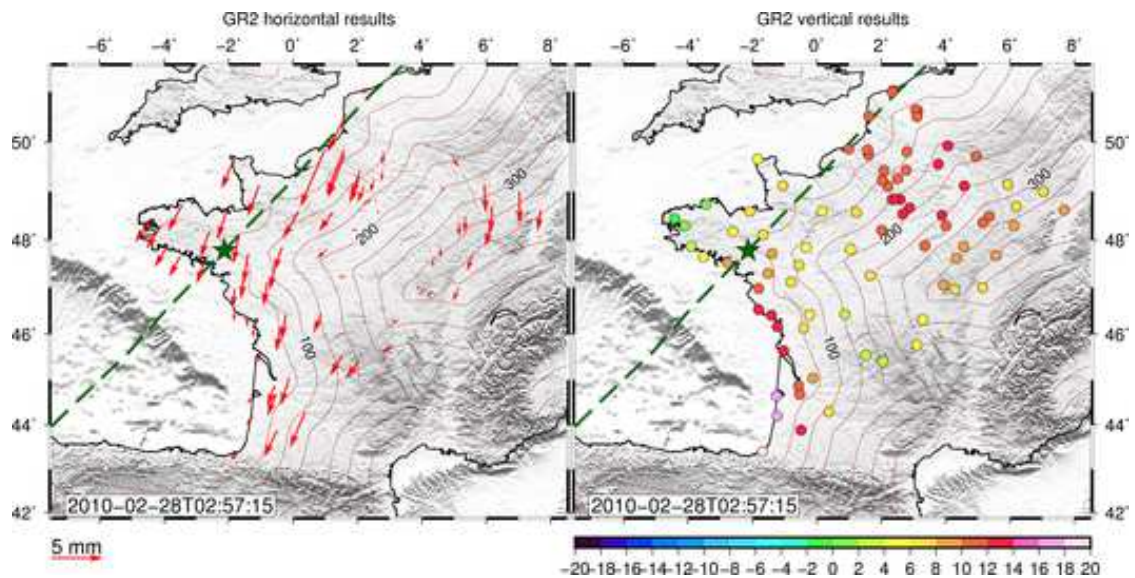


Figure 6.38 – Epoch 2: Horizontal (left) and vertical (right) GPS results (in mm) after *a posteriori* correction with the sum of NTOL and CWSL. The green stars indicate the center of Xynthia (estimated location of depression) and the dashed line indicates the storm ground track. The contour lines represent the coastal distance at every 50 km.

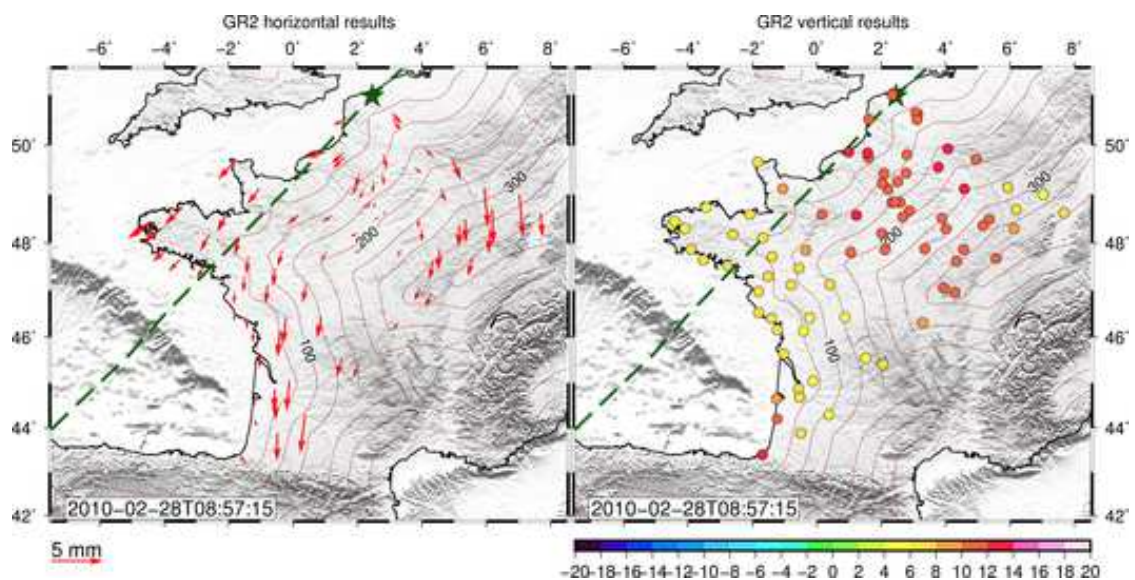


Figure 6.39 – Epoch 3: Horizontal (left) and vertical (right) GPS results (in mm) after *a posteriori* correction with the sum of NTOL and CWSL. The green stars indicate the center of Xynthia (estimated location of depression) and the dashed line indicates the storm ground track. The contour lines represent the coastal distance at every 50 km.

6.7. RESULTS

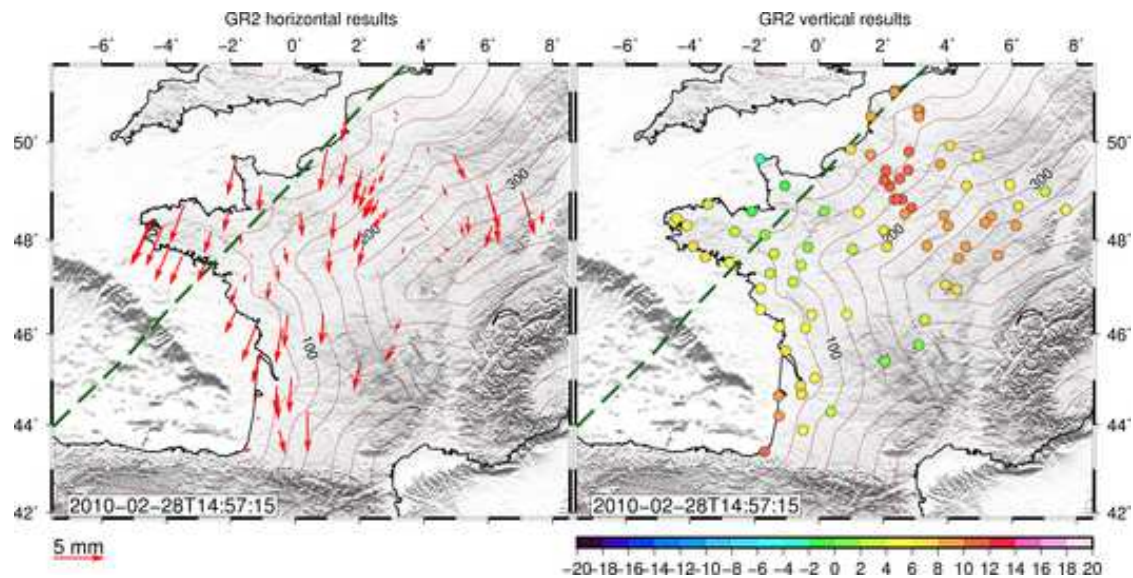


Figure 6.40 – Epoch 4: Horizontal (left) and vertical (right) GPS results (in mm) after *a posteriori* correction with the sum of NTOL and CWSL. The green stars indicate the center of Xynthia (estimated location of depression) and the dashed line indicates the storm ground track. The contour lines represent the coastal distance at every 50 km.

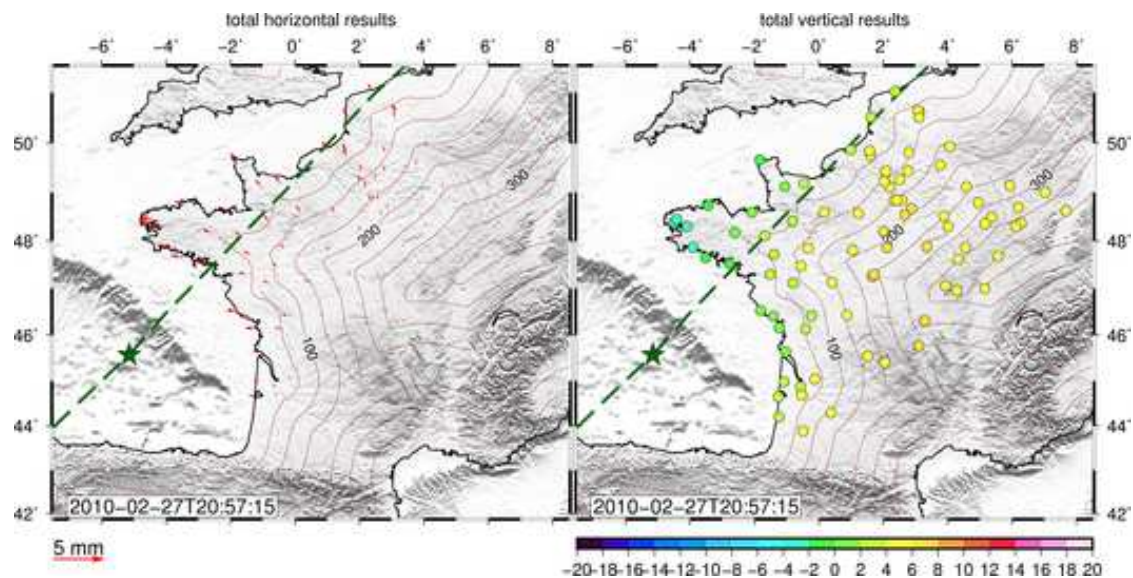


Figure 6.41 – Epoch 1: Horizontal and vertical components of the sum of ATML, CWSL and NTOL models (in mm). The green stars indicate the center of Xynthia (estimated location of depression) and the dashed line indicates the storm ground track. The contour lines represent the coastal distance at every 50 km.

6.7. RESULTS

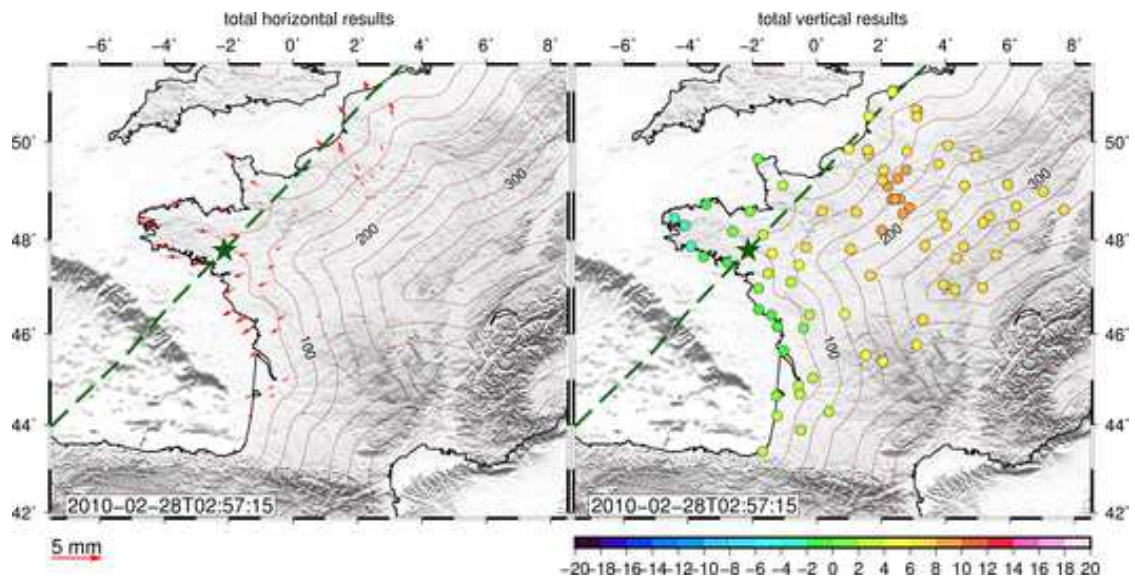


Figure 6.42 – Epoch 2: Horizontal and vertical components of the sum of ATML, CWSL and NTOL models (in mm). The green stars indicate the center of Xynthia (estimated location of depression) and the dashed line indicates the storm ground track. The contour lines represent the coastal distance at every 50 km.

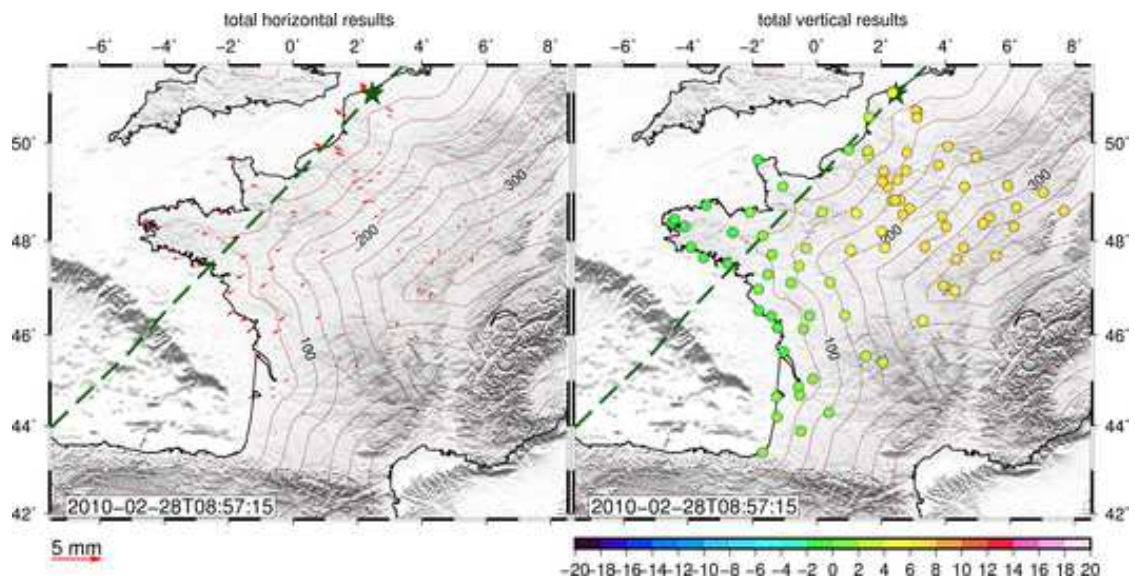


Figure 6.43 – Epoch 3: Horizontal and vertical components of the sum of ATML, CWSL and NTOL models (in mm). The green stars indicate the center of Xynthia (estimated location of depression) and the dashed line indicates the storm ground track. The contour lines represent the coastal distance at every 50 km.

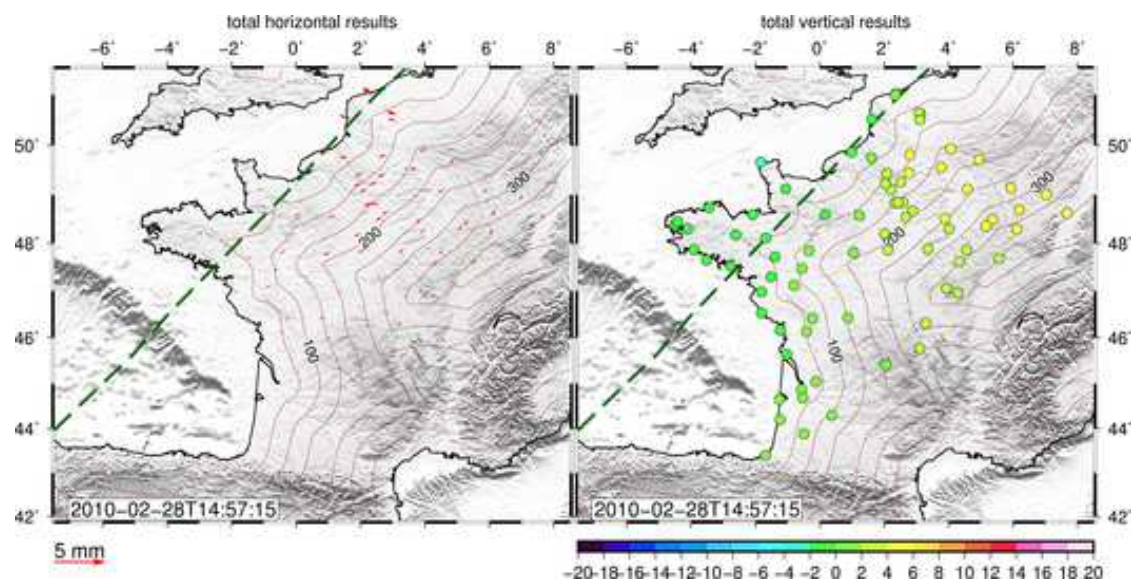


Figure 6.44 – Epoch 4: Horizontal and vertical components of the sum of ATML, CWSL and NTOL models (in mm). The green stars indicate the center of Xynthia (estimated location of depression) and the dashed line indicates the storm ground track. The contour lines represent the coastal distance at every 50 km.

6.7.2.2.1.5 A posteriori corrected GPS time series by the sum of the models

Figures 6.45 to 6.48 present the *a posteriori* correction of the GPS with the sum of the ATML, CWSL and NTOL models. In the case of absolutely correct models and GPS results we should see no horizontal and vertical effect for this scenario. That is, no, or tiny arrows on the horizontal maps (left of Figures 6.45 to 6.48) and green colors on the vertical maps (right of Figures 6.45 to 6.48). We do not see exactly this on our figures, although we see much reduced vertical displacements compared to Figures 6.25 to 6.28. Since the storm evolved over land closed to the coast, it is difficult to differentiate between the effects. However, it seems the atmosphere is dominating in the total loading and the sum of the models did a reasonable job compared to the GPS.

6.7.2.2.2 Variations in function of coastal distance

We have tried to track the spatial and temporal evolution of the storm Xynthia by looking at the vertical displacements according to the coastal distance. Figures 6.50 to 6.57 show these instantaneous states at 4 consecutive epochs during Xynthia for GPS and

6.7. RESULTS

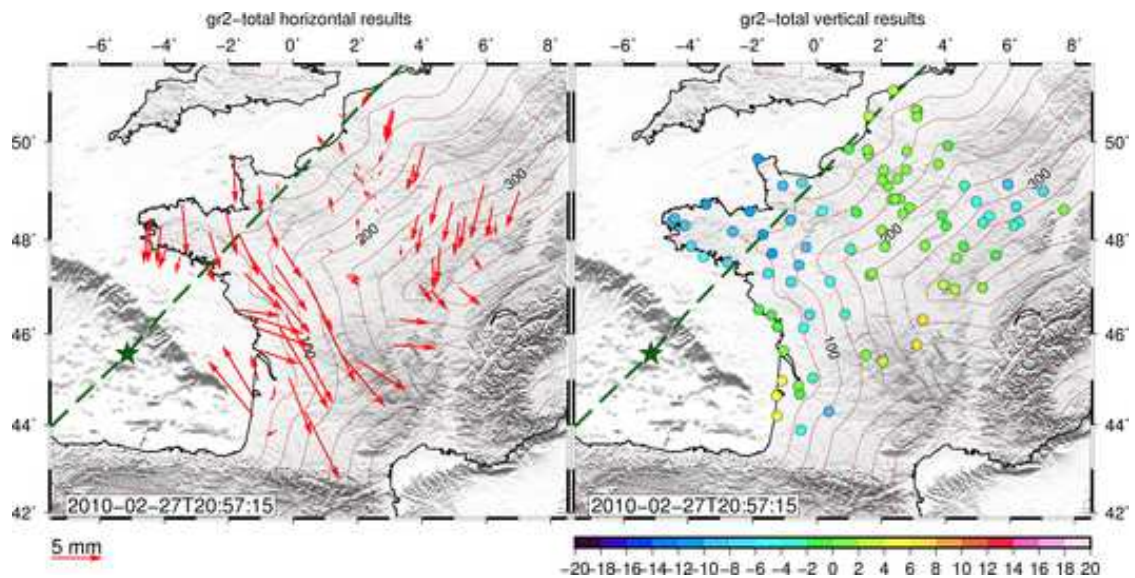


Figure 6.45 – Epoch 1: Horizontal (left) and vertical (right) GPS results (in mm) after *a posteriori* correction with the sum of ATML, CWSL and NTOL. The green stars indicate the center of Xynthia (estimated location of depression) and the dashed line indicates the storm ground track. The contour lines represent the coastal distance at every 50 km.

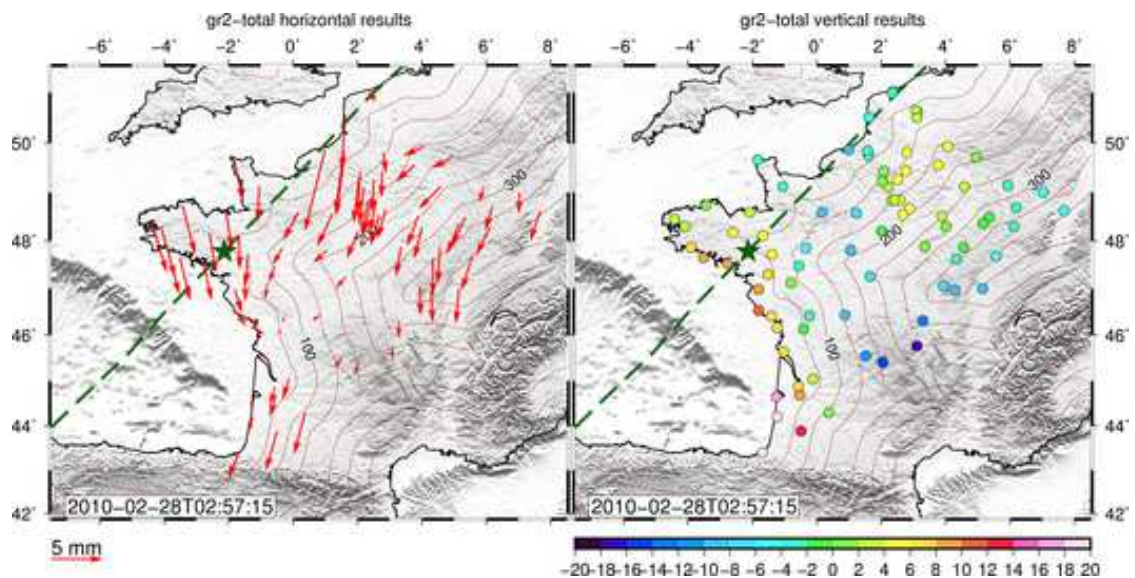


Figure 6.46 – Epoch 2: Horizontal (left) and vertical (right) GPS results (in mm) after *a posteriori* correction with the sum of ATML, CWSL and NTOL. The green stars indicate the center of Xynthia (estimated location of depression) and the dashed line indicates the storm ground track. The contour lines represent the coastal distance at every 50 km.

6.7. RESULTS

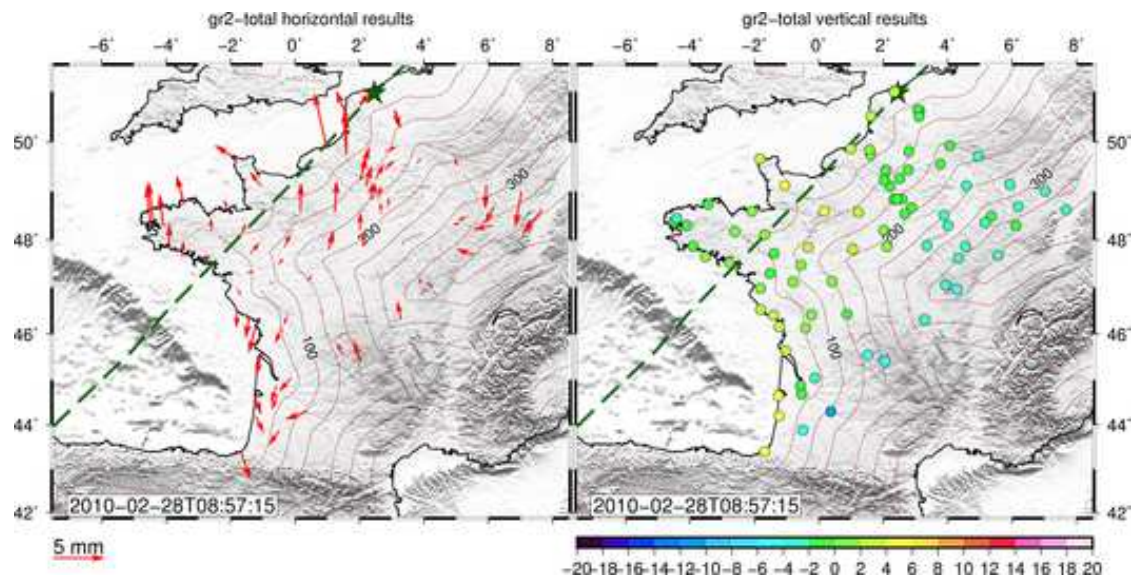


Figure 6.47 – Epoch 3: Horizontal (left) and vertical (right) GPS results (in mm) after *a posteriori* correction with the sum of ATML, CWSL and NTOL. The green stars indicate the center of Xynthia (estimated location of depression) and the dashed line indicates the storm ground track. The contour lines represent the coastal distance at every 50 km.

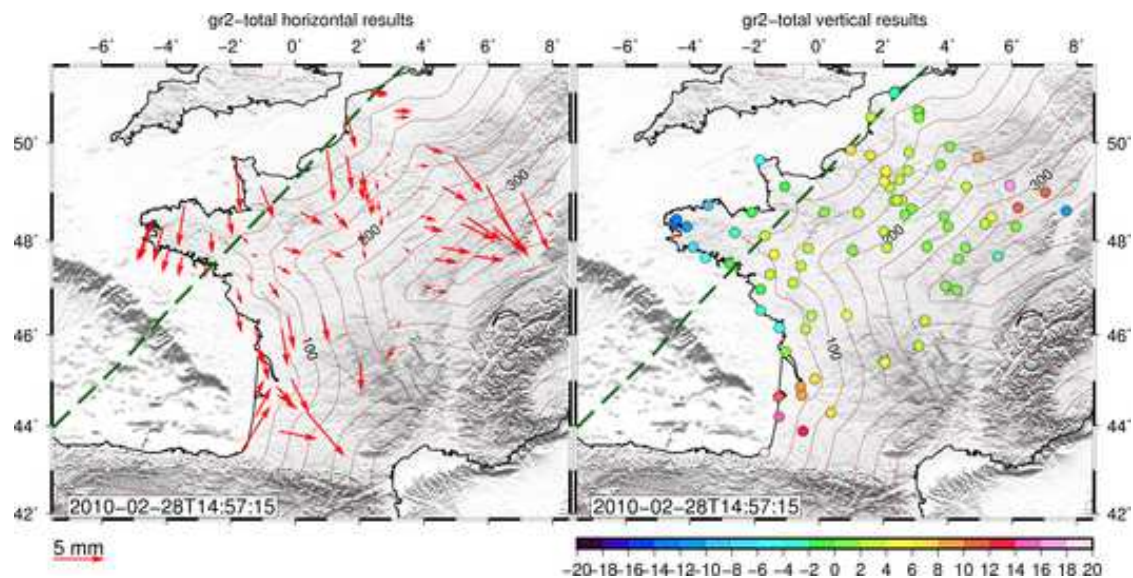


Figure 6.48 – Epoch 4: Horizontal (left) and vertical (right) GPS results (in mm) after *a posteriori* correction with the sum of ATML, CWSL and NTOL. The green stars indicate the center of Xynthia (estimated location of depression) and the dashed line indicates the storm ground track. The contour lines represent the coastal distance at every 50 km.

the different models. The interpretation of the horizontal deformations would be difficult in this kind of figures, because we should see two plots (north and the east components) at a time. Also, the orientation of the horizontal deformation depends on the relative position of the center of the vertical uplift or subsidence (See Figure 6.20).

Figures 6.50 to 6.53 show the coastal distances in linear scale in order to better see the behaviour of distant sites from the coast. Meanwhile, in Figures 6.54 to 6.57 we used logarithmic scale to improve the visibility of the data that belongs to the coastal regions. We remark here that we smoothed the time series with a Gaussian filter (temporal filter, Footnote 19) only for figures for better visibility.

The hydrological loading seems to have slightly less influence within 25 km coastal range, that is 0.6 and 2.9 mm mean RMS subsidence for the horizontal and the vertical components, respectively. Also, it seems to be constant over inland sites and in time, with mean RMS subsidence of 0.4 mm for the horizontal and 3.4 mm for the vertical components. That is, farther inland it reaches its maximum effect and does not show visible spatial and temporal variations after at this scale (See Figures 6.50 to 6.53 for epoch 1 to epoch 4).

We can see how the non-tidal ocean loading weakens as a function of increasing coastal distance (spatial aspect). It is visible that the NTOL loading has a very important effect in the first 50 km from the coast. Stations within 50 km coastal range have 3.4 mm mean RMS subsidence for the vertical component. Moreover, it also has significant impact until ≈ 200 km coastal distance. Given that between 100 and 200 km coastal range it can reach in absolute value the ≈ 15 % of the atmospheric loading, which corresponds to about 1.2 mm mean RMS for the vertical component. In temporal aspect (from Figures 6.50 to 6.53), we can see also this mitigation over the storm epochs.

Not surprisingly we can see that the ATMMO and the ATML+NTOL combination agree quite well within 150-200 km coastal range, with a mean RMS of 6.9 mm and 7.6 mm for the vertical components of ATMMO and ATML+NTOL, respectively. However, within the first few kilometers (until $\approx 10 - 15$ km) they differ possibly due to their distinct ocean and atmospheric models (MOG2D vs. ocean model of Xavier Bertin and ECMWF vs. MERRA, for ocean and atmosphere, respectively). At sites deeper inland (> 150 -200 km) their mean RMS difference is 1.2 mm, which maybe can reflect the differences between

their atmospheric pressure models.

The dynamic ocean response seems to be the most suitable hypothesis for the period of this quick storm. For example looking Figure 6.8 we can see that the *a posteriori* corrected GPS with the sum of NTOL and CWSL (claret color in Figure 6.8) quite well recovers the atmospheric loading. Also, the choice of ATMMO or the ATML+NTOL combination is irrelevant compared to the GPS formal error.

The variations of the NTOL effect between 50 and 150 km coastal range (mean RMS of about 1.7 mm) possibly reflects the findings presented in Williams and Penna [2011]; Geng et al. [2012]; van Dam [2012]; Mémin et al. [2014]. That is the effect that the NTOL loading does not only depends on the nearest coast but also on the coastline geometry, which in our study region is quite complex. In general the GPS results see smaller amplitudes than the models predict.

Figure 6.49 aims to help the interpretation of Figures 6.50 to 6.57 indicating the estimated location of the depression (center of Xynthia) at the four consecutive epochs.

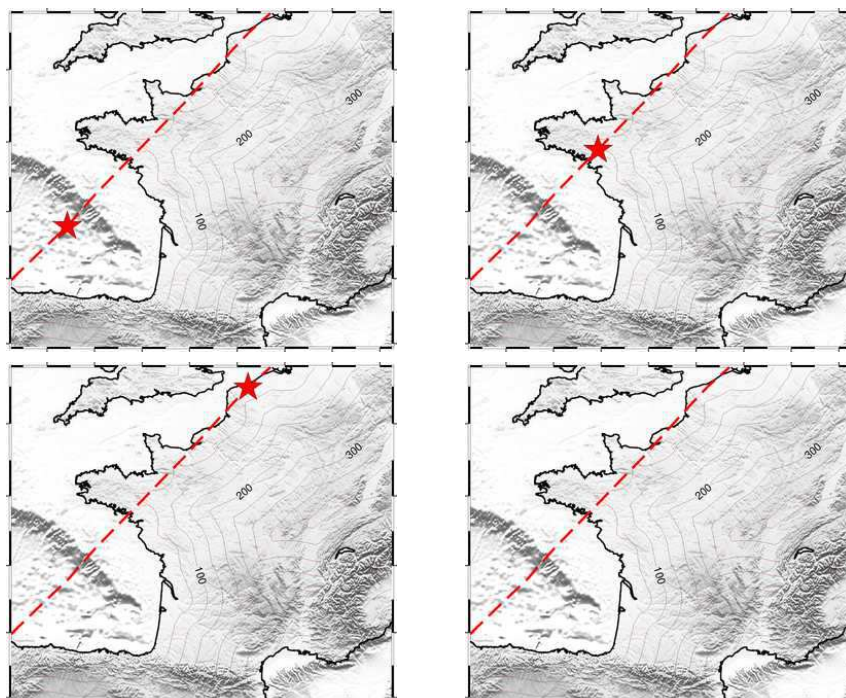


Figure 6.49 – The estimated location of the depression (center of Xynthia) at four consecutive epochs. Epoch 1 (top left), epoch 2 (top right), epoch 3 (bottom left), and epoch 4 (bottom right) that correspond to Figure [6.50,6.54], [6.51,6.55], [6.52,6.56], and [6.53,6.57], respectively.

6.7. RESULTS

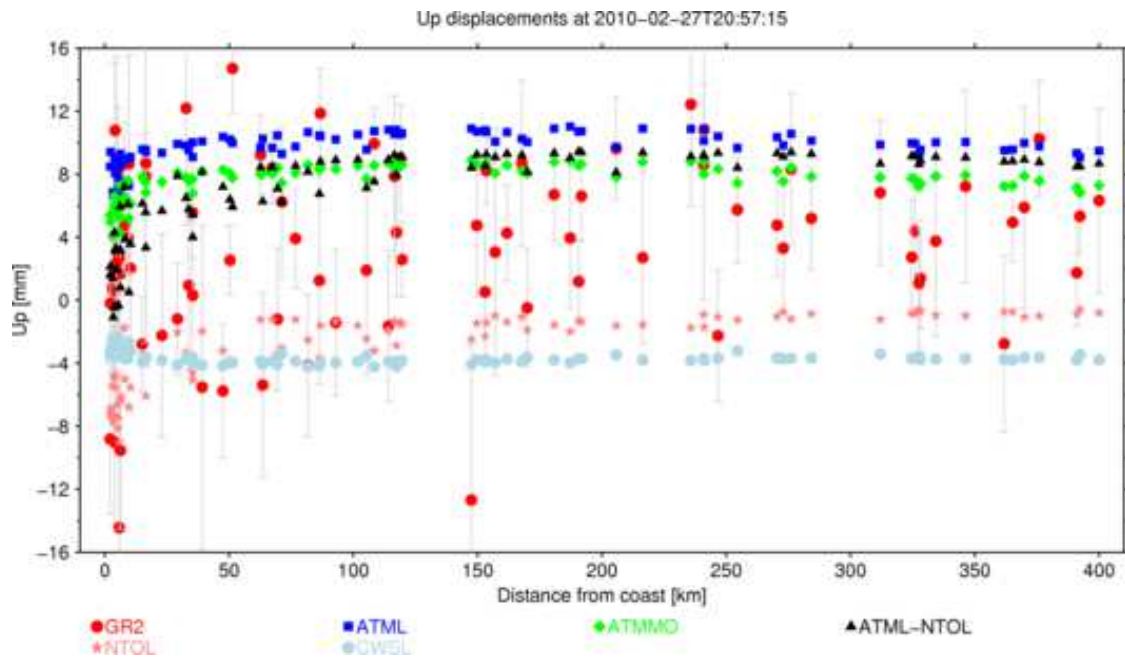


Figure 6.50 – Epoch 1: Instantaneous plot of up displacements as a function of coastal distance.

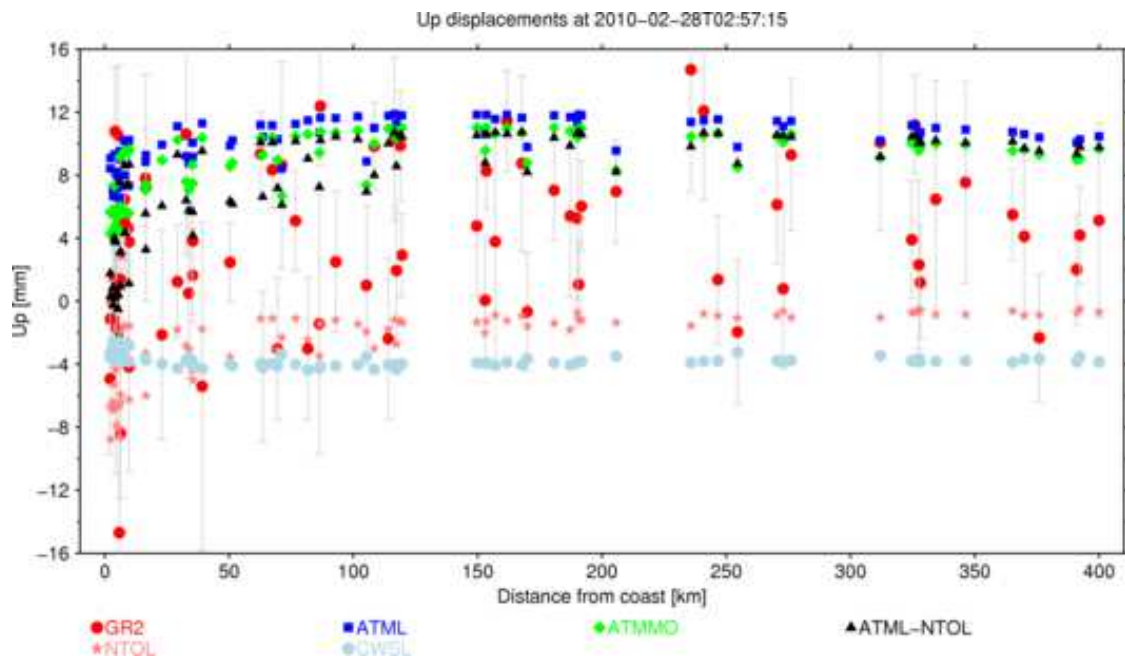


Figure 6.51 – Epoch 2: Instantaneous plot of up displacements as a function of coastal distance.

6.7. RESULTS

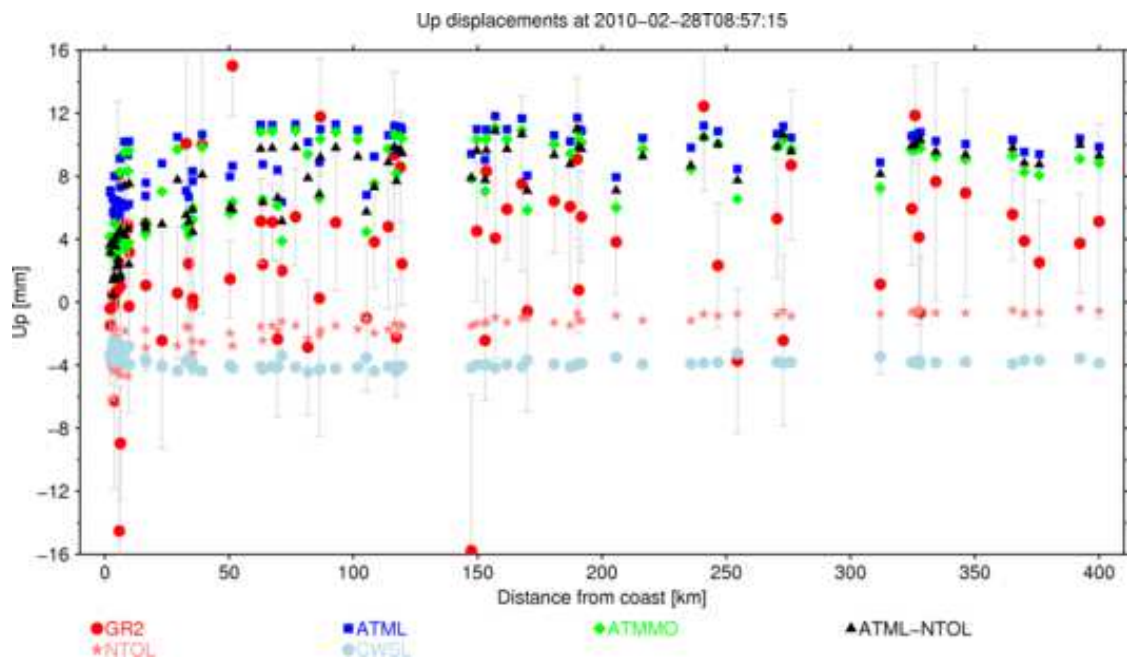


Figure 6.52 – Epoch 3: Instantaneous plot of up displacements as a function of coastal distance.

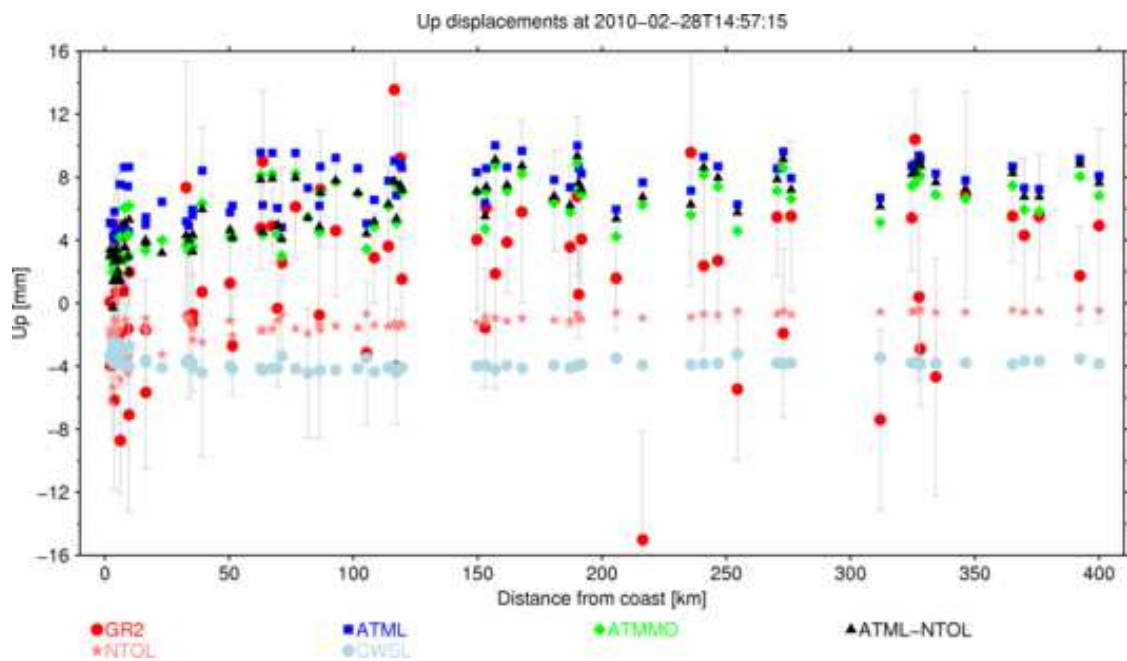


Figure 6.53 – Epoch 4: Instantaneous plot of up displacements as a function of coastal distance.

6.7. RESULTS

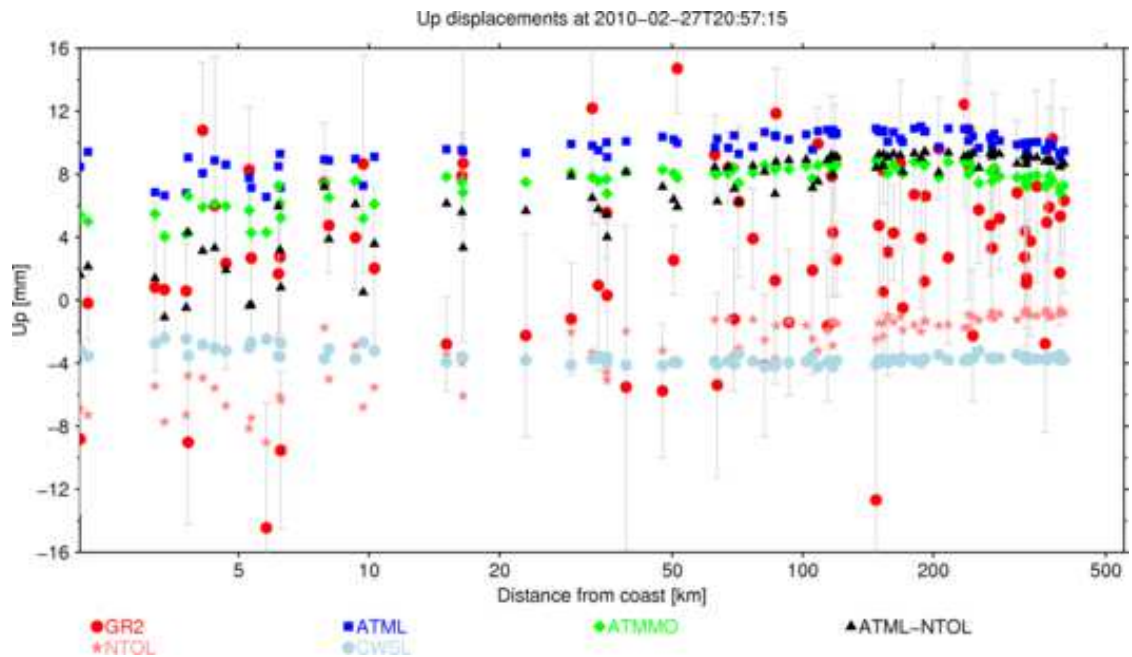


Figure 6.54 – Epoch 1: Instantaneous plot of up displacements as a function of coastal distance (logarithmic scale).

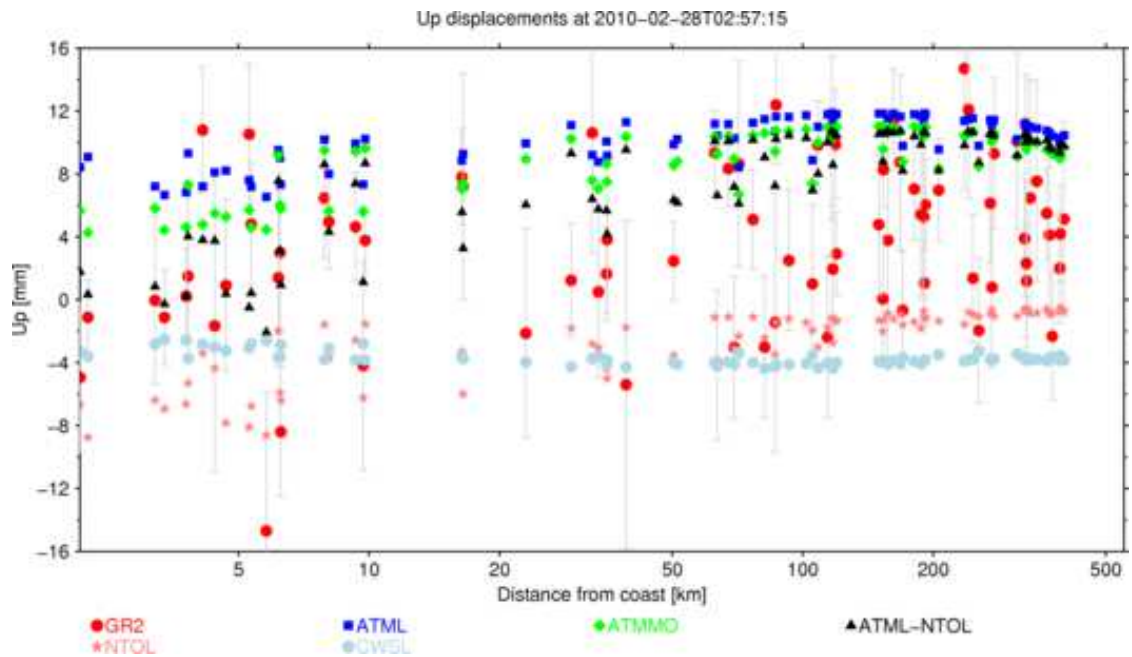


Figure 6.55 – Epoch 2: Instantaneous plot of up displacements as a function of coastal distance (logarithmic scale).

6.7. RESULTS

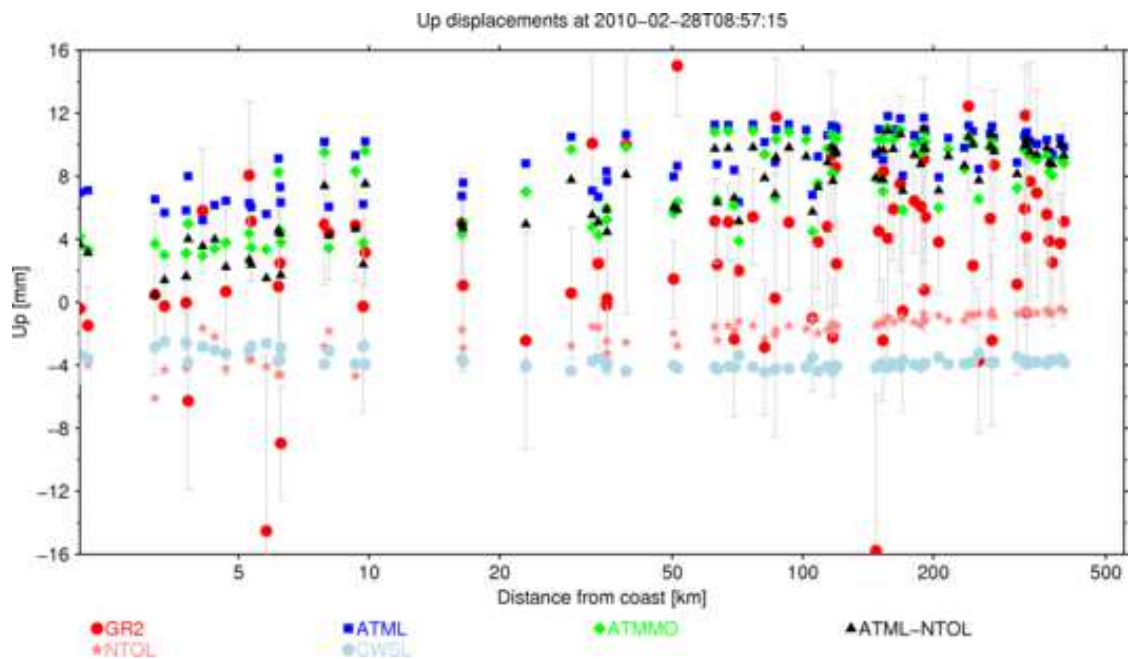


Figure 6.56 – Epoch 3: Instantaneous plot of up displacements as a function of coastal distance (logarithmic scale).

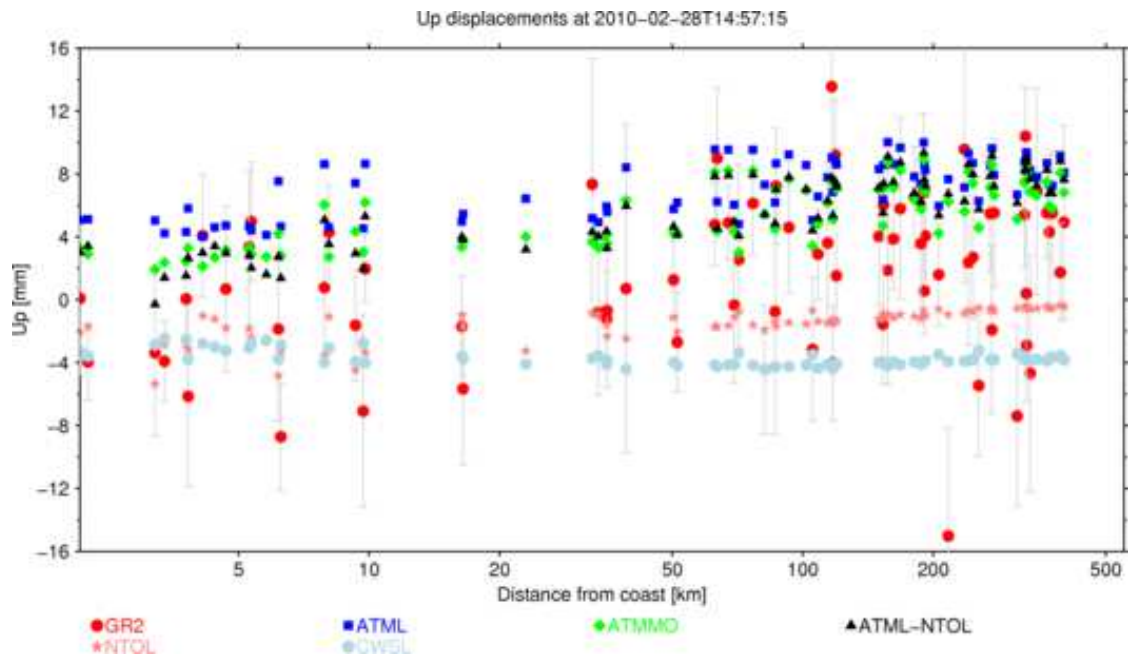


Figure 6.57 – Epoch 4: Instantaneous plot of up displacements as a function of coastal distance (logarithmic scale).

6.7.2.3 Correlation between GPS and the models

We decided to show here the correlation maps of the two monthly grid interpolated ATMMO time series (Figure 6.58). We selected these figures because the ATMMO series improved the repeatability of our GPS time series to a better extent or reduced it in less extent in general, similarly to the ATML+NTOL combination. The other correlation maps are presented in Appendices B.1 to B.4.

The correlation between GPS and the atmospheric models is stronger at inland than at coastal sites. The RMS of the correlations during the two months are 0.33 and 0.52, and for the two days of Xynthia are 0.67 and 0.57 for inland and coastal sites, respectively. During the perturbed period we have a more pronounced correlation over all the stations than during the calm period. It shows the extensive impact of the fast moving storm.

At the bottom of each figure we can see the critical correlation value that is related to the given sample size as well as the number of stations that passed or failed the significance test. In the case of two month time series with 6-hourly sampling, we have ≈ 240 records. To reject the Null hypothesis at the 95 % probability level we have to observe at least ≈ 0.106 for the correlation coefficient.

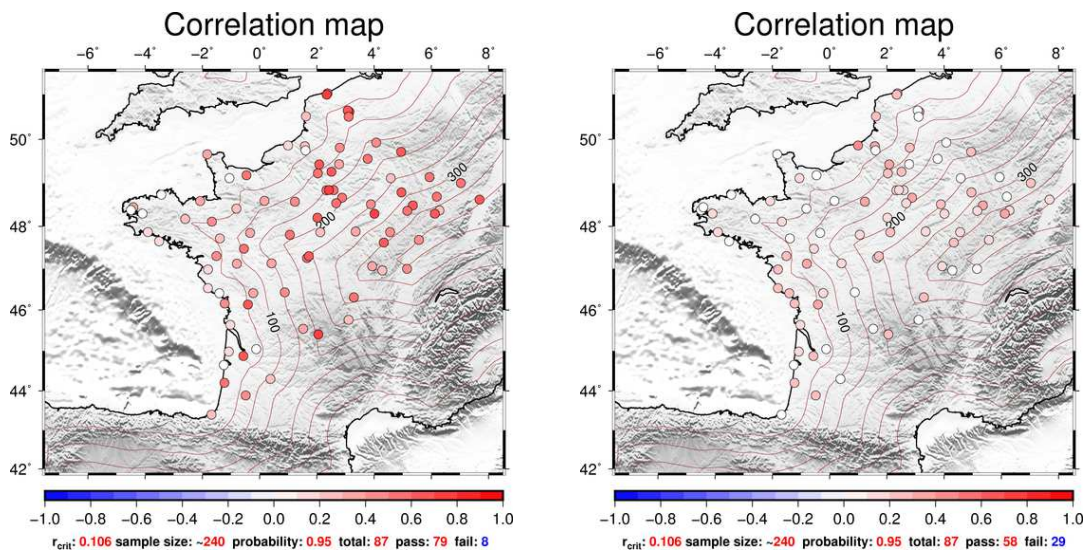


Figure 6.58 – Correlation between the GR2 and the grd-ATMMO time series during two months centered on the storm Xynthia (left) and during two calm summer months (right).

6.8 Conclusion

We investigated the space and time evolution of a violent European windstorm at a subset of RGP stations. We looked at the behaviour of the coastal and inland sites by comparing GPS results to atmospheric models that are based on different ocean response assumptions. We have also compared the estimated position time series to predicted non-tidal ocean loading displacements. We took into account the loading induced by continental water storage variations since the studied period was at the end of a wet season and the hydrology models suggested an important subsidence for the region. These values suggested that they could amplify the subsidence caused by the ocean bottom pressure variations due to the dynamic ocean response to the fast moving storm over the continental shelf. We were not able to improve the repeatability of all of our time series at their different spatial selection. However, we showed that the ATMMO and the ATML+NTOL improved the repeatability of the estimated GPS positions to a better or at least increased the noise to a lesser extent compared to the other atmospheric models (ATML, ATMIB, NOIB). This observation reflects that we have to take into account NTOL, in particular for coastal sites and short periods.

We saw that the sub-daily loading displacements are significantly different at coastal and inland sites. Both, the model predictions and the GPS results confirmed this behaviour. We also see this pattern from the correlation values between the position estimates and the different models. We saw that the correlation between the GPS times series and the atmospheric models is weaker on coast than inland sites, however this relation was more pronounced during the perturbed period. It is indicating the huge impact of the storm. In the case of ATMMO, the correlation is even slightly stronger, which may reflect that the ocean response was more dynamic and the IB assumption applied in ATML is not the most adequate in the case of fast moving storms, especially given that this region is near a wide, shallow continental shelf. It seems the best configuration of models is that when we account for the dynamic ocean together with the atmospheric and the hydrological loading models. Although, we investigated two atmospheric models that involves a dynamic ocean response (ATMMO and ATML+NTOL), their difference is insignificant compared to the

obtained GPS formal errors. Besides the current GPS errors the resolution differences do not show up absolutely clear. Following the perception that more information is better, higher spatial and temporal resolution models should be used whenever they are available.

When we looked at the differences between the point calculated and grid derived loading time series we saw important differences that can appear over short periods or extreme environmental events. We suggest to GPS users to apply point calculated displacement series whenever it is possible for a posteriori correction for studies over short periods.

The spatially and temporally filtered maps need to be more investigated, however the capability of iPPP GPS to track the evolution of a windstorm is promising.

There are existing atmospheric pressure data series that have higher spatial and temporal resolution than the presented ones (MERRA or ECMWF) for our study region. The atmospheric pressure grids of Météo France are such grids. Thus, these datasets could provide additional information to refine and improve atmospheric loading models for future studies for this region. Also, the intercomparison of different GPS solutions (existing results and products of other softwares) could enhance our understanding, confirm our findings or open up newer ideas. The investigation of other violent storm events (the ones that are listed in the XWS) could further deepen our knowledge and enrich experiences of loading generated surface deformation.

Chapter 7

Challenges

This chapter is a brief overview of the limitations that occurred during my PhD thesis and also the perspectives that can be foreseen to improve this study and to show future research possibilities. We have shown the feasibility of GPS positioning for monitoring geophysical deformations and displacements and for revealing loading effects in the signal. However, the results and their repeatability depend on the computational method used. Indeed, different hypotheses, different computation strategies, different input geodetic parameters lead to differences in the results that may be more important than the amplitude of the phenomenon and that could be interpreted as meaningful phenomena. Moreover, we have used the GINS-PC software and the version that is provided to users is under continuous development so that the scientific community can be part of its active improvement. This thesis can contribute to this development provided that the artifacts that may have affected the results are identified and analysed.

In this research we have estimated time series from few months up to several years of length with sub-daily sampling using the iPPP mode benefiting the recent developments in the GINS-PC software. Meanwhile we have encountered some limiting factors that have never been reported or revealed before. Three main constraints had to be faced: jumps in the time series, the provided ocean-tidal loading correction file and the limitations of the user interface of the software.

This first section is aiming at (1) clarifying the origin of the encountered problems in order to make appropriate decisions and (2) drawing the attention of the GINS-PC

community - mainly colleagues involved with GPS-iPPP developments - who might face the same problems in similar situations.

7.1 Discontinuities in the time series

In our GPS time series we have observed jumps. These jumps have 1 week or longer period and random amplitude (up to 1 cm). They are visible on all the computed time series for all the stations everywhere on the Earth. They appear simultaneously for the different stations, however with slightly different magnitudes. It mostly affects the East component and to a lesser extent it is visible also in the North component. This problem was discovered in May 2013. After investigation, the jumps seem to correspond to a GRG referencing problem. It may also be correlated to the 3.66 days signal found only in GRG time series by Ray et al. [2013]. Figure 7.1 illustrates these jumps in iPPP time series that were obtained using GRG products at different European stations.

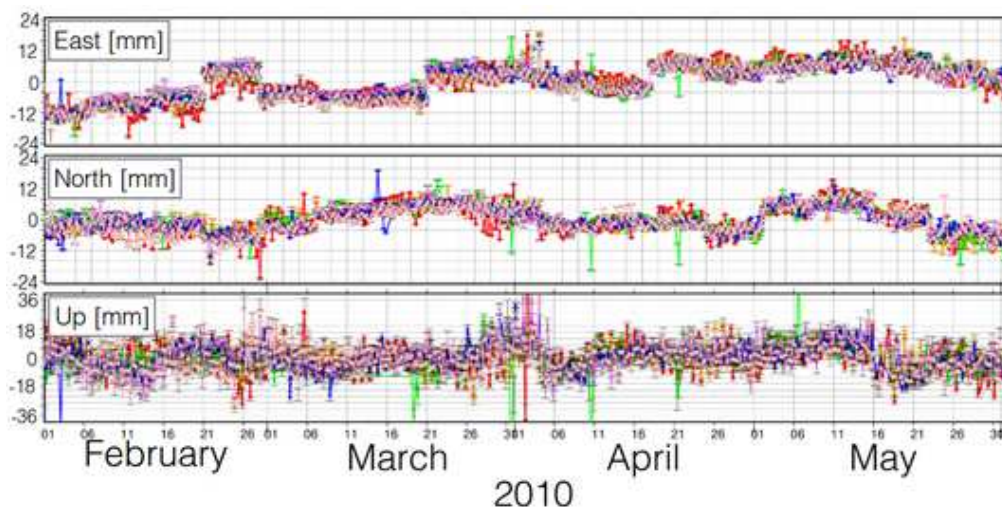


Figure 7.1 – Superposition of four month long iPPP time series, estimated with GRG products at different European stations: *BRST* (red), *LROC* (yellow), *PENC* (green), *POTS* (blue), *RIGA* (purple) and *TLSE* (pink).

We observed these jumps also in the PPP (float) time series using the GRG satellite orbit and clock data. In order to check if these discontinuities are linked to the GRG products we wanted to compare our solution to the one obtained using IGS products. Since iPPP computation is only possible with the GRG products we performed the comparison

7.1. DISCONTINUITIES IN THE TIME SERIES

on PPP time series using the same processing parameters. The only difference concerns the clock and orbit products (GRG vs. IGS). The PPP IGS solutions are illustrated in Figure 7.2. It is obvious that these new time series do not show any discontinuities. This confirms that the problem may come from GRG products. We note that the period of analysis corresponds to a period of great improvements in the GRG products computation.

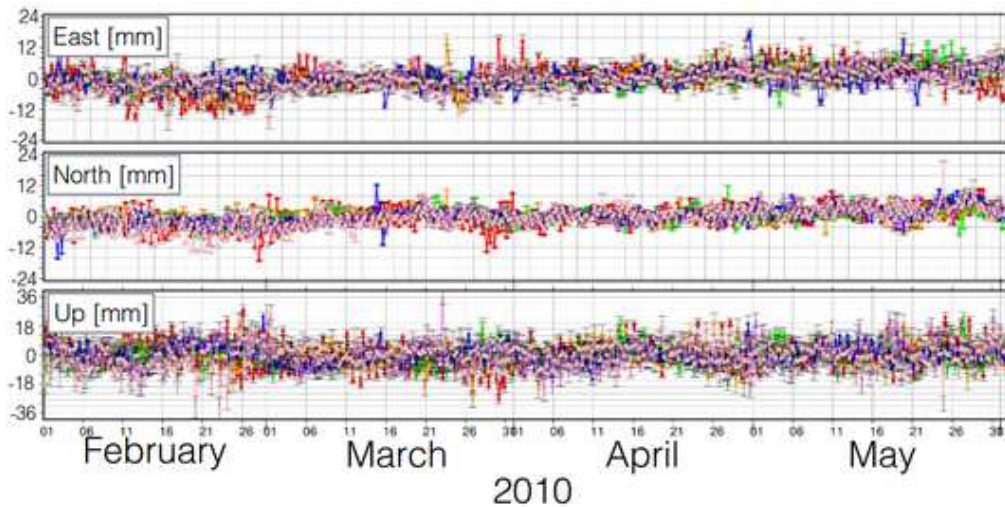


Figure 7.2 – Superposition of four months long PPP time series, estimated with IGS products at different European stations: *BRST* (red), *LROC* (yellow), *PENC* (green), *POTS* (blue), *RIGA* (purple) and *TLSE* (pink) (same as in Figure 7.1).

To correct these discontinuities we applied datum transformation using the Combination and Analysis of Terrestrial Reference Frame (CATREF) software [Altamimi 2006; Collilieux 2013] (IGN), but then it appears that some part of the signal can be absorbed in the transformation parameters (even if we use a globally well distributed reference network constructed from our global results). Figure 7.3 shows an example of the time series before and after the datum transformation.

Figures 7.4 and 7.5 represent the translation and scale parameters of our network (≈ 30 global stations). The big translation values (in absolute value > 10 cm for the X, between 0.6 and 2.2 cm for the Y, and > 5 cm for the Z components) are related to the used products or the processing. It seems that we have a weekly signal in the scale. Also the common error in the East coordinates of the time series are represented in the translation in Y direction.

7.1. DISCONTINUITIES IN THE TIME SERIES

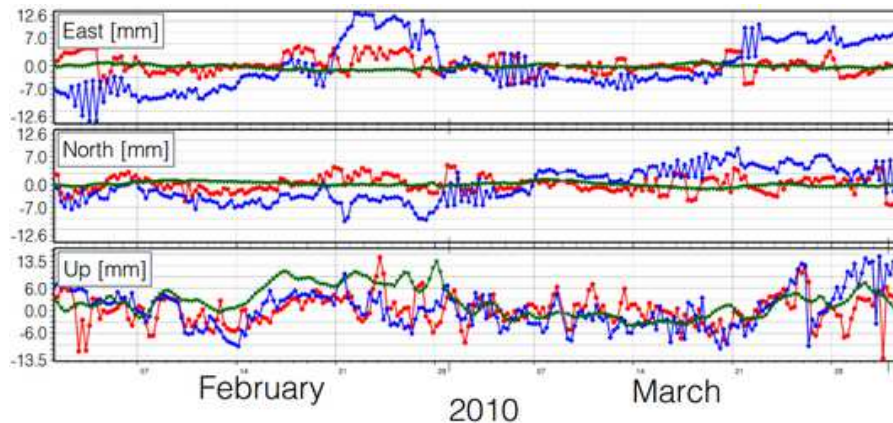


Figure 7.3 – Two months long, 6-hourly sampled iPPP time series (GRG) at *MAN2* station: before (blue), after (red) CATREF and predicted atmospheric pressure loading series (green) (in mm).

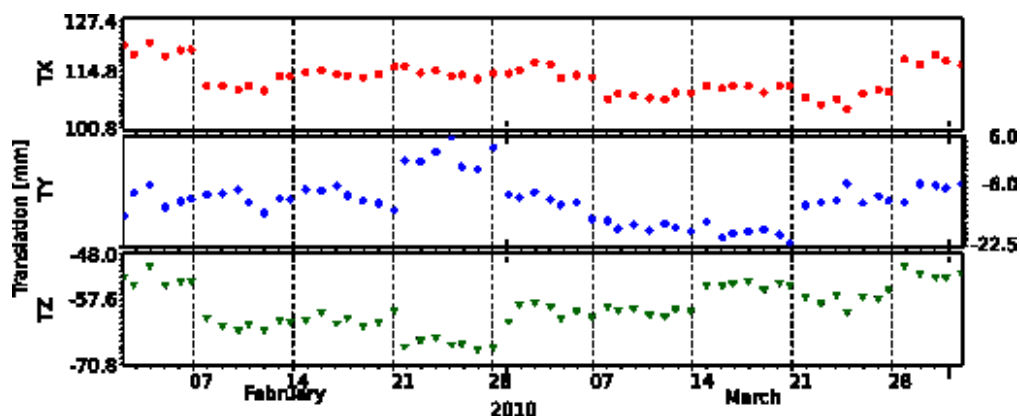


Figure 7.4 – Translation parameters obtained with CATREF.

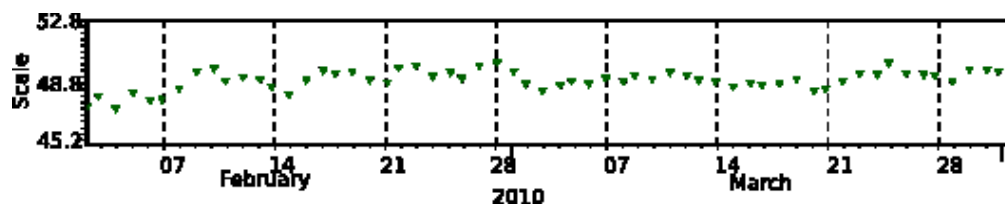


Figure 7.5 – Scale parameters obtained with CATREF.

7.1. DISCONTINUITIES IN THE TIME SERIES

This solution was not satisfactory in terms of seasonal signal analysis. Taking benefits of the new REPRO2 products (GR2) we compute new time series in order to see if the discontinuities are still present in the results. Figure 7.6 shows the results of new computations performed with GR2 products¹.

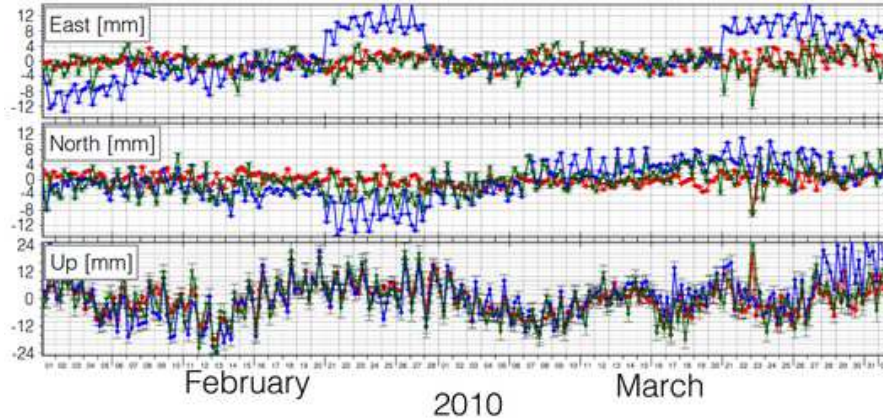


Figure 7.6 – Two months long time series, estimated with GRG (iPPP)(blue), GR2 (iPPP)(red) and IGS (PPP)(green) products at *RIGA* station.

In these new time series the artifact disappeared, which confirms that all our previous results were contaminated by the possible errors of the GRG products. The GR2 products provide constant quality over time because the latest models and processing strategy were applied uniformly throughout the time span by the CNES-CLS AC to generate the products. A rigorous study of GRG time series requires very cautious and prudent analysis because the used models and parameters are not homogeneous, they were continuously updated by time. We have verified the processing parameters that were applied in our analysis in GINS-PC and the discontinuities were reproducible when we used the GRG products. We have attempted to find relationship between our resulting discontinuities and the input orbit and clock products but we did not find any obvious evidence. However, the origin of these discontinuities is still unknown.

Thus we concluded that new computations using REPRO2 products would solve this problem. Therefore we were constrained to perform new computations of all the time series already computed in order to have reliable results and interpretation. Considering the remaining time for the thesis we had unfortunately to reduce the number of considered

¹Available for GINS-PC IHM users from 19th of May 2014.

sites for Xynthia and mostly for the global study. For the same reason, i.e. the required computational time, we also reduced the length of our time series (6 years) relative to the feasible time span with the GR2 products to obtain iPPP results for the global study of seasonal signal.

7.2 Ocean tidal correction in GINS-PC

During the Xynthia study we were surprised of diurnal and semi-diurnal remaining signals. Then we wonder about the ocean tidal loading correction made *a priori* in our GPS processing [Boy 2014]. This subsection aims to give an overview about the differences found between two ocean tidal loading correction files what we have applied during our GPS analysis. Namely between the *nominal_FES2004* that has been used in all of our previous studies and the *Scherneck_FES2004* that has been generated using the website of H.G. Scherneck (<http://holt.oso.chalmers.se/loading>). The *nominal_FES2004* file is the official OTL correction that is provided together with the GINS-PC software. It seems that there is a problem with it within the GINS-PC. Probably the files provided to the users and the one used by the CNES-CLS AC are different. Therefore we would suggest to supply only one OTL correction file, specifically the one that is used by the AC to generate their orbit and clock products. The following two maps show the differences of the $M2$ and $S2$ vertical amplitudes between the two files for the up component (Figure 7.7).

The following six figures (7.8 to 7.13) give information about the $M2$ amplitudes from both files and also about their differences in function of coastal distance for up, east and north directions, respectively.

Looking to Figures 7.7 to 7.13 it is clear that there are strong differences in the first 25 km in each component (up, East and North). We could find differences over 2 mm in the up component over a 200 km coastal range. It is possible to observe differences over 2 mm in the East and North components over a 150 km coastal range. Notably the differences in the horizontal directions are less pronounced than in the vertical one. Tables 7.1 and 7.2 show the RMS values of the iPPP time series for 10 stations in France².

²From 2010-02-01 until 2010-04-01.

7.2. OCEAN TIDAL CORRECTION IN GINS-PC

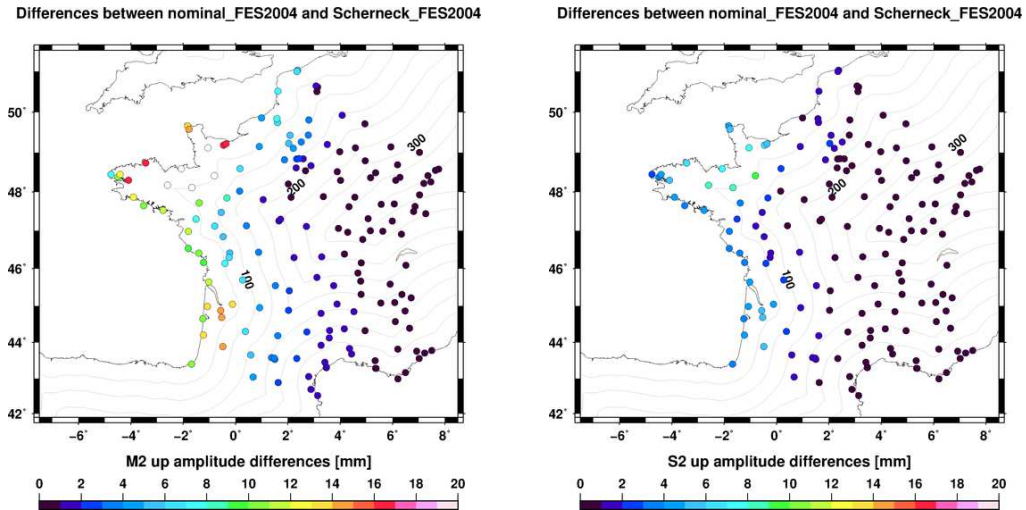


Figure 7.7 – Absolute differences between *nominal_FES2004* and *Scherneck_FES2004* OTL files in terms of $M2$ (left) and $S2$ (right) tidal wave up amplitudes (in mm). The contour lines represent the coastal distance at every 50 km. The circles with white color indicate a difference that is greater than 20 mm.

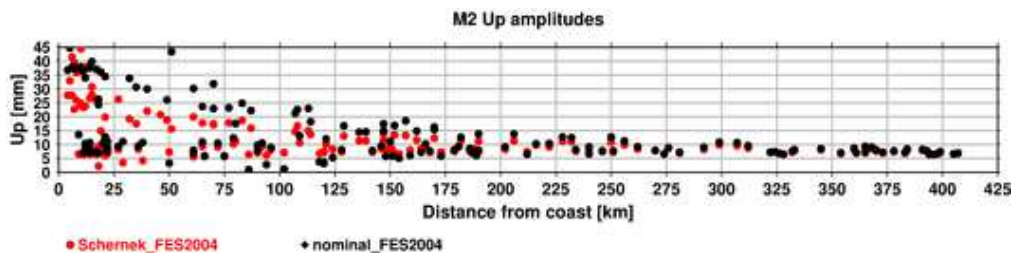


Figure 7.8 – *nominal_FES2004* (black) and *Scherneck_FES2004* (red) $M2$ tidal wave up amplitudes (in mm) in function of coastal distance.

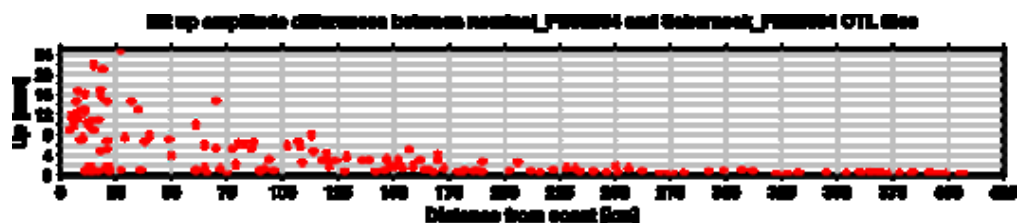


Figure 7.9 – *nominal_FES2004* and *Scherneck_FES2004* $M2$ tidal wave up amplitude differences (in mm) in function of coastal distance.

7.2. OCEAN TIDAL CORRECTION IN GINS-PC

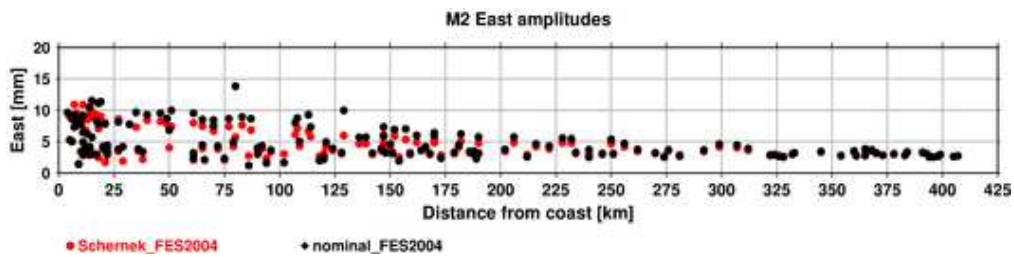


Figure 7.10 – *nominal_FES2004* (black) and *Schernek_FES2004* (red) *M2* tidal wave east amplitudes (in mm) in function of coastal distance.

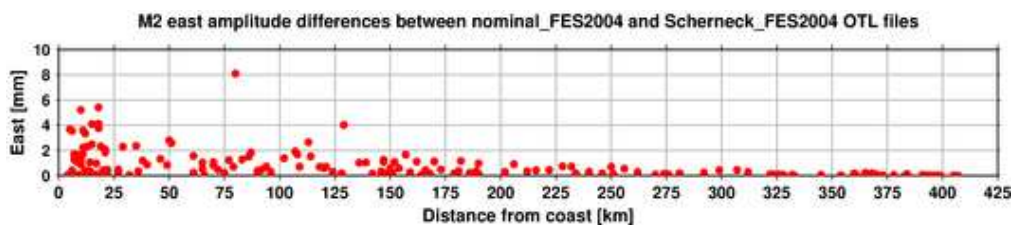


Figure 7.11 – *nominal_FES2004* and *Schernek_FES2004* *M2* tidal wave east amplitude differences (in mm) in function of coastal distance.

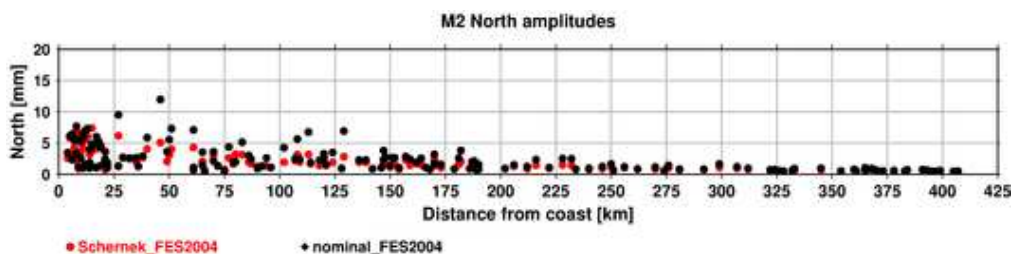


Figure 7.12 – *nominal_FES2004* (black) and *Schernek_FES2004* (red) *M2* tidal wave north amplitudes (in mm) in function of coastal distance.

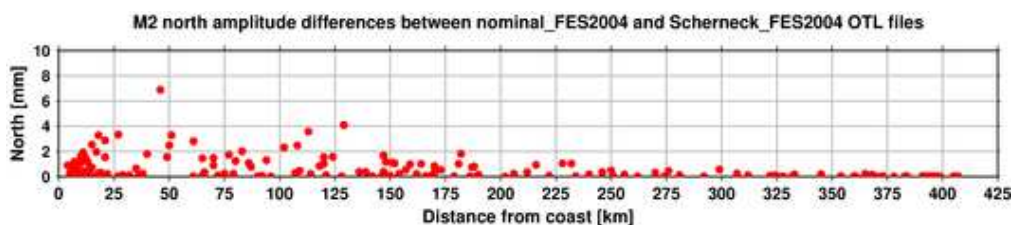


Figure 7.13 – *nominal_FES2004* and *Schernek_FES2004* *M2* tidal wave north amplitude differences (in mm) in function of coastal distance.

7.2. OCEAN TIDAL CORRECTION IN GINS-PC

Table 7.1 – Root-mean-square values of iPPP results at 10 RGP stations. The GPS time series were estimated using the *nominal_FES2004* OTL correction file and GRG orbit and clock products.

Station	East [mm]	North [mm]	Up [mm]
ANGE	6.3	4.9	8.1
BRES	6.8	5.9	11.7
CHIZ	6.7	5.7	8.2
DIPL	8.8	9.1	18.2
EOST	7.1	5.7	9.5
LROC	6.1	5.0	7.9
MAN2	7.3	5.5	8.0
MLVL	5.6	4.9	9.3
NICA	7.0	6.4	12.7
OPMT	7.7	5.9	8.4

Table 7.2 – Root-mean-square values of iPPP results at 10 RGP stations. The GPS time series were estimated using the *Scherneck_FES2004* OTL correction file and GRG orbit and clock products.

Station	East [mm]	North [mm]	Up [mm]
ANGE	6.1	4.6	7.5
BRES	6.7	5.8	11.4
CHIZ	6.7	5.5	7.5
DIPL	8.3	8.4	15.9
EOST	7.1	5.7	9.5
LROC	6.1	4.9	6.7
MAN2	6.9	4.6	7.0
MLVL	5.6	4.9	9.5
NICA	7.0	6.4	12.6
OPMT	7.7	5.8	8.3

7.2. OCEAN TIDAL CORRECTION IN GINS-PC

Table 7.3 – Root-mean-square values of iPPP result differences (Tables 7.2 and 7.1): $\text{RMS}(PPP_{\text{Scherneck_FES2004}} - PPP_{\text{nominal_FES2004}})$.

Station	East [mm]	North [mm]	Up [mm]
ANGE	0.9	1.6	3.2
BRES	0.7	1.0	2.6
CHIZ	0.5	1.3	3.2
DIPL	2.6	3.1	10.3
EOST	0.1	0.1	0.4
LROC	0.2	1.2	4.3
MAN2	2.4	2.5	5.6
MLVL	0.6	1.0	1.2
NICA	0.1	0.2	0.4
OPMT	0.8	0.8	1.7

The results were obtained using *nominal_FES2004* and *Scherneck_FES2004* OTL corrections together with *GRG* orbit and clock products. Meanwhile Table 7.3 shows the RMS of the difference of the two GPS time series obtained with the 2 OTL files. Table 7.4 represents the number of stations (also expressed in percentage) for which we can observe a certain amount of difference in the *M2* up amplitude. We draw the reader’s attention on the fact that the iPPP results presented here are obtained using the GRG orbits and clocks because the GR2 products were not available at that time.

The tables here detail the differences of *M2* and *S2* amplitudes between the *nominal_FES2004* and *Scherneck_FES2004* OTL files. Table 7.4 only considers the *M2* up differences meanwhile Table C.1 in the Appendix details the agreement for both tidal waves (*M2* and *S2*) and up, East and North components together with the site’s distance from the nearest coast. Also the values presented in Figures 7.7, 7.9, 7.11 and 7.13 are detailed in Table C.1.

11 tidal waves are presented in Figure 7.14 for *nominal_FES2004* and *Scherneck_FES2004* OTL files at 4 stations that are presented in Table 7.1, 7.2 and 7.3.

We have also looked to the spectra of our iPPP time series when the two different OTL corrections were applied. Important differences are clearly visible that were introduced by the distinct OTL corrections. Figures 7.15 and 7.16 show the power spectral density plots at *LROC* stations. With colored dashed lines we have indicated different periods,

7.2. OCEAN TIDAL CORRECTION IN GINS-PC

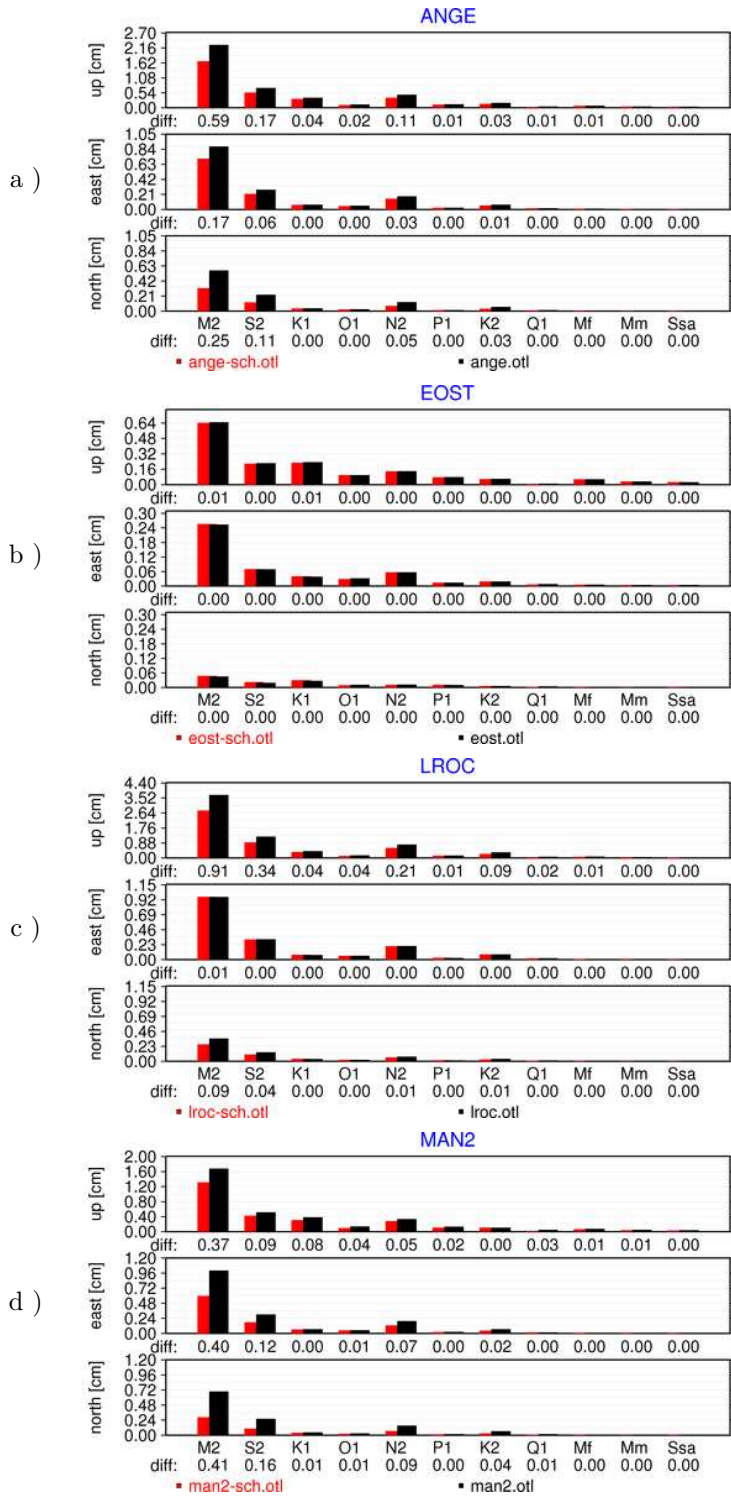


Figure 7.14 – Comparison of 11 tidal waves ($M2$, $S2$, $K1$, $O1$, $N2$, $P1$, $K2$, $Q1$, Mf , Mm and Ssa) from *nominal FES2004* (black) and *Scherneck FES2004* files (red) at a) *ANGE* [≈ 108 km], b) *EOST* [≈ 396 km], c) *LROC* [≈ 4 km] and d) *MAN2* [≈ 129 km].

Table 7.4 – Number of stations with $M2$ up tidal wave absolute differences above certain values between *nominal_FES2004* and *Scherneck_FES2004 OTL* files. The number of the found differences are expressed in percentage compared to the total number of 169 sites we have processed in France.

$M2$ Up difference	# of stations	Percentage [%]
> 2 mm	74	43.8
> 3 mm	67	39.6
> 4 mm	53	31.4
> 5 mm	50	29.6
> 6 mm	42	24.9
> 7 mm	35	20.7
> 8 mm	30	17.8
> 9 mm	30	17.8

corresponding to 8 tidal and 3 GRG related frequencies.

Finally, Figure 7.17 shows two iPPP residual time series which only differ in the applied OTL correction file. It is visible that the vertical direction is strongly affected and the effects on the horizontal components are less significant (in the North it is more pronounced).

These revealed differences justified the use of the new OTL corrections based on FES2012 for later uses. Since we have to rerun our calculations with the GR2 products we opted to apply the latest OTL file. Furthermore the FES2012 based OTL corrections had been used to produce GR2 orbit and clock estimates. Thus only with these corrections we can achieve the essential consistency. We remark here we attempted to compare the results obtained using GRG and GR2 products and then we have applied the FES2012 corrections to minimize the differences between the resulting time series.

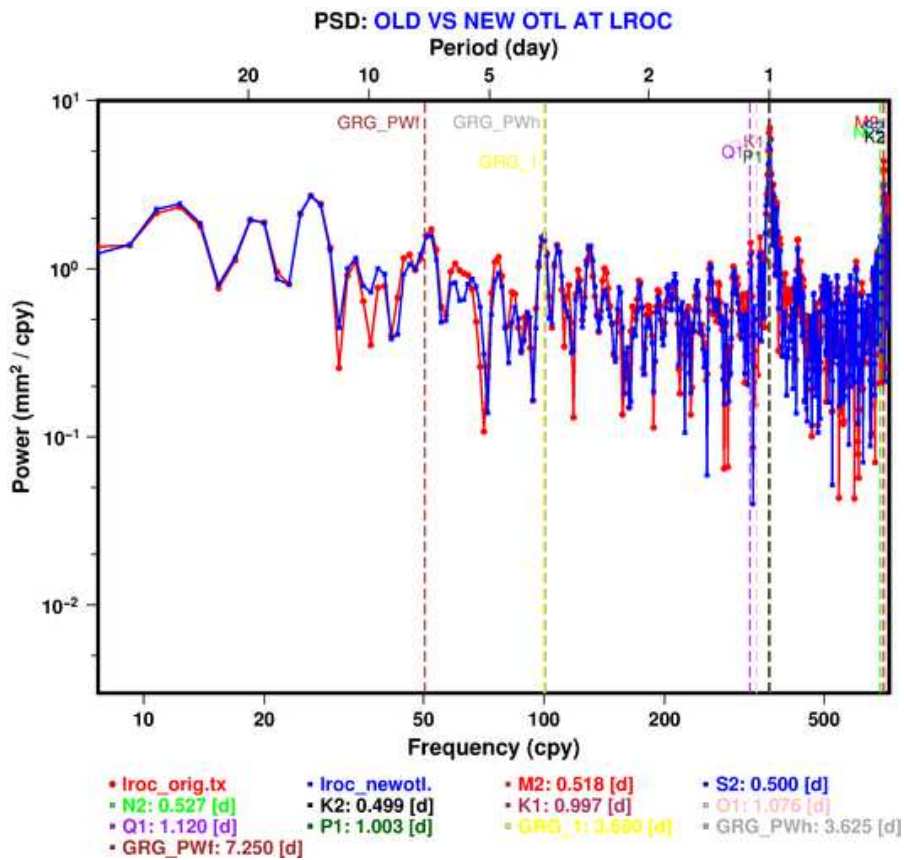


Figure 7.15 – Power spectral density at *LROC*, represents periods between 0.5 day and 50 days. The series estimated using the *nominal_FES2004* (red) and the *Scherneck_FES2004* (blue) OTL corrections. 8 tidal frequencies and 3 GRG related frequencies are indicated with vertical, colored dashed lines. *GRG_1* is the period of the signal reported by Ray et al. [2013], *GRG_PWh* is a half and *GRG_PWf* is a full GRG processing week (174 hours)

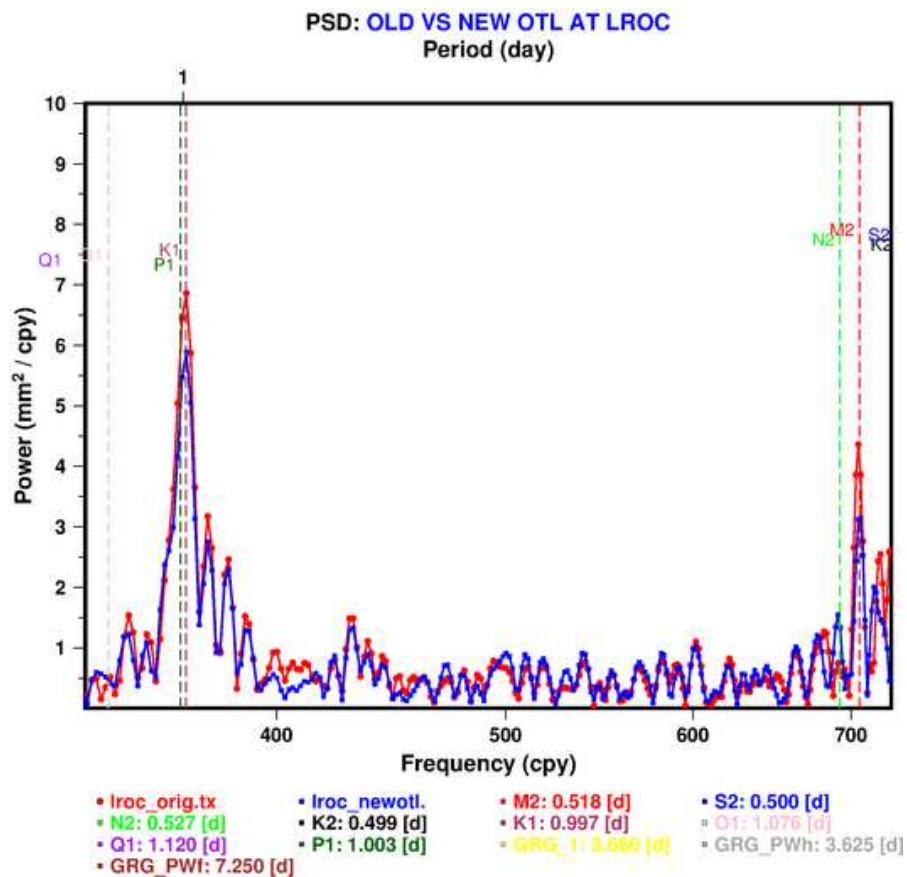


Figure 7.16 – Power spectral density at *LROC*, zoom between 0.5 and 1.1 day periods.

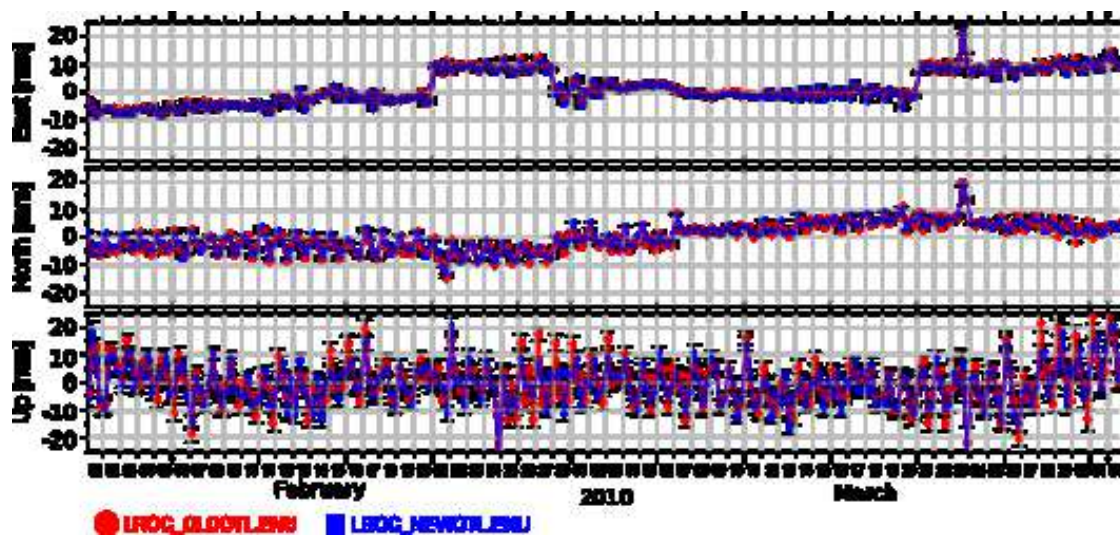


Figure 7.17 – Two months long iPPP GRG time series (in mm) of *LROC* station with two different OTL files: *nominal_fes2004* (red) and *nominal_fes2012* (blue).

7.3 Processing time using the interface

In this work we also had to face to another constraint. The use of the *GINS-PC* interface (*IHM*) is a limiting factor in our work since the processing time (due to its connection to Berenice server at Toulouse) is a little bit longer compared to other softwares³ (or to a desired possibility where simultaneous runs are enabled). When we have the necessary data for the calculation in our local server (after *PREPARS*⁴), the estimation process is quite quick, it is between some 15-25 seconds for one RINEX file and we can run simultaneous calculations, so the processing time could be decreased. However this scenario needs a previous run of the *PREPARS* that takes approximatively another 30-40 seconds for each *RINEX* files. The processes of *PREPARS* cannot run simultaneously, only one instance of *PREPARS* is authorized in one user account at a time and we must treat the desired input one by one because we need to use the *IHM* at this step. Summarising this, approximately 45-60 seconds are needed to process one observation file. To obtain a 3 year long time series for one station, we need to process more than 1000 daily observation files: that takes some 12-18 hours. According to the processing scheme that we apply at the moment (Figure 7.18) we run *IHM* for *PREPARS* and in the background we run the *exe_gins* from the command-line with the output of *PREPARS*, we treat the observation files in a sequential order, one by one for N stations. In this case the computational time is $N \times 12-18$ hours.

To overcome this limitation we have a plan that we did not yet managed to apply on our server. It is represented in Figure 7.19. According to this scheme in the first step we would need to run *PREPARS* for one station for a particular period in order to obtain all the common global parameters for the desired time span. It would take 12-18 hours since at this point only a sequential execution is authorized. However, it would result in a set of files that could be used as a database of parameteres that were specified during the first step. Then with dedicated command-line tools we would extract the necessary informations

³The computational time for example in *GIPSY-OASIS* is around 30 seconds per observation file. Furthermore simultaneous runs are possible. This means we need ≈ 9 hours for a 3 year long time series and we can imagine even 15 simultaneous tasks on our server, thus the computational burden can be reduced to ≈ 40 minutes for such a time series. For *GINS-PC* it would take approximatively 12 hours according to the best scenario.

⁴*PREPARS* includes the preprocessing and the collection of all the common processing parameters.

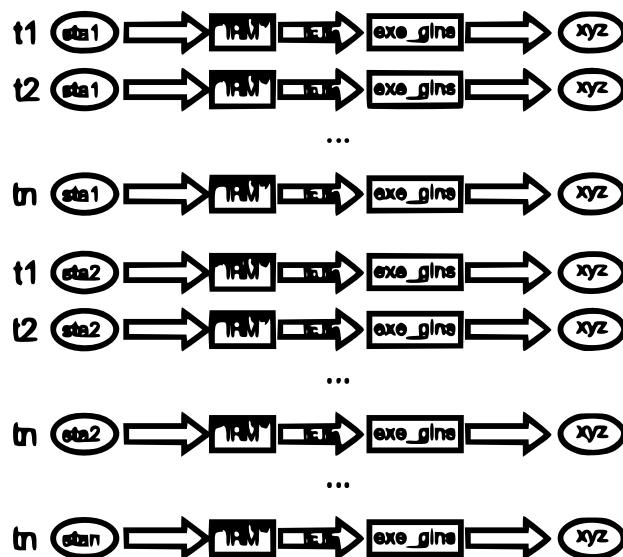


Figure 7.18 – Processing scheme that we apply at the moment.

and rebuild the intermediate processing file corresponding to the desired station at a given epoch. In this case we would be able to run up to 15 simultaneous processes (of course this number depends on the performance of the used server) which would significantly improve the required processing time for GINS-PC iPPP users.

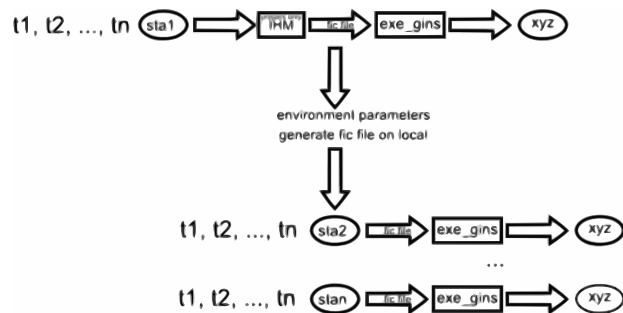


Figure 7.19 – Processing scheme that we would like to achieve.

Conclusion and Perspectives

Conclusion

To achieve the most accurate estimates of geodetic positions which are used later for geodynamical studies all the possible site displacement effects have to be considered. Some of them are already deeply investigated (e.g.: solid earth tide, ocean tidal loading). Their positive impact on geodetic time series were proven and they can be predicted with deterministic models. Thereby, they are routinely corrected during geodetic data analysis, in our case during GPS positioning. However, there are remaining signals in the GPS time series that are presumably present due to the neglect of non-tidal site displacement effects. It is of course under the assumption that all the known signals were properly corrected. These non-tidal loading phenomena can have important amplitudes and firmly fluctuate over the course of 24 hours. There are existing models to mitigate their influence, however the investigation of the models is still an ongoing process. Therefore they are not yet suggested to be applied during the estimation of the conventional instantaneous positions. They should be rather considered as *a posteriori* corrections for the moment. This work can be viewed as a small portion of the ongoing analysis of these effects. Thus the investigation of the phenomena to point out agreement and disagreement between the geodetic observations and the geophysical models to deliver information for the model and the GPS software developers for possible future improvements. It showed the performance of the present day's GPS technique and data analysis that was performed using the iPPP method with the GINS-PC software with GRG and GR2 products.

We have overviewed the structure of the Earth and the ongoing deformations on its surface in general. Then we discussed the loading effects, especially the non-tidal loading phenomena and presented their modeling. Later we have outlined the observation techniques and detailed the GPS technique that we have applied to obtain our results. Finally we presented our results concerning the feasibility of a global study and two regional studies. This work brought a contribution to the geodetic community in general and to the GINS-PC users community in particular. It is also a confirmation for the GINS-PC community and the CNES-CLS Analysis Center concerning their recent

development efforts.

This study was among the first ones to use sub-daily long iPPP time series estimated with GINS-PC to investigate loading effects and also to demonstrate the performance of the GR2 products. We have demonstrated that the improvements in the applied models and estimation strategy for the GR2 products greatly improved our results. Further investigation of the loading effects using GINS-PC and the advantages of its iPPP capability and the new GR2 products is very promising. We also showed that the loading effects can influence our geodynamical interpretation and suggested to apply their sum effect in geodynamical studies. We have demonstrated that the choice of geophysical models are very important during short period and for local studies.

Perspectives

If we would have extra time we could continue the global and the regional research with an extended network to confirm our findings. Thus, in the case of the Xynthia storm, for example the application of all the GPS observation data collected from the RGP and the European Permanent GNSS Network (EPN) network for the studied period would provide a better platform for model comparison and validation. The augmented number of stations is essential also for global testing and conclusions.

Nowadays, due to the reprocessing endeavour of the IGS and its analysis centers PPP users can process their own high quality time series with unified precision over time using state-of-the art GPS orbit and clock products. This improvement is attributed to the application of the cutting edge models and fine-tuned processing strategies during the GPS product generation at the analysis centers as well as the use of the coherent models on the user's side. Due to these conditions, long⁵ and precise time series can be obtained easily for any continuously measuring GPS stations all over the world. Therefore various loading phenomena as regards to natural hazard events can be rigorously analysed to improve global or even regional site displacement models by the means of GPS. As a guideline one could capitalize the benefits of the recently established eXtreme Wind Storms (XWS) catalogue⁶

⁵back to 1998 in the case of GR2 products

⁶<http://www.europeanwindstorms.org> (since May 2014)

to identify and gather information from the most violent European winter storms. These past extra-tropical cyclones and their assumed impact on the Earth's crust providing a challenging field to show the capability of the present day GPS precision and to perform a comprehensive evaluation of the different loading models over tens of powerful events. Since such hazards are quite frequent in Europe (around 4-5 during winter) and also all over the world and have various impacts on the Earth surface, maybe it is possible that their effect on station positions do not average out by time. Thus the thorough study of their impact and validation of loading models could contribute to the geodetic terrestrial reference frame.

If we succeed to speed up our estimation process then we do not need to limit ourselves for a restricted number of stations and a truncated time span. Thus, we could simultaneously go forward with the study of an extended global network as well as the maximum feasible iPPP data span (more than 14 years).

The long, GINS-PC estimated iPPP time series of large number of stations also would provide a platform for the intercomparison of different existing GPS solutions and various GPS processing softwares⁷. Different GPS estimates should provide similar results, therefore these comparisons could point out significant discrepancies of the divers products and help future decisions considering the applied processing strategy. Furthermore, the scientific community could benefit from a comparison based on iPPP and DD estimates of broad global and regional networks in the aspect of loading study to choose the best tool for an analysis.

Information based on comprehensive loading studies of different GPS processing strategies and results of other space geodetic techniques⁸ are complementary to improve our understanding of Earth deforming loading phenomena and enhance their models. Although, the space geodetic techniques presented in Chapter 2 have lower spatial and time resolution in general than the GPS, in turn they could provide very precise displacement estimates.

⁷For example GIPSY-OASIS [Zumberge et al. 1997], BERNESE [Dach et al. 2007a] or PANDA [Jing-nan and Mao-rong 2003].

⁸Such as VLBI, SLR, GRACE or InSAR.

Bibliographie

Altamimi Z. CATREF Software. Presentation, 2006. Ecole d'été GRGS, Forcalquier, 5 Août, 2006.

Altamimi Z., Collilieux X., Legrand J., Garayt B., and Boucher C. ITRF2005: A new release of the International Terrestrial Reference Frame based on time series of station positions and Earth Orientation Parameters. *Journal of Geophysical Research: Solid Earth*, 112(B9), 2007. ISSN 2156-2202. doi: 10.1029/2007JB004949.

Altamimi Z., Collilieux X., Métivier L., Rebischung P., and Lercier D. The International Terrestrial Reference Frame: current status and future challenges. Presentation, February 2014. GSFC Seminar, Greenbelt, February 10, 2014.

Altamimi Z., Sillard P., and Boucher C. ITRF2000: A new release of the International Terrestrial Reference Frame for earth science applications. *Journal of Geophysical Research: Solid Earth*, 107(B10):1–19, 2002. ISSN 2156-2202. doi: 10.1029/2001JB000561.

Altamimi Z., Collilieux X., and Métivier L. ITRF2008: an improved solution of the international terrestrial reference frame. *Journal of Geodesy*, 85(8):457–473, 2011. ISSN 0949-7714. doi: 10.1007/s00190-011-0444-4.

Asri A. Développement d'un outils d'analyse des séries temporelles pour l'étude des effets saisonniers déterminés par GPS. Master's thesis, University of Rennes, September 2014.

Balsamo G., Albergel C., Beljaars A., Boussetta S., Cloke H., Dee D., Dutra E., Muñoz Sabater J., Pappenberger F., de Rosnay P., Stockdale T., and Vitart F. ERA-

BIBLIOGRAPHIE

- Interim/Land: a global land water resources dataset. *Hydrology and Earth System Sciences Discussions*, 10(12):14705–14745, 2013. doi: 10.5194/hessd-10-14705-2013.
- Bertiger W., Desai S., Haines B., Harvey N., Moore A., Owen S., and Weiss J. Single receiver phase ambiguity resolution with GPS data. *Journal of Geodesy*, 84(5):327–337, 2010. ISSN 0949-7714. doi: 10.1007/s00190-010-0371-9.
- Bertin X. Personal communication, 02 2014.
- Bertin X., Bruneau N., Breilh J.-F., Fortunato A. B., and Karpytchev M. Importance of wave age and resonance in storm surges: The case Xynthia, Bay of Biscay. *Ocean Modelling*, 42(0):16 – 30, 2012. ISSN 1463-5003. doi: <http://dx.doi.org/10.1016/j.ocemod.2011.11.001>.
- Bevis M., Alsdorf D., Kendrick E., Fortes L. P., Forsberg B., Smalley R., and Becker J. Seasonal fluctuations in the mass of the Amazon River system and Earth’s elastic response. *Geophysical Research Letters*, 32(16), 2005. ISSN 1944-8007. doi: 10.1029/2005GL023491.
- Blewitt G. and Lavallée D. A. Effect of annual signals on geodetic velocity. *Journal of Geophysical Research: Solid Earth*, 107(B7), 2002. ISSN 2156-2202. doi: 10.1029/2001JB000570.
- Blewitt G., Altamimi Z., Davis J., Gross R., Kuo C.-Y., Lemoine F. G., Moore A. W., Neilan R. E., Plag H.-P., Rothacher M., Shum C. K., Sideris M. G., Schöne T., Tregoning P., and Zerbini S. *Geodetic Observations and Global Reference Frame Contributions to Understanding Sea-Level Rise and Variability*, pages 256–284. Wiley-Blackwell, 2010. ISBN 9781444323276. doi: 10.1002/9781444323276.ch9.
- Blewitt G. Carrier phase ambiguity resolution for the Global Positioning System applied to geodetic baselines up to 2000 km. *Journal of Geophysical Research: Solid Earth*, 94 (B8):10187–10203, 1989. ISSN 2156-2202. doi: 10.1029/JB094iB08p10187.
- Blewitt G. Self-consistency in reference frames, geocenter definition, and surface loading of the solid Earth. *Journal of Geophysical Research: Solid Earth*, 108(B2), 2003. ISSN 2156-2202. doi: 10.1029/2002JB002082.

BIBLIOGRAPHIE

- Boehm J., Niell A., Tregoning P., and Schuh H. Global Mapping Function (GMF): A new empirical mapping function based on numerical weather model data. *Geophysical Research Letters*, 33(7), 2006. ISSN 1944-8007. doi: 10.1029/2005GL025546.
- Boehm J., Heinkelmann R., Mendes Cerveira P., Pany A., and Schuh H. Atmospheric loading corrections at the observation level in VLBI analysis. *Journal of Geodesy*, 83(11):1107–1113, 2009. ISSN 0949-7714. doi: 10.1007/s00190-009-0329-y.
- Böhm J. and Schuh H. *Atmospheric Effects in Space Geodesy*. Springer Atmospheric Sciences. Springer, 2013. ISBN 9783642369322.
- Boy J.-P. *Modélisation des surcharges induites par les fluides superficiels*. PhD thesis, l'Université Louis Pasteur, Strasbourg I, 2007.
- Boy J.-P. Personal communication, 01 2014.
- Breilh J. F., Chaumillon E., Bertin X., and Gravelle M. Assessment of static flood modeling techniques: application to contrasting marshes flooded during Xynthia (western France). *Natural Hazards and Earth System Science*, 13(6):1595–1612, 2013. doi: 10.5194/nhess-13-1595-2013.
- Calais E., Han J. Y., DeMets C., and Nocquet J. M. Deformation of the North American plate interior from a decade of continuous GPS measurements. *Journal of Geophysical Research: Solid Earth*, 111(B6), 2006. ISSN 2156-2202. doi: 10.1029/2005JB004253.
- Carrère L. and Lyard F. Modeling the barotropic response of the global ocean to atmospheric wind and pressure forcing - comparisons with observations. *Geophysical Research Letters*, 30(6), 2003. ISSN 1944-8007. doi: 10.1029/2002GL016473.
- Carrère L., Lyard F., Cancet M., Guillot A., and Roblou L. FES2012: A new global tidal model taking taking advantage of nearly 20 years of altimetry, Proceedings of meeting "20 Years of Altimetry", Venice, 2012.
- Chambers D. P., Tamisiea M. E., Nerem R. S., and Ries J. C. Effects of ice melting on GRACE observations of ocean mass trends. *Geophysical Research Letters*, 34(5), 2007. ISSN 1944-8007. doi: 10.1029/2006GL029171.

BIBLIOGRAPHIE

- Chen Q., van Dam T., Sneeuw N., Collilieux X., Weigelt M., and Rebischung P. Singular spectrum analysis for modeling seasonal signals from GPS time series. *Journal of Geodynamics*, 72(0):25 – 35, 2013a. ISSN 0264-3707. doi: <http://dx.doi.org/10.1016/j.jog.2013.05.005>. SI: Geodetic Earth System.
- Chen Q., Zhang J., Wang L., van Dam T., Weigelt M., Devaraju B., and Sneeuw N. Comparison of seasonal hydrological loading information from GPS and GRACE observations, 2013b. IAG Scientific Assembly 2013, Potsdam, Germany, 1 - 6 September 2013, Poster.
- Chen Q., van Dam T., Sneeuw N., Collilieux X., and Rebischung P. Extracting seasonal signals from continuous GPS time series with singular spectrum analysis, April 2012. EGU General Assembly, Vienna, Austria, 22 - 27 April 2012, Poster.
- Collilieux X. *Analyse des séries temporelles de position des stations de géodésie spatiales: Application au Repère International de Référence Terrestre (ITRF)*. PhD thesis, École Doctorale D'Astronomie et D'Astrophysique D'Île-De-France, June 2008. (Analyses of space geodetic station time series: Application for the International Terrestrial Reference Frame (ITRF)).
- Collilieux X. Personal communication, 12 2013.
- Collilieux X., Altamimi Z., Ray J., van Dam T., and Wu X. Effect of the satellite laser ranging network distribution on geocenter motion estimation. *Journal of Geophysical Research: Solid Earth*, 114(B4), 2009. ISSN 2156-2202. doi: [10.1029/2008JB005727](https://doi.org/10.1029/2008JB005727). URL <http://dx.doi.org/10.1029/2008JB005727>. B04402.
- Collilieux X., Métivier L., Altamimi Z., Dam T., and Ray J. Quality assessment of GPS reprocessed terrestrial reference frame. *GPS Solutions*, 15(3):219–231, 2011. ISSN 1080-5370. doi: [10.1007/s10291-010-0184-6](https://doi.org/10.1007/s10291-010-0184-6).
- Collilieux X., van Dam T., Ray J., Coulot D., Métivier L., and Altamimi Z. Strategies to mitigate aliasing of loading signals while estimating GPS frame parameters. *Journal of Geodesy*, 86(1):1–14, 2012. ISSN 0949-7714. doi: [10.1007/s00190-011-0487-6](https://doi.org/10.1007/s00190-011-0487-6).

BIBLIOGRAPHIE

- Collilieux X., Altamimi Z., Coulot D., van Dam T., and Ray J. Impact of loading effects on determination of the International Terrestrial Reference Frame. *Advances in Space Research*, 45(1):144 – 154, 2010. ISSN 0273-1177. doi: <http://dx.doi.org/10.1016/j.asr.2009.08.024>.
- Dach R., Hugentobler U., Fridez P., and Meindl M. *Bernese GPS Software Version 5.0*. Astronomical Institute, University of Bern, January 2007a.
- Dach R., Hugentobler U., Fridez P., and Meindl M. *Bernese GPS Software, Version 5.0*. Astronomical Institute, University of Bern, 01 2007b. URL <http://www.bernese.unibe.ch/docs/D0CU50.pdf>.
- Dach R., Böhm J., Lutz S., Steigenberger P., and Beutler G. Evaluation of the impact of atmospheric pressure loading modeling on GNSS data analysis. *Journal of Geodesy*, 85(2):75–91, 2011. ISSN 0949-7714. doi: 10.1007/s00190-010-0417-z.
- Darwin G. On variations in the vertical due to elasticity of the Earth's surface. *Phil. Mag.*, 14(90):409–427, 1882. Ser. 5.
- Davis J. L., Elósegui P., Mitrovica J. X., and Tamisiea M. E. Climate-driven deformation of the solid Earth from GRACE and GPS. *Geophysical Research Letters*, 31(24), 2004. ISSN 1944-8007. doi: 10.1029/2004GL021435.
- Davis J. L., Wernicke B. P., and Tamisiea M. E. On seasonal signals in geodetic time series. *Journal of Geophysical Research: Solid Earth*, 117(B1), 2012. ISSN 2156-2202. doi: 10.1029/2011JB008690.
- Dong D., Yunck T., and Heflin M. Origin of the International Terrestrial Reference Frame. *Journal of Geophysical Research: Solid Earth*, 108(B4), 2003. ISSN 2156-2202. doi: 10.1029/2002JB002035.
- Dow J. M., Neilan R., and Rizos C. The International GNSS Service in a changing landscape of Global Navigation Satellite Systems. *Journal of Geodesy*, 83(3-4):191–198, 2009. ISSN 0949-7714. doi: 10.1007/s00190-008-0300-3.

BIBLIOGRAPHIE

- Farrell W. E. Deformation of the Earth by surface loads. *Reviews of Geophysics*, 10(3): 761–797, 1972. ISSN 1944-9208. doi: 10.1029/RG010i003p00761.
- Ferenc M., Nicolas J., van Dam T., Polidori L., Rigo A., and Vernant P. An estimate of the influence of loading effects on tectonic velocities in the Pyrenees. *Studia Geophysica et Geodaetica*, 58(1):56–75, 2014. ISSN 0039-3169. doi: 10.1007/s11200-012-0458-2.
- Fratepietro F., Baker T. F., Williams S. D. P., and Camp M. V. Ocean loading deformations caused by storm surges on the northwest European shelf. *Geophysical Research Letters*, 33(6), March 2006. doi: 10.1029/2005GL025475.
- Fu Y., Freymueller J. T., and Jensen T. Seasonal hydrological loading in southern Alaska observed by GPS and GRACE. *Geophysical Research Letters*, 39(15), 2012a. ISSN 1944-8007. doi: 10.1029/2012GL052453.
- Fu Y., Freymueller J. T., and van Dam T. The effect of using inconsistent ocean tidal loading models on GPS coordinate solutions. *Journal of Geodesy*, 86(6):409–421, 2012b. ISSN 0949-7714. doi: 10.1007/s00190-011-0528-1.
- Fukumori I. A Partitioned Kalman Filter and Smoother. *Monthly Weather Review*, 130(5):1370–1383, May 2002. ISSN 0027-0644. doi: 10.1175/1520-0493(2002)130<1370:APKFAS>2.0.CO;2.
- Fund F., Morel L., and Mocquet A. A discussion of height reductions for Zenith Hydrostatic Delays derived from weather models. *Journal of Applied Geodesy*, 5(2):71–80, 2011a. doi: 10.1515/jag.2011.006.
- Fund F., Morel L., Mocquet A., and Boehm J. Assessment of ECMWF-derived tropospheric delay models within the EUREF Permanent Network. *GPS Solutions*, 15(1):39–48, 2011b. ISSN 1080-5370. doi: 10.1007/s10291-010-0166-8.
- Fund F., Perosanz F., Testut L., and Loyer S. An Integer Precise Point Positioning technique for sea surface observations using a GPS buoy. *Advances in Space Research*, 51(8):1311 – 1322, 2013. ISSN 0273-1177. doi: <http://dx.doi.org/10.1016/j.asr.2012.09.028>.

BIBLIOGRAPHIE

- Geng J., Meng X., Dodson A., and Teferle F. Integer ambiguity resolution in precise point positioning: method comparison. *Journal of Geodesy*, 84(9):569–581, 2010. ISSN 0949-7714. doi: 10.1007/s00190-010-0399-x.
- Geng J., Williams S. D., Teferle F. N., and Dodson A. H. Detecting storm surge loading deformations around the southern North Sea using subdaily GPS. *Geophysical Journal International*, 191(2):569–578, 2012. ISSN 1365-246X. doi: 10.1111/j.1365-246X.2012.05656.x.
- Grenerczy G., Jámbor T., Ferenc M., and Kenyeres A. Dynamic deformation of seismic waves: Investigating the extremities with high rate GNSS, 2011. American Geophysical Union, Fall Meeting.
- Herring A. T., King W. R., and McClusky C. S. Introduction to GAMIT/GLOBK, October 2010. URL http://www-gpsg.mit.edu/~simon/gtgk/Intro_GG.pdf.
- Hofmann-Wellenhof B. and Moritz H. *Physical Geodesy*. Springer, 2005. ISBN 9783211335451.
- Hofmann-Wellenhof B., Lichtenegger H., and Wasle E. *GNSS – Global Navigation Satellite Systems: GPS, GLONASS, Galileo, and more*. Springer, 2007. ISBN 9783211730171.
- Ilk K. H., Flury J., Rummel R., Schwintzer P., Bosch W., Haas C., Schröter J., Stammer D., Zahel W., Miller H., Dietrich R., Huybrechts P., Schmeling H., Wolf D., Götze H., Riegger J., Bardossy A., Güntner A., and Gruber T. Mass Transport and Mass Distribution in the Earth System (Contribution of the New Generation of SSatellite Gravity and Altimetry Missions to Geosciences). GOCE-Projektbüro Deutschland, Technische Universität München; GeoForschungsZentrum Potsdam, January 2005.
- Jiang W., Li Z., van Dam T., and Ding W. Comparative analysis of different environmental loading methods and their impacts on the GPS height time series. *Journal of Geodesy*, 87(7):687–703, 2013. ISSN 0949-7714. doi: 10.1007/s00190-013-0642-3.
- Jing-nan L. and Mao-rong G. PANDA software and its preliminary result of positioning and orbit determination. *Wuhan University Journal of Natural Sciences*, 8(2):603–609, 2003. ISSN 1007-1202. doi: 10.1007/BF02899825.

BIBLIOGRAPHIE

- Kalnay E., Kanamitsu M., Kistler R., Collins W., Deaven D., Gandin L., Iredell M., Saha S., White G., Woollen J., Zhu Y., Leetmaa A., Reynolds R., Chelliah M., Ebisuzaki W., Higgins W., Janowiak J., Mo K. C., Ropelewski C., Wang J., Jenne R., and Joseph D. The NCEP/NCAR 40-Year Reanalysis Project. *Bull. Amer. Meteor. Soc.*, 77(3):437–471, March 1996. doi: [http://dx.doi.org/10.1175/1520-0477\(1996\)077<0437:TNYRP>2.0.CO;2](http://dx.doi.org/10.1175/1520-0477(1996)077<0437:TNYRP>2.0.CO;2).
- Kim S.-B., Lee T., and Fukumori I. Mechanisms Controlling the Interannual Variation of Mixed Layer Temperature Averaged over the Niño-3 Region. *Journal of Climate*, 20(15): 3822–3843, Aug 2007. ISSN 0894-8755. doi: 10.1175/JCLI4206.1.
- King M., Colemar R., and Nguyen L. N. Spurious periodic horizontal signals in sub-daily GPS position estimates. *Journal of Geodesy*, 77(1-2):15–21, 2003. ISSN 0949-7714. doi: 10.1007/s00190-002-0308-z.
- King M. A., Altamimi Z., Boehm J., Bos M., Dach R., Elosegui P., Fund F., Hernández-Pajares M., Lavalée D., Mendes Cerveira P. J., Penna N., Riva R. E. M., Steigenberger P., van Dam T., Vittuari L., Williams S., and Willis P. Improved Constraints on Models of Glacial Isostatic Adjustment: A Review of the Contribution of Ground-Based Geodetic Observations. *Surveys in Geophysics*, 31(5):465–507, 2010. ISSN 0169-3298. doi: 10.1007/s10712-010-9100-4.
- King M. A., Watson C. S., Penna N. T., and Clarke P. J. Subdaily signals in GPS observations and their effect at semiannual and annual periods. *Geophysical Research Letters*, 35(3), 2008. ISSN 1944-8007. doi: 10.1029/2007GL032252. URL <http://dx.doi.org/10.1029/2007GL032252>.
- Kintner, Humphreys, and Hinks. GNSS and Ionospheric Scintillation, How to Survive the Next Solar Maximum. *InsideGNSS*, pages 22–30, July/August 2009.
- Kouba J. A Guide to Using International GNSS Service (IGS) Products. Technical report, Geodetic Survey Division, Natural Resources Canada, May 2009. URL http://igs.org/igs_cb/resource/pubs/UsingIGSProductsVer21.pdf.

BIBLIOGRAPHIE

- Kovalevsky J., Mueller I. I., and Kolaczek B. *Reference frames in astronomy and geophysics*. Astrophysics and space science library. Kluwer Academic Publishers, 1989. ISBN 9780792301820.
- Lambeck K. *The Earth's Variable Rotation*. Cambridge University Press, 1980. ISBN 9780511569579. Cambridge Books Online.
- Laurichesse D. and Mercier F. Integer Ambiguity Resolution on Undifferenced GPS Phase Measurements and its Application to PPP. *Proceedings of the 20th International Technical Meeting of the Satellite Division of The Institute of Navigation (ION GNSS 2007)*, Fort Worth, TX, pages 839–848, September 2007.
- Laurichesse D., Mercier F., Berthias J.-P., Broca P., and Cerri L. Integer Ambiguity Resolution on Undifferenced GPS Phase Measurements and Its Application to PPP and Satellite Precise Orbit Determination. *NAVIGATION, Journal of the Institute of Navigation*, 56(2):135–149, 2009.
- Lavallée D. A., Moore P., Clarke P. J., Petrie E. J., van Dam T., and King M. A. J2: An evaluation of new estimates from GPS, GRACE, and load models compared to SLR. *Geophysical Research Letters*, 37(22), 2010. ISSN 1944-8007. doi: 10.1029/2010GL045229.
- Legru B. *Apport de la fusion de mesures GPS et Topométriques pour l'auscultation de précision*. PhD thesis, L'école doctorale du CNAM, 2011.
- Leick A. *GPS Satellite Surveying*. Wiley, 3 edition, 2004. ISBN 9780471059301.
- Li Z., Jiang W., Ding W., Deng L., and Peng L. Estimates of Minor Ocean Tide Loading Displacement and Its Impact on Continuous GPS Coordinate Time Series. *Sensors*, 14(3):5552–5572, 2014. ISSN 1424-8220. doi: 10.3390/s140305552.
- Llubes M., Florsch N., Boy J.-P., Amalvict M., Bonnefond P., Bouin M.-N., Durand S., Esnault M.-F., Exertier P., Hinderer J., Lalancette M.-F., Masson F., Morel L., Nicolas J., Vergnolle M., and Wöppelmann G. Multi-technique monitoring of ocean tide loading in northern France . *Comptes Rendus Geoscience*, 340(6):379 – 389, 2008. ISSN 1631-0713. doi: <http://dx.doi.org/10.1016/j.crte.2008.03.005>.

BIBLIOGRAPHIE

- Loyer S., Perosanz F., Mercier F., Capdeville H., and Marty J.-C. Zero-difference GPS ambiguity resolution at CNES-CLS IGS Analysis Center. *Journal of Geodesy*, 86(11): 991–1003, 2012. ISSN 0949-7714. doi: 10.1007/s00190-012-0559-2.
- Lyard F., Lefèvre F., Letellier T., and Francis O. Modelling the global ocean tides: modern insights from FES2004. *Ocean Dynamics*, 56(5-6):394–415, 2006. ISSN 1616-7341. doi: 10.1007/s10236-006-0086-x.
- Malardel S. *Fondamentaux de météorologie: à l'école du temps*. Editions Cépaduès, 2009. ISBN 9782854288513.
- Manabe S., Sato T., Sakai S., and K. Y. Atmospheric Loading Effect on VLBI Observations. Proceedings the AGU Chapman Conference on Geodetic VLBI: Monitoring Global Change. Technical report, NOAA, April 1991. NOS 137 NGS 49, pp. 111-122. of Meeson, B. W., F. E. Corprew, J. M. P. McManus, D.
- Marty C. J., Loyer S., Perosanz F., Mercier F., Bracher G., Legresy B., Portier L., Capdeville H., Fund F., Lemoine M. J., and Biancale R. GINS: The CCNES/GRGS GNSS Scientific Software, 2012. URL http://hpiers.obspm.fr/combinaison/documentation/articles/GINS_Marty.pdf.
- Mathews P. M., Dehant V., and Gipson J. M. Tidal station displacements. *Journal of Geophysical Research: Solid Earth*, 102(B9):20469–20477, 1997. ISSN 2156-2202. doi: 10.1029/97JB01515.
- Melachroinos A. S., Biancale R., Llubes M., Perosanz F., Lyard F., Vergnolle M., Bouin M.-N., Masson F., Nicolas J., Morel L., and Durand S. Ocean tide loading (OTL) displacements from global and local grids: comparisons to GPS estimates over the shelf of Brittany, France. *Journal of Geodesy*, 82(6):357–371, 2008. ISSN 0949-7714. doi: 10.1007/s00190-007-0185-6.
- Melachroinos S., Biancale R., and Perosanz F. Ocean loading effects in a high time resolution GPS analysis: Implications and artefacts with GINS software. In *International Global Navigation Satellite Service (IGS) Workshop proceedings*. ESA European operation space center, Darmstadt, Germany, 2006.

BIBLIOGRAPHIE

- Melbourne G. W. The case for ranging in GPS-based geodetic systems. In *Goad CC (ed) First International Symposium on Precise Positioning with GPS*, pages 373–386. US Department of Commerce, Rockville, M. D., 1985.
- Mémin A., Watson C., Haigh I. D., MacPherson L., and Tregoning P. Non-linear motions of Australian geodetic stations induced by non-tidal ocean loading and the passage of tropical cyclones. *Journal of Geodesy*, 88(10):927–940, 2014. ISSN 0949-7714. doi: 10.1007/s00190-014-0734-8.
- Mignard F. FAMOUS: Famous Analysis Mapping On Unusual Sampling, 2005. OCA.
- Nahmani S. *Méthodologies en traitement de données GPS pour les Sciences de l'Environnement: Contributions à l'étude de la Mousson en Afrique de l'Ouest*. PhD thesis, Université Pierre et Marie Curie, Paris, 2012.
- Nahmani S., Bock O., Bouin M.-N., Santamaría-Gómez A., Boy J.-P., Collilieux X., Métivier L., Panet I., Genthon P., de Linage C., and Wöppelmann G. Hydrological deformation induced by the West African Monsoon: Comparison of GPS, GRACE and loading models. *Journal of Geophysical Research: Solid Earth*, 117(B5), 2012. ISSN 2156-2202. doi: 10.1029/2011JB009102.
- Nicolas J., Perosanz F., Rigo A., Le Bliguet G., Morel L., and Fund F. Impact of Loading Phenomena on Velocity Field Computation from GPS Campaigns: Application to RESPYR GPS Campaign in the Pyrenees. In Kenyon S., Pacino M. C., and Marti U., editors, *Geodesy for Planet Earth*, volume 136 of *International Association of Geodesy Symposia*, pages 643–649. Springer Berlin Heidelberg, 2012. ISBN 978-3-642-20337-4. doi: 10.1007/978-3-642-20338-1_79.
- NOAA. ETOPO5, Data Announcement 88-MGG-02, Digital relief of the Surface of the Earth, 1988. National Geophysical Data Center, Boulder, Colorado.
- Nocquet J.-M. Present-day kinematics of the Mediterranean: A comprehensive overview of GPS results. *Tectonophysics*, 579(0):220 – 242, 2012. ISSN 0040-1951. doi: <http://dx.doi.org/10.1016/j.tecto.2012.03.037>. Orogenic processes and structural heritage in Alpine-type mountain belts.

BIBLIOGRAPHIE

- Nordman M., Mäkinen J., Virtanen H., Johansson J. M., Bilker-Koivula M., and Virtanen J. Crustal loading in vertical GPS time series in Fennoscandia. *Journal of Geodynamics*, 48(3-5):144 – 150, 2009. ISSN 0264-3707. doi: <http://dx.doi.org/10.1016/j.jog.2009.09.003>. New Challenges in Earth's Dynamics - Proceedings of the 16th International Symposium on Earth Tides.
- Penna N. T., King M. A., and Stewart M. P. GPS height time series: Short-period origins of spurious long-period signals. *Journal of Geophysical Research: Solid Earth*, 112(B2), 2007. ISSN 2156-2202. doi: 10.1029/2005JB004047.
- Perosanz F. Personal communication, 07 2013.
- Petit G. and Luzum B. IERS Conventions (2010). Technical report, Frankfurt am Main: Verlag des Bundesamts für Kartographie und Geodäsie, 2010. (IERS Technical Note ; 36), 2010. 179 pp., ISBN 3-89888-989-6.
- Petrov L. and Boy J.-P. Study of the atmospheric pressure loading signal in very long baseline interferometry observations. *Journal of Geophysical Research: Solid Earth*, 109 (B3), 2004. ISSN 2156-2202. doi: 10.1029/2003JB002500.
- Polidori L., Bacci P.-A., Simonetto E., Morel L., Durand F., Durand S., and Nicolas J. On the potential of GPS-InSAR combination to improve the accuracy of ground deformation monitoring: simulation-based validation. In *Anais XVI Simpósio Brasileiro de Sensoriamento Remoto - SBSR, Foz do Iguaçu, PR, Brasil, INPE*, volume 16, pages 8467–8474, April 2013.
- Rabbal W. and Zschau J. Static deformations and gravity changes at the earth's surface due to atmospheric loading. *J. Geophys.*, 56:81–99, 1985.
- Ramos F. L. G., de Miranda F. P., Trouvé E., and Soler L. Urban subsidence as a local response of Amazonas River flooding observed by satellite SAR Interferometry. *IGARSS & 35th Canadian Symposium on Remote Sensing*, 2014. Québec, Canada, July 13-18.
- Ray J., Altamimi Z., Collilieux X., and Dam T. Anomalous harmonics in the spectra of GPS position estimates. *GPS Solutions*, 12(1):55–64, 2008. ISSN 1080-5370. doi: 10.1007/s10291-007-0067-7.

BIBLIOGRAPHIE

- Ray J., Rebeschung P., Kouba J., and Chen W. Rotational errors in IGS orbit & ERP products, July 2012. IGS Workshop, Orbit Modeling Session, Olsztyn, Poland.
- Ray J., Griffiths J., Collilieux X., and Rebeschung P. Subseasonal GNSS positioning errors. *Geophysical Research Letters*, 40(22):5854–5860, 2013. ISSN 1944-8007. doi: 10.1002/2013GL058160.
- Ray R. D. and Ponte R. M. Barometric tides from ECMWF operational analyses. *Annales Geophysicae*, 21(8):1897–1910, 2003. doi: 10.5194/angeo-21-1897-2003.
- Reichle R. H., Koster R. D., De Lannoy G. J. M., Forman B. A., Liu Q., Mahanama S. P. P., and Touré A. Assessment and Enhancement of MERRA Land Surface Hydrology Estimates. *J. Climate*, 24(24):6322–6338, December 2011. doi: <http://dx.doi.org/10.1175/JCLI-D-10-05033.1>.
- Rigo A. and Vernant P. Personal communication, 2014.
- Roberts F. J., Champion J. A., Dawkins C. L., Hodges I. K., Shaffrey C. L., Stephenson B. D., Stringer A. M., Thornton E. H., and Youngman D. B. The XWS open access catalogue of extreme European windstorms from 1979 to 2012. *Natural Hazards and Earth System Sciences Discussions*, 2(3):2011–2048, 2014. doi: 10.5194/nhessd-2-2011-2014.
- Rodell M., Houser P. R., Jambor U., Gottschalck J., Mitchell K., Meng C.-J., Arsenault K., Cosgrove B., Radakovich J., Bosilovich M., Entin J. K., Walker J. P., Lohmann D., and Toll D. The Global Land Data Assimilation System. *Bulletin of the American Meteorological Society*, 85(3):381–394, Mar 2004. ISSN 0003-0007. doi: 10.1175/BAMS-85-3-381.
- Rui H., Teng W., Vollmer B., Mocko D., Beaudoin H., Whiteaker T., Valentine D., Maidment D., and Hooper R. Bridging the Gap between NASA Hydrological Data and the Geospatial Community. In *American Society for Photogrammetry and Remote Sensing (ASPRS) Annual Conference*, 2011. 2011 Milwaukee, Wisconsin, 1-5 May.
- Santamaría-Gómez A., Bouin M.-N., Collilieux X., and Wöppelmann G. Correlated errors in GPS position time series: Implications for velocity estimates. *Journal of Geophysical*

BIBLIOGRAPHIE

- Research: Solid Earth*, 116(B1), 2011. ISSN 2156-2202. doi: 10.1029/2010JB007701.
URL <http://dx.doi.org/10.1029/2010JB007701>.
- Scherneck H.-G., Johansson J. M., Koivula H., van Dam T., and Davis J. L. Vertical crustal motion observed in the BIFROST project. *Journal of Geodynamics*, 35(4-5):425 – 441, 2003. ISSN 0264-3707. doi: [http://dx.doi.org/10.1016/S0264-3707\(03\)00005-X](http://dx.doi.org/10.1016/S0264-3707(03)00005-X).
- Schoellhamer D. H. Singular spectrum analysis for time series with missing data. *Geophysical Research Letters*, 28(16):3187–3190, 2001. ISSN 1944-8007. doi: 10.1029/2000GL012698.
- Schuh H., Estermann G., Crétaux J.-F., Bergé-Nguyen M., and Dam T. Investigation of Hydrological and Atmospheric Loading by Space Geodetic Techniques. In Hwang C., Shum C., and Li J., editors, *Satellite Altimetry for Geodesy, Geophysics and Oceanography*, volume 126 of *International Association of Geodesy Symposia*, pages 123–132. Springer Berlin Heidelberg, 2004. ISBN 978-3-642-62329-5. doi: 10.1007/978-3-642-18861-9_15.
- Seeber G. *Satellite Geodesy*. Walter de Gruyter, 2003. ISBN 9783110175493.
- Simonetto E. Personal communication, 10 2014.
- Sośnica K., Thaller D., Dach R., JÄdłggi A., and Beutler G. Impact of loading displacements on slr-derived parameters and on the consistency between gnss and slr results. *Journal of Geodesy*, 87(8):751–769, 2013. ISSN 0949-7714. doi: 10.1007/s00190-013-0644-1. URL <http://dx.doi.org/10.1007/s00190-013-0644-1>.
- Souriau A. and Pauchet H. A new synthesis of Pyrenean seismicity and its tectonic implications. *Tectonophysics*, 290(3-4):221 – 244, 1998. ISSN 0040-1951. doi: [http://dx.doi.org/10.1016/S0040-1951\(98\)00017-1](http://dx.doi.org/10.1016/S0040-1951(98)00017-1).
- Subirana J. S., Juan Zornoza J., and Hernández-Pajares M. *GNSS Data Processing, Vol. 1: Fundamentals and Algorithms*. ESA Communications, 2013. ESA TM-23/1, May 2013.

BIBLIOGRAPHIE

- Takasu T. PPP Ambiguity Resolution Implementation in RTKLIB v 2.4.2, 2012. PP-RTK & Open Standards Symposium, March 12-13, Frankfurt am Main, Germany.
- Tapley B. D., Bettadpur S., Watkins M., and Reigber C. The gravity recovery and climate experiment: Mission overview and early results. *Geophysical Research Letters*, 31(9), 2004. ISSN 1944-8007. doi: 10.1029/2004GL019920.
- Tesmer V., Steigenberger P., Rothacher M., Boehm J., and Meisel B. Annual deformation signals from homogeneously reprocessed VLBI and GPS height time series. *Journal of Geodesy*, 83(10):973–988, 2009. ISSN 0949-7714. doi: 10.1007/s00190-009-0316-3.
- Tesmer V., Steigenberger P., van Dam T., and Mayer-Gürr T. Vertical deformations from homogeneously processed GRACE and global GPS long-term series. *Journal of Geodesy*, 85(5):291–310, 2011. ISSN 0949-7714. doi: 10.1007/s00190-010-0437-8.
- Tolman H. L. User manual and system documentation of WAVEWATCH III version 3.14., May 2009. NOAA/NWS/NCEP/MMAB Technical Note 276.
- Tregoning P. and van Dam T. Atmospheric pressure loading corrections applied to GPS data at the observation level. *Geophysical Research Letters*, 32(22), 2005. ISSN 1944-8007. doi: 10.1029/2005GL024104.
- Tregoning P., Watson C., Ramillien G., McQueen H., and Zhang J. Detecting hydrologic deformation using GRACE and GPS. *Geophysical Research Letters*, 36(15), 2009. ISSN 1944-8007. doi: 10.1029/2009GL038718.
- Trenberth K. E. and Smith L. The Mass of the Atmosphere: A Constraint on Global Analyses. *J. Climate*, 18(6):864–875, March 2005. doi: doi:http://dx.doi.org/10.1175/JCLI-3299.1.
- Valty P. *Apport de la géodésie à l'étude des transferts de masse d'origine climatique*. PhD thesis, Institut de physique du globe de Paris Ecole doctorale des sciences de la terre, 2013.
- Valty P., de Viron O., Panet I., Van Camp M., and Legrand J. Assessing the precision

BIBLIOGRAPHIE

- in loading estimates by geodetic techniques in Southern Europe. *Geophysical Journal International*, 194(3):1441–1454, 2013. doi: 10.1093/gji/ggt173.
- van Dam T. Personal communication, 07 2012.
- van Dam T., Wahr J., Milly P. C. D., Shmakin A. B., Blewitt G., Lavallée D. A., and Larson K. M. Crustal displacements due to continental water loading. *Geophysical Research Letters*, 28(4):651–654, 2001. ISSN 1944-8007. doi: 10.1029/2000GL012120.
- van Dam T., Altamimi Z., Collilieux X., and Ray J. Topographically induced height errors in predicted atmospheric loading effects. *Journal of Geophysical Research: Solid Earth*, 115(B7), 2010. ISSN 2156-2202. doi: 10.1029/2009JB006810.
- van Dam T., Collilieux X., Wuite J., Altamimi Z., and Ray J. Nontidal ocean loading: amplitudes and potential effects in GPS height time series. *Journal of Geodesy*, 86(11): 1043–1057, 2012. ISSN 0949-7714. doi: 10.1007/s00190-012-0564-5.
- van Dam T. M. and Herring T. A. Detection of atmospheric pressure loading using very long baseline interferometry measurements. *Journal of Geophysical Research: Solid Earth*, 99 (B3):4505–4517, 1994. ISSN 2156-2202. doi: 10.1029/93JB02758.
- van Dam T. M. and Wahr J. M. Displacements of the Earth’s surface due to atmospheric loading: Effects on gravity and baseline measurements. *Journal of Geophysical Research: Solid Earth*, 92(B2):1281–1286, 1987. ISSN 2156-2202. doi: 10.1029/JB092iB02p01281.
- van Dam T. M., Blewitt G., and Heflin M. B. Atmospheric pressure loading effects on Global Positioning System coordinate determinations. *Journal of Geophysical Research: Solid Earth*, 99(B12):23939–23950, 1994. ISSN 2156-2202. doi: 10.1029/94JB02122.
- van Dam T. M., Wahr J., Chao Y., and Leuliette E. Predictions of crustal deformation and of geoid and sea-level variability caused by oceanic and atmospheric loading. *Geophysical Journal International*, 129(3):507–517, 1997. ISSN 1365-246X. doi: 10.1111/j.1365-246X.1997.tb04490.x.
- van Dam T. and Wahr J. Modeling environment loading effects: a review. *Physics and*

BIBLIOGRAPHIE

- Chemistry of the Earth*, 23(9-10):1077 – 1087, 1998. ISSN 0079-1946. doi: [http://dx.doi.org/10.1016/S0079-1946\(98\)00147-5](http://dx.doi.org/10.1016/S0079-1946(98)00147-5).
- Vautard R., Yiou P., and Ghil M. Singular-spectrum analysis: A toolkit for short, noisy chaotic signals. *Physica D: Nonlinear Phenomena*, 58(1-4):95 – 126, 1992. ISSN 0167-2789. doi: [http://dx.doi.org/10.1016/0167-2789\(92\)90103-T](http://dx.doi.org/10.1016/0167-2789(92)90103-T).
- Vergnolle M., Bouin M.-N., Morel L., Masson F., Durand S., Nicolas J., and Melachroinos S. A. GPS estimates of ocean tide loading in NW-France: Determination of ocean tide loading constituents and comparison with a recent ocean tide model. *Geophysical Journal International*, 173(2):444–458, 2008. doi: [10.1111/j.1365-246X.2008.03734.x](https://doi.org/10.1111/j.1365-246X.2008.03734.x).
- Webster I. R. A Regional Model for Prediction of Ionospheric Delay for Single Frequency Users of the Global Positioning System. Technical Report 166, University of New Brunswick, Department of Surveying Engineering, Canada, 1993. Reproduction of M.Sc.E. thesis, 124 pp.
- Williams S. D. P. and Penna N. T. Non-tidal ocean loading effects on geodetic GPS heights. *Geophysical Research Letters*, 38(9), 2011. ISSN 1944-8007. doi: [10.1029/2011GL046940](https://doi.org/10.1029/2011GL046940).
- Witchayangkoon B. *Elements of GPS Precise Point Positioning*. PhD thesis, The University of Maine, 2000.
- Wolff M. Direct measurements of the Earth's gravitational potential using a satellite pair. *Journal of Geophysical Research*, 74(22):5295–5300, 1969. ISSN 2156-2202. doi: [10.1029/JB074i022p05295](https://doi.org/10.1029/JB074i022p05295).
- Wunsch C. and Stammer D. Atmospheric loading and the oceanic "inverted barometer" effect. *Reviews of Geophysics*, 35(1):79–107, 1997. ISSN 1944-9208. doi: [10.1029/96RG03037](https://doi.org/10.1029/96RG03037).
- Xu G. *GPS: Theory, Algorithms and Applications*. Springer, 2007. ISBN 9783540727156.
- XWS-Datasets. XWS Datasets, 2014. (c) Copyright Met Office, University of Reading and University of Exeter. Licensed under Creative Commons CC BY 4.0 International Licence: http://creativecommons.org/licenses/by/4.0/deed.en_GB.

Zerbini S., Richter B., Negusini M., Romagnoli C., Simon D., Domenichini F., and Schwahn W. Height and gravity variations by continuous GPS, gravity and environmental parameter observations in the southern Po Plain, near Bologna, Italy. *Earth and Planetary Science Letters*, 192(3):267 – 279, 2001. ISSN 0012-821X. doi: [http://dx.doi.org/10.1016/S0012-821X\(01\)00445-9](http://dx.doi.org/10.1016/S0012-821X(01)00445-9).

Zerbini S., Matonti F., Raicich F., Richter B., and van Dam T. Observing and assessing nontidal ocean loading using ocean, continuous GPS and gravity data in the Adriatic area. *Geophysical Research Letters*, 31(23), 2004. ISSN 1944-8007. doi: [10.1029/2004GL021185](http://dx.doi.org/10.1029/2004GL021185).

Zhang Y. and Baptista M. A. SELFE: A semi-implicit Eulerian-Lagrangian finite-element model for cross-scale ocean circulation. *Ocean Modelling*, 21(3-4):71–96, 2008. ISSN 1463-5003. doi: <http://dx.doi.org/10.1016/j.ocemod.2007.11.005>.

Zhang Y., Wallace J. M., and Battisti D. S. Enso-like interdecadal variability: 1900–93. *J. Climate*, 10:1004–1020, 1997. doi: [http://dx.doi.org/10.1175/1520-0442\(1997\)010<1004:ELIV>2.0.CO;2](http://dx.doi.org/10.1175/1520-0442(1997)010<1004:ELIV>2.0.CO;2).

Zumberge J. F., Heflin M. B., Jefferson D. C., Watkins M. M., and Webb F. H. Precise point positioning for the efficient and robust analysis of GPS data from large networks. *Journal of Geophysical Research: Solid Earth*, 102(B3):5005–5017, 1997. ISSN 2156-2202. doi: [10.1029/96JB03860](http://dx.doi.org/10.1029/96JB03860).

Appendix

Appendix A

Global

Table A.1 – Correlation table of GPS and CWSL model up component at BRAZ station.

Data type	Model	GPS
Component	1	1
Order of correlation		0.83
Period of the component	303.38 days	303.38 days
Amplitude of the component	5.8 mm	11.4 mm
Proportion in the signal	98.43 %	48.45 %

Table A.2 – Correlation table of GPS and sum of models up component at BRAZ station.

Data type	Model	GPS
Component	1	1
Order of correlation		0.85
Period of the component	303.38 days	303.38 days
Amplitude of the component	5.5 mm	11.4 mm
Proportion in the signal	93.88 %	48.45 %
Component	2	5
Order of correlation		0.32
Period of the component	17.85 days	12.21 days
Amplitude of the component	0.1 mm	0.3 mm
Proportion in the signal	0.65 %	0.42 %
Component	3	8
Order of correlation		0.31
Period of the component	10.93 days	9.24 days
Amplitude of the component	0.1 mm	0.3 mm
Proportion in the signal	0.28 %	0.35 %
Component	4	2
Order of correlation		0.33
Period of the component	1.00 days	1.00 days
Amplitude of the component	0.1 mm	2.4 mm
Proportion in the signal	0.31 %	10.84 %

Table A.3 – Correlation table of GPS and ATML model up component at BRAZ station.

Data type	Model	GPS
Component	1	4
Order of correlation		0.07
Period of the component	303.38 days	23.34 days
Amplitude of the component	1.4 mm	0.4 mm
Proportion in the signal	66.01 %	0.54 %
Component	2	5
Order of correlation		0.26
Period of the component	17.85 days	12.21 days
Amplitude of the component	0.1 mm	0.3 mm
Proportion in the signal	4.10 %	0.42 %
Component	3	8
Order of correlation		0.29
Period of the component	9.79 days	9.24 days
Amplitude of the component	0.0 mm	0.3 mm
Proportion in the signal	1.89 %	0.35 %
Component	4	2
Order of correlation		0.33
Period of the component	1.00 days	1.00 days
Amplitude of the component	0.1 mm	2.4 mm
Proportion in the signal	2.57 %	10.84 %
Component	5	12
Order of correlation		0.14
Period of the component	6.37 days	4.77 days
Amplitude of the component	0.0 mm	0.2 mm
Proportion in the signal	0.79 %	0.24 %
Component	6	12
Order of correlation		0.22
Period of the component	4.41 days	4.77 days
Amplitude of the component	0.0 mm	0.2 mm
Proportion in the signal	0.68 %	0.24 %
Component	7	18
Order of correlation		0.05
Period of the component	2.53 days	2.15 days
Amplitude of the component	0.0 mm	0.1 mm
Proportion in the signal	0.14 %	0.10 %
Component	8	7
Order of correlation		0.07
Period of the component	1.04 days	1.04 days
Amplitude of the component	0.0 mm	0.1 mm
Proportion in the signal	0.02 %	0.18 %

Table A.4 – Correlation table of GPS and NTOL model up component at BRAZ station.

Data type	Model	GPS
Component	1	1
Order of correlation		0.15
Period of the component	788.80 days	303.38 days
Amplitude of the component	0.3 mm	11.4 mm
Proportion in the signal	76.37 %	48.45 %
Component	2	5
Order of correlation		0.19
Period of the component	14.24 days	12.21 days
Amplitude of the component	0.0 mm	0.3 mm
Proportion in the signal	3.04 %	0.42 %
Component	3	8
Order of correlation		0.20
Period of the component	8.00 days	9.24 days
Amplitude of the component	0.0 mm	0.3 mm
Proportion in the signal	1.54 %	0.35 %
Component	4	9
Order of correlation		0.15
Period of the component	6.11 days	6.86 days
Amplitude of the component	0.0 mm	0.2 mm
Proportion in the signal	0.92 %	0.33 %
Component	5	12
Order of correlation		0.11
Period of the component	4.63 days	4.77 days
Amplitude of the component	0.0 mm	0.2 mm
Proportion in the signal	0.68 %	0.24 %
Component	6	12
Order of correlation		0.05
Period of the component	3.92 days	4.77 days
Amplitude of the component	0.0 mm	0.2 mm
Proportion in the signal	0.44 %	0.24 %
Component	7	18
Order of correlation		0.02
Period of the component	3.15 days	2.15 days
Amplitude of the component	0.0 mm	0.1 mm
Proportion in the signal	0.31 %	0.10 %
Component	8	18
Order of correlation		0.02
Period of the component	2.74 days	2.15 days
Amplitude of the component	0.0 mm	0.1 mm
Proportion in the signal	0.28 %	0.10 %
Component	9	18
Order of correlation		0.07
Period of the component	2.37 days	2.15 days
Amplitude of the component	0.0 mm	0.1 mm
Proportion in the signal	0.22 %	0.10 %
Component	10	18
Order of correlation		0.08
Period of the component	2.23 days	2.15 days
Amplitude of the component	0.0 mm	0.1 mm
Proportion in the signal	0.11 %	0.10 %

Table A.5 – Correlation table of GPS and ATML up component at ALIC station.

Data type	Model	GPS
Component	1	1
Order of correlation		0.17
Period of the component	331.07 days	794.60 days
Amplitude of the component	3.4 mm	4.0 mm
Proportion in the signal	80.33 %	23.10 %
Component	2	5
Order of correlation		0.40
Period of the component	11.69 days	13.07 days
Amplitude of the component	0.1 mm	0.3 mm
Proportion in the signal	3.12 %	0.57 %
Component	3	10
Order of correlation		0.42
Period of the component	7.52 days	6.37 days
Amplitude of the component	0.1 mm	0.4 mm
Proportion in the signal	1.43 %	1.71 %
Component	4	12
Order of correlation		0.35
Period of the component	5.13 days	4.50 days
Amplitude of the component	0.1 mm	0.2 mm
Proportion in the signal	0.50 %	0.30 %
Component	5	14
Order of correlation		0.22
Period of the component	1.00 days	4.13 days
Amplitude of the component	0.1 mm	0.2 mm
Proportion in the signal	0.50 %	0.32 %

Table A.6 – Correlation table of GPS and the sum of models up component at ALIC station.

Data type	Model	GPS
Component	1	1
Order of correlation		0.32
Period of the component	305.62 days	794.60 days
Amplitude of the component	3.1 mm	4.0 mm
Proportion in the signal	82.19 %	23.10 %
Component	2	9
Order of correlation		0.45
Period of the component	10.27 days	8.89 days
Amplitude of the component	0.2 mm	0.3 mm
Proportion in the signal	4.98 %	0.56 %
Component	3	12
Order of correlation		0.37
Period of the component	5.13 days	4.50 days
Amplitude of the component	0.1 mm	0.2 mm
Proportion in the signal	1.18 %	0.30 %
Component	4	14
Order of correlation		0.34
Period of the component	1.00 days	4.13 days
Amplitude of the component	0.1 mm	0.2 mm
Proportion in the signal	0.40 %	0.32 %
Component	5	15
Order of correlation		0.26
Period of the component	3.26 days	3.53 days
Amplitude of the component	0.0 mm	0.2 mm
Proportion in the signal	0.09 %	0.30 %

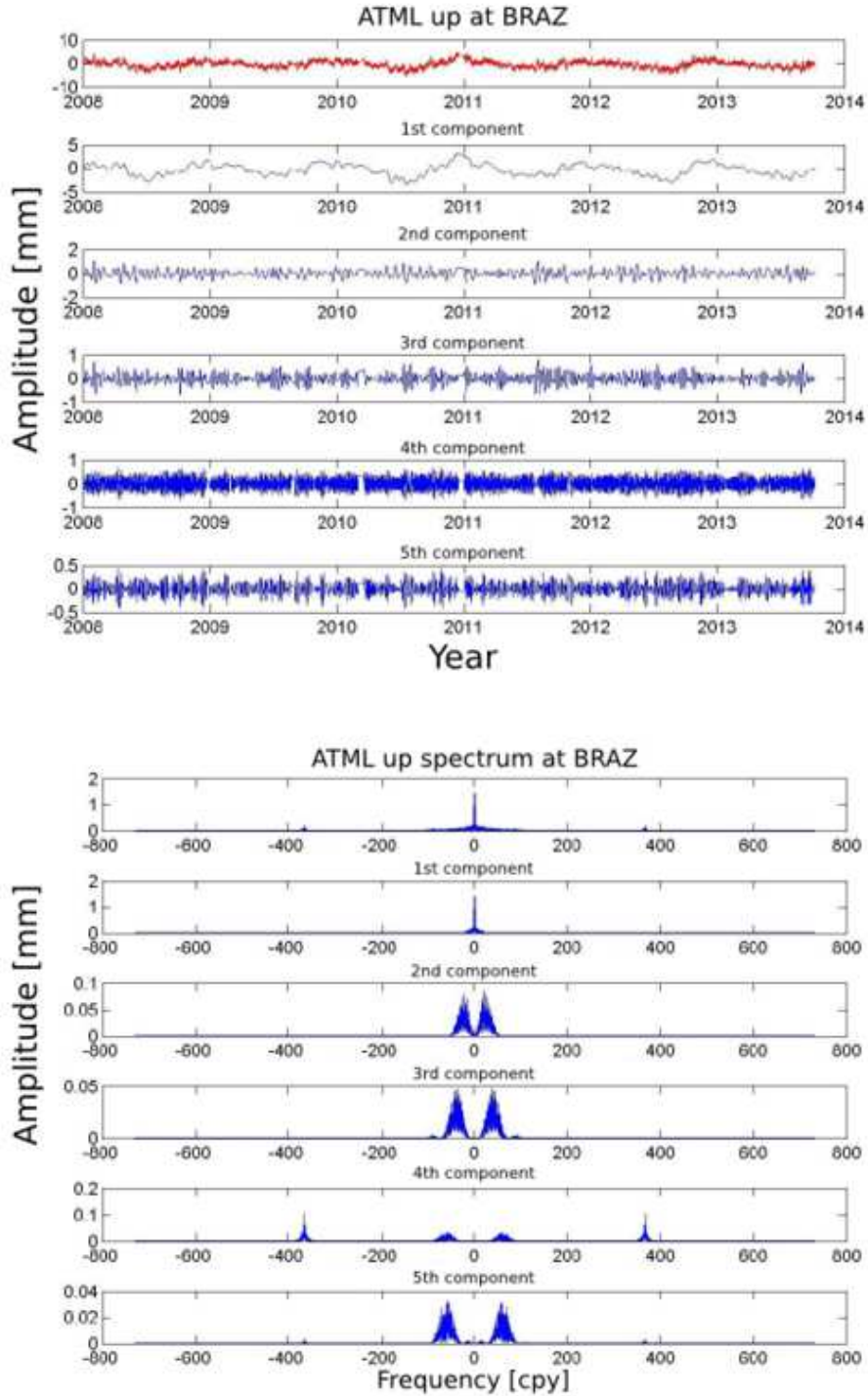


Figure A.1 – ATML time series components (top) and their spectrum (bottom) at BRAZ station up component in decreasing order of amplitude (in mm). For example the first component corresponds to an annual period.

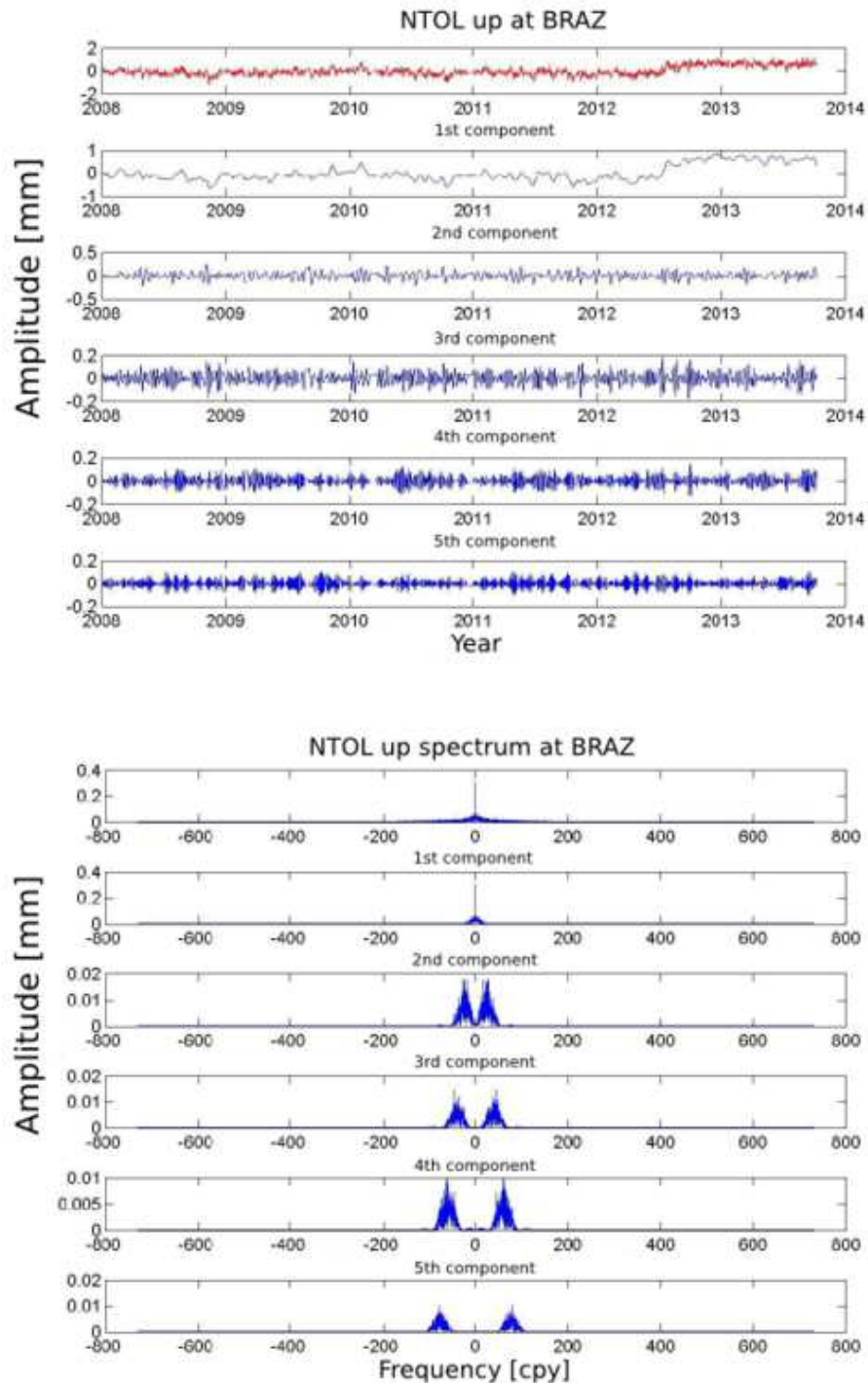


Figure A.2 – NTOL time series components (top) and their spectrum (bottom) at BRAZ station up component in decreasing order of amplitude (in mm). For example the first component corresponds to an annual period.

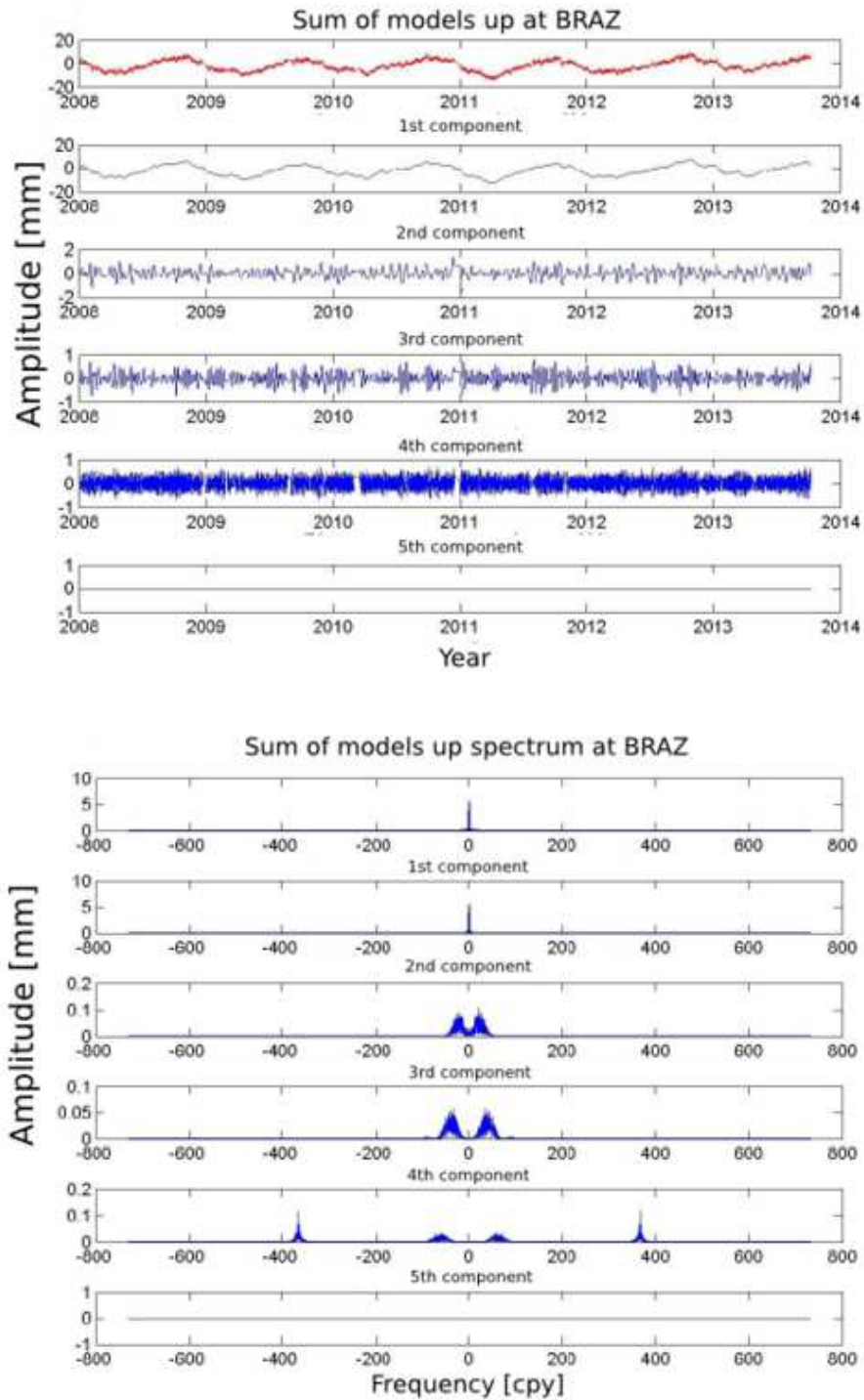


Figure A.3 – Sum of loading time series components (top) and their spectrum (bottom) at BRAZ station up component in decreasing order of amplitude (in mm). For example the first component corresponds to an annual period.

Appendix B

Xynthia

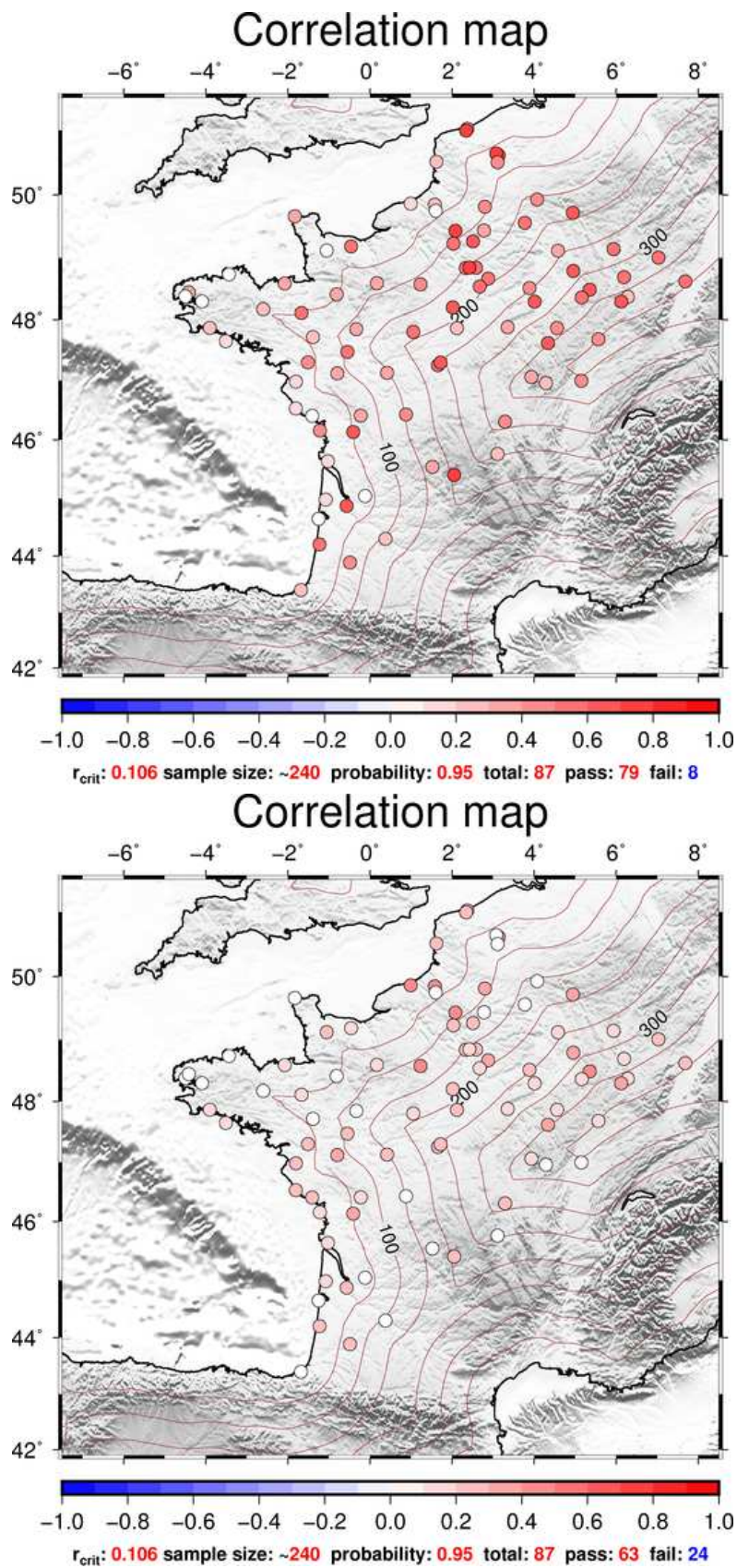


Figure B.1 – Correlation between GR2 and ATML for two months centered on the storm (top) and for two summer months (bottom).

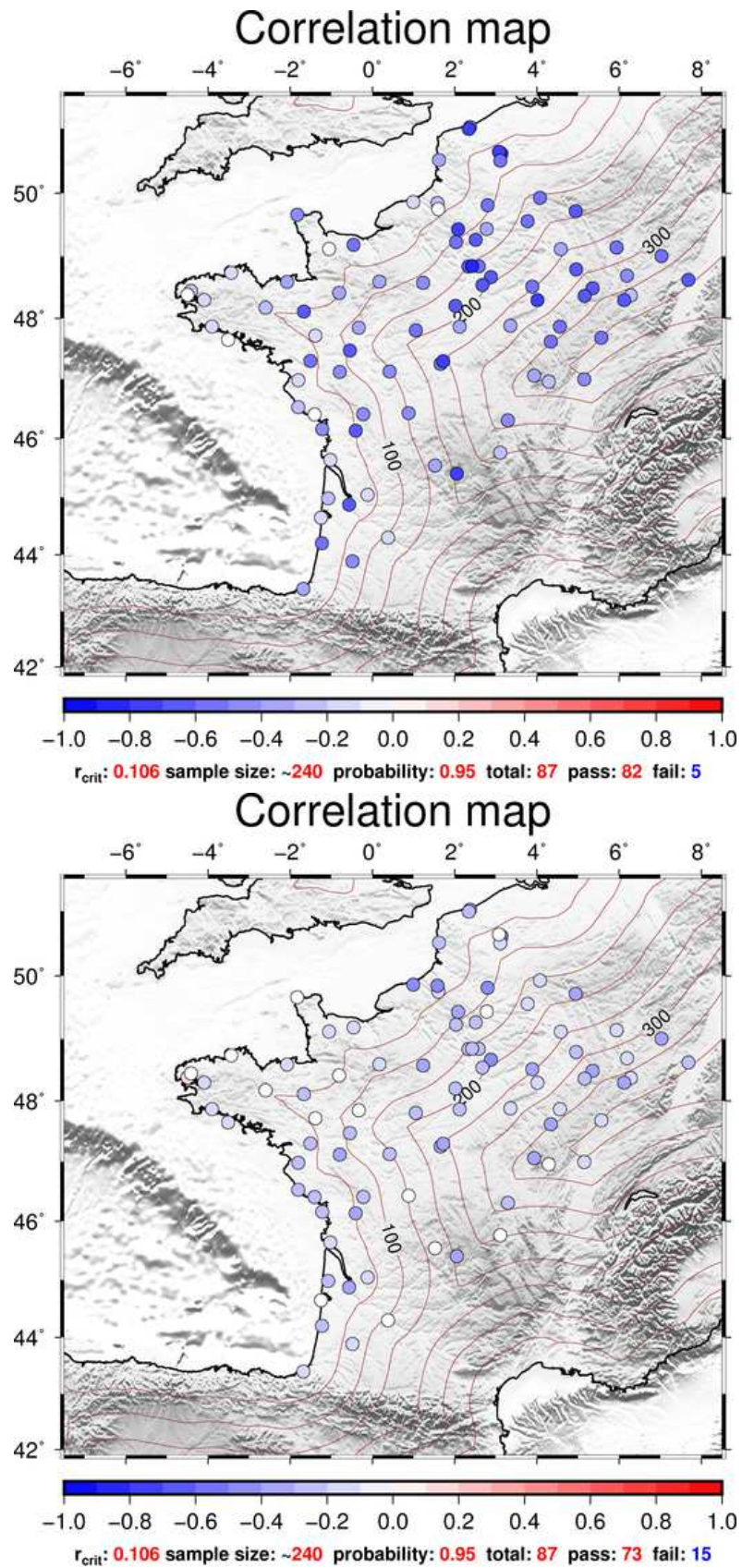


Figure B.2 – Correlation between GR2 and MERRA atmospheric pressure for two months centered on the storm (top) and for two summer months (bottom).

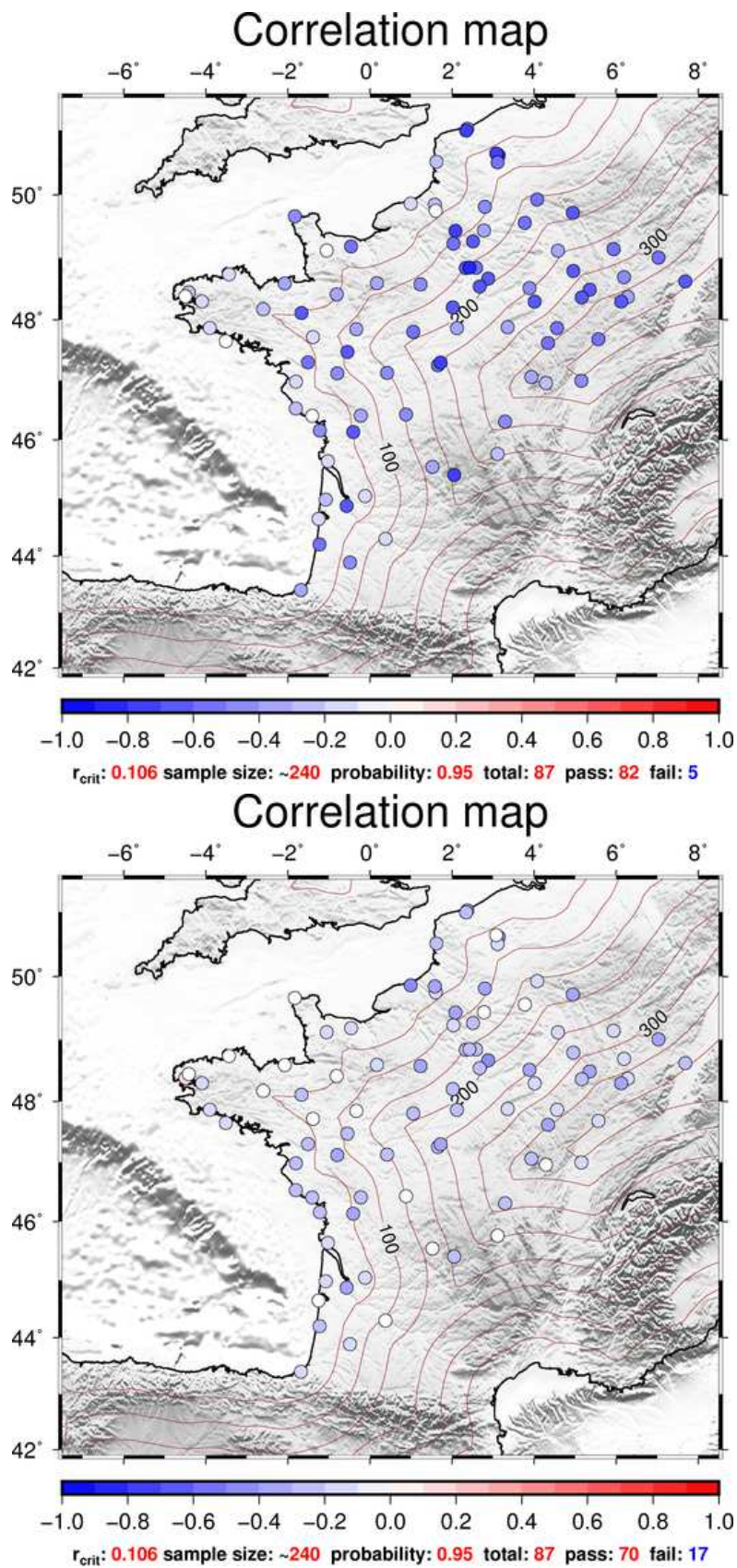


Figure B.3 – Correlation between GR2 and ECMWF atmospheric pressure for two months centered on the storm (top) and for two summer months (bottom).

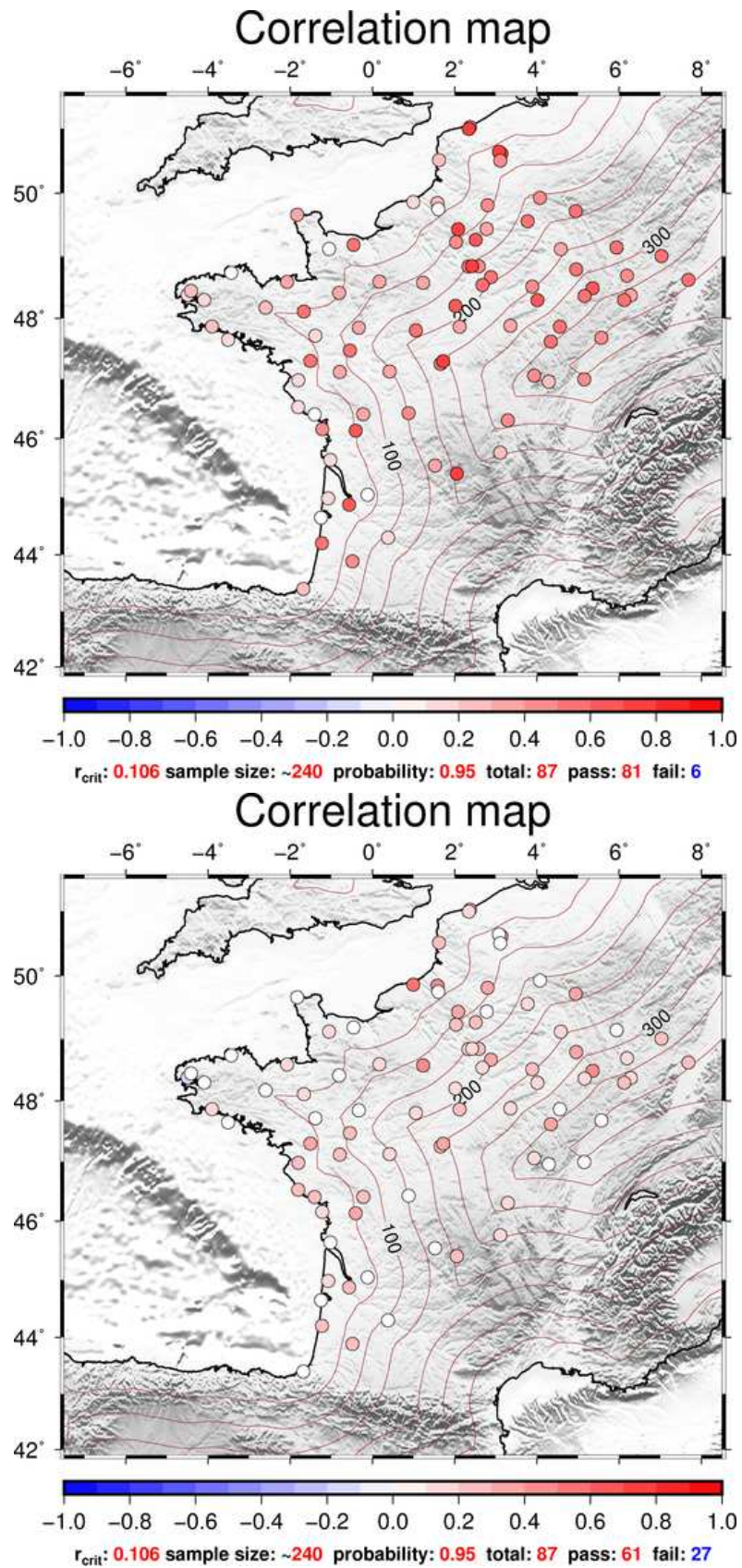


Figure B.4 – Correlation between GR2 and NOIB for two months centered on the storm (top) and for two summer months (bottom).

Appendix C

Challenges

Table C.1 – Absolute differences between *nominal_FES2004* and *Scherneck_FES2004* OTL files in terms of *M2* and *S2* tidal waves up, east and north amplitudes. Stations are presented with their coastal distances from the nearest coast and those that have greater than 2 mm *M2* up difference are highlighted in red.

site	\approx distance[km]	up [cm]		east [cm]		north [cm]	
		M2	S2	M2	S2	M2	S2
AGDE	13	0.15	0.04	0.04	0.01	0.01	0.01
AGDS	12	0.15	0.04	0.04	0.01	0.01	0.01
AIGL	72	0.14	0.04	0.05	0.02	0.01	0.01
AILT	276	0.02	0.00	0.01	0.00	0.04	0.01
ALPE	179	0.06	0.02	0.02	0.01	0.00	0.00
AMB2	222	0.12	0.04	0.04	0.01	0.01	0.00
AMBL	18	0.47	0.09	0.54	0.17	0.33	0.04
ANDE	281	0.03	0.01	0.02	0.01	0.01	0.01
ANGE	108	0.59	0.17	0.17	0.06	0.25	0.11
ANGL	14	1.08	0.37	0.11	0.04	0.08	0.03
AUBU	398	0.01	0.00	0.00	0.00	0.00	0.00
AUCH	157	0.53	0.18	0.17	0.06	0.05	0.02
AUTN	368	0.06	0.02	0.02	0.00	0.02	0.00
AXPV	22	0.09	0.02	0.02	0.01	0.00	0.00
BACT	90	0.06	0.02	0.02	0.00	0.00	0.00
BANN	90	0.12	0.03	0.04	0.01	0.00	0.00
BARY	170	0.40	0.13	0.11	0.04	0.08	0.03
BEA2	14	0.15	0.04	0.03	0.01	0.02	0.01
BEAU	86	0.55	0.18	0.15	0.05	0.11	0.02
BLFT	383	0.02	0.01	0.00	0.00	0.00	0.00
BMHG	11	1.32	0.45	0.17	0.03	0.19	0.05
BOUS	250	0.19	0.05	0.07	0.02	0.05	0.02
BRES	77	0.54	0.16	0.12	0.04	0.17	0.07
BRET	164	0.13	0.05	0.01	0.00	0.10	0.02
BRST	6	1.02	0.37	0.35	0.11	0.01	0.01

Continued on next page

APPENDIX - CHALLENGES

site	\approx distance[km]	up [cm]		east [cm]		north [cm]	
		M2	S2	M2	S2	M2	S2
BSCN	378	0.03	0.01	0.01	0.00	0.00	0.00
BUAN	322	0.01	0.00	0.01	0.00	0.01	0.00
CACI	365	0.07	0.02	0.02	0.01	0.02	0.00
CAEN	18	1.69	0.61	0.38	0.13	0.03	0.00
CARQ	40	0.79	0.24	0.09	0.04	0.18	0.08
CAUS	162	0.32	0.10	0.11	0.04	0.02	0.01
CBRY	234	0.06	0.02	0.02	0.01	0.00	0.00
CHAL	360	0.06	0.02	0.02	0.01	0.01	0.00
CHAS	333	0.02	0.00	0.00	0.00	0.02	0.00
CHBR	61	1.02	0.31	0.16	0.07	0.28	0.12
CHBS	228	0.16	0.04	0.07	0.02	0.11	0.03
CHEB	187	0.11	0.04	0.02	0.01	0.08	0.01
CHIZ	49	0.72	0.24	0.08	0.03	0.16	0.06
CHLN	94	0.33	0.07	0.07	0.03	0.13	0.02
CHRM	361	0.01	0.00	0.01	0.00	0.00	0.00
CHTL	190	0.06	0.02	0.02	0.00	0.01	0.00
CLFD	256	0.15	0.04	0.05	0.02	0.02	0.01
CNNS	17	0.07	0.01	0.01	0.00	0.01	0.00
COUD	21	0.52	0.14	0.18	0.04	0.15	0.09
COUT	35	1.32	0.45	0.24	0.08	0.07	0.02
CPSN	38	0.66	0.15	0.12	0.03	0.02	0.06
CREI	120	0.35	0.11	0.07	0.03	0.10	0.02
CSTN	136	0.31	0.10	0.10	0.03	0.04	0.01
CUBX	21	1.46	0.50	0.01	0.00	0.01	0.01
DGLG	21	0.68	0.18	0.21	0.05	0.29	0.12
DIJO	391	0.04	0.01	0.01	0.00	0.01	0.00
DIPL	15	2.20	0.79	0.25	0.12	0.25	0.13
DOCO	274	0.02	0.00	0.02	0.00	0.00	0.01
DOJX	324	0.00	0.00	0.01	0.00	0.01	0.00
EGLT	206	0.25	0.08	0.09	0.03	0.02	0.01
ENTZ	394	0.01	0.00	0.00	0.00	0.00	0.00
EOST	396	0.01	0.00	0.00	0.00	0.00	0.00
EPRN	18	1.60	0.58	0.41	0.14	0.01	0.01
ESAB	202	0.09	0.03	0.03	0.01	0.00	0.00
EZEV	11	0.07	0.01	0.01	0.00	0.01	0.00
FERR	6	1.01	0.34	0.04	0.01	0.07	0.02
FETA	173	0.15	0.04	0.05	0.02	0.05	0.00
FJCP	22	0.17	0.05	0.05	0.02	0.02	0.01
FLOI	189	0.08	0.02	0.04	0.01	0.00	0.01
FLRC	92	0.14	0.04	0.05	0.02	0.01	0.01
FOUC	29	0.76	0.17	0.23	0.06	0.01	0.04
FRTT	393	0.02	0.01	0.00	0.00	0.00	0.00
GLRA	146	0.10	0.03	0.03	0.01	0.00	0.00
GORN	51	2.78	0.94	0.26	0.15	0.33	0.15
GRAS	22	0.07	0.01	0.01	0.00	0.00	0.00
GROI	13	1.00	0.34	0.23	0.07	0.12	0.05
GRON	299	0.10	0.03	0.04	0.01	0.06	0.02

Continued on next page

APPENDIX - CHALLENGES

site	\approx distance[km]	up [cm]		east [cm]		north [cm]	
		M2	S2	M2	S2	M2	S2
GUIP	7	1.23	0.44	0.13	0.04	0.06	0.02
HEAU	7	1.46	0.51	0.17	0.02	0.12	0.02
HRSN	154	0.16	0.03	0.06	0.01	0.02	0.01
ILBO	147	0.34	0.09	0.13	0.04	0.17	0.07
ISLA	120	0.42	0.14	0.06	0.02	0.15	0.03
IVRY	102	0.59	0.22	0.14	0.05	0.23	0.06
JARG	216	0.04	0.00	0.04	0.01	0.09	0.03
KONE	11	1.25	0.43	0.36	0.11	0.01	0.01
LANN	8	1.66	0.60	0.17	0.04	0.08	0.02
LBRD	32	1.46	0.50	0.01	0.00	0.01	0.01
LBUG	114	0.46	0.15	0.15	0.05	0.02	0.01
LCAU	10	1.31	0.45	0.13	0.04	0.00	0.01
LENE	50	0.40	0.15	0.28	0.09	0.25	0.07
LETO	9	0.70	0.18	0.01	0.02	0.03	0.04
LGAR	107	0.66	0.22	0.19	0.07	0.03	0.01
LIL2	66	0.02	0.03	0.00	0.01	0.03	0.00
LMCU	61	0.13	0.05	0.02	0.02	0.00	0.02
LPPZ	10	0.75	0.26	0.52	0.15	0.11	0.05
LROC	4	0.91	0.34	0.01	0.00	0.09	0.04
LRTZ	326	0.00	0.00	0.01	0.00	0.00	0.01
LUCE	354	0.02	0.01	0.00	0.00	0.00	0.00
MACH	17	1.10	0.36	0.10	0.03	0.20	0.08
MAKS	407	0.01	0.01	0.00	0.00	0.00	0.00
MAN2	129	0.37	0.09	0.40	0.12	0.41	0.16
MARG	251	0.05	0.01	0.01	0.00	0.00	0.00
MARS	12	0.09	0.02	0.03	0.01	0.00	0.00
MELN	188	0.09	0.04	0.00	0.01	0.08	0.01
MERY	246	0.04	0.01	0.02	0.01	0.04	0.00
MIMZ	10	1.31	0.44	0.09	0.03	0.16	0.06
MIRE	365	0.01	0.00	0.01	0.00	0.00	0.00
MLVL	159	0.19	0.07	0.03	0.01	0.10	0.02
MNBL	373	0.02	0.01	0.00	0.00	0.01	0.00
MODA	168	0.05	0.01	0.02	0.00	0.01	0.00
MOGN	292	0.08	0.02	0.02	0.01	0.00	0.00
MONB	345	0.03	0.01	0.01	0.00	0.02	0.00
MORN	87	0.64	0.21	0.18	0.06	0.08	0.03
MSGT	109	0.25	0.08	0.07	0.02	0.05	0.02
MSMM	61	0.07	0.02	0.02	0.00	0.00	0.00
MSRT	170	0.31	0.10	0.11	0.04	0.04	0.01
MTDM	70	1.47	0.50	0.08	0.03	0.09	0.03
MTMN	152	0.33	0.10	0.11	0.03	0.11	0.04
NICA	14	0.07	0.01	0.01	0.00	0.01	0.00
NIME	36	0.11	0.03	0.04	0.01	0.01	0.00
OPMT	148	0.23	0.08	0.02	0.01	0.12	0.02
OUT2	181	0.02	0.02	0.04	0.01	0.10	0.03
PAYR	79	0.22	0.07	0.07	0.02	0.02	0.01
PERP	14	0.16	0.04	0.04	0.01	0.02	0.01

Continued on next page

APPENDIX - CHALLENGES

site	\approx distance[km]	up [cm]		east [cm]		north [cm]	
		M2	S2	M2	S2	M2	S2
PEVL	75	0.02	0.03	0.02	0.02	0.03	0.02
PLCQ	212	0.08	0.02	0.03	0.01	0.04	0.00
PLEM	27	2.47	0.86	0.05	0.01	0.33	0.14
PNDB	11	1.61	0.57	0.22	0.06	0.04	0.01
POBU	312	0.09	0.02	0.03	0.01	0.01	0.00
PQRL	13	0.07	0.02	0.02	0.01	0.00	0.00
PRIE	12	0.09	0.02	0.03	0.01	0.00	0.00
PRNY	332	0.04	0.01	0.01	0.00	0.00	0.00
PUYA	142	0.06	0.02	0.02	0.00	0.00	0.00
PUYV	166	0.12	0.04	0.04	0.01	0.01	0.00
PZNA	20	0.15	0.04	0.04	0.01	0.01	0.01
RAYL	15	0.08	0.01	0.01	0.00	0.00	0.00
RENN	46	2.60	0.87	0.13	0.08	0.69	0.28
ROYA	8	1.16	0.40	0.11	0.04	0.12	0.04
SABL	15	0.91	0.30	0.41	0.14	0.07	0.03
SARL	328	0.00	0.00	0.01	0.00	0.00	0.00
SARZ	5	1.18	0.40	0.37	0.12	0.03	0.03
SBLS	113	0.80	0.22	0.27	0.09	0.36	0.15
SCDA	150	0.16	0.05	0.06	0.02	0.01	0.00
SCOA	12	1.03	0.35	0.33	0.11	0.15	0.05
SEES	80	0.63	0.21	0.81	0.26	0.12	0.05
SEUR	384	0.05	0.01	0.01	0.00	0.00	0.00
SGIL	27	0.11	0.03	0.03	0.01	0.01	0.00
SJDV	262	0.08	0.02	0.03	0.01	0.00	0.00
SLVT	65	0.16	0.05	0.05	0.02	0.01	0.01
SMLE	70	0.55	0.18	0.11	0.04	0.15	0.06
SMNE	151	0.22	0.08	0.02	0.01	0.11	0.02
SMSP	240	0.06	0.01	0.03	0.01	0.02	0.01
SOUS	190	0.26	0.08	0.10	0.03	0.02	0.01
STLO	19	2.12	0.76	0.23	0.09	0.03	0.02
STPS	307	0.12	0.03	0.04	0.01	0.02	0.01
STV2	128	0.07	0.02	0.02	0.01	0.00	0.00
TANZ	405	0.01	0.00	0.00	0.00	0.00	0.00
THOR	65	0.60	0.19	0.10	0.04	0.15	0.06
TLIA	139	0.31	0.10	0.10	0.04	0.04	0.01
TLMF	147	0.33	0.11	0.11	0.04	0.04	0.01
TLSE	139	0.31	0.10	0.10	0.04	0.04	0.01
TREM	83	0.62	0.19	0.13	0.05	0.20	0.08
TRMO	121	0.20	0.06	0.07	0.02	0.01	0.01
TRYS	270	0.02	0.01	0.01	0.01	0.03	0.00
VAUD	370	0.04	0.01	0.01	0.00	0.00	0.00
VDOM	182	0.11	0.01	0.12	0.03	0.18	0.06
VFCH	232	0.15	0.03	0.07	0.02	0.10	0.03
VILR	186	0.07	0.02	0.02	0.01	0.00	0.00
VISN	96	0.09	0.03	0.03	0.01	0.00	0.00
VNTE	118	0.31	0.08	0.07	0.03	0.08	0.01
VOUR	240	0.09	0.02	0.03	0.01	0.00	0.00

Continued on next page

APPENDIX - CHALLENGES

site	\approx distance[<i>km</i>]	up [cm]		east [cm]		north [cm]	
		M2	S2	M2	S2	M2	S2
V ^{SFR}	124	0.30	0.12	0.03	0.01	0.16	0.04
VSOL	399	0.02	0.01	0.00	0.00	0.00	0.00
WLBH	394	0.01	0.00	0.00	0.00	0.00	0.00

Résumé :

La redistribution temporelle et spatiale des masses environnementales déforment la surface de la Terre. Ces déformations sont observables par des techniques de géodésie spatiale telles que le GPS (Global Positioning System). Depuis que les produits d'orbite et d'horloge très précis de l'IGS (International GNSS Service) sont disponibles, que des algorithmes sophistiqués ont été développés, l'iPPP (integer fixed ambiguity Precise Point Positioning) a ouvert une nouvelle ère pour l'analyse du GPS et pour son application dans les études géophysiques. Ce travail fait partie des premières études pour analyser les différents effets de surcharge, en utilisant des séries temporelles de positionnement, en particulier avec le logiciel GINS-PC et les nouveaux produits d'orbite et d'horloge REPRO2 du GRGS (Groupe de Recherche en Géodésie Spatiale) (GR2). Nous visons à exploiter les positions sub-diurnes d'iPPP pour étudier divers effets de déformation de la Terre à différentes échelles de temps : sub-diurne à saisonniers et annuels. Notre objectif est de contribuer à la validation des modèles géophysiques, à l'observation des différents phénomènes non-maréaux, mais aussi de présenter la performance du mode iPPP et du logiciel GINS-PC. Ce dernier est un outil puissant pour les applications géodynamiques, qui permet d'étudier l'influence des effets de surcharge sur l'interprétation géodésique des séries temporelles de positionnement. Après un aperçu des principales déformations de la surface de la Terre induites par les effets de surcharge, nous présentons les techniques de géodésie qui ont déjà démontré leur potentiel dans l'analyse de déformation, en particulier dans les études de déformation de surcharge. Nous présentons ensuite la technique GPS et le mode de traitement iPPP que nous utilisons pour l'analyse des données. Nous continuons vers une étude globale qui pose les bases pour de futures recherches. Nous montrons ensuite les résultats de deux études régionales. La première analyse étudie l'influence des effets de surcharge sur la détermination des vitesses tectoniques dans la chaîne des Pyrénées à partir de campagnes GPS espacées dans le temps. Le deuxième cas d'étude tente de suivre l'évolution spatiale et temporelle des déformations induites par un événement de tempête extrême, à savoir la tempête Xynthia qui a eu lieu en France en 2010. Cette étude tente également d'identifier la réponse dynamique de l'océan pour le système de basse pression atmosphérique se déplaçant rapidement en utilisant des séries temporelles sub-diurnes.

Mots clés :

GPS, GINS-PC, déformation, surcharge non-maréale, Xynthia, Pyrenees

Abstract :

The temporal and spatial redistribution of the environmental masses deform the surface of the Earth. These deformations are observable by space geodetic techniques such as GPS. Since highly accurate IGS satellite and clock data are available and sophisticated algorithms have been developed, the integer fixed ambiguity Precise Point Positioning (iPPP) method opened a new era for the Global Positioning System (GPS) analysis and its application in geophysical studies. This work is among the first studies to investigate the different loading effects using iPPP time series, particularly using the GINS-PC software and the new, reprocessed REPRO2 orbit and clock products of GRGS (GR2). We aim to exploit the sub-daily iPPP time series to study various Earth deformation effects at different time scales, from sub-daily to seasonal and annual periods. Our goal is to contribute to the validation of geophysical models, to the observation of the various non-tidal phenomena, as well as the presentation of the performance of the iPPP mode and the GINS-PC package that is a powerful tool for geodynamical applications, and to investigate the influence of the loading effects on geodetic time series interpretation. After an overview of the main deformations of the Earth's surface induced by loading effects, we present the geodetic techniques that already demonstrated their potential in deformation analysis, in particular in loading deformation studies. We then review the GPS technique and the iPPP processing mode as it was our choice for the data analysis. We continue towards a global study which gives base for future research. After, we demonstrate two regional studies. The first one investigates the influence of the loading effects on GPS campaign to determine tectonic velocities in the Pyrenees mountain chain. The second case study attempts to track the spatial and temporal evolution of an extreme storm event, the Xynthia windstorm that occurred in France, in 2010. This study also tries to identify the ocean's response to the fast moving low pressure system using sub-daily iPPP time series.

Keywords :

GPS, GINS-PC, deformation, non-tidal loading, Xynthia, Pyrenees